DESIGN, DEVELOPMENT AND APPLICATION OF A NOVEL SEVEN-SENSOR PROBE SYSTEM FOR THE MEASUREMENT OF DISPERSED PHASE FLOW PROPERTIES IN MULTIPHASE FLOWS

A THESIS SUBMITTED IN PARTIAL FULFILMENT OF THE REQUIREMENTS FOR THE DEGREE OF DOCTOR OF PHILOSOPHY AT THE UNIVERSITY OF HUDDERSFIELD

By

Dlir Albarzenji

M.Sc. Teesside University, UK, 2012

B.Sc. Al-Mustaniriya University, Iraq, 1996

School of Computing and Engineering

University of Huddersfield

UK

May 2018

Abstract

Local measurements of the dispersed phase properties in air-water bubbly flows are of primary importance to understand the hydrodynamic characteristics of multiphase flows. One of the essential requirements in designing multiphase flow systems is to determine its flow regime since many constitutive models are flow regime dependent. In bubbly multiphase flow, the bubble diameter plays a vital role in hydrodynamics of flow.

In this study, a novel invasive measuring instrumentation system has been designed and developed to determine the bubble size and shape accurately by minimising the effects of the bubble-sensor interactions. This instrumentation system has been used to determine the effects of the bubble size on the volume fraction distribution and the hydrodynamic behaviour of air-water two-phase flow. The novelty of this probe arises from the fact that the data is collected from the first bubble-sensor contact, unlike the previous methods in which the data has been collected from two points namely, first when the sensors' tips immersed a bubble and second when the sensors' tips left the bubble.

The seven-sensor conductivity probe subsequently has been used to determine the dispersed phase local parameters. These parameters include bubble velocity, time-averaged local void fraction and bubble shape and size. The data from this probe has been acquired using National Instruments Data Acquisition (DAQ) and LabVIEW software.

The experiments have comprised of two methods, namely bubble column and flow loop. For the bubble column experiments, a new image processing code has been developed for capturing the dispersed phase properties, including the void fraction from the images that have been captured by the high-speed cameras. From the comparison between both methods, the seven-sensor probe and the high-speed camera measurements, good agreement has been achieved.

In the flow loop experiments, the novel seven-sensor probe system has been used for measuring the dispersed phase properties from the first bubble sensor contact; moreover, the effect of variation of gas superficial velocity, with the values of 0.05, 0.07 and 0.1 m/s, on the dispersed phase properties have been also investigated.

Declaration

- The author of this thesis (including any appendices and/or schedules to this thesis) owns any copyright in it (the “Copyright”) and he has given The University of Huddersfield the right to use such Copyright for any administrative, promotional, educational, and/or teaching purposes.
- Copies of this thesis, either in full or in extracts, may be made only in accordance with the regulations of the University Library. Details of these regulations may be obtained from the Librarian. This page must form part of any such copies made.
- The ownership of any patents, designs, trademarks and any and all other intellectual property rights except for the Copyright (the “Intellectual Property Rights”) and any reproductions of copyright works, for example graphs and tables (“Reproductions”), which may be described in this thesis, may not be owned by the author and may be owned by third parties. Such Intellectual Property Rights and Reproductions cannot and must not be made available for use without the prior written permission of the owner(s) of the relevant Intellectual Property Rights and/or Reproductions.

Acknowledgements

I would like to take this opportunity to thank all who supported me either directly or indirectly towards the establishment of this thesis. Foremost, I would like to thank almighty Allah for giving me the health and the ability to contribute and fill part of the knowledge gaps in literature. Secondly, I would like to acknowledge my deepest gratitude to my parents and siblings for their patience and support during my PhD journey.

I am also thankful to my supervisor Professor Rakish Mishra for his supervision, advice and guidance which made this work possible. Moreover, I would like to thank all the technicians in the mechanical engineering department and colleagues; espically Dr. Khaldoon Breatha for his support during my PhD work.

Finally, I would like to thank my lovely wife Ghadeer Mashni and my children Abdullah, Seren, and Naz for their patience and constant support throughout my PhD journey, without their help I would not be able to achieve this.

List of Contents

List of Figures

List of tables

Nomenclature

f_o	Oil volume fractions, dimensionless
V_{os}	Oil superficial velocity, m s^{-1}
V_m	Mixture superficial velocity, m s^{-1}
$V_{\infty\theta}$	Terminal rise velocity, m s^{-1}
V_∞	Terminal velocity of single bubble, m s^{-1}
k	Constant in k-ε model, dimensionless
cp	Centi Poises, viscosity unit equivalents to 0.001 ($N{\cdot}s/m^2$, or kg/(m.s))
ID	Internal Diameter, m
Δp	Local dynamic pressure, Pa
$\vec{v}$	Absolute velocity, m s^{-1}
S_m	The mass added to the continuous phase from the dispersed second phase
U_W	Water velocity, m s^{-1}
v_x	Axial velocity, m s^{-1}
v_r	Radial velocity, m s^{-1}
r	Radial coordinate
$\vec{F}$	External body forces, N
F_X	Axial external body forces, N
F_r	Radial external body forces, N
E	Internal specific energy, J kg^{-1}
P	Static pressure, Pa
J_j	Flux term of species j
S_h	Energy Sources Due to Reaction
u_i	Velocity vector of surface point
G_k	Represents the generation of turbulence kinetic energy due to the mean velocity gradients
G_b	Generation of turbulence kinetic energy due to buoyancy
Y_M	Contribution of the fluctuating dilatation incompressible turbulence to the overall dissipation rate
S_k, S_ε	User-defined source terms
$C_{1\varepsilon}$, $C_{3\varepsilon}$,	Constants in k-ε model, dimensionless
$C_{2\varepsilon}$, C_μ	Constants in k-ε model, dimensionless

L	Pipe length, m
K_{pq}	Exchange coefficient for bubbly, dimensionless
f	Drag function, dimensionless
d_p	Bubbles diameter or droplets of phase p, m
C_D	Drag coefficient, dimensionless
Re	Reynolds number, dimensionless
d_h	Hydraulic diameter, m
U	Mean velocity, m s^{-1}
R_{erel}	Relevant Reynolds number, dimensionless
I	Turbulence intensity, dimensionless
μ_q	Viscosity of the phase q, kg/m s
τ_p	Particulate relaxation time, s
α_q	Local Volume fraction of phase q, dimensionless
$\bar{\alpha}$	Mean volume fraction dimensionless
α_p	Local Volume fraction of phase p, dimensionless
ρ_p	Density of phase p, kg m^{-3}
ρ_q	Density of phase q, kg m^{-3}
β	Volumetric quality, dimensionless
ρ	Density, kg m^{-3}
∇	Del operator
μ_t	Turbulent viscosity, Pa s
$\sigma_k, \sigma_\varepsilon$	The turbulent Prandtl numbers for k and ε respectively
ν	Kinematic viscosity, cm^2 s^{-1}
μ_{rp}	Mixture viscosity of the phases: p and r, kg/m s
μ_p	Viscosity of the phase p, kg/m s
μ_r	Viscosity of the phase r, kg/m s
α_1	Local volume fraction, dimensionless
ε	Turbulent energy dissipation, m^2/s^3
$\rho\vec{g}$	Gravitational body force, N
μ	Dynamic viscosity, kg/m s
i, j, k	Unit vectors in x, y and z direction (probe coordinate system (m))
$\cap_i$	The unit vector in the direction of r
$\cap_v$	The unit vector in the direction of V
$\vec{r}$	Position vector of point of first contact of bubble with sensor 0(m)

r	Magnitude of r (m)
r_1	Position vector of point of first contact of bubble with sensor 1(m)
r_1	Magnitude of r (m)
V	Velocity vector
v	Velocity magnitude (m/s)
V_y	Velocity at the Y-axis (m/s)
V_z	Velocity at the z-axis (m/s)
V_x	Velocity or the velocity at the X-axis (m/s)
x, y, z	Probe Coordinate (m)
x_i	X-coordinates of i^{th} sensor with respect to sensor 0 (m)
y_i	Y-coordinates of i^{th} sensor with respect to sensor 0 (m)
z_i	Z-coordinates of i^{th} sensor with respect to sensor 0 (m)
α	Polar angle ($^{\circ}$)
β	Azimuthal angle ($^{\circ}$)
δt_{0a}	Time delays equal to zero (s)
δt_{0b}	Time taken for bubble to cross the sensor 0 (s)
$\delta t_{ia}, \delta t_{ib}$	Time delay between first bubble contact with the sensor 0 and first and last bubble contacts respectively with i^{th} sensor (s)

Chapter 1.

Introduction

Multiphase flows are integral to many engineering applications; such as boiling, condensing, cavitation, chemical reactions, heat exchanger, oil and gas industries, nuclear plants, etc. Therefore, this chapter provides information regards an overview on multiphase flows' measurement and instrumentation techniques and the hydrodynamics of bubbly flow. The motivation of this work has been established and presented in this chapter, and thereafter the three-main research aims have also been established and presented. Finally, the thesis lay out has also been presented in this chapter.

1.1 Introduction

The local flow properties of multiphase flows are of fundamental importance in many natural physical processes and in a host of industrial and engineering applications, such as power generation, nuclear reactor, automotive industry, aerospace and oil industry. Multiphase flows occur when two substances or more flow simultaneously with different densities in a pipe or a duct. Each phase is considered to have distinct flow properties. These properties include volume fraction, mean velocity and turbulent intensity etc. where, volume fraction is defined as the ratio of occupied volume of the substance to the overall volume at the point of examination. The orientation of the pipe has a major influence on the flow regimes since it affects the phases' flow behaviour, thus it affects the density distribution between the phases. Multiphase flows in pipelines can be comprised of flow of two or more phase. Two-phase flows can be in form of gas-liquid flow, liquid-liquid flow, gas-solid flow, liquid-solid flow and gas-liquid-solid flow. The flow models regarding the flowing mixtures of two immiscible liquids are frequently included in the design of several industrial equipment. For example, studies have been carried out to understand the reduction in apparent viscosity of heavy crudes oil by adding less viscous liquid, which is usually water. Reduction in viscosity reduces the pressure gradient, and the viscous liquid can be transported at a higher rate as a two-phase flow rather than as a single component under the condition of equal pressure drop. The distribution of the phases in a pipe has a strong effect on the important properties of two-phase flow such as pressure drop behaviour and volume fraction, which has been reported by Zavareh, et al. [1]. Prior to the investigation of multiphase flow measuring instrumentations and their capabilities, it is necessary to develop an overview of multiphase flow phenomenon. Besides, the selection of the best strategy to investigate multiphase flow characteristics is not possible without a clear understanding of the nature of the multiphase flow, as mentioned by Falcone, et al. [2].

1.2 The basic concepts of multi-phase flow

It is difficult to establish and develop mathematical formulations for quantifying the multiphase flows hydrodynamics, comparing to the single-phase flow, due to complex nature of multiphase flows. The multiphase flows structures are classified into flow regimes, the flow regimes distribution in any conduit depend on several physical parameters such as surface tension and gravity. The phases distribution in multiphase flows differs from case to other in term of time and location.

The main factors affecting the flow regimes formations are fluid properties, the pipe's geometry and orientation operating, conditions, and flow rates.

1.2.1 The primary and secondary phase(s) in two-phase flow:

Two-Phase Flows are considered to be the most common type of multiphase flows. Two-phase flows can be in form of gas-solid flow, liquid-solid flow, gas-liquid flow, and liquid-liquid flow.
In two-phase flows, one of the phases is denoted as continuous/ primary phase, whilst the other is denoted as secondary / dispersed phase. The continuous phase, phase 1, is the phase in which any two points or regions within the phase are joined by a line, straight or curved, which passes through the same phase without crossing the interface. Whilst discontinues phase, phase 2, is the phase in which any two points or regions of the phase cannot be joined neither in a straight nor curved line. However, in some circumstances the two can be continuous such as a stratified, wavy and annular flow in these cases the phase with lighter density is referred to be the secondary phase.

1.2.2 Superficial velocity and local, In situ, velocity

The superficial velocity is the phase velocity that can be measured from the inlet phase flow rate, Q_i, as:

$$U_L = \frac{Q_L}{A} \tag{1.1}$$

where here, U_L is liquid superficial velocity, Q_L is liquid inlet volumetric flow rate and A is the pipe cross-section.
The same way the gas superficial velocity can be calculated as:

$$U_G = \frac{Q_G}{A} \tag{1.2}$$

where, U_G is gas superficial velocity, Q_G is gas inlet volumetric flow rate and A is the pipe cross-section. whereas, the local or in situ velocity, u_i, can be defined as the ratio between the inlet phase flow rate, Q_i, where, i, refers to the phase status, liquid or gas, and the area that is occupied by each phase and the local or in situ liquid velocity can be written as:

$$u_L = \frac{Q_L}{A_L} \tag{1.3}$$

where, A_L is the local area occupied by the liquid phase.
And for the local or in situ gas velocity can be written as:

$$u_G = \frac{Q_G}{A_G} \quad (1.4)$$

where, A_G is the local area occupied by the gas phase.

1.2.3 The volume / void fraction (α), and the hold-up (H_L).

The local void fraction or volume fraction (α) is local measurement of the existence of the dispersed phase across the test pipe; moreover, it is a function of time and distance across a pipe or duct.
where, $\alpha = f(Physical\ properties, Phase\ distribution)$

$$\alpha = \frac{1}{t}\int_0^t P_k\,(r,t)dt \quad (1.5)$$

Chordal void fraction:

$$\alpha_{chordal} = \frac{L_G}{L} \quad (1.6)$$

Cross-sectional void fraction definition:

$$\alpha_{c\_s} = \frac{A_G}{A} \quad (1.7)$$

and for the liquid hold up, H_L, can be calculated as:

$$H_L = 1 - \alpha \quad (1.8)$$

1.2.4 The inlet volume fraction (β)

The quantity is measurable and depends on the flow rate measurement for both phase and calculated as:

$$\beta = \frac{Q_G}{Q_G + Q_L} \quad (1.9)$$

It is noticeably worth to mention that

$$\alpha \neq \beta \quad (1.10)$$

1.2.5 Phase Slip ratio and relative velocity

The phases of a multiphase flows, flow at different velocities, the liquid phase velocity generally is much slower than gas phase velocity. The difference between the local gas velocity and the local liquid velocity is known as the relative velocity, u_R, and it can be calculated as;

$$u_R = u_G - u_L \tag{1.11}$$

whereas the slip ratio, k, can be calculated as:

$$k = \frac{u_G}{u_L} \tag{1.12}$$

where, $\alpha, k = f(\dot{m}_G, \dot{m}_L \ fluid\ properties\ and\ geometry)$

where, $\dot{m}_G, \dot{m}_L$ are the gas and liquid mass flow rate respectively.

and

$$k = f(\alpha\ and\ x) \tag{1.13}$$

where x is Mass fraction

1.2.6 Mass Fraction (x)

Mass fraction is the ratio between the mass flow rate of the phase, $\dot{m}_i$, and the mixed mass flow rate, $\dot{m}$, and can calculated as

$$x = \frac{\dot{m}_G}{\dot{m}} \tag{1.14}$$

Or

$$1 - x = \frac{\dot{m}_L}{\dot{m}} \tag{1.15}$$

where, mixed mass flow rate, $\dot{m}$, is

$$\dot{m} = \dot{m}_G + \dot{m}_L \tag{1.16}$$

1.2.7 The nun-dimensional numbers, Reynolds number, (Re) and Etovos number (Eo)

Reynolds number, Re, is the ratio between the inertial forces and the viscous force. In multiphase flows, the Re can be written as:

$$Re = \frac{DU_M\rho_M}{\mu_M} \tag{1.17}$$

where, U_M is the mixture velocity and can be calculated as

$$U_M = \frac{Q_G + Q_L}{A} \tag{1.18}$$

ρ_M is the mixture density and can be calculated as

$$\rho_M = \alpha\rho_G + (1-\alpha)\rho_L \tag{1.19}$$

whilst Etovos number Eo, is the ratio between bouncy forces and surface tension forces and can be written as

$$Eo = \frac{g\Delta\rho d_e^2}{\sigma} \tag{1.20}$$

where, $d_e = (6V/\pi)^{0.334}$ is the volume-equivalent diameter of a bubble of volume V, and U is its terminal rise velocity; ρ, μ and σ are, the density, viscosity and surface tension of the liquid, respectively, g is the acceleration of gravity and $\Delta\rho$ is difference in density of the two phases.

.

1.3 Multiphase flows measurement techniques

The measurement of multiphase flows' properties is essential for understanding the nature and the behaviour of such flows in order to make a proper design of the system, providing accurate operational conditions and finally operating the system safely. It is also a prerequisite for proper code development, modelling and verification. The history of measurement techniques has started with visual observations of the multiphase flows properties through transparent pipes. Thereafter, and with the aid of novel technologies, different techniques have been introduced.

Boyer, et al. [3] have classified the instrumentation techniques according to their presence, in or out, of the flow domain, and have categorised them into two groups:

- Non-invasive techniques.
- Invasive techniques.

1.3.1 Non-invasive techniques

Many types of non-invasive techniques are being used for flow characteristics' measurement, these include:

1. Visual observations by using transparent pipes; this technique includes photographic and high-speed cameras. The weakness of this method lies in the fact that its application is limited to where the test section wall is transparent. Furthermore, it can be used in primarily 2D flow fields and in the 3D flow fields only where the gas void fraction is very low. Whilst for high volume fraction multiphase flow, the video imaging method can capture the near wall bubbles only.
2. Gamma-ray densitometry has been introduced for oil-water flow measurement recently. The non-intrusiveness, the low in cost and the portability are the advantages of using the Gamma-ray densitometry whilst the difficulty to obtain the local information due to the collimated beam of the gamma ray producing a line-averaged value is a big limitation. Moreover, the strength of the gamma source depends on the thickness of the pipe wall is considered to be another disadvantage of using this method, this requires increasing the radiation protection consequently reducing the device portability.
3. Differential pressure technique: this technique is used to measure pressure drop, liquid holdup, and flow regime. Whereas it cannot measure the bubble size and shape and the secondary and primary phase velocities.
4. Pressure fluctuation: this technique is used to capture flow regime and turbulence flow characteristics. However, this technique cannot measure the bubble size and shape and the secondary and primary phase velocities.
5. Dynamic gas disengagement technique, DGD, this technique is used for the global gas-solid holdup in a slurry bubble-column measurement, or for the gas holdup structure measurement in bubble columns. However, this technique cannot measure the bubble size and shape and the secondary and primary phase velocities.
6. Tracers: this technique is used to measure the mean volume fraction and characterizing the multiphase properties.
7. Conductimetry is a technique in which the liquid holdup can only be measured in an electrically conductive medium.
8. Neutron absorption: this technique uses a neutron source for measuring liquid holdup.
9. X-ray absorption: this technique employs x-ray for liquid holdup measurements.

10. Light attenuation can be used for measuring gas holdup and interfacial area. This is a proper technique for micro-bubbly flows measurement where the size of bubble is much smaller than the area imaged by a single pixel and where are many bubbles attenuating light within each pixel. The working principle of this method depends on light attenuation; when the flow domain is lit from the back side, the front view regions of high bubble concentration appear darker than rest region of flow field. The disadvantage of this method is when bubbles flow at higher velocities, the smaller bubbles may not be distinguished from the seeding particles.
11. Laser Doppler Anemometry, LDA, and Phase Doppler Anemometry, PDA, are mainly used to measure liquid velocity, gas velocity, and bubble size. PDA is extension of the LDA principle. The disadvantage of using this method is the overestimation of bubble velocity measurements of a dense bubbly flow due to the LDA's systematic error, moreover this system has shown limitation in measuring the largest bubble size and the highest bubble velocity.
12. Polarography (microelectrodes): this technique works with support of electrolyte to measure wall shear stress.
13. Capacitive or resistive tomography: this technique is for deciding phase holdup distribution. Due to the electrical field's non-uniformity inside the flow field; the Capacitance tomography cannot measure the distribution of volume fraction accurately. This default can be compensated by identifying the flow pattern first [4]. The other variable that affects capacitance measurements is temperature that changes the electrical properties of the two phases.

1.3.2 Invasive techniques

These techniques are much preferable to be used for the multiphase flows' properties measurement as compared to the non-invasive techniques due to the fact, that many of the non-invasive techniques become ineffective because of the effect of wall barrier. However, in this technique probe-flow interaction occurs, which may affect the probe's measurement accuracy. The most popular invasive techniques are:

1. Needle probe: This is a technique that uses a very thin-ended sensor directed to face flow direction. It is used to trace high gas holdup systems. In some cases, it could measure the whole gas phase characteristics.

   Needle probes are divided into two types:

   - Optical fibre probes.
   - Resistive or impedance probes.

   Needle probe techniques use a single or multiple sensor/s depending on the data to be collected. Single-sensor probes are used for measuring volume fraction and bubble frequencies, whereas

multi-sensors probes are used for collecting time-related measurements such as bubble velocity, time-average local interfacial area and average bubble chord length.

2. Heat transfer probe (hot film anemometry). This is a technique that uses the sensor's thermal sensitivity for distinguishing one phase from other and can measure both phases' velocities. The operational principle for hot film anemometry depends on the change in the electrical resistance due to the heat exchange occurrence between the probe's head and the surrounding media, which as a consequence produces signals that are finally interpreted to multiphase flow properties that can be measured. The sensitive element thickness varies between (25-100 μm), it is made of a quartz substrate (thermal insulation) re-covered with a platinum or nickel film and is protected from oxidation and abrasion by a quartz layer (1 or 2 μm thickness). This technique has been used for measuring bubbly flow characteristic since the bubbles exchange the heat as they pass the probe head. The characteristics that could be measured include drop velocity, continuum velocity, void fraction and bubble chord length in case of single hot film. Whilst Reynolds shear stress can then be determined in case of double hot film.
3. Pitot tube is one of the oldest devices for measuring flow direction, flow velocity, and pressure drop. It has frequently been used to determine the velocity profile in a pipe by measuring the velocity at various points. In its simplest form, the Pitot tube comprises of a small tube inserted into a pipe with the head bent, so that the mouth of the tube faces the flow, as shown in Figure 1.1. The pipe should be quite thin, usually 1-2 mm, to avoid any flow disturbance.

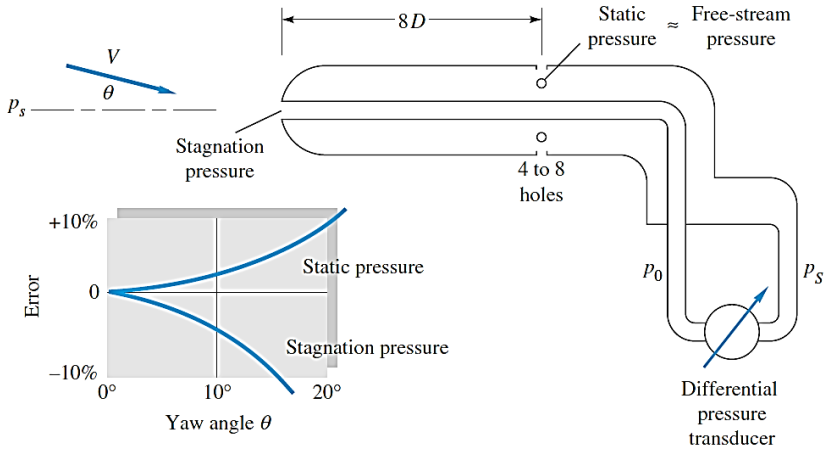

Figure 1.1. The schematic of Pitot- tube [5].

The measuring principle of the pitot tube uses the differences between the upstream and the downstream static pressures and by using Bernoulli's equation the water velocity, U_W, can be obtained from local dynamic pressure (Δp) and water density (ρ) as

$$U_W = \sqrt{\frac{2\Delta p}{\rho}} \quad (1.21)$$

4. Ultrasound probe: This technique uses Ultrasound technology for predicting gas hold up, bubble velocity, bubble diameter, and interfacial area concentration. The main advantage of using this technique is that no transparencies of flow or pipe wall are required. This method provides a relationship between either the transmission time difference or the energy attenuation of ultrasound and the solid loading to obtain the gas and the solid holdups by neglecting the change of bubble diameter occurring in the column. The drawback of using this method is that only one of the local secondary phase property is allowed to be measured by this technique; moreover, in cases where the void fraction is more than 20% this technique is ineffective method. Based on the comparison between the Ultrasound probe and the photographic technique that have been held by [6], a 20% of measurement error have reported when the Pulse Echo Technique has been used for ellipsoidal bubble size evaluation.

1.4 CFD Prediction

Multiphase flows are complex phenomenon. Therefore, it is difficult to model this phenomenon using the conventional techniques.

Currently, researchers are using the computational fluid dynamics (CFD) to examine this complexity of multiphase flows. CFD simulations have been used over the last few decades to better understand the interaction between the moving bubbles and the stagnant fluid in bubble-column [7]. Many attempts therefore have been made to develop this tool. Recent developments of the numerical modelling have been discussed by several authors [7-11]. Different methods toward modelling of bubbly flow have been shown in literature. These methods can be classified as:

1. Simple one-dimensional models [12-15].
2. Two-dimensional gas-liquid mixture models [16-19].
3. Two- and three-dimensional turbulent CFD approaches for flow field computations combined with a compartmental model for handling chemistry computations [20],
4. Two- and three-dimensional, two-fluid turbulent models with variations in the formulation of the Euler-Euler or the Euler Lagrangian approach [19, 21-40], and large-eddy simulation (LES) attempts [41] and [42].

The advent of digital computer with the improvements of computer resources gave the ability to solve a full set of fluid dynamic and multiphase flow equations numerically. This process is carried out by solving the balance equation set via domain discretization, using control volume approach, and by

converting the complex partial differential equations into simple algebraic equations. The advantages of using CFD is its ability to predict a detailed analysis of the flow combined with mass and heat transfer. Moreover, CFD simulation can show the detailed results in form of contour plots, which are difficult to be observed by using conventional techniques.

1.5 Driving forces in multiphase flow

According to Newton's first law, the fluid remains at rest unless acted on by an unbalanced force. Therefore, any fluid motion establishes from forces acting on the fluid elements. In case of multiphase flow, the forces that generate the flow motion can be classified as [43]:

1. Pressure force, this force acts on fluids surface and tends to accelerate the fluid phases in direction of the pressure gradient.
2. Inertia force, this force acts on the fluid volume and tends to maintain the velocity vector and magnitude unchanged.
3. Viscous force, this force acts on fluids surface and tends to modify the flow field from fluctuated flow to a uniform, in turn reduces the velocity fluctuations.
4. Gravity force is the force that drives the fluid density to accelerate toward the gravity vector direction
5. Buoyancy force is the force that is generated due to the difference between the force generated due to the difference phases density and the gravity force.
6. Surface tension force, this force forms wherever there are two fluids or more. Moreover, this force tends to reduce the surface area of the interfaces between the two fluids.

1.6 The interfacial surface forces[44]

Bubble's trajectory in Gas-liquid two-phase bubbly flow changes in direction during its motion. This change can be attributed to the surrounding forces acting on the bubble surface and diverting the bubble velocity vectors' directions consequently, forming different flow regimes. These forces can be mentioned as:

1. Drag Force.
2. Lift Force.
3. The Basset Force.
4. Wall Lubrication Force.
5. The Added Mass Force (or Virtual Mass Force).
6. Turbulent Dispersion Force.

1.6.1 Drag Force

When any object moves through a fluid, an interaction between the object and the fluid occurs, this effect can be described in terms of the forces at the fluid–object interface. Therefore, drag force can be defined as a force acting on a bubble/ particle in a parallel to the flow direction. Stokes is known to be the first researcher to establish the drag force exerted on a solid sphere in the flow of a very viscous incompressible flow [45]. He defined the drag coefficient, C_D, as:

$$C_D = \frac{24}{Re} \tag{1.22}$$

Since that time, many empirical models have been introduced to represent the drag coefficient [45-50]. However, the latter study, which has represented the Universal Drag Laws, is the most suitable for the drag coefficients calculation in a range of gas-liquid flow regimes. Moreover, the advantage of using these laws is that it can be used in both spherical and non-spherical droplets/bubbles cases flow in a fixed pipe diameter (not in variable pipe diameter).

1.6.2 Lift Force

Generally, lift force is the perpendicular to flow stream component of resultant pressure and shear forces. Saffman [51] is known to be the first researcher who derived the lift force in high viscous fluid, whilst Auton [52] is known to be the first researcher who derived the lift force in inviscid fluid. In bubbly two-phase flow, the action of the lift forces on a bubble surface is mainly due to the predominate-phase velocity gradients between the pipe wall vicinity and pipe centre vicinity. Lift force is more substantial in cases where large bubble diameter is presented. The lift force, $\overrightarrow{F_L}$, can be calculated as [53] :

$$\overrightarrow{F_L} = C_L / \rho_l (\overrightarrow{w_g} - \overrightarrow{w_l}) \text{ X } (\overrightarrow{w_l}) \tag{1.23}$$

where, C_L is lift coefficient, ρ_l is liquid density, $\overrightarrow{w_g}$ is gas velocity, and $\overrightarrow{w_l}$ is liquid velocity.

1.6.3 The Basset force

The Basset force is the force that is generated due to the development of the boundary layer with the alteration of the object's acceleration [54]. The Basset term, or so-called history term, tracks the time-based postponement in boundary layer development for the viscous effects during the object acceleration. The implementation of this force is hard. Therefore, it is neglected when the dispersed phase acceleration is low; while its effect cannot be neglected in cases of high accelerated objects [55].

1.6.4 Wall Lubrication, lift, Force

The wall lubrication force is a force that has the tendency to drift the bubbles away from pipe's wall. This tendency arises from the effect of the slow velocity between the bubble and the wall comparing to higher velocity between the bubble and the flow stream, which in turn causes a pressure gradient that forces the bubbles to create pipe-centre peak region. This force has first been introduced by Antal [56]. Later, Tomiyama et al [50] have improved the model and introduced the wall lubrication force as:

$$\overrightarrow{F_W} = -C_W \frac{d_{bubb}}{2}\left(\frac{1}{y^2} - \frac{1}{(D-y)^2}\right)\rho_l w_{rel}^2 \overrightarrow{n_r} \quad (1.24)$$

where, D is pipe diameter, y is the distance to the nearest wall, C_W is a constant depends on the Eotvos number, $\overrightarrow{n_r}$ is the unit outward normal vector on the wall surface, d_{bubb} is bubble diameter, ρ_l liquid density and w_{rel} is relative velocity.

Many attempts have been conducted to get better understanding of the wall lubrication forces, however, there is not a complete description of the cause of these forces available [57].

1.6.5 Turbulent Dispersion Force

The effect of the turbulent fluctuation of liquid on the bubbles has been known to be one of the main sources of the turbulent dispersion force side by side to the drag force between the phases and the effects of the turbulent eddies [58]. Furthermore, this force acts as a turbulent diffusion force in bubbly flow, which is in turn drives the bubbles away from the vicinity of the wall towards the vicinity of the pipe centre.

1.6.6 The added mass force (or virtual mass force)

Generally, the acceleration of any object in fluid displace some of the surrounding fluid, consequently extra force is required to displace the surrounding fluid. This extra force is known as the added mass force or virtual mass force. The virtual mass force can be calculated from

$$\frac{\alpha_d F_d^V}{B_d} = -C_M \rho_c \left(\frac{D_d v_r}{Dt} - v_r \cdot \nabla v_c\right) \quad (1.25)$$

where C_M is an induced mass coefficient B_d, the volume of a bubble α_d is the average overall void fraction, F_d^V is virtual mass force, ρ_c is continuous phase density, v_r is relative velocity and v_c is continuous phase velocity.

It can be obvious from the above that bubble diameter is a significant dispersed phase property to be measured accurately to measure these forces.

1.7 Bubble Shape, Motion, and Size Distribution

Bubbles and drops have a tendency to deform during their motion. This occurs due to their subjection to the unbalanced external fluid field, normal and shear stresses at the fluid-fluid interface [46]. These external deforming forces oppose by the bubble or particle surface tension force that always forces the bubble to have a uniform spherical shape, since spherical shape occupies the smallest volume in a medium.

In vertical pipes, when gas and liquid flow upward, in the opposite direction of the gravity vector, bubbles tend to flow faster than the nearby liquid due to buoyancy effect, moreover, large bubbles flow faster than small bubbles. The motion of bubbles is very complex. Fan and Tsuchiya [59] have stated that bubble shape has a direct effect on the bubble trajectories and the bubble polar angle.

Bubbles in motion are generally classified by their shapes such as spherical, oblate ellipsoidal and spherical/ellipsoidal cap, as illustrated in Figure 1.2 [60].

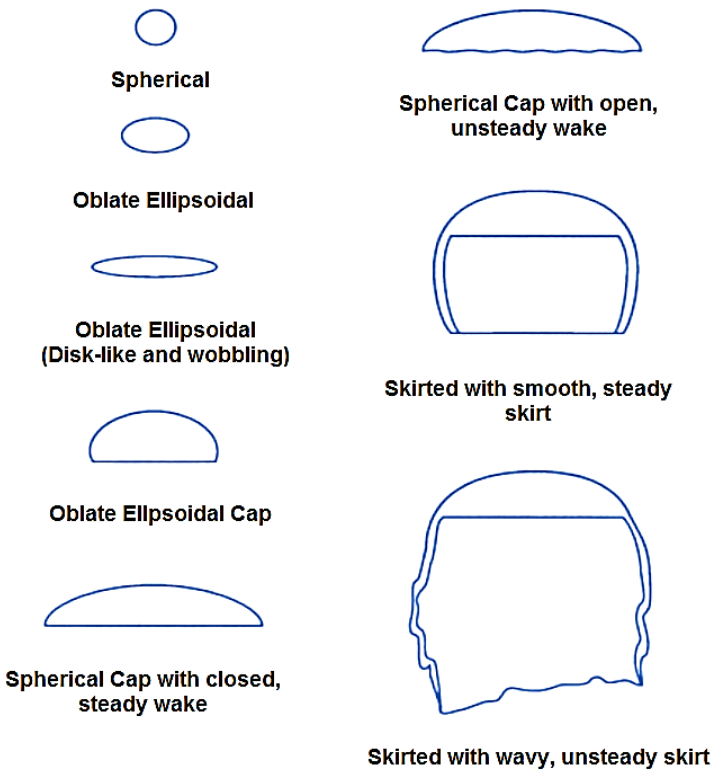

Figure 1.2. Sketches of various bubble shapes observed by Bhaga and Weber [60].

Clift and Weber [46] have classified bubble shapes in a free rise or fall in infinite media under the influence of gravity as Spherical, Ellipsoidal and Spherical/Ellipsoidal cap. These bubbles take spherical shapes when the interfacial tension and/or viscous forces overcome the external inertia forces acting on the bubble surface. The authors have observed that pipe wall has a significant effect on the bubbles shape as well as the mentioned forces. Furthermore, the authors have correlated bubble shapes in term of the Eotvos number, Eo; Morton number, M; and Reynolds number, Re and plotted the outcome as Figure 1.3.

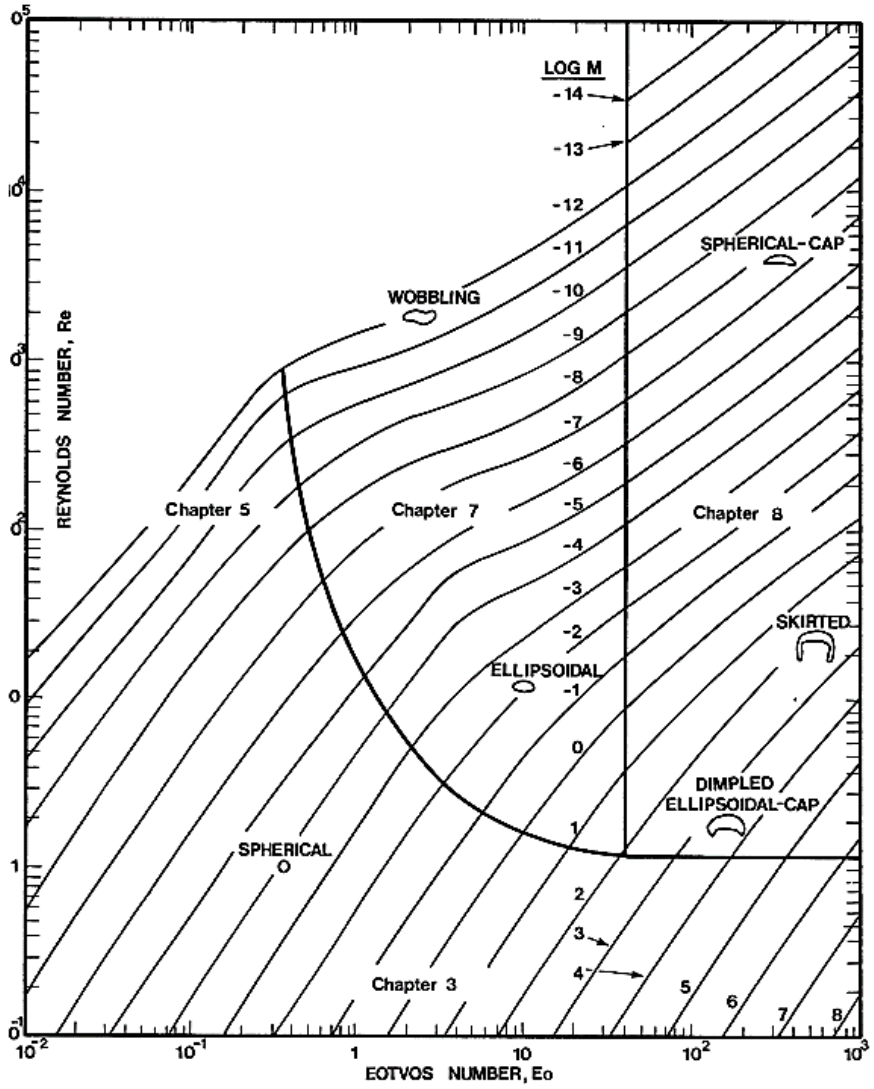

Figure 1.3. Bubbles shape regimes and drops in unhindered gravitational motion through liquids [46].

where,

$$Eo = \frac{g\Delta\rho d_e^2}{\sigma} \tag{1.26}$$

and

$$M = \frac{g\mu^4\Delta\rho}{\rho^2\sigma^3} \tag{1.27}$$

whereas,

$$Re = \frac{\rho d_e U}{\mu} \tag{1.28}$$

Bhaga and Weber [60] have suggested when the bubble shapes are represented in term of dimensionless equations; the use of drag coefficient, C_D, and Weber number, W, are related through a set of relations that had been presented by Clift and Weber [46] and cannot be used separately.

$$C_D = \frac{4gd_e}{3U^2} \tag{1.29}$$

$$W = \frac{\rho U^2 d_e}{\sigma} \tag{1.30}$$

where, $d_e = (6V/\pi)^{0.334}$ is the volume-equivalent diameter of a bubble of volume V, and U is its terminal rise velocity; ρ, μ and σ are, the density, viscosity and surface tension of the liquid, respectively, g is the acceleration of gravity and $\Delta\rho$ is difference in density of the two phases.

1.8 Bubble Interaction Mechanisms

In order to briefly demonstrate the mechanisms responsible for bubbles' coalescence and breakup, Wu, et al. [61] have classified these phenomenon :

- Coalescence through random collision driven by turbulent eddies.
- Coalescence due to the acceleration of the following bubble in the wake of the preceding bubble.
- Break-up due to the impact of turbulent eddies shearing-off of small bubbles from larger cap bubbles.
- Breakup of large cap bubbles due to interfacial instabilities.

Kocamustafaogullari and Ishii [62] have classified the Break-up and the collision mechanisms for a bubbly two-phase flow according to different sources that causes these phenomenon, as shown in

Figure 1.4. As for the Break-up phenomenon is concerned, the authors have summarized the causing mechanisms as:

- In turbulent flow, Break-up occurs due to local turbulent impact.
- In laminar flow, Break-up occurs due to viscous shearing-off.
- Interfacial instability, Break-up occurs due to Rayleigh-Taylor and Kelvin-Helmholtz instabilities.

Whilst, for the the collision phenomenon they have explained the causes due to:

- Shear layer induced velocity differences
- Wake entrainment
- Size dependent rise velocity differences
- Turbulent fluctuations

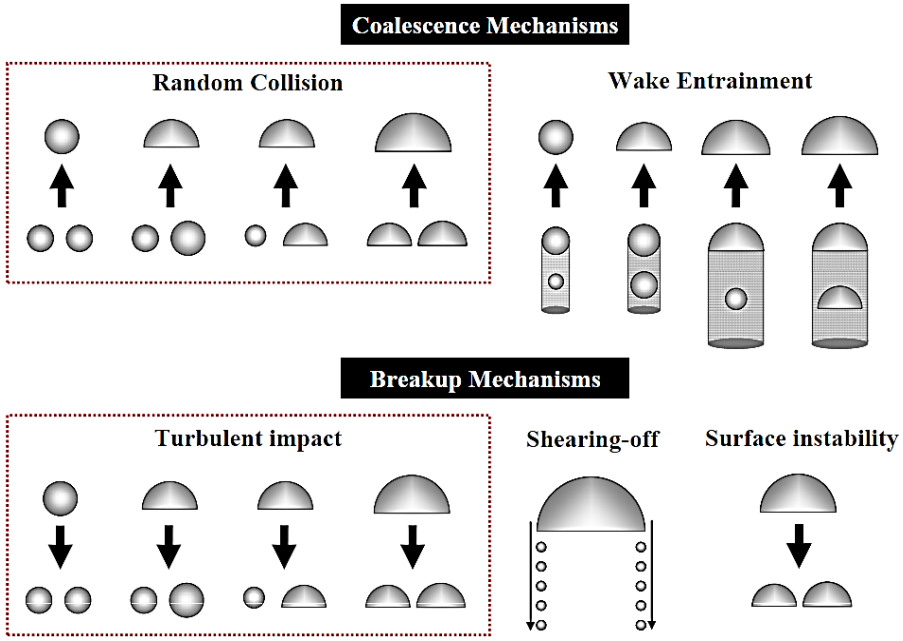

Figure 1.4. The bubble coalescence and the breakup mechanism [62].

1.9 Bubble columns

In biochemical chemical and petrochemical industries, Bubble columns are utilized as multiphase reactors. Several advantages can be provided whilst using the Bubble columns such as low maintenance and operating costs and high rates of mass and heat transfer.

In recent years, due to influence on transport characteristics and complex hydrodynamics of bubble columns; a considerable attention has been given to the design of these systems. Despite of the

simplicity of bubble columns construction, accurate and successful design requires an improved understanding of multiphase fluid dynamics and its influences. Generally, bubble columns applications depend on its aspect ratio, length-to-diameter ratio, for instance industrial bubble columns usually operate with an aspect ratio of at least 5, whilst in case of biochemical applications, these operate with aspect ratio in the range between 2 - 5 [63]. Bubble columns, operates under two mode types, namely the continuous mode and the semi-batch mode. In continuous mode, the gas and the liquid phases flow simultaneously upward into the column thereafter the liquid phase returns to the feed tank. In this operating mode, the liquid phase superficial velocity is kept being lower than the gas phase superficial velocity at certain value. Whilst in case of semi-batch operating mode, the liquid phase is kept stationary, and the gas phase is compressed into flow domain in form of bubbles moving upwards. The bubble column reactors designs are based on the three phenomena [64]:

1. The characteristics of transferring heat and mass.
2. The characteristics of mixing phases.
3. The chemical kinetics of the reacting system.

Therefore, previous studies have highlighted the requirements of improving the understanding of the multiphase flows hydrodynamics and its impact on void fraction, transport characteristics and mixing of phases.

1.10 The Effect of Bubble Size Distribution on Mass Transfer

The bubble column reactors are most frequently characterized by the overall volumetric mass transfer coefficient, k_La, which consequently depends on Interfacial area that allows mass to transfer across the gas and /or liquid interfaces.

where k_L is the true mass-transfer coefficient and the gas-liquid interfacial area, a, can be related to the gas void fraction, ε_g, and the Sauter mean diameter, the volume-surface mean diameter of bubbles, ds, that can be calculated by:

$$a = \frac{6\varepsilon_g}{\mathrm{ds}} \tag{1.31}$$

where the Sauter mean diameter is calculated from:

$$\mathrm{ds} = \frac{\sum_{i=1}^{n} n_i \, d_{b,i}^3}{\sum_{i=1}^{n} n_i \, d_{b,i}^2} \tag{1.32}$$

where $d_{b,i}$ is the volume-equivalent diameter of the mid-sized bubbles within the i-th size-class, and n_i is the number of bubbles with size db,i.

In multiphase flow systems, k_L is estimated either from the knowledge of the surface renewal rates or the contact time [65]. Therefore, measuring the bubble diameter accurately increases the mass transfer rate measurement accuracy.

1.11 Motivation

The knowledge of bubble properties including bubble velocity, bubble size and shape, volume fraction and specific interfacial area are highly important for an appropriate design and operation in many engineering disciplines, as power generation, nuclear reactor, automotive industry, aerospace and oil industry, bubble columns reactors, etc. In a bubble column reactor, the variation in the volumetric mass transfer coefficient is primarily due to variations in the specific interfacial area. The specific gas-liquid interfacial area is related to the volume fraction and the bubble size distribution, whilst volume fraction is determined by the bubble size distribution, bubble velocity and bubble frequency.

Regardless the pioneer researches which has been carried out in multiphase flows field, the state of knowledge has not yet satisfied the design process of the multiphase flow system equipment. This circumstance is a consequence of the extreme complexity of the multiphase flows and remembering the fact that there are no completely satisfactory theoretical models for turbulent flows of even single-phase fluids. In multiphase flow systems, the interface between the phases are very complex, therefore, a completely satisfactory theoretical model has not been achieved.
Bubble properties play key role in determining the heat transfer rate in bubble columns as mentioned by Yang, et al. [66]. Furthermore, bubble size distribution and bubble velocity distribution are key parameters in evaluating the drag forces acting on bubbles and in using the bubble population balance in Computational Fluid Dynamics (CFD).

Many Methods are available to measure the bubble size distribution. These methods have been surmised by [67]:

1. Video imaging [46], [68] and [69]. This method is a non- invasive method that has been used by many researches to study bubbles properties in gas-liquid bubbly flow and columns. The drawback of using this method is its application is limited to where the test section wall is transparent. Furthermore, it can be used in primarily 2D flow fields and in the 3D flow fields only where the gas void fraction is very low. Whilst for high volume fraction multiphase flow, the video imaging method can capture the near wall bubbles only. Furthermore, the transparent walls such as glass or Plexiglas cannot bear high pressures. This in turn limits its application to high pressure flow fields. Therefore, the usage of video imaging will be limited in certain cases where the pressure is not high in the measurement field.

2. Dynamic gas disengagement technique [70]; [71]; [72] and [73]. This method holds a lot of approximations and impractical assumptions, especially the way of obtaining the bubble size from the connection of the bubble size to the terminal rise velocity in a stagnant medium. Moreover, the bubble rise velocities has been calculated by incorporating several approximations [71].
3. Needle probes [74-83]. This is an intrusive method with a wider application comparing to the previous methods. It has the ability to measure flow properties in a high dense bubbly flow and under high-pressure media, therefore, until now invasive-techniques are considered to be the state of the art techniques for measuring the dispersed phase properties including the bubble size. In general, the drawback of this method for measuring bubble size is that bubble size is measured by converting bubble chord length to bubble diameter. The chord length is the product of the time duration of the corresponding pulse of the probe signal and the rise velocity of bubble at that moment; this in turn does not measure the real velocity due to the fact that bubble slows down during the traveling process through the sensor.

As it was mentioned above, none of the proposed techniques can claim a universal applicability, moreover, some of them have considerable drawbacks and may fail in particular practical situations.

The motivation for the work presented in this thesis is to develop and implement an innovative invasive multi-sensor probe that can measure the true size and shape of bubbles, has the ability to measure irregular bubble shape, is low cost in fabrication, simplicity of operation and easily infer the results at low bubble-sensor interactions. Moreover, it is appropriate to obtain bubble properties in a dense and high bubble velocity bubbly flow media. Consequently, this novel probe is going to be applied in measuring and imaging the multiphase flows properties in large pipelines and in water column reactors, which may fulfil the gap left open by current measuring techniques.

1.12 The research aims

This section describes the precise research aims in this research study. However, the objectives for this study will be discussed after carrying out an extensive literature review in the next chapter. Based on the motivation of this study, the research aims have been specified into the following:

1. Introducing a novel intrusive measuring system that has the ability to measure bubbles size and shape in addition to the other dispersed phase properties.
2. Reducing the bubble-sensor interactions, enhancing the measurement accuracy and extending the flow-field velocity range application of multi-sensor probes.

3. Investigating the local dispersed phase property in bubbly multiphase flows experimentally in cases of a stagnant and moving primary phase.

1.13 Organization of the Thesis

Chapter 1: This chapter provides an overview of the multiphase flows. The multiphase flow measurement techniques and the bubble interaction mechanisms have been presented. From this synopsis, the motivation for carrying out this research has been described. It identifies key areas to be reviewed in Chapter 2.

Chapter 2: This chapter comprises of a detailed review of the research works that have been carried out in multiphase flows in general and in the development of multi-sensor probes. It includes the review of published literature regarding the two, four and five sensors probe in particular. Moreover, the signal and data processing schemes have also been reviewed. Details of the scope of research has been provided in the form of specific research aims and objectives.

Chapter 3: This chapter sheds light on the project methodology. These include water tank, flow loop construction, a new traversing system mechanism and electrical circuit boards. Furthermore, a detailed discussion on material and component selection has been highlighted in this chapter.

Chapter 4: This chapter presents the results. The mathematical model has been developed to convert the time-delays into a valuable dispersed phase data. The novel probe design and fabrication procedures have been illustrated in detail. The signal processing code and signal conditioning methods also have been presented. Detailed studies on the effect of the flow-sensor interactions on the sensor and the probe body bending moments have been conducted. Moreover, the effect of the variation of pipe diameters, flow velocities and the probe radial locations has been analysed. Thereafter, mathematical expressions have been introduced that collect all these variables in three dimensional equations for each sensor. Thereafter, these expressions will be embedded in the signal processing code.

Chapter 5: This chapter represents the discussions. Two types of experiments have been carried out in this chapter namely, bubble column tests, where the primary phase is not in motion and flow loop tests, where both phases are in moving status. Furthermore, the data has been critically analysed and discussed in this chapter.

Chapter 6: This chapter shows the conclusions of the study, clearly mentions the objectives that have been achieved and the contributions of knowledge made. Finally, recommendations for future work have also been introduced.

Chapter 2.

Literature review

The general area of the research and the research background have been discussed in the previous chapter. Moreover, the specific area where further research is needed has been identified. Furthermore, the purpose and the motivation of the study, which have outlined the aims of the study, have been stated. Finally, the outline of the chapters of the thesis has also been stated. A critical literature review has been carried out in this chapter; highlighting the different techniques of multi-sensor needles probe for measuring multiphase flows properties. Moreover, the knowledge gaps in the existing literature have been identified. Depending on the gaps in knowledge that have been found in the literature, the research's scope and objectives of this study have been identified.

2.1 Literature review

Multiphase flows are integral to many engineering applications; such as boiling, condensing, cavitation, chemical reactions, heat exchanger, oil and gas industries, nuclear plants, etc. Therefore, a wide spectrum of literature is available in which various aspects of multiphase flows have been investigated experimentally, mathematically and by using the commercial codes available. The dispersed phase flow parameters have been investigated experimentally primarily using two types of methods i.e. intrusive methods and non-intrusive methods. Among the intrusive group, various multi-sensor probes have been used successfully for measuring flow properties by various researchers. In this chapter, the operational principal of multi-sensor probe systems, such as the sensor sizes arrangements and signal processing, moreover the knowledge gaps in the existing literature will be introduced. Moreover, scope of the research has been defined and the research objectives of this study have been conveyed based on the knowledge gaps that have been found in the literature review.

2.2 Multiphase Flow patterns

From a practical engineering prospect, the mass, momentum, and energy transfer rates are considered to be the main design difficulties facing multiphase flow systems operator. The phase distribution in multiphase flow is quite sensitive to the transport geometry. Therefore, the interfacial area between the phases for exchanging the mass, momentum and energy may strongly be affected by the nature of the pipe geometry. Moreover, it has been established that there is a complicated two-way coupling between the phases and each phase and the geometry of the pipe.

It is difficult to predict pressure dope, heat and mass transfer chrematistics and the rate and kinetic of reaction, in case of reaction, without the knowledge of flow distributions within the transport pipe, which is the flow pattern. The flow pattern represents the phase distribution under a particular circumstance, phases velocities and pipe diameter and inclination. The flow regime, or flow pattern, can be defined as a graphical representation that represents all range of existence flow regimes in term of two axes. The typical multiphase flow patterns can be illustrated in Figure 2.1.

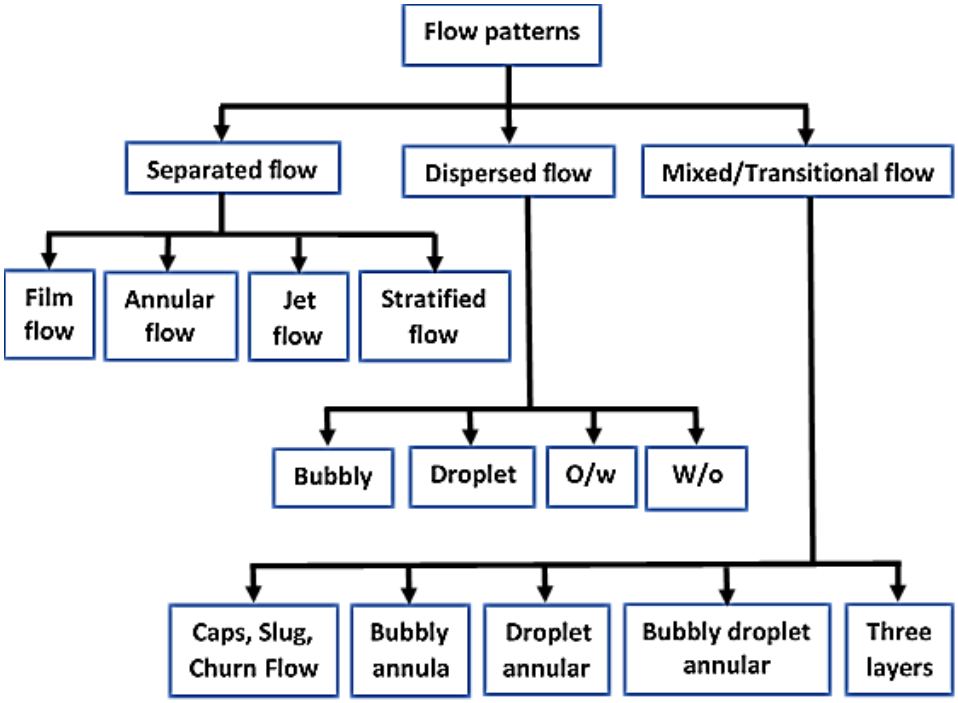

Figure 2.1. The typical multiphase flow patterns

A large number of attempts have been conducted to identify the flow pattern axes in three pipe inclinations at different flow circumstances:

2.2.1 Multiphase flows in horizontal pipelines

Multiphase flows investigation in horizontal pipes have been carried out by researchers to quantify the flow properties in horizontal pipelines. Many multiphase flows patterns have been observed in horizontal pipes, for instance, Baker [84] has introduced the most widely quoted flow pattern maps of gas-liquid two-phase flow in horizontal pipes and this map predicts the transition between two-phase flow regimes for adiabatic flow in small-diameter pipes. The mass fluxes of the phases as the characteristics of the fluid have been introduced as the map's axes. The author has also accounted for the effect of surface tension and density in the flow pattern maps. Russel, et al. [85] have studied oil-water flow in a horizontal transparent pipe. They have used white mineral oil with a viscosity of 18 cp at 77˚ F. Three distinct flow patterns have been found: bubbly, stratified, and mixed flow. Charles, et al. [86] have observed four flow patterns in two-phase oil-water flow in 2.5 cm pipes. These patterns have been water droplets in continuous oil, concentric water flow with oil flowing in the core, oil slugs in water, and oil bubble in water. Three different oil viscosities of 6.29, 16.8 and 65 cp have been used in the study. It has been perceived that oil-water flow regimes are mostly independent of the viscosities of oil.

Mandhane, et al. [87] have created a flow regime map based on extensive observations by several researchers in the literature, as presented in Figure 2.2. This type of maps is considered the most commonly accepted flow patterns map for horizontal pipes. Moreover, it covers a vast range of gas-liquid two-phase flow parameters, such as gas and liquid superficial velocities, pipe diameter, gas and liquid densities, viscosities, and surface tension.

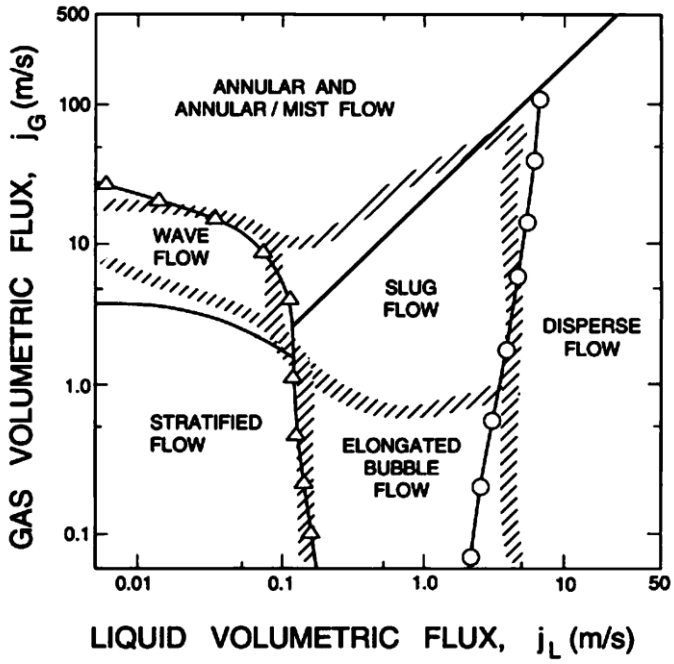

Figure 2.2. Horizontal flow pattern map [87].

Figure 2.2. Horizontal *flow pattern map [87].*depicts the horizontal flow pattern map that has been created by [6], this map has been created by plotting the gas volumetric flux, J_G , against the liquid volumetric flux, J_L, based on the data that had been collected from the experimental data. In this map, 6 of two-phase patterns have been presented namely, bubbly, wavy, Annular and Annular/mist, slug, stratified and dispersed flows.

Taitel and Dukler [88] have produced a flow regime map using a theoretical approach which has been used widely with some revisions to the interfacial factor of friction. The flow patterns, that have been created by Trallero, *et al*. [89], as shown in Figure 2.3, have matched the previous published data by Taitel and Dukler. However, this map has excluded the observation of clean water layer as one of the flow patterns in water-oil flows.

Shi, et al. [90] have studied the flow characteristics and the effect of surfactant on oil–water mixing and oil-wetting of the pipe wall. The experiment has been conducted at a temperature of 25˚C and a pressure of 0.136 MPa in a horizontal pipeline with an internal diameter of 100 mm, and a length of

4000 mm. The investigation has been carried out at input water cuts of 20, 40, 60, and 80 percentages. ASTM standard seawater and oil, of viscosity 3 cp at 25˚C, have been used. The mixed superficial velocities have been varied between 0.4 to 3.0 m/s in this investigation. Angeli and Hewitt [91] have studied the flow structure of water-oil two-phase flows in two test pipes, steel and acrylic, with inner diameters of 24.3 mm and 24 mm respectively. Two methods have been used for the flow regime investigations, namely high-speed video recording and high-frequency impedance method. Ranges of flow properties have been investigated in the experiment; the mixture velocity was varied between 0.2 to 3.9 m/s and volumetric quality was in the range of 6% to 86%. It has been found that the pipe wall material has a significant effect on the volume fraction distribution at low mixture velocities. In a certain range of conditions, the distribution of the phases differs dramatically between the stainless steel and the acrylic pipes. Xu, et al. [92] have investigated the effect of the inlet flow-rate, the inner diameter of the pipe and different oil viscosities on the slip occurrence between phases in water-oil two-phase flows horizontal pipe. The holdup measurement has been also investigated using two horizontal pipes of 50 mm and 25 mm inner diameter.

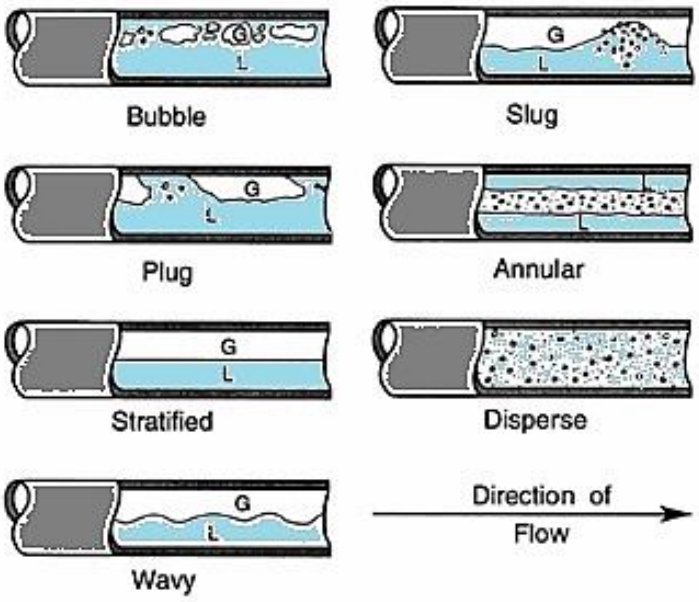

Figure 2.3. Flow pattern of gas-liquid observed by Trallero, et al. [89].

Al-Yaari and Abu-Shakh [93] have studied the oil-water two-phase flow patterns in a horizontal pipe using a commercial CFD code ANSYS 6.2. The modelled pipe has had an inner diameter of 25.4 mm. Volume of Fluid (VOF) and an adopted RNG k–ε turbulence model have been used for the multiphase flows' investigation. The CFD model has predicted the oil layer successfully. However, water layer could not be clearly observed in this investigation. Bottin, et al. [94] have investigated the local

properties for the dispersed phase in air-water two-phase flows in a horizontal pipe. These properties include velocity, turbulent kinetic energy and dissipation rate, void fraction and bubble size profiles. Optical probe, hot film anemometry, and video camera have been used for the investigations. A test pipe of 4500 mm long and 100 mm inner diameter has been utilised for the experiment. It has been observed that the flow in horizontal layers has been organised by buoyancy effects and the axial slip velocity between liquid and gas has been almost zero in the central region of the pipe. Furthermore, the optical probes' measurement has revealed that the bubble axial velocity has been 10% below the liquid phase velocity.

2.2.2 Multiphase flows in inclined pipes

Extensive studies have been conducted to assess the effect of pipe inclination on the multiphase flows' properties. This assessment has included the study of balancing between the effect of inertial forces, viscous forces and body forces and their effects on the flow regime. It has been observed that two-phase gas-liquid in inclined pipelines flow as bubbly, slug, churn and annular flow as shown in Figure 2.4.

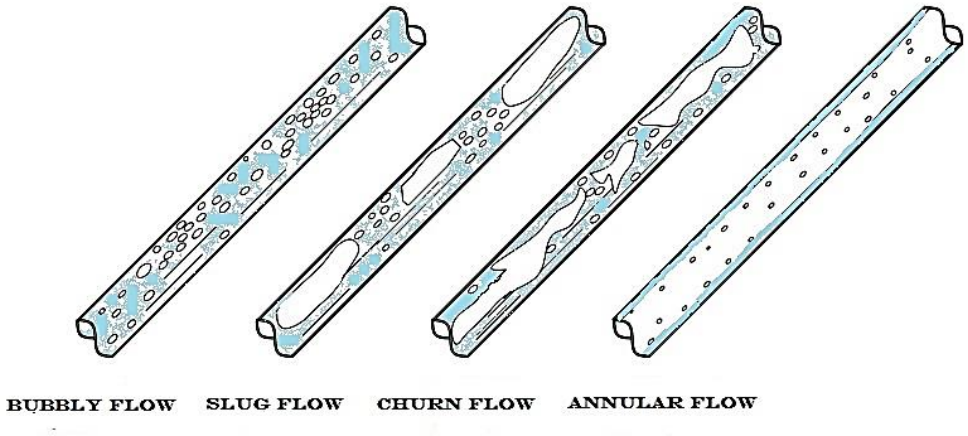

Figure 2.4. Flow pattern of gas-liquid in inclined pipelines.

Beggs and Brill [95] have investigated the effect of pipe inclination on liquid holdup and pressure losses of gas-liquid two-phase flows in inclined pipes. The liquid hold-up has been measured by trapping the liquid in the test section using several valves, whereas the pressure-drop has been measured by using pressure transducers. Two acrylic pipes of 27.4 m long with 25.4 and 38.1 mm internal diameters have been used. It has been reported that the water holdup has a direct dependency on the pipes' inclination angles. It has also been reported that the friction loss is greatly affected by water holdup.

Wicks and Fraser [96] have reported that the corrosion in pipes could be commonly found in areas where water may be accumulated, such as bends and valleys. For instance, the corrosion rates in highly turbulent flow have been observed to be much lower than those in low turbulent flow. The authors have related this phenomenon to the formation of a separate water phase layer at the bottom of the pipes. The effect of the minimum oil velocity, that has been required to drag the water droplets, has also been studied. It has been concluded that Kelvin-Helmholtz waves have been formed on the surface of the water because of increasing oil velocity over an accumulated mass of water. At higher velocities, the waves have become unstable and water-droplets have been formed as the waves break. Then, these droplets have circulated in an axial vortex and have travelled several pipe diameters, slid back and re-joined the primary water mass.

Mukherjee, et al. [97] have studied the effect of inclination of pipe on pressure drop and water holdup for inclinations ranging from ±30˚ to ± 90˚ from the horizontal in a 38.1 mm diameter pipe. Diesel fuel and water have been used- in the study. It has been found that the maximum slippage has occurred at the smallest inclination angle of -30˚. Based on the studies, authors have recommended that further studies are required to carry out further investigations for pipe inclination angles between +30˚ and -30˚, as maximum slippage may be observed in this range.

Vigneaux, et al. [98] have conducted experiments on kerosene (density = 0.74 g/cc) and water mixture for inclinations between 5˚ and 65˚ from the vertical in 10 cm and 20 cm internal diameter pipes. The mixture velocities in the range of 0.1 to 0.5 m/s have been used. The authors' studies have concentrated on the effect of the inclination and the mixture velocity on the slip velocity between the oil and the water, and on radial water volume fraction. In the case of low oil volume fraction, the slip velocity has been very high with the presence of the pipe inclination effect. Thus, the oil droplets have tended to move as a swarm. As the oil volume fraction has increased, the oil content at the bottom of the pipe has increased, and the slip velocity has reduced due to the recirculating bubbles. A higher interaction has been observed, and the back-flowing droplets have reduced the mean oil velocity.

Zavareh, et al. [1] have investigated the flow pattern in vertical and inclined transparent acrylic pipe. The test pipe specifications include a length of 12.8 m with an internal diameter of 184.15 mm. The dispersed phase has been injected at of 57.15 mm from the pipe inlet. Oil with density of 0.783 g/cc and viscosity of 2.46 cp, and distilled water with density of 1.0 g/cc and viscosity of 1 cp have been used in this study. In case of the 5˚ pipe inclination to the vertical, the authors have observed that at a high-flow rate the nature of oil droplets' flow has been in the same manner as the one seen in the vertical pipe. Whilst at low flow rate, the phases have tended to segregate, where the oil bubbles have tended to gather in the upper side of the test pipe, and the continuous phase has tended to flow in the lower pipe part. In the case of the 15˚ pipe inclination to the vertical, the authors have found that it has been similar to the 5˚ inclination case with smaller oil droplets sizes at higher flow rates. The authors

have also observed flow regime of a counter current bubbly flow when the pipe has inclined at 5˚ or 15° from vertical.

Spindler and Hahne [99] have studied the effect of the tube inclination on the void fraction profile in a water-air two-phase flow experimentally. A fibre optics probe has been utilised to investigate the void fraction and bubble frequency of adiabatic bubbly flows. The experimental setup has comprised of two test tubes with the inner diameters of 22 and 16 mm for 4000 mm of length; the tube inclinations have been in the range of 0-90º. The authors have observed that the angle of inclination has had a direct effect on the void fraction profile. Moreover, the effect of bubble diameters on the flow pattern transition has also been observed.

Experimental and theoretical studies of oil-water flow have been carried out by Flores et al. [100] in vertical and inclined pipes to characterize flow patterns and to develop models that predict flow pattern transitions, hold up and pressure drop. The studies have been carried out in a transparent test section of 25.4 mm ID and 1.5 m long using a mineral oil (0.02 kg·m−1·s−1. of viscosity and 845 kg/m^3 of density) and water. The inclination angles of 90˚, 75˚, 60˚, and 45˚ from horizontal have been used. In case of water dominant flow patterns, significant slippage has been observed. This slippage has been pipe's inclination depended, whereas as the pipe inclination has decreased, the slip has increased. Whilst, in case of low to moderate superficial oil and water velocities, dispersed oil in water counter-current flow pattern has been observed. This flow pattern has been characterized by the oil droplets flowing at the top and a localised counter-current flow within the water layer at the bottom.

Al-Sarkhi, et al. [101] have investigated the correlation between drag reduction polymer and the pipe inclination of air-water two-phase flow in a pipe of 12.5 mm internal diameter. It has been found that the injected drag reducing polymer solution for 100 polymer chains per minute has reduced the generated drag by 71%. It has also been found that maximum drag reduction could be achieved when the pipe inclination has been 1.28°. The gas superficial velocity has been at the lowest and liquid superficial velocity has been at the highest under this condition.

Atmaca, et al. [102] have studied the oil-water two-phase flow characterisation in an inclined pipe of 0˚, ∓1˚, ∓2˚ and -5˚ inclination with vertical. A high-speed video camera has been employed to capture flow properties in a transparent pipe with an internal diameter of 50.8 mm. It has been observed that by increasing the mixture flow rate, the oil droplets tend to be smaller, this in turn increases the turbulent intensity. Hamad, et al. [103] have studied numerically the characteristics of kerosene–water flows in vertical and inclined pipe of 77.8 mm inner diameter and 4500 mm length. The authors have conducted the simulations at three inclination angles of 0°, 5° and 30° from vertical. Moreover, ranges of flow properties have been used; with the superficial water velocities have been in range of 0.29–1.6 m/s and the volumetric qualities have been in range of 9.2–65.5%. It has been observed that by increasing the superficial water velocity and volumetric quality, the distributions of flow parameters have been

modified due to the movement of kerosene drops toward the lower part of the pipe. CFD predictions have revealed that at 30° inclination, the phase inversion phenomenon has occurred when the volumetric quality has passed 65%.

2.2.3 Multiphase flows in vertical pipelines

Multiphase flows in vertical pipes become the area of interest for many researchers due to the fact that oil extraction process from wells usually, occurs via vertically or deviates to the vertical pipelines. It has been observed that two-phase gas-liquid in inclined pipelines flow as bubbly, slug, churn, annular and disperse flow as shown in Figure 2.5.

Figure 2.5. Flow pattern of gas-liquid in vertical pipelines.

Gould, et al. [104] have introduced a vertical flow regimen, as shown in Figure 2.6, based on the data that had been collected from different sources namely the literature data and the laboratory experiments sources.

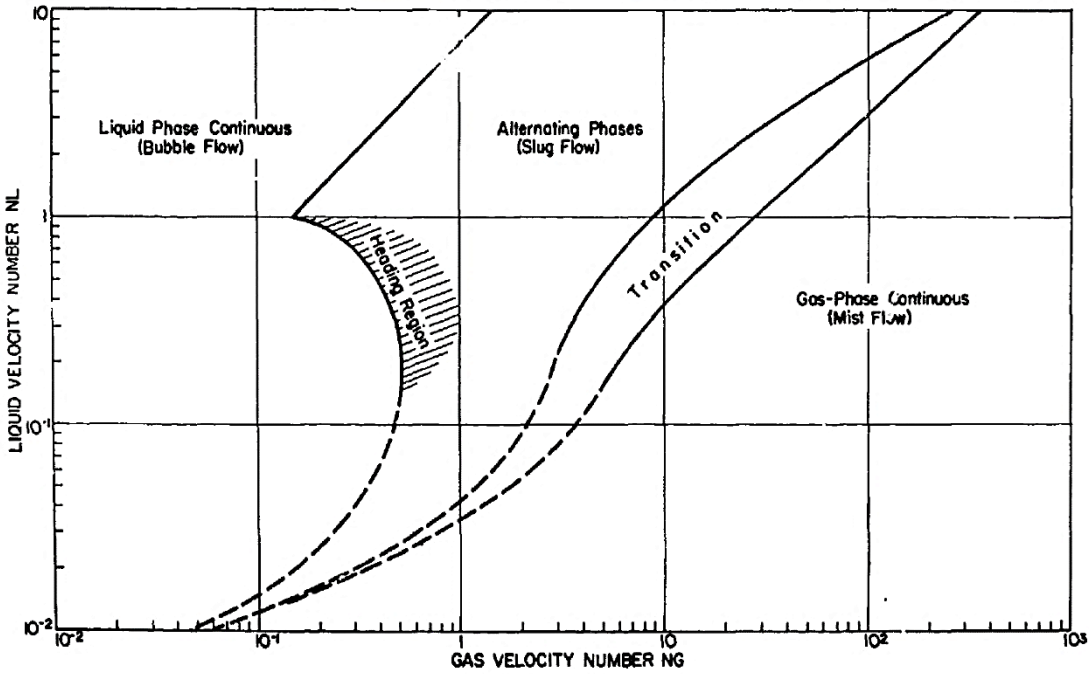

Figure 2.6. Flow pattern for vertical pipe [104].

Serizawa, et al. [105] have studied the development of air-water two-phase flows characteristics and the effect of the entrance distance on the local flow properties. The study has been based on experiments that consisted of a vertical pipe with an internal diameter of 60 mm with a flow domain of air-water at a mixture superficial velocity of 1.03 m/s in upward direction. The average volume fraction of 20% has been examined at three different length ratios (L/D) of 10, 20 and 30. It has been observed that the bubbly flow has been fully developed at L/D =30.

Beyerlein, et al. [106] have investigated the bubbly flow of air-water two-phase flows in a 510 mm ID vertical pipe. The effect of the relative velocity of the two phases and the eddy diffusivity of the liquid on the bubble distributions and the equation of motion have been analysed through this investigation. The investigation outcomes subsequently have been compared with experimental data from the literature. The comparison has showed a good agreement. The eddy-diffusivity transport coefficient has been introduced so that it can be used as a parameter for finding the radial volumetric bubble flux for concurrent flows. Zavareh, et al. [1] have studied the flow regime behaviour of upward oil-water two-phase flow using a Plexiglas pipe of 12800 mm length, and 184.151 mm ID. Four flow regimes have been observed, namely flow of large oil bubbles dispersed in continues water, flow of very small oil bubbles dispersed in continues water phase, inverted large water droplets flow in a continuous oil phase and inverted small water droplets flow in a continuous oil phase.

Morriss and Hill [107] have studied oil-water velocity in a vertical pipe using pulsed ultrasound Doppler techniques. The experimental rig has consisted of a pipe with an internal diameter (ID) of 184 mm and length of 12800 mm. Farrar and Bruun [108] have investigated the structure of oil-water two-phase flow in a vertical transparent cast acrylic pipe of 1500 mm length and 78 mm ID using a hot-film anemometer probe. It has been found that at low volumetric quality, the radial profile of the local void fraction $\alpha(r)$ has been uniform, as the $\alpha(r)$ increased; the bubble size at the pipe centreline increases significantly. It has been also found that when the volumetric quality has increased, the velocity profile has become uniform.

Hassan and Kabir [109] have focused on a water-continuous flow regime where the flow has different patterns namely bubbly, pseudo slug and churn flow patterns. A drift-flux approach has been taken into consideration for the flow behaviour of oil-water two-phase flow analysis. It has been found that the drift-flux of the oil phase in addition to bubble-rise has depended on their local void fraction. A single expression has been developed for the drift flux, U_{ow}. Additionally, a correlation between local oil volume fractions, f_o, oil superficial velocity, v_{os}, and the terminal rise velocity, $v_{\infty\theta}$, have been found, and has been expressed as:

$$f_o = v_{os} / (1.2v_m + v_{\infty\theta}(1 - f_o)^2) \quad (2.1)$$

where

$$v_{\infty\theta} = v_\infty (\cos\theta)^{0.5} (1 + \sin\theta)^2 \quad (2.2)$$

Flores, et al. [100] have studied oil-water two-phase flow regimes in vertical and inclined pipes using a conductance probe. The most important finding in the study has been the characterization of the flow patterns into oil dispersed-water-continuous regimes. A significant slippage phenomenon has been observed between the oil and water phases in water continuous flow.

Hua, et al. [110] have investigated the flow of oil-water in vertical pipe using dual-plane electric resistance tomography (ERT). The experimental pipe has consisted of 2500 mm length and 80 mm internal diameter ID. At a fixed water flow rate of 7.5 m^3/h, the flow pattern has been observed during the increase of the oil flow rate at 0.75, 1.5 and 2.25 m^3/h. The ERT technique has been used to successfully measure the volume fraction and velocity distribution for the oil phase.

Zhao, et al. [111] have experimentally studied the local flow characteristic of oil-water flow in a vertical pipe of 40 mm internal diameter and 3800 mm length. A double-sensor conductivity probe has been used to measure the interfacial area concentration, void fractions, interfacial velocity and oil drops' Sauter mean diameter. Different superficial velocities have been used; the water velocity has been varied from 0.12 m/s to 0.89 m/s, and the oil velocity has been varied from 0.024 m/s to 0.198 m/s. It

has been found that the local and cross-section-average interfacial area concentration has changed with the change of water flow rate under fixed oil flow rate. Hu, et al. [112] have studied the turbulent characteristics of oil-water upward and downward flows. Two stainless steel pipes have been used. of an inner diameter of 38 mm ID with two different length of 3200 mm for the upward flow experimental and 3200 mm for downward flow. The mean velocity profiles for droplet and continue phases have been investigated. Hamad and He [113] have investigated experimentally and numerically the local structure of kerosene-water two-phase flows in a vertical pipe. Hot-film, dual optical and Pitot tube probes have been used as measurement tools. The test pipe has been cast acrylic with an inner diameter, ID, of 77.8 mm and length of 4500 mm. Variable water superficial velocities of 0.29, 0.59 and 0.77 m/s have been employed, with variable volumetric qualities of 4.2%, 9.2%, 18.6% and 28.2%. ANSYS Fluent 6.3.23 has been employed as an investigating CFD code. It has been found that the experimental single-phase characteristics have been quite in agreement with the predictions of FLUENT. It has also been found that the error percentage of optical probes results comparing to the hot-film results has been less than 10% for the drop and water velocities' measurements.

As a conclusion from this part, it can be clearly noticed that the verification and adjustment of the most existing models have been conducted in small pipes of 10 −100 mm internal diameter. Moreover, the researches in this field do not agree to accept any universal models to be used as a general equation for multiphase flow predictions. Furthermore, the entrance lengths for multiphase flows are not yet well established. Finally, many of the flow patterns have been reported to be depended on the initial conditions

2.3 Needle probes

Needle probe is a well-established intrusive instrument for measuring the local disperse phase properties in multiphase flows. This method identifies the phase properties from the needle tips. The needle's probes comprised of two main measuring techniques, namely conductivity, and optical measurement techniques.

2.3.1 Optical needle-probe measurement technique

The working principle of the multi-sensor fiber-optic probe is based on the light refractive beams that are generated from the difference in density between the phases in a multiphase flow. The operational principles of these optical probe types are based on the Snell–Descartes law, also known as the law of refraction. The application of this law is based on equation 2.3, which describes the relationship between the angles of incidence and refraction. This angle occurs when light passes through two different isotropic media, such as water, glass, or air, as shown in Figure 2.7.

$$\frac{\sin\theta_1}{\sin\theta_2} = \frac{n_2}{n_1} = \frac{v_2}{v_1} \tag{2.3}$$

where θ_1 and θ_2 are the angles of incidence and refraction respectively measured from the normal line of the boundary, v is the velocity of light in the respective medium (m/s) and n is the refractive index (unit less) of the respective medium.

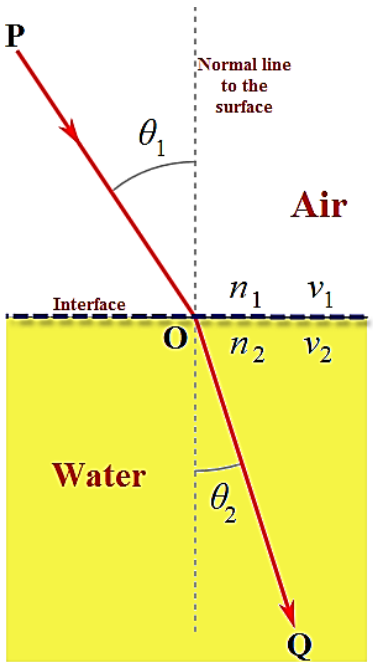

Figure 2.7. The refraction phenomenon in air-water media.

As the light beam passes the interface between media, the light is either refracted to smaller or larger angle with respect to the normal line to the surface. When the light travels from the air medium into the water medium, the light beam refracts towards the normal line, as shown in Figure 2.7, due to the decrease of light velocity while travelling through the two different densities. Moreover, this happens in reverse when light travels from water to air, i.e. the light beam refracts away from the normal line. In general, Snell's law is applicable only for isotropic or specular material such as glass.

Accordingly, the multi-sensor fiber-optic probe has been successfully used by many researchers for the dispersed phase recognition. Rinne and Loth [114] have conducted experimental studies of two-phase air-water bubbly flow. The study has been primarily concerned with the measurement of the two-phase flow properties such as void fraction, bubble velocity, bubble frequency, bubble chord length, bubble size, and local interfacial area concentration in sudden expansion vertical pipe.

The experimental data have been obtained from air-water two-phase flow in an upward vertical sudden expansion (40 - 90 mm ID) pipe at atmospheric conditions, as shown in Figure 2.8. The secondary phase has been injected perpendicular to the water flow via 1 mm ID of 160 holes, which have been arranged in eight rows with 2 mm distance between each row. Whilst the primary phase has been driven by a frequency-controlled pump.

The test pipe has consisted of a 3.8 m length with 40 mm internal diameter pipe which has been then connected to a pipe of 90 mm ID and 3.3 m in length. A cone shape tip of fiber-optic sensors probe, and a high-speed video camera have been used as measuring instruments. The fiber-optic sensor probe has been placed in two positions, namely the tip facing the flow and double horizontal sensors with the tips perpendicular to the flow direction, as shown in Figure 2.9.

Three types of error have been reported: errors due to bubble-sensor interactions, errors due to the flow control units such as water and air flow meters and errors due to signal processing method. The authors have quantified the percentage errors by comparing the measured gas flow rate (Q_G) with the gas flow rate that has been calculated using equation 2.4.

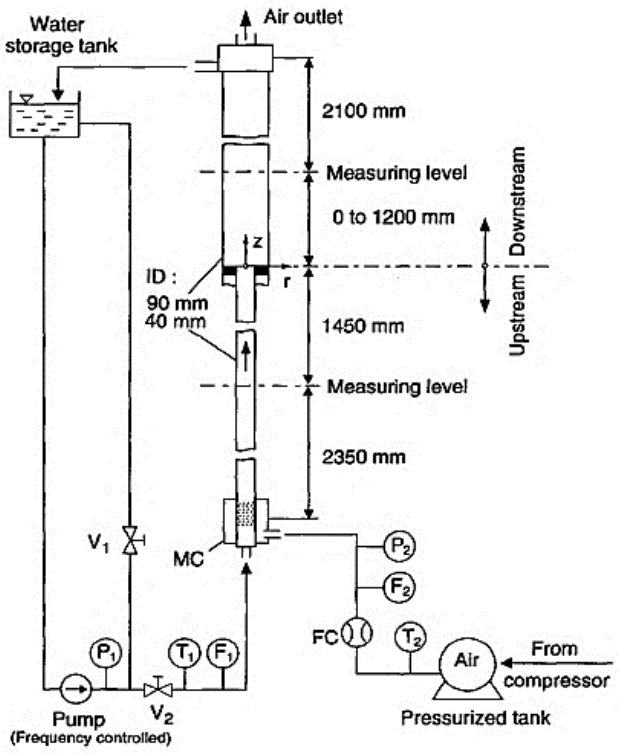

Figure 2.8. Schematic diagram of the experimental test rig [114].

$$Q_G = 2\pi \int_{r=0}^{r=R} \bar{v}_b \, \alpha \, r \, dr \tag{2.4}$$

where, $\bar{v}_b$ is mean bubble velocity and α is local void fraction.

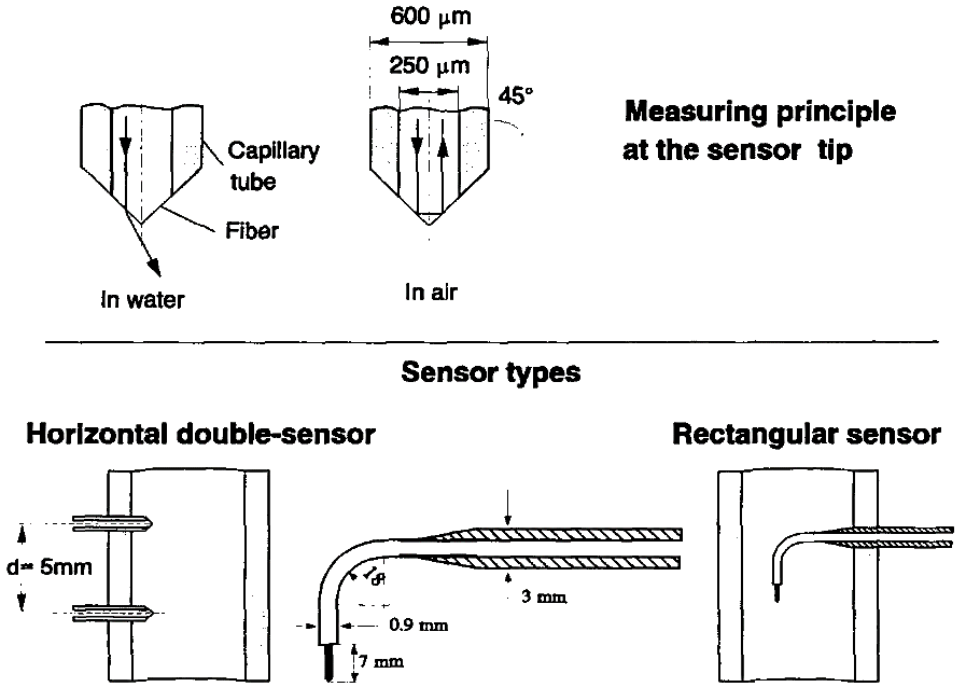

Figure 2.9. The mono-fibre optic sensor probe [114].

It should be noted that neither the data repeatability nor accuracy have been reported by the authors.

Hamad, et al. [115] have introduced a new optical probe system, as shown in Figure 2.10, which is a Normal Reflection Probe, for liquid-liquid two-phase flow measurement. It has been found that the new probe with a flat tip has captured a clearer kerosene-water interface reference signature. Moreover, the new probe has the ability to capture the very low signals. The authors have concluded that for kerosene drop diameter larger than 1 mm; probe with the tip diameter of 100 μm could provide accurate measurements. The authors have justified the results that they have obtained from the new probe by comparing them with the results that have been obtained from the use of hot-film anemometry. In general, a good agreement has been observed between the two methods. However, a small variation has been reported in the radial profile of $\alpha(r)$. The experimental setting consisted of a 5 m long optical probe cable, which had a core diameter of 100 µm and a 140 µm cladding diameter, for distinguishing the water–kerosene interface in a 30 mm inner diameter vertical pipe. The optical probe has been

placed at the centreline of the pipe. The optical fibre has been supported by surrounding it with a stainless-steel tube of 0.25 mm. ID. The light in the infrared waveband has been provided by a battery-operated 160 μW emitter. A photo-diode has been used to produce the current signal which consequently has been converted into a voltage signal. As the obtained signals have been so small, typically 0.5–1.0 mV; an amplifier circuit has been used to amplify the output signals to 0.5–1.0 V. Finally, the output signals have been passed through a low-pass passive filter with a cut-off frequency of 16 kHz, to eliminate the undesired noises that have been generated during the process of amplifying and manipulating the signals. The data have been acquired at each sensing point for sampling period of 30 sec.

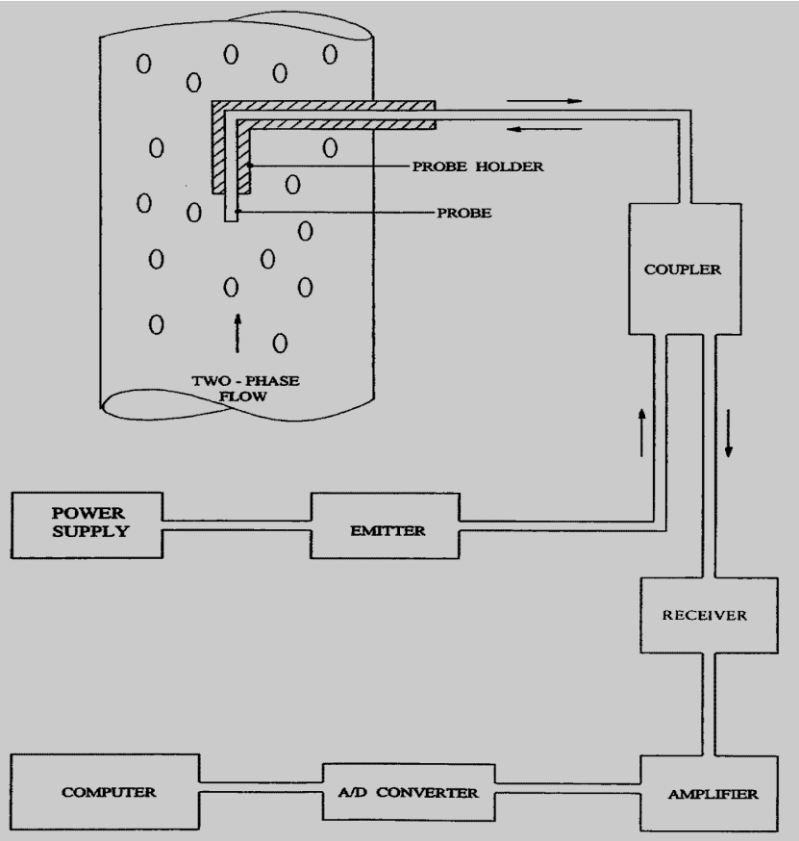

Figure 2.10. Schematic diagram of the optical probe system [115].

It should be noticed that neither the data repeatability nor accuracy have been reported by the authors. However, the authors have reported that high reproducibility of measurements could be obtained when using the new optical probe system.

Cartellier [116] has presented new optimized mono-fiber technique optical probes for phase detection and gas velocity measurements. In his study, double cone mono-fibre probe has been used for the investigations with separation length between the two cones, L, as shown in Figure 2.11. This technique has produced two optical signals which have enabled the probe to measure the bubble velocity. Furthermore, a real-time signal processing has been adapted in the measurements process.

The experimental setting consisted of upward air/water flows in a vertical 50 mm ID pipe at ambient temperature and pressure. Several kinds of air injectors have been utilised for obtaining different bubble sizes, namely porous plates and array of calibrated 90 or 200 mm ID needles. Rotameters with 1% of relative uncertainty have been used for both flow rates measurements. Water superficial velocities in range of 0 -1 m/ s have been considered in the investigations. Whilst the bubble sizes of 3–7 mm have been generated.

From the conducted experiments, it has been proved that the mono-fiber technique could measure the gas velocity with a reasonable accuracy of ∓10%. However, this accuracy has decreased with the presence of large bubbles in the flow.

For the measurement repeatability test, the two-phase flow properties have been measured five times under the same experimental conditions at 600 sec for each run; error of ∓ 2.4% has been reported for the void fraction measurement.

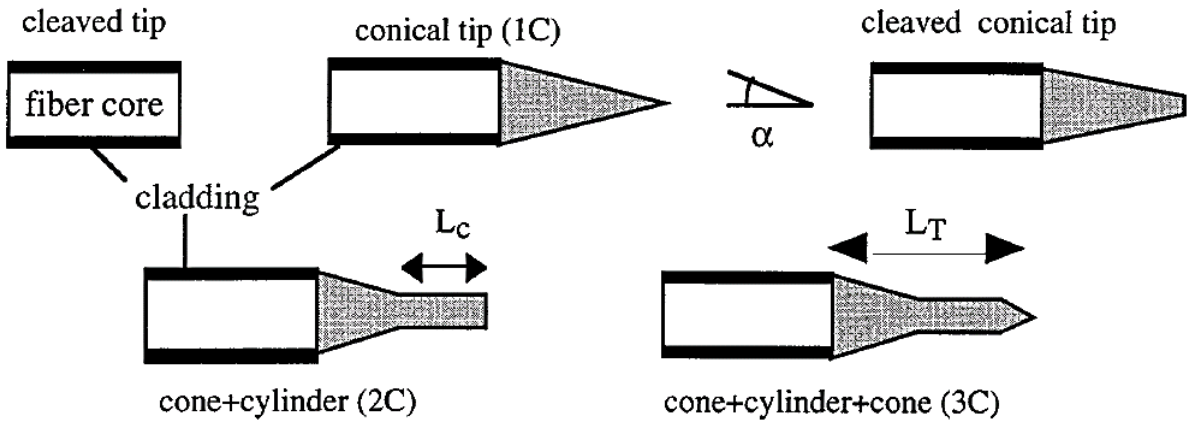

Figure 2.11 The basic of cone-cylinder-cone mono-fibre probe [116].

Barrau, et al. [117] have carried out experimental studies on the feasibility of gas velocity measurements using a mono-fiber probe in gas-liquid two-phase flows. A real-time processing for volume fraction and dispersed phase velocity measurements has been adopted in the investigation for either mono-or bi-probes. To recognize the bubble phase, the authors have evaluated two magnitudes, as shown in Figure 2.12: the peak to peak noise amplitude V_B and the amplitude corresponding to a fully wetted probe V_L as shown in Figure 2.12.

where V_G and V_P are the mean peak levels for the types I and II respectively and ΔV is the maximum difference of the wet and dry breadth. It has been found that the bubble could be recognized only when the signal exceeding the level, V_T.

where, V_T is the summation of $V_L + CS_1$, where CS_1 is a security coefficient measurement for the arbitrariness of the noise.

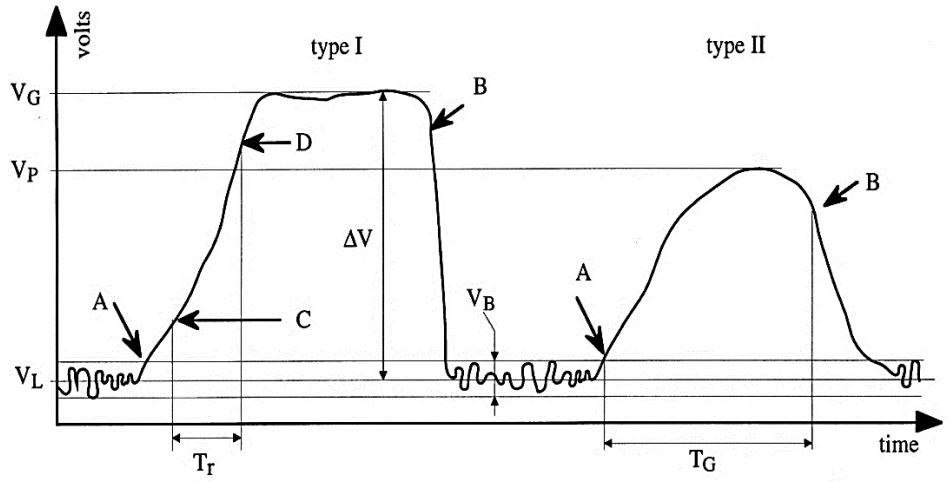

Figure 2.12. Sketch of characteristic events detected on bubble signatures [117].

The experiment has consisted of investigating the co-current, upward two-phase flows properties in a vertical plexiglass pipe with internal diameter of 50 mm and 5000 mm long. The secondary phase has been injected from the upstream end of the pipe with three kinds of injectors, namely a porous plate, two capillaries with either internal diameter of 90 or 200 µm of 200 mm long. These injectors have been used to keep the bubble sizes in range of 2-6 mm. The water superficial velocities that have been used in the investigations were 0, 0.2 and 1 m/s. Whilst the air volumetric flow-rate was between 3 to 3830 Nm^3/h, where Nm^3/hr is Normal Meter Cubed per hour, and Normal refers to normal conditions of 0 °C and 1 atm.

In this study, the gas velocity has been found to be virtually continuously overestimated. Moreover, at a sensible volume fraction the error has been less than 10%, nevertheless; the error has been found to be enlarged progressively when the volume fraction has been higher than 20%. It has been concluded that by increasing the mixture velocity the measurement uncertainty increases due to the complex flow structure which increases the bubble-probe interactions.

Hamad, et al. [118] have utilized a dual-optical probe for drop characteristic's measurements in kerosene–water liquid–liquid two-phase flow. The dual-optical probe has consisted of an optical cable of 5 m long, which has had a 100 μm core diameter and a 140 μm cladding diameter, the typically probe that has been used is shown in Figure 2.13.

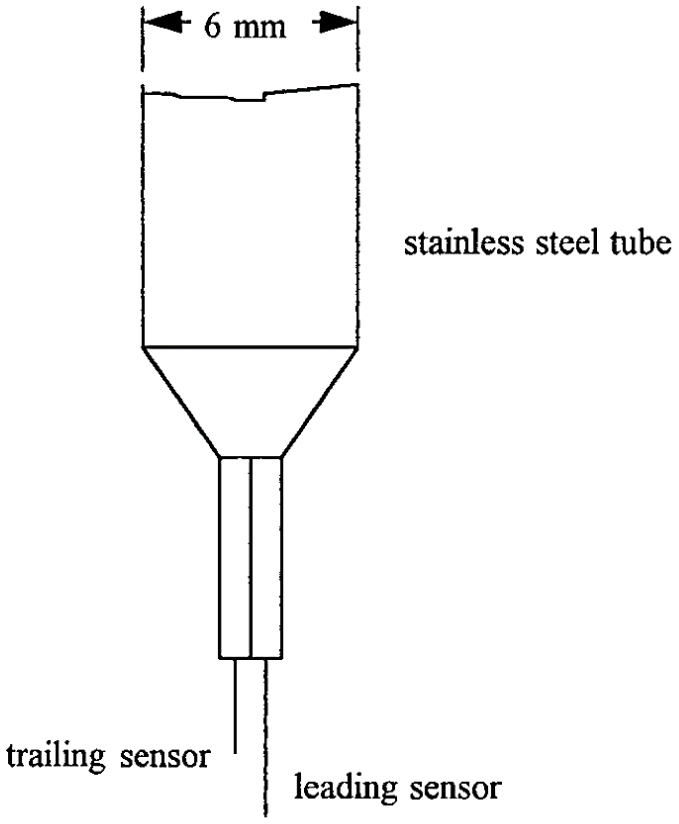

Figure 2.13. Dual-optic probe [118].

In this study, the dispersed-phase density function $X_{G(X,T)}$ has been introduced as

$$X_G(x,t) = \begin{cases} 1 & \text{If } x \text{ is within the secondary phase at time t.} \\ 0 & Otherwise. \end{cases}$$

Therefore, the local volume fraction has been calculated using:

$$\alpha(x) = \lim_{T\to\infty}\left(\int_{t}^{t+T} X_G(x,t')\,dt'/T\right) \quad (2.5)$$

Accordingly, the local volume fraction has been obtained from the time-average process as:

$$(x) = \lim_{T\to\infty}\left(\sum T_G\,/T\right) \quad (2.6)$$

where $\sum T_G$ is the summation of the dispersed phase time delay that is measured at (r, θ) and T is the data acquisition period.

From the comparison that has been done between the two-sensor optical probe and the sampling tube measurement in term of volume fraction and drop velocity profiles, good agreement has been found. In this research, no repeatability check has been reported.

Guet et al. [119] have employed a four-sensor optical-fibre probe for measuring the volume fraction distribution, the bubble shape and the bubbles orientation throughout bubble-probe interaction in air-water two-phase flow in a vertical pipe. The probe has consisted of four sensors which have been made from fiber with a 200 μm in diameter of quartz glass core, having a refractive index of 1.45. A 380 μm diameter of silicon insulation with a 600 μm Teflon protective layer have been used as an insulation material around the sensors apart from the tips. The probe operational method has comprised of light emitting into each fibre by an LED, wavelength of 680 nm, via standard glass fiber connectors and a photodiode to detect the reflected light due to the presence of bubbles. The four fibres have been bonded together and have been enclosed by a 6 mm external diameter tube. The detection method is based on the light reflection due to the existence of bubble-water interface. The reflected light was then converted into a voltage form to be use in signal processing. The four sensors have been arranged in such a way that the lead sensor has been situated in the middle of the rear sensors whilst it is taller than them by Δs = 1.66 ± 0.03 mm. Whereas the radial separation between the middle sensor and the peripheral sensors has been 0.2 mm, as shown in Figure 2.14.

The experimental facility that has been used for investigating the bubbly flow properties, as shown in figure 2.15, has been consisted of 18 m height and 72 mm ID vertical Perspex pipe. The continues phase has consisted of a tap water mixed with 0.5% of ethanol. Whilst the gas phase has been injected through two different means, namely a porous material and a nozzle. The inlet void fraction has been used of 0 and 0.3.

It has been reported that bubbles void fraction profile has been wall peaking. It has been observed that bubbles that are 5 mm in diameter or smaller have accumulated near wall regions. As the size of bubble has increased, the void fraction distribution has altered from wall peaking to a centre line peaking. It has also been reported that positive value of the orientation angle, i.e. the polar angle, could be obtained if the bubble diameter is smaller than 5 mm, whilst negative value of the orientation angle could be obtained when the bubble diameter is 5 mm or larger. The authors have noted that ellipsoidal shape is not valid assumption for bubble that has large diameter. A good accuracy has been reported from the comparison results between the probe system measurement and the high-speed stereoscopic imaging measurement. No measurement repeatability test has been reported by the authors.

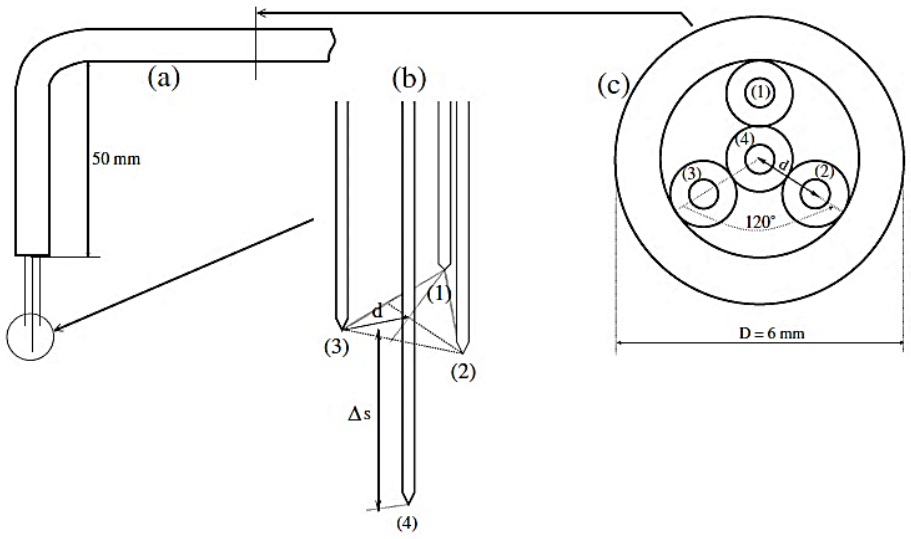

Figure 2.14. A schematic of the four sensor optical probe [119].

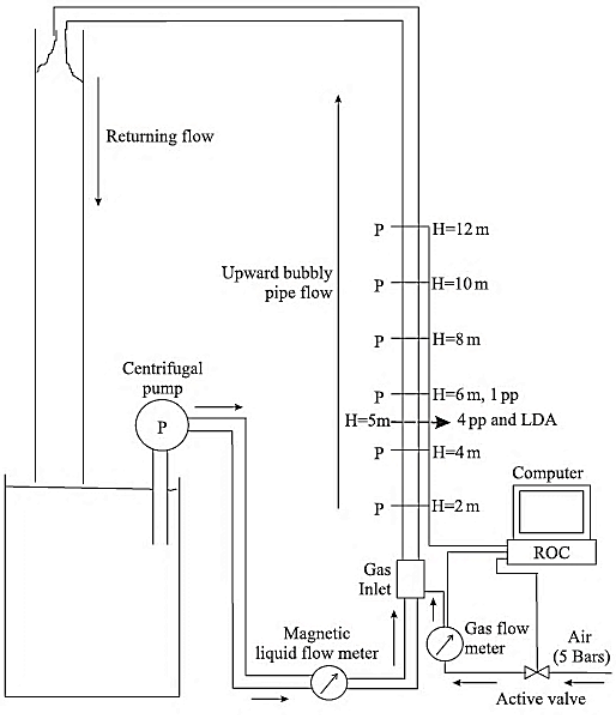

Figure 2.15. Experimental setup [119].

.

The authors have reported an interesting subject of further research; to analyse the bubble shape and orientation situations related to bubble transverse migration in bubbly multi-phase flows in more details.

Xue, J et al. [120] have experimentally investigated the bubble characteristics namely, velocity, void fraction, chord length, bubble frequency, and specific interfacial area over a range of gas superficial velocities. They have used four-point optical probes in bubbly flow and highly churn-turbulent flow. The test rig has comprised of 162 mm stainless steel pipe bubble column as shown in Figure 2.16.The four-sensor optical probe has been configured in such a way that the leading sensor has been taller than the three trailing sensorsby a distance of 20 mm. Furthermore, the leading sensor has been situated at the centre of the probe frontal area and has been surrounded by the trailing sensors forming a triangle shape as shown in Figure 2.17.

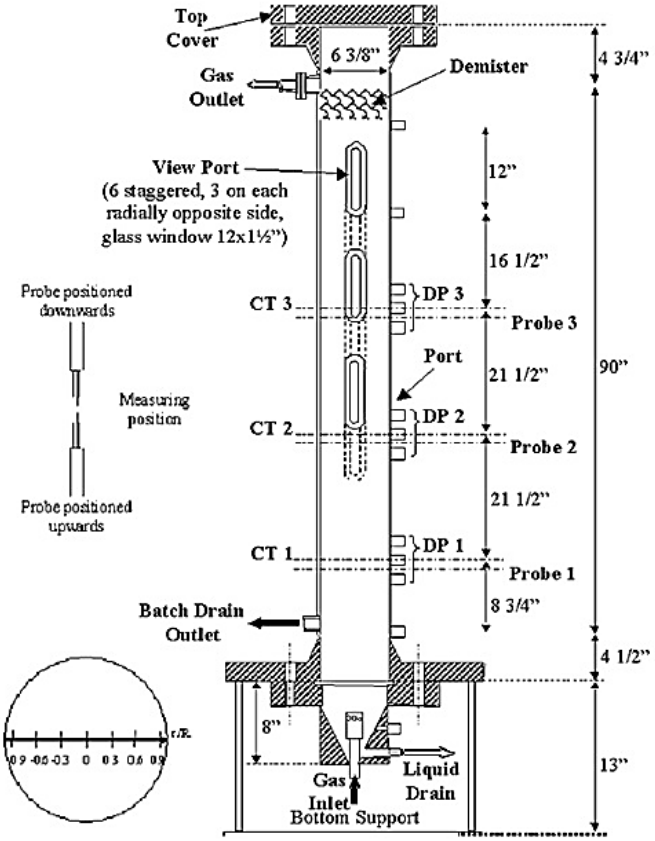

Figure 2.16. Bubble column used by Xue, J et al. [120].

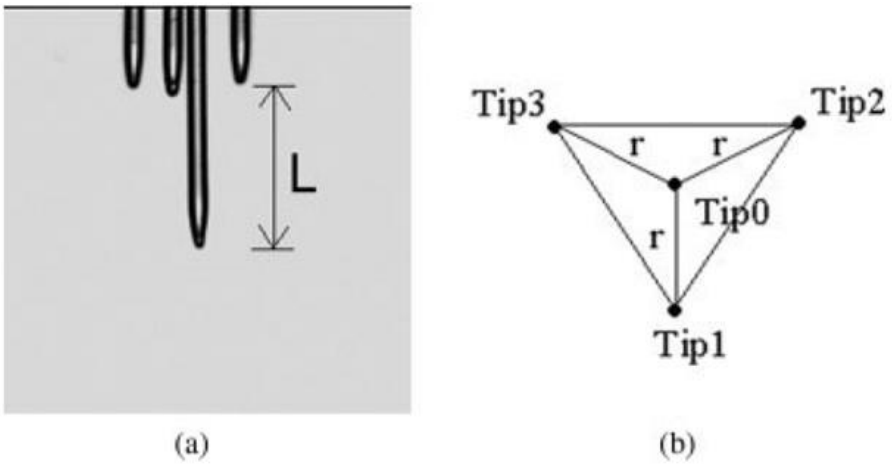

Figure 2.17. A schematic of the four sensor optical probe [120].

The authors have concluded that four-sensor optical probe has the ability to measure local dispersed phase flow properties for both cases, the bubbly and the highly churn-turbulent flows, efficiently. The effects of increasing gas superficial velocity on the radial profiles of specific interfacial area, bubble frequency, and mean bubble velocity have been investigated. It has been found that by increasing the gas superficial velocity the mentioned properties' profiles have changed from flat to parabolic distributions. Moreover, it has been observed that the bubble chord length tends to increase by the increase of gas superficial velocity at the pipe centre, whereas it is still unaffected near the pipe wall. It should be noticed that neither the data repeatability nor accuracy have been reported by the authors.

Shen, et al. [121] have experimentally investigated error reduction techniques in the optical conical four-sensor probe fabrication by utilizing reduced frontal area tips probe, as shown in Figure 2.19. The measurement errors have been classified into two groups, i.e. signal processing errors and hydrodynamic errors. The former errors have been related to threshold selecting accuracy. However, this error has been so small, less than 1.05%, and it could be neglected in both the void fraction and IAC measurement. Whereas, the hydrodynamic errors have been related to the bubble-sensor interaction and transversal or missing bubbles. The probe stiffness has been examined against pressurized air. It has been concluded that the optical sensors should be short in length to overcome any trace of deflection. In this study, three possible measurement error sources have been identified as: the deformation of the bubble surface, the alteration in the magnitude and direction of the bubble velocity, and missing bubble. The authors have considered that bubble deformation effect has not had a significant influence on the time delays measurement since this deformation has affected all sensors similarly. Therefore, it couldn't be considered as a large source of the void fraction and IAC measurement error. The authors have stated that although the bubbles slow down, and the motion direction diversifies as a sensor immerses and exits the bubble; the measurement error stays so small that can be neglected, in cases where bubbles have diameters much larger than the probe diameter. Therefore, it has been concluded that the main source for the error has been caused by the bubble escape. It has been recommended that probe frontal area should be so small as to avoid this source of error. In their study, the expression for true void fraction, α_{true} calculation has been proposed as,

$$\alpha_{\text{true}} = \frac{1}{1-0.98r_{\text{rec}}}\alpha_{eff} \qquad r_{\text{rec}} \in [0,1] \qquad (2.7)$$

where α_{eff} is the amount of the volume fraction obtained from the front sensor, and r_{rec} is the receding bubble ratio. It is noticeable, that authors have not conducted FE or any other deflection analysis to quantify the amount of the sensor deflections.

The experimental setup for investigating the upward air-water two-phase flow in a vertical pipe with 200 mm ID and 12000 mm long has been carried out, as shown in Figure 2.18. 10 kHz has been used as a sampling frequency for each optical fibre sensor.

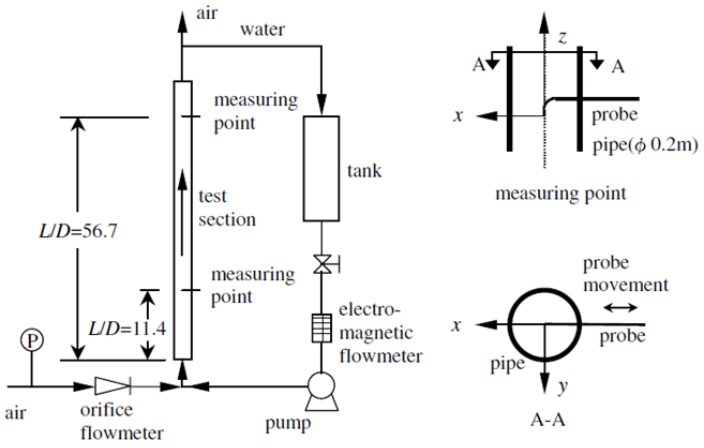

Figure 2.18. The schematic diagram for the experimental test rig [121].

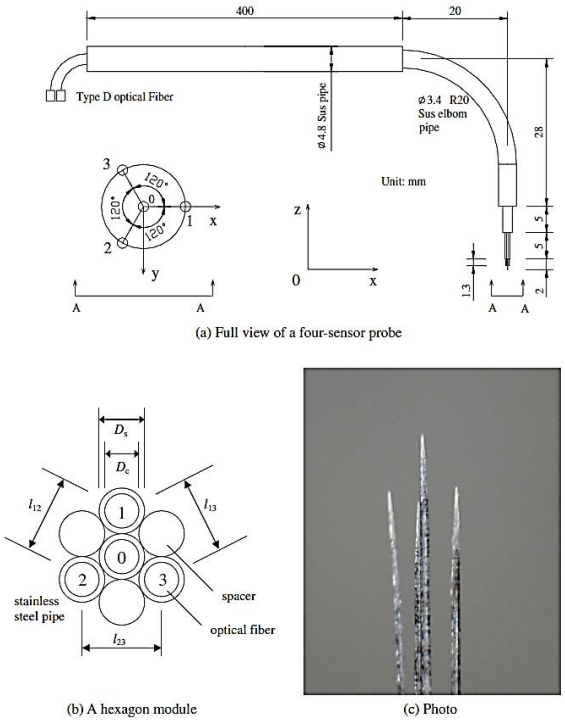

Figure 2.19. Four-sensor fibre optic probe [121].

Vejrazka, et al. [122] have conducted an experimental study on the rising bubble behaviour in a stagnant liquid with the aid of mono-fiber optical probe and high speed cameras. The authors have investigated the residence-time of the probe tip within the bubble. It has been observed that the bubble shape has been modified due to the effect of the probe's intrusive nature when it has come into contact with the probe tip. In turn, this phenomenon has increased the residence-time when the bubble has been pierced by the probe near its pole and has decreased when the bubble has been pierced near the equator. Therefore, the volume fraction measurements are underestimated. The authors have linked the error in the volume fraction with a modified Weber number M.

$$M = \frac{\rho {u_1}^2 D^2}{\sigma D_{op}} \tag{2.8}$$

where D is the bubble volume-equivalent size, D_{op} is the diameter of the fibre-probe, u_1 is the bubble velocity before encountering the probe, ρ is the liquid density and σ is the liquid surface tension. Moreover, it has been observed that the modified Weber number M can distinguish the ability of the probe tip to overcome the bubble surface-tension resistance that is generated from bubble the probe tip contact. Furthermore, it has been observed that the modified Weber number above 50 reduces the measurement uncertainty to less than 10% on both maximum chord length and the void fraction. Whilst, the optical rigidity of probe tip has been advised to be sufficient to limit its deformation.

2.3.2 Conductance needle-probe measurement technique

The principle of the multi-sensor conductance probes is based on the difference in conductivity between the phases in a multiphase flow. As the bubble comes into contact with the sensor, the conductivity falls sharply as the tip of the sensor immerses into air, a non-conductive material, unlike the water, a high electrical conductive material. The measured voltage stays low, as long as the sensor's tip remains in the air. When the bubble leaves the tip of the sensor, the voltage sharply rises as the sensor's tip surrounds with water.

2.3.2.1 One sensor conductivity probes

Niel, et al. [123] have disclosed a new technique of conductivity probes for measuring local properties for the dispersed phase in multiphase flows. The conductivity probe has consisted of an insulated stainless-steel needle (sensor) with an exposed tip pointing into the flow, which has been connected to an insulated steel wire and has been enclosed in a stainless-steel tube, as shown in Figure 2.20. The conductive probe has accurately captured the void fraction of bubbly nitrogen-mercury two-phase flow in a vertical tube of 25.3 mm inner diameter. It has been observed that this technique cannot measure the bubble frequency accurately.

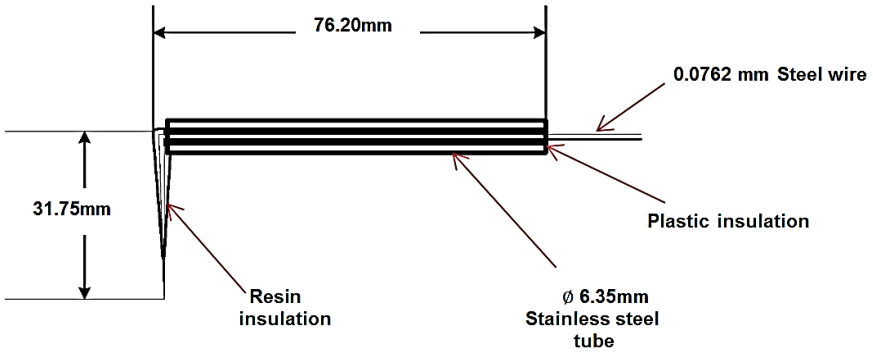

Figure 2.20. Schematic of a single-sensor probe [123].

It has been reported that the new sensor has measured the local volume fraction with uncertainty less than ± 0.004.

2.3.2.2 Two-sensor conductivity probes

Theory of the dual-sensor conductivity probe

The main reason for using a dual-sensor conductivity probe in multiphase flows is to measure the local velocity and volume fraction of the secondary phase from the difference in the electrical conductivity between the phases.

Generally, the volume fraction of the secondary phase can be measured using one sensor, nevertheless for the secondary phase velocity measurement dual-sensor probe is required. The dual-sensor conductivity probe operation is based on the difference in electrical conductivity between the fluid flow phases, i.e. if the phases' electrical conductivity is too close it will be very difficult to use any multi-sensors conductivity probes for measuring the multiphase properties.

As the tip of each sensor breaches the boundary between the fluid phases, i.e. from the high conductance zone, which is water, to low conductance zone, which is air, an electrical single generates. Because of the large variance in electrical conductivity between air and water, the signal falls sharply. During the use of a dual-sensor probe for measuring bubbly two-phase flow properties in a vertical pipe ,as shown in *Figure 2.21*, the bubble surface makes a contact with the lead sensor, S_1, tip at t_{1f} time. As a result, the reading voltage falls sharply due to the air's low electrical conductivity, and when the bubble leaves the sensor, S_1, tip at t_{2f} time, the reading voltage rises sharply due to the water's high electrical conductivity. Similarly, at t_{1r} and t_{2r} times electrical signal can be obtained from the rear sensor, S_2, as shown in Figure 2.22.

If there are N bubbles striking the dual-sensor probe, assuming that these bubbles come into contact with both of the front and the rear sensors during a sampling period T, the time intervals, δt_{1i} for the i[th] bubble can be calculated as:

$$\delta t_{1i} = t_{1r,i} - t_{1f,i} \tag{2.9}$$

and

$$\delta t_{2i} = t_{2r,i} - t_{2f,i} \tag{2.10}$$

Since the axial distance between the front and the rear sensor tips, s, is known, the bubble's mean local axial velocity can be calculating as:

$$v = \frac{2s}{N} \sum_{i=1}^{N} \frac{1}{(\delta t_{1i} + \delta t_{2i})} \tag{2.11}$$

and the volume fraction, α, can be calculated from the lead sensor as:

$$\alpha = \frac{1}{T} \sum_{i=1}^{N} (t_{1r,i} - t_{1f,i}) \tag{2.12}$$

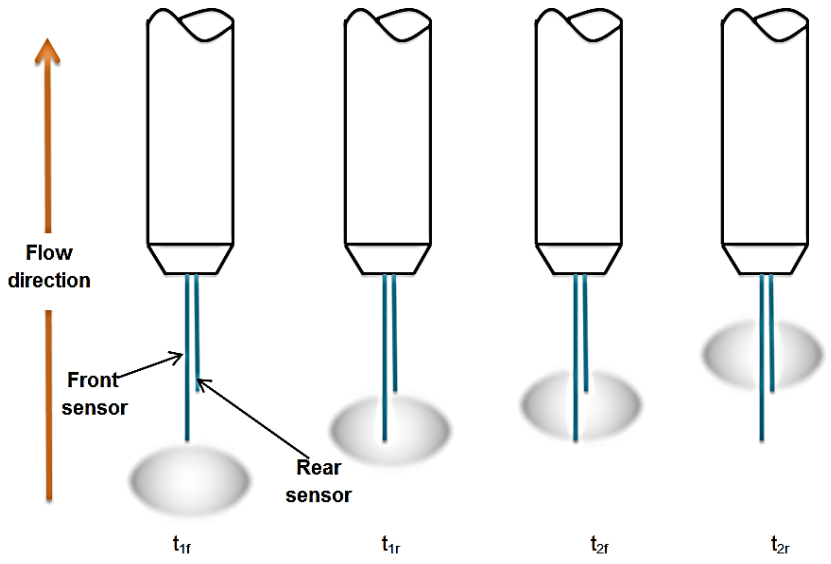

Figure 2.21. The time intervals generation as the bubble strikes the dual-sensor probe.

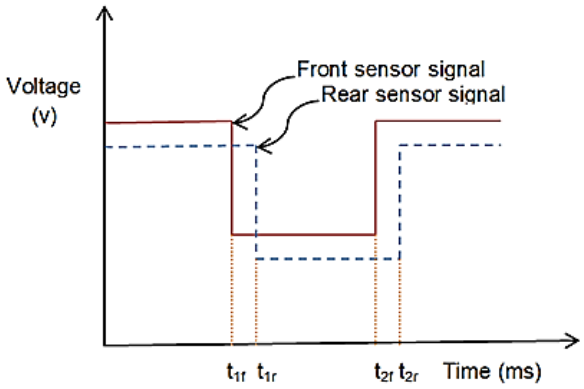

Figure 2.22. Ideal signals captured by a dual-sensor probe.

Serizawa, et al. [105], [124] and [125] have carried out series of experimental tests to investigate the local dispersed phase properties in two-phase air-water flow. The experimental setup, as shown in Figure 2.23, has consisted of a 2100-mm long and 60 mm ID vertical Lucite tubing. The secondary phase, air, has been injected at the bottom of the mixer through a 150-mesh stainless steel screen that had a sequence of 84 holes with 1.5 mm ID.

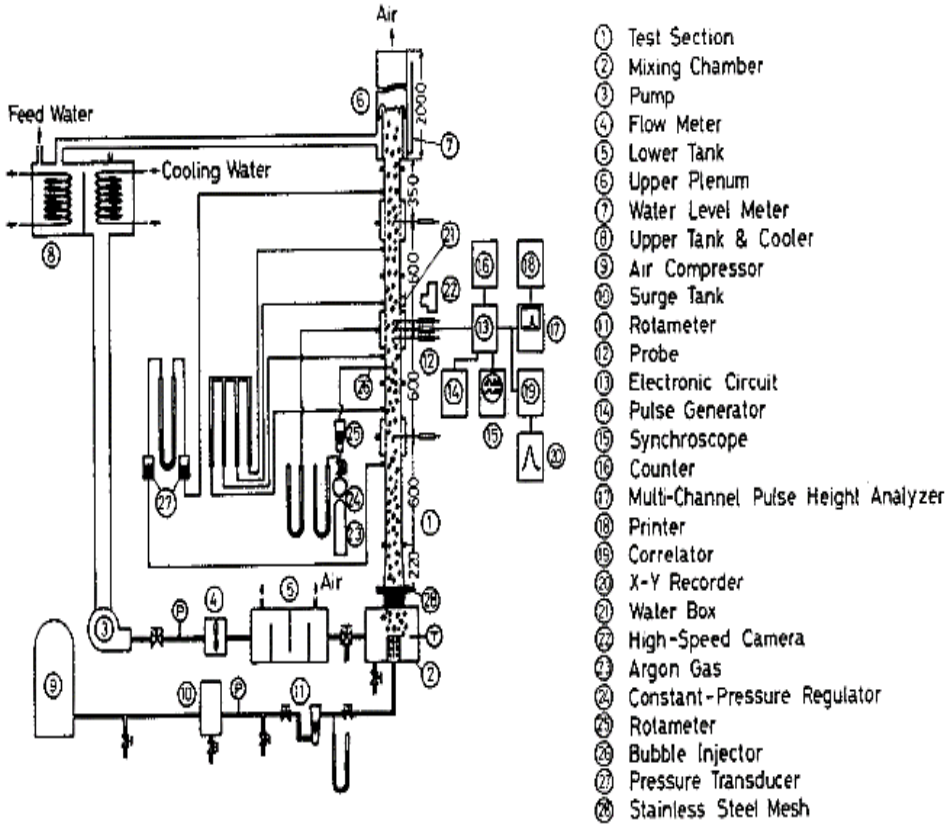

Figure 2.23. Schematic diagram of experimental facility [124].

The authors have introduced an electrical resistance probe comprising of two stainless steel needle sensors situated in parallel position. Both needles have been insulated excluding the tips. Each needle has had 0.2 mm diameter and have been separated axially by 5 mm in the flow stream direction. The longer and the shorter sensors have been denoted as a start and a stop sensor respectively, as shown in *Figure 2.24*.

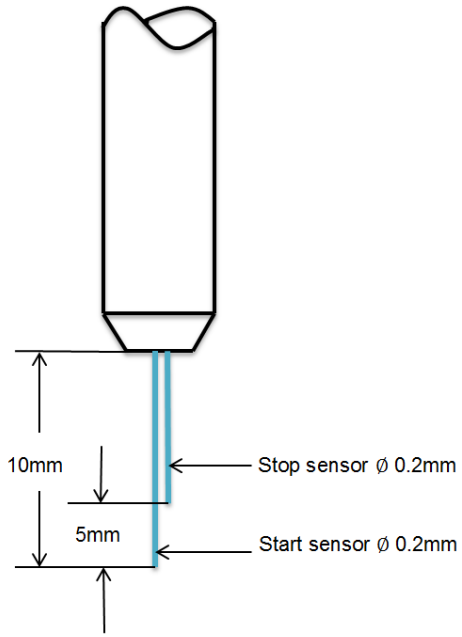

Figure 2.24. Schematic of a dual-sensor probe [105].

The authors have used double-sensor electrical conductivity probe, along with a newly established electronic circuit, a digital counter and a multichannel analyser in their study. For the data analysis, Cross-correlation function has been used to calculate the average time lag of the bubble's contact: with the upstream and the downstream sensors. A small discrepancy of 5% has been observed in the bubble's average velocity between the cross-correlation technique and the multichannel technique. (the latter technique has used the time-pulse converter to produce the time lag for each bubble). This discrepancy has been justified due to the bubble-probe interaction and the bubble shape deformation. Furthermore, local volume fraction, bubble impact rate, bubble velocity and its distribution in a bubbly air-water flow have been measured during their studies.

Buchholz and Schugerl [126] have utilized two-sensor conductivity probe and photographic method to measure two-phase flow properties such as bubble frequency, bubble size, void fraction and bubble velocity. The probe has been made of two Platinum Iridium sensors 0.08 mm in diameter as shown in Figure 2.25. The radial distance between the two sensors has been chosen depending on the bubble size, 0.1 mm in their test, whilst, the axial distance between the sensors tips has been 0.2 mm.

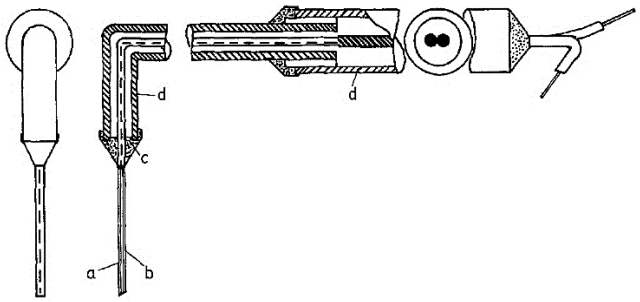

Figure 2.25. Double-sensor conductivity probe [126].

The experimental setup has consisted of a stagnant solution of water with 0.5% of methanol in a cuvette with cross-section of 70 x 42 mm, whilst the air has been injected from the bottom of the cuvette through a porous plate of 5 and 50µm holes internal diameter.

The authors have stated that by utilising hydrophobic insulations around the sensors, the generated signal has been similar to an ideal square-wave. From the comparison between the results that had been obtained by the two-sensor conductivity probe and the photographic method, it has been found that the former method has measured bubble size better in case of large bubble diameter.

Van der Welle [127] has obtained correlations for the power law exponents for the gas velocity and volume fraction profiles from intensive experimental investigations. The experiments have been carried out by employing a dual-sensor conductive probe for investigating the air-water two-phase flow under a range of liquid superficial velocities: 1.3, 1.7 and 2.1 m/s, and at different volumetric qualities, 0.25 and 0.75m in a vertical Perspex pipe of 100 mm internal diameter. The author has suggested that the needle tips' axial-separation distance should not exceed 20 mm as it losses the correlation between the signals due to the effect of turbulence, as shown in Figure 2.26 . On the other hand, this distance should not be too small as it affected the determination of time-delay accuracy. Therefore, it has been found that the most suitable distance between the tips was 10 mm. The authors have used glass cladding to prevent the sensor deflection that can affect the measurement accuracy.

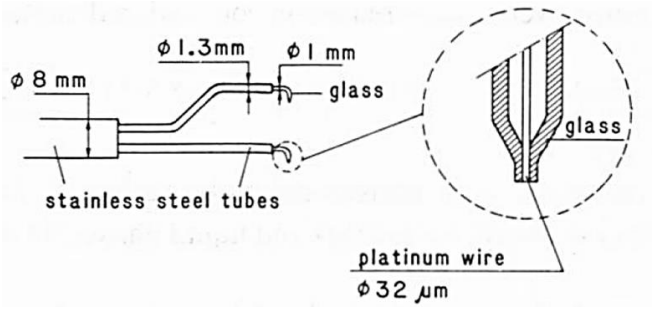

Figure 2.26. Dual-sensor probe used by Van der Welle [127].

Herring and Davies [128] have used a dual-sensor probe to study the dispersed local properties in air-water two-phase vertical flow such as void fraction, air velocity, bubble size distribution and space-time distribution function.

The experimental setups have been designed to investigate upward air water two-phase flow properties in a vertical Perspex pipe with 50.8 mm internal diameter. Six sets of flow conditions have been used in their investigations, each set has consisted of air and water velocities in a fraction by which the flow regime has been kept as bubbly flow.

The probe has consisted of two surgical stainless-steel needles covered by a stainless tube. Both needles have been insulated apart from their tips, as shown in Figure 2.27.

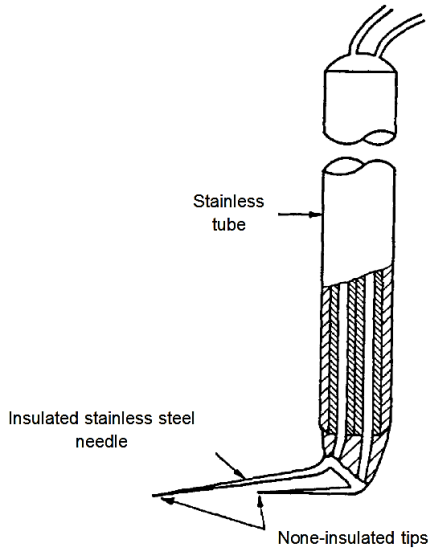

Figure 2.27: Schematic of dual-sensor probe [128].

The authors have established that there have been other factors that have affected the local void fraction profiles than the air inlet conditions (the way of how the air has been injected). Furthermore, it has been found that void fraction, which has been measured by the second sensor, has been lower than the front sensor. This has been concluded as the generated wakes by the front sensor has prevented the bubbles to reach the rear sensor.

Liu [129] has experimentally studied the effect of bubble size and the entering length on the void fraction in vertical pipe air-water two-phase flow by employing a dual-sensor resistivity probe. The study also includes investigation on the effect of the water superficial velocity on the bubble size distribution. The two-phase flows have been examined at four different axial locations, L/D, along the test pipe namely, 30, 60, 90 and 120 respectively of 8000 mm long and 57.2 mm inner diameter pipe. The author has reported that bubble diameter has had a direct effect on the local void fraction distribution at a fixed air and water flux; moreover, bubble diameter has depended on the water flux magnitude.

Wu, et al.[130] have analysed the designing criteria of dual-sensor probes. The analysis has included the effect of lateral bubble motion on the dual-sensor conductive probe. Stainless steel wires of 89 μm diameters has used as a sensor which has been insulated with a 5 μm insulation resin. The axial separation distance between the front and rear sensor has been 2.65 mm, as shown in Figure 2.28.

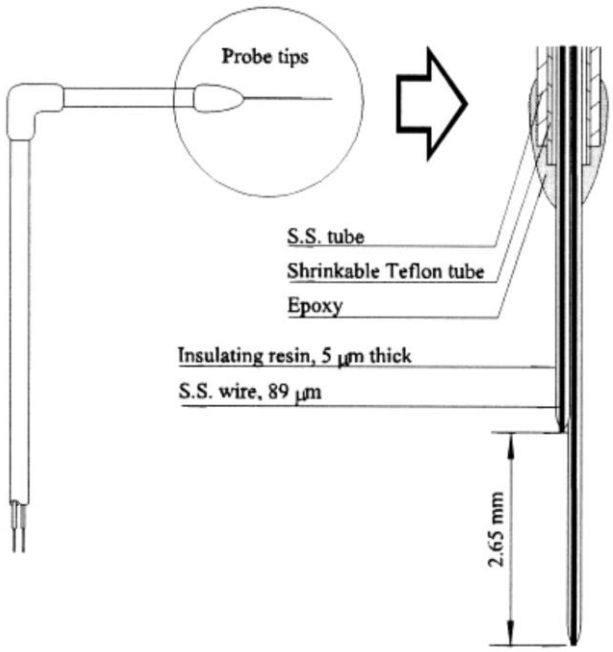

Figure 2.28. Dual-sensor conductance probe [130].

The authors have concluded that if the axial sensor separation distance to the bubble's diameter ratio has been smaller than the maximum relative fluctuation of the bubble velocity; the measured bubble velocity has approached infinity value. Therefore, minimum axial separation distance has been suggested to be one-half of the bubble diameters for overcoming this issue. The authors have also reported that accurate results could be achieved if the range of the axial sensor separation distance is within 0.5 to 2 of the bubble diameter. However, this finding contradicted the finding of Kataoka, et al. [131] who have reported that accurate measurements could be achieved using a dual-sensor probe with the axial sensor separation distance to be smaller than 0.2 of the bubble's diameter. Cheremisinoff [132] has recommended that the axial separation distance between the lead and the trailer sensors should be set at a distance equal to the maximum estimated bubble size. Kocamustafagullari and Wang [133] have suggested a 2.5 mm axial separation distance between the lead and rear sensors, to achieve more accurate bubble size and bubble velocity.

Angeli and Hewitt [91] have carried out experimental studies on the oil-water two phase flows in two horizontal pipes, steel and acrylic. High speed video cameras supported by a high-frequency impedance probe have been utilized for the flow pattern detection, whereas the dispersed phase flow

has been identified using a conductivity needle probe. A broad range of mixture velocities varying from 0.2 to 3.9 m/s and input water volume fractions from 6% to 86% have been used in this investigation. In this study, the signals processing techniques have been focused on the detection of the first point of the voltage rise or the fall of the generated signal, followed by adapting the raw signal into a rectangular wave signal, as shown in Figure 2.29. Each signal sample has been associated with two self-adjusting trigger levels. Moreover, each signal amplitude has been compared with the previous signal amplitude for adjusting the maximum, A_{max} , and the minimum, A_{min}, signal amplitude values. The threshold for cutting the noise has been defined in term of the margin x. Furthermore, the signals have transformed in terms of 0 and 1 values as,

If $A_n > A_{min} + x$ is applicable then signal amplitude is 1, whilst $A_n < A_{max} - x$ is applicable then signal amplitude is 0.

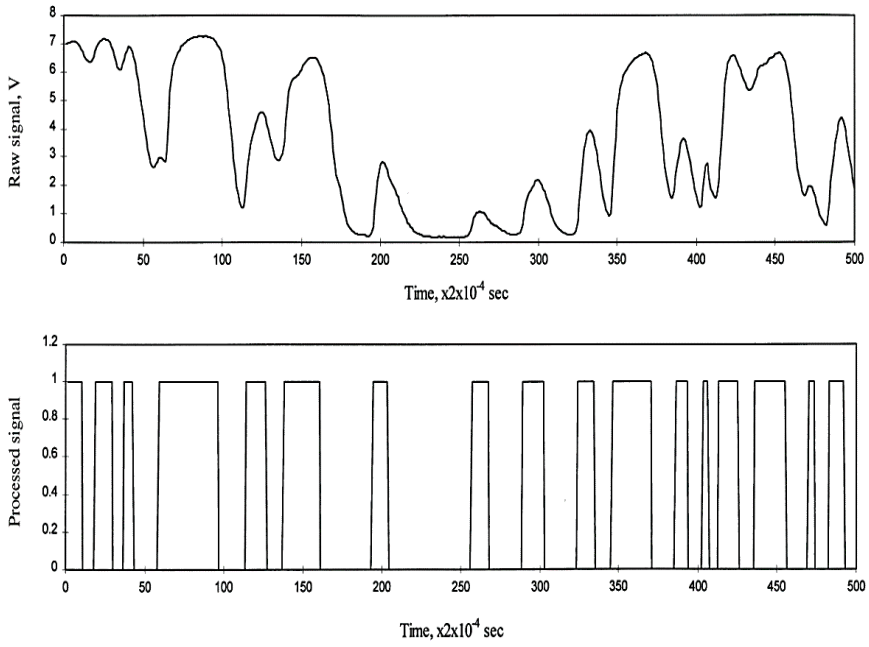

Figure 2.29. The raw and processed square wave [91].

Sanaullah et al. [79] have investigated the impact of dual-sensor probe inclination on two-phase bubbly flow properties measurements. The two-sensor probe has comprised of two Teflon coated stainless steel sensors. These sensors have been placed at three different angles of inclination 90°, 110° and 145°. The axial separation distance between the two sensors has been chosen to be 5 mm as shown in Figure 2.30.

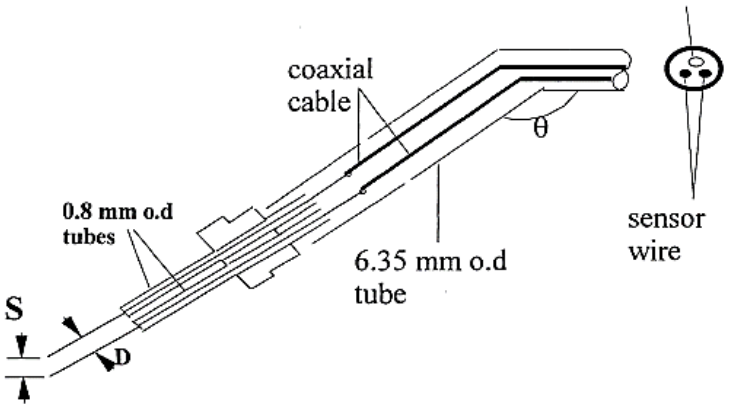

Figure 2.30. A schematic of inclined two-sensor probe [79].

The sampling frequency used in the investigation has been 25 kHz for each sensor with 60 sec of sampling duration. From the investigation, it has been observed that probe inclination could have a significant effect on the bubbles' fraction measurement by both probes, but less effect has been found on the other measured parameters. Furthermore, it has been also found that the probe inclination of 110° has given the best measurement.

Felder and Chanson [134] have carried out experimental investigations on the flow characteristics of air–water two-phase flow in a large size stepped channel model with a slope of 26.6˚. Two types of phase detection double-sensor conductivity probes have been used for the measurements of air–water interfaces in the bubbly free-surface flow, namely double-sensor probe and two single tip sensors. The double-sensor probe consisted of two sensors with diameter of 0.25 mm which have been separated by an axial distance, Δx, of 7.2 mm and a radial separation distance, Δz, of 2.1 mm, whereas the two-single tip probe consisted of two single tip sensors. Each sensor has had a diameter of 0.25 mm, axial separation distance, Δx, of 7.2 mm and a radial separation distance, Δz, of 2.1 mm, as shown in Figure 2.31. it is apparent that the authors have used stainless steel enclosure to support the sensors against sensor deflections.

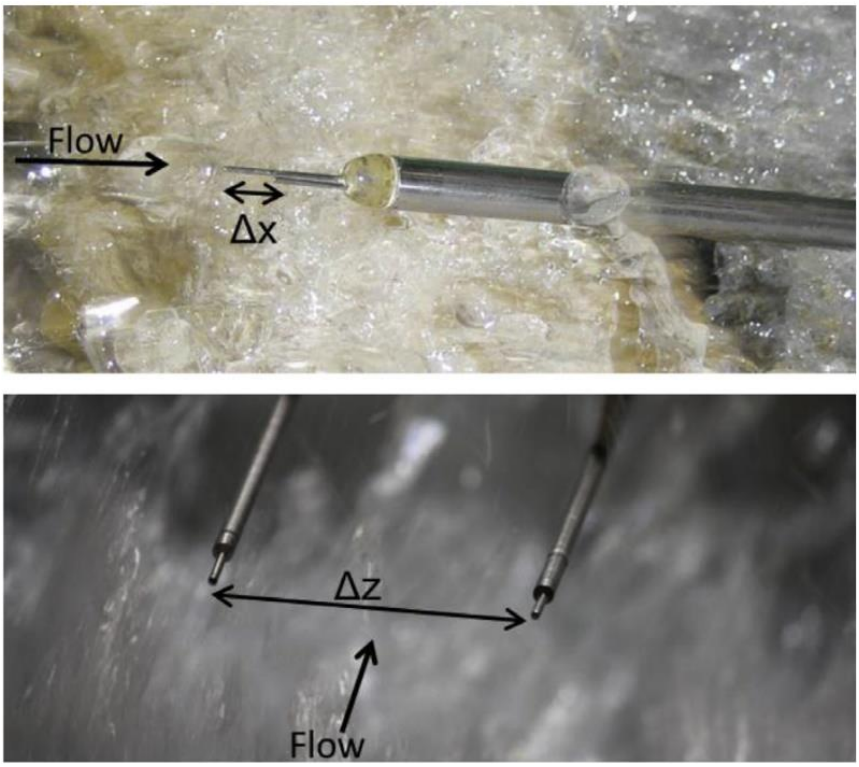

Figure 2.31. Conductivity probe designs[134].

The effect of sampling frequency and the sampling rate on the results accuracy has been investigated. It has been observed that the most accurate results could be obtained when the sampling frequency has been 20–40 kHz along with a sampling duration of 45 sec and above. The conductivity probe accuracy has been reported to be 4% for the void fractions measurement, whilst 5% has been reported for the interfacial velocities measurements.

2.3.2.3 Four- sensor conductivity probes

Theory of the four-sensor conductivity probe

Since the local dual-sensor conductivity probe is limited to measure the local secondary phase axial velocity and volume fraction only, four-sensor probe has been introduced to extend the conductivity probe ability to measure the velocity components in x, y and z directions of the dispersed bubbles in multiphase bubbly flow.

Generally, four output signals will be generated from a four-sensor conductivity probe whilst using it for multiphase flow properties measurement. The generated signals represent the time interval between the first bubble-sensor contact and the last contact at each of the rear sensors. These time delays can be seen in Figure 2.32, which depicts the idealized signals from the four sensors.

The four-sensor probe theory, as it has been explained explicitly by [135], has been derived from the bubble movement at a velocity vector, V. The velocity vector, V, can be represented mathematically using the coordinate system shown in Figure 2.33 as:

$$V = v(sin\alpha\ sin\beta i + sin\alpha\ cos\beta j + cos\alpha k\ ) \tag{2.13}$$

The velocity vector, V, can be written as:

$$V = v\hat{\eta}_v \tag{2.14}$$

where β , is the azimuthal angle between the velocity vector, V, projection in x-y plane and the y-axis and α is the polar angle between the velocity vector, V, and the z-axis,

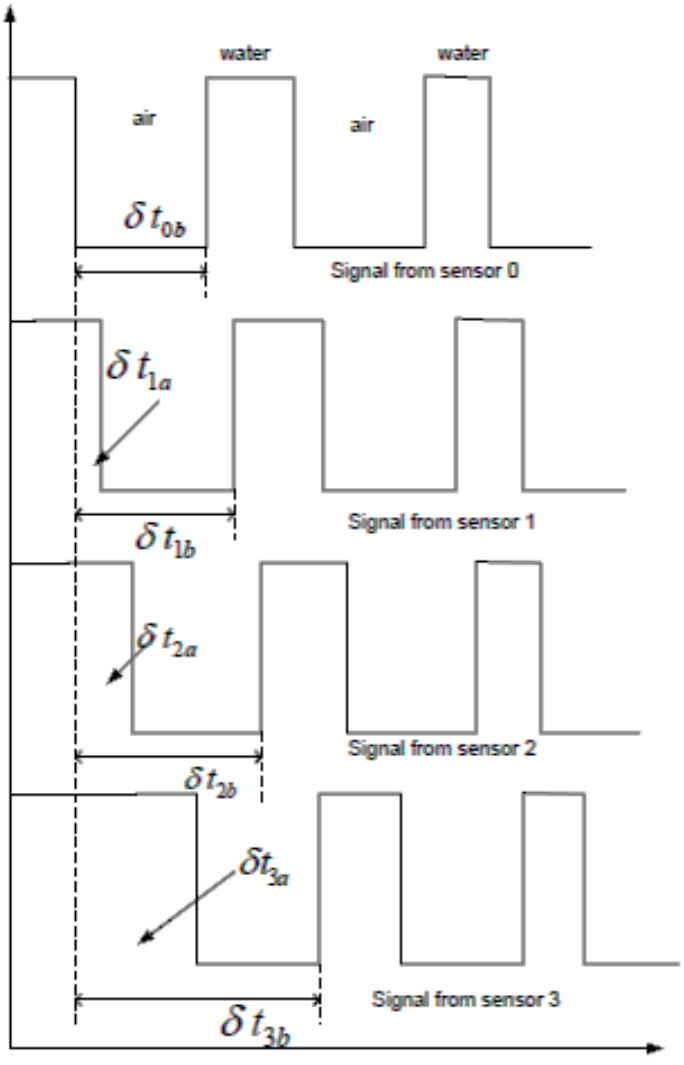

Figure 2.32. The idealized signals from the four-sensor probe [135].

v is the velocity magnitude of V, $\hat{\eta}_v$ is the velocity's unit vector, and i, j, k are unit vectors in the direction of the x, y, and z axes respectively.

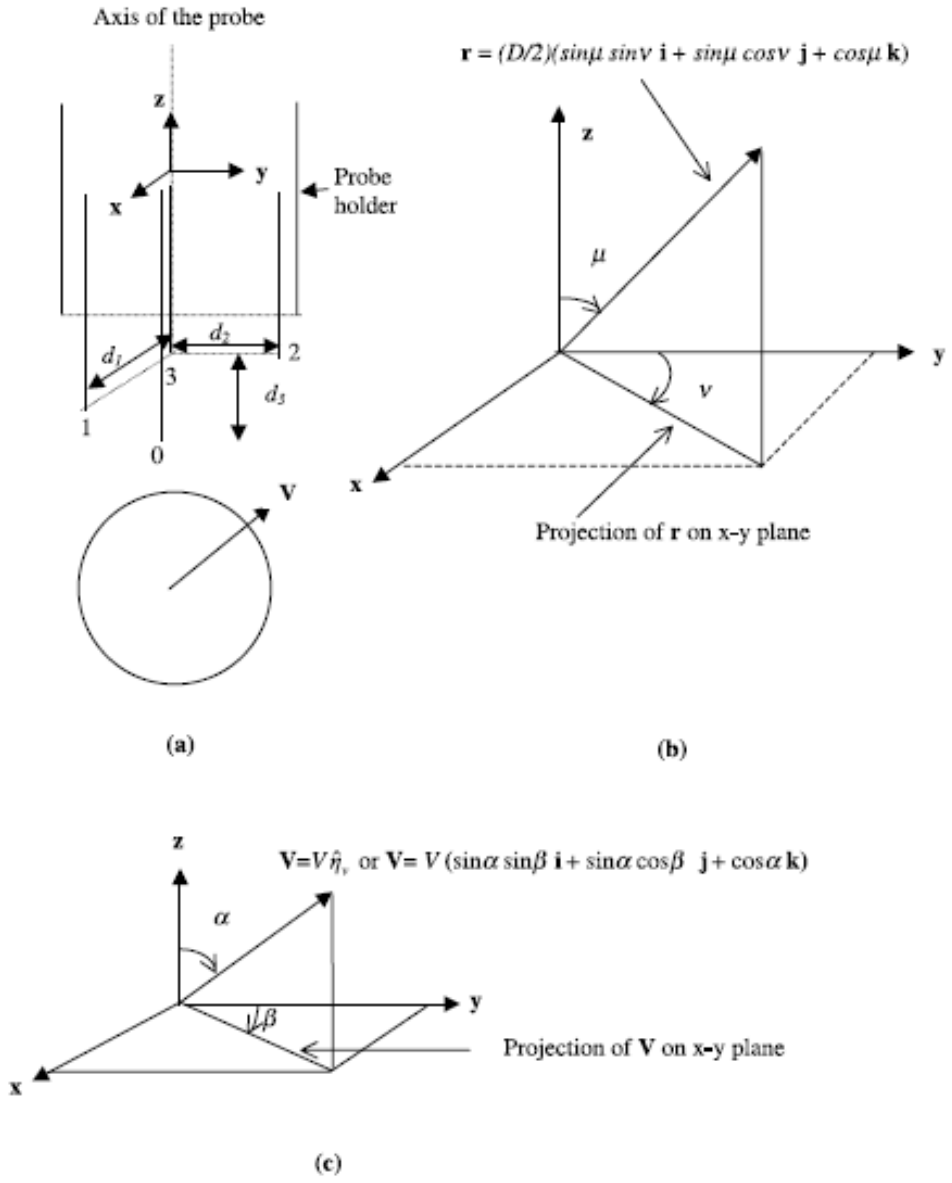

Figure 2.33. The coordinate systems of the four-sensor probe [135].

As a bubble comes into contact with the front sensor, S_0, the position vector, $\vec{r}$, can be defined as:

$$\vec{r} = r\hat{\eta}_i \tag{2.15}$$

where $\hat{\eta}_i$ is a unit vector. After δ_1 the same bubble comes into contact with the rear sensor, S_1, that is situated at $x_1, y_1 \; and \; z_1$ from the front sensor, the position vector $\vec{r}_1$ between the rear sensor S_1 and the bubble centre of gravity will be created and expressed by:

$$\vec{r}_1 = (\vec{r} + x_1 i + y_1 j + z_1 k - V\delta_1) \tag{2.16}$$

By squaring equation 2.16, we get

$$r_1^2 = (r + x_1 \mathrm{i} + y_1 \mathrm{j} + z_1 \mathrm{k} - V\delta \mathrm{t}_1).(r + x_1 \mathrm{i} + y_1 \mathrm{j} + z_1 \mathrm{k} - V\delta \mathrm{t}_1) \tag{2.17}$$

Expanding equation, 2.17, and substituting $\vec{V} = v\,\hat{\cap}_v$ and $\vec{r} = r\,\hat{\cap}_i$ we get

$$\begin{aligned} r_1^2 = \; & r^2 + rx_1(\hat{\cap}_i.\mathrm{i}) + ry_1(\hat{\cap}_i.\mathrm{j}) + rz_1(\hat{\cap}_i.\mathrm{k}) - rv\delta t_1(\hat{\cap}_v.\hat{\cap}_i) + rx_1(\hat{\cap}_i.\mathrm{i}) + x_1^2 \\ & - x_1 v\delta t_1(\hat{\cap}_v.\mathrm{i}) + ry_1(\hat{\cap}_i.\mathrm{j}) + y_1^2 - y_1 v\delta t_1(\hat{\cap}_v.\mathrm{j}) + rz_1(\hat{\cap}_i.\mathrm{k}) \\ & + z_1^2 - z_1 v\delta t_1(\hat{\cap}_v.\mathrm{k}) - rv\delta t_1(\hat{\cap}_v.\hat{\cap}_i) - x_1 v\delta t_1(\hat{\cap}_v.\mathrm{i}) \\ & - y_1 v\delta t_1(\hat{\cap}_v.\mathrm{j}) - z_1 v\delta t_1(\hat{\cap}_v.\mathrm{k}) + v^2\delta t_1^2 \end{aligned} \tag{2.18}$$

Thus, the equation, 2.18, can be simplified as equation, 2.19, for each sensor as a bubble passes through it:

$$\begin{aligned} & v^2\delta t_i^2 - v\delta t_i\big(2r(\hat{\cap}_i.\hat{\cap}_v) + 2x_i(\hat{\cap}_v.i) + 2y_i(\hat{\cap}_v.j) + 2z_i(\hat{\cap}_v.k)\big) + [x_i^2 + y_i^2 + \\ & z_i^2 + 2rx_i(\hat{\cap}_i.i) + 2ry_i(\hat{\cap}_i.j) + 2rz_i(\hat{\cap}_i.k)\,] = 0 \end{aligned} \tag{2.19}$$

$$\begin{aligned} \big(v_x + v_y + v_z\big)^2\delta t_i^2 - 2\delta t_i\big(v_x r_x + v_y r_y + v_z r_z + x_i v_x + y_i v_y + z_i v_z\big) \\ + \left[x_i^2 + y_i^2 + z_i^2 + 2x_i r_x + 2y_i r_y + 2z_i r_z\right] = 0 \end{aligned} \tag{2.20}$$

where *i= 1, 2, 3 and 4.*

By using the quadratic equation, equation 2.20 can written as:

$$\delta t_1 = \frac{-b \pm \sqrt{(b^2 - 4ac)}}{2a} \tag{2.21}$$

where

$$a = v^2 \tag{2.22}$$

$$b = -v\left(2r(\hat{\cap}_i.\hat{\cap}_v) + 2x_i(\hat{\cap}_v.i) + 2y_i(\hat{\cap}_v.j) + 2z_i(\hat{\cap}_v.k)\right) \quad (2.23)$$

and

$$c = (x_i^2 + y_i^2 + z_i^2 + 2rx_i(\hat{\cap}_i.i) + 2ry_i(\hat{\cap}_i.j) + 2rz_i(\hat{\cap}_i.k) + r^2 - r_i^2) \quad (2.24)$$

where

$$\delta t_{1a} = \frac{-b - \sqrt{(b^2 - 4ac)}}{2a} \quad (2.25)$$

and

$$\delta t_{1b} = \frac{-b + \sqrt{(b^2 - 4ac)}}{2a} \quad (2.26)$$

Steinemann and Buchholz [136] have utilised four-sensor conductivity probe for investigating two-phase air-water flow properties including bubbles size and shape. The probe consisted of four platinum wires each 20 µm in diameter. The probe's frontal diameter has been 500 µm and it has been cladded by glass, and the sensors has been arranged in such a way that the central lead sensor has been surrounded by the rear three sensors as shown in Figure 2.34.

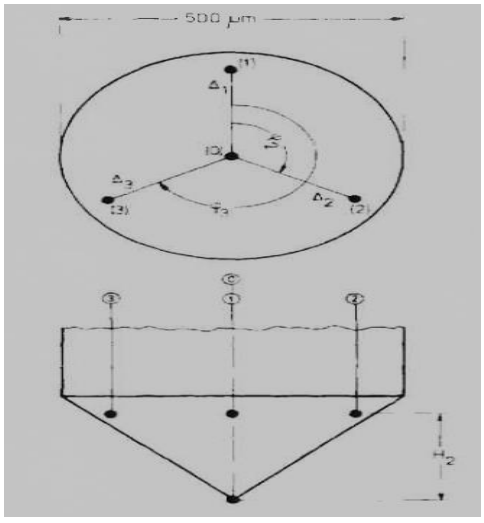

Figure 2.34. Four-sensor probe arrangement [136].

The notion behind adding the extra two sensors by the authors to the existing sensors is to eliminate the errors measured from the lateral bubble movement. The authors has advised that for exact estimation of the bubble properties, at least a four-point probe should be utilised.

For eliminating the effect of bubble curvature on the accuracy of bubble velocity measurement, the authors have proposed a new equation, see equation 2.7. This equation has taken into account both start and stop times for the bubble as it approaches the sensors and leaves the sensors. Further, the authors have claimed that by using equation 2.7, it is also possible to determine the velocity of non-centrally pierced bubbles.

$$V = \frac{2H_i}{\left(t_{start,i} - t_{start,0}\right) + \left(t_{stop,i} - t_{stop,0}\right)} \tag{2.27}$$

The authors have assumed that the bubble would not change its shape and direction of movement whilst interacting with the sensors. It has also been assumed that bubbles had ellipsoids shape.

The experimental investigations have been carried out by two means, namely bubble column with 15 cm diameter and 2600 mm height and loop reactor in 600 mm internal diameter and 8700 mm height. A wide range of water superficial velocities of 1-14 cm/s has been used throughout the investigations.

From their experiments, it has been concluded that by employing the four-sensor probe, reliable results could be obtained even when the flow velocity exceeds 3 m/s. However, the sensors have been subjected to bending loads due to the lateral flow. It has also concluded that the bubble size has not been measured accurately due to the discrepancies between the idealised ellipsoids shape and the real bubble shape. It should be noticed that neither the data repeatability nor accuracy have been reported by the authors.

Le Corre and Ishii [137] have numerically simulated the effect of probe geometry of the four-sensor conductivity probes on the dispersed phase velocity and the interfacial concentration. The authors have introduced a non-dimensional sensor separation parameter (axial separation divided by bubble diameter) (S/X) in the range of 0.6–1 for obtaining accurate velocity measurements for cases where the bubble velocity fluctuating is relatively low.

Kim, et al. [138] have conducted experimental studies on air-water two-phase flows utilizing a multi-sensor conductivity probe. The multi-sensor probe has consisted of four golden acupuncture-needle sensors of 0.13 mm outer diameter with sharply tapered tips. Figure 2.35 typically shows the sensors arrangement by Kim, et al. [138]. All sensors have been coated by a conformal coating that has given a very thin and uniform distribution coat. The signal-processing scheme that has been employed in this study isbased on two procedures, namely conditioning the raw signals, using moving median filter scheme, and normalizing the obtained signals, to obtain the desired multiphase flow parameters from processed the signals.

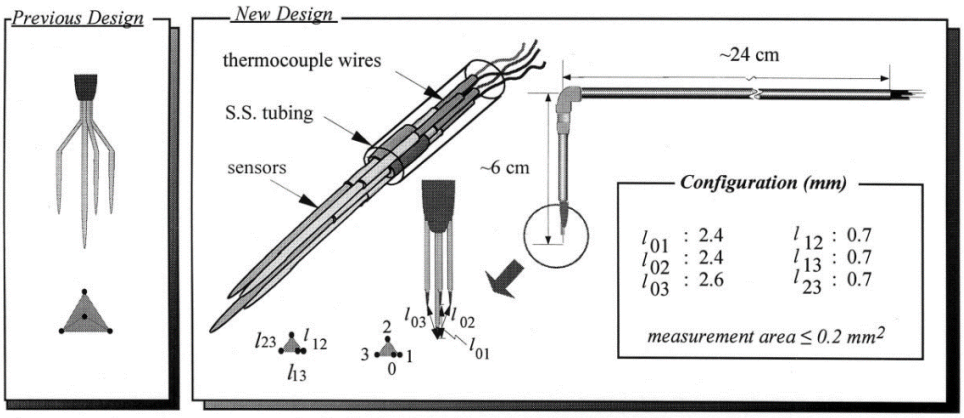

Figure 2.35. Schematic diagrams of four-sensor conductivity probes [138].

The experimental setup, as shown in Figure 2.36, has consisted of a Lucite pipe of 50.8 mm internal diameter with height of 3750 mm test section. The air has been injected through a 20 x 20 square matrix stainless steel tubes of 0.12 mm internal diameter. The water superficial velocity has been fixed at 0.321 m/s, whilst different air velocities have been used in range of 0.052, 0.179 and 0.432 m/s. Two sampling frequencies of 6 and 8 kHz have been used for obtaining the data depending on the flow conditions.

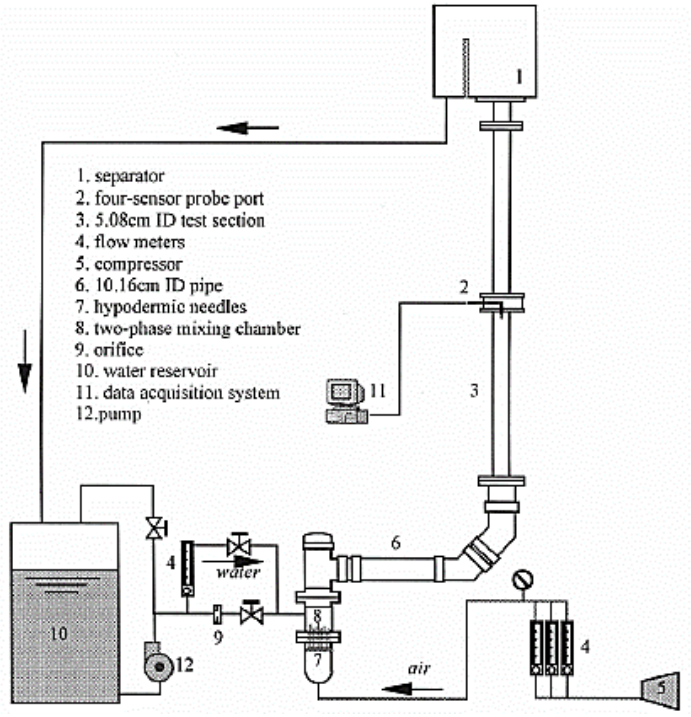

Figure 2.36. Schematic diagram of the experimental loop [138].

Mishra, et al. [135] have developed a novel measurement technique that consisted of a mathematical model which is used to determine the velocity vectors and diameters of spherical droplets in oil-water multiphase flows from the signal outputs of an intrusive local four-sensor probe.

This technique has been governed by seven assumptions:

1. The model can be used for droplets when it is spherical only and in cases where the slip velocity between the phases is very small.
2. The droplet surface contacts all of the rear sensors as it initially contacts a sensor and when it leaves the sensor.
3. The droplets should contact the lead sensor S_0 prior contacting the rear sensors.
4. All sensors have to situated in an orthogonal arrangement.
5. The impact of droplets - probe contact should not affect the velocity vector, V.
6. The output signals from each sensor are in ideal shape
7. The droplets keep their shapes and not deformed whilst immersed by the sensors.

The computational scheme for solving the equations that measures the flow properties has been presented as Figure 2.37.

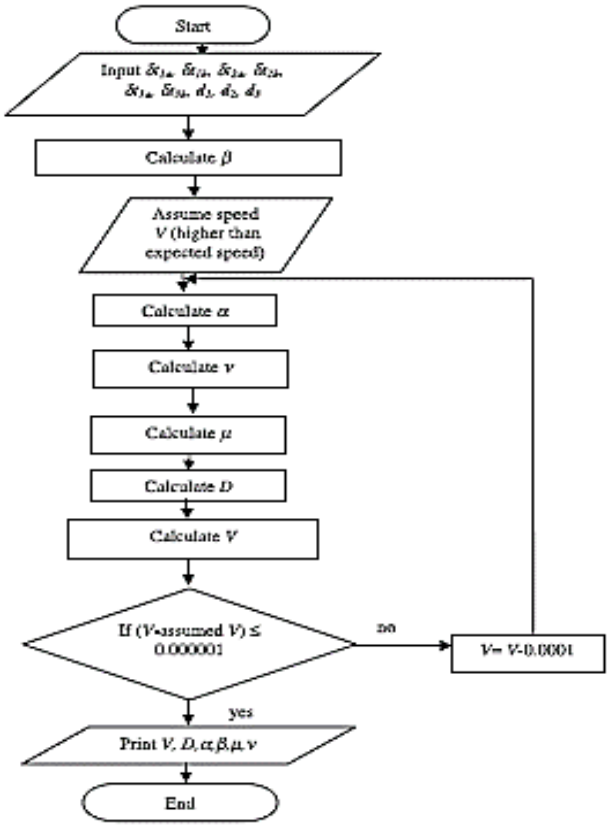

Figure 2.37. The iterative computational scheme flow chart [135]

Lucas and Mishra [139] have introduced a novel measurement technique for measuring the local axial, radial and azimuthal velocity components of the gas in bubbly gas-liquid flows using a local four-sensor conductance probe that has overcome the most of the limitations that had been assumed in Mishra, et al. [135] study. The four-sensor probe has been manufactured from four stainless steel acupuncture needles that has offered a relatively high level of rigidity. Each probe has been of 0.3 mm in diameter, as shown in Figure 2.38.

The Experiments have been carried out in a PVC vertical pipe with 80 mm internal diameter, the bubbly air–water two-phase flows properties have been measured with and without swirl flow. Throughout the experiments, a range of 0.41 m/s - 0.91 m/s of water superficial velocities and range of 0.037 m/s - 0.081 m/s of gas superficial velocities have been used where the gas volume fraction has been always kept less than 0.1.

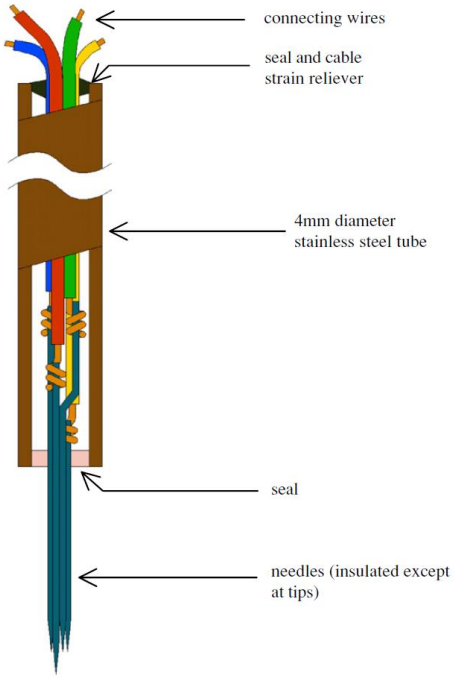

Figure 2.38. Four-sensor conductance probe [139].

This technique has included a mathematical model that has been valid for bubbles that have a plane of symmetry normal to their direction of motion, including spherical and oblate spheroidal bubbles. It has been reported that the dispersed bubbles and droplets in many multiphase flows have tended to become flattened into oblate spheroids whilst they have been moving through the continuous liquid phase. The novel mathematical technique, which has been developed by the authors, has been represented in three independent equations: 2.28, 2.29 and 2.30, in terms of the bubbles' velocity

magnitude v, the polar angle α of bubbles' velocity vector and the azimuthal angle β of the bubbles' velocity vector.

$$x_1 \sin\alpha \sin\beta + y_1 \sin\alpha \cos\beta + z_1 \cos\alpha = \frac{v\delta t_{11}}{2} \quad (2.28)$$

$$x_2 \sin\alpha \sin\beta + y_2 \sin\alpha \cos\beta + z_1 \cos\alpha = \frac{v\delta t_{22}}{2} \quad (2.29)$$

$$x_3 \sin\alpha \sin\beta + y_3 \sin\alpha \cos\beta + z_1 \cos\alpha = \frac{v\delta t_{33}}{2} \quad (2.30)$$

where, x_i, y_i and z_i represent the coordinates of the i^{th} rear sensor (i = 1, 2, 3) in the probes' coordinate system of the four-sensor probe and the terms δt_{ii} (i = 1, 2, 3) are defined as:

$$\delta t_{ii} = \delta t_{ia} + \delta t_{ib} - \delta t_{ob} \quad (2.31)$$

With reference to Figure 2.39, firstly, δt_{ia} is the time interval between the first contact of the bubble's surface with sensor 0, and the first contact of the bubble's surface with the i^{th} rear sensor. Secondly δt_{ib} is the time interval between the first contact of the bubble's surface with sensor 0, and the last contact of the bubble's surface with the i^{th} rear sensor. Lastly, δt_{0b} is the time between the first and last contacts of the bubble's surface with sensor 0. By solving Equations (2.28-2.30) simultaneously the following expressions for tan β and tan α are obtained.

$$\tan\beta = \frac{\left(\frac{z_1}{\delta t_{11}} - \frac{z_2}{\delta t_{22}}\right)\left(\frac{y_1}{\delta t_{11}} - \frac{y_3}{\delta t_{33}}\right) - \left(\frac{z_1}{\delta t_{11}} - \frac{z_3}{\delta t_{33}}\right)\left(\frac{y_1}{\delta t_{11}} - \frac{y_2}{\delta t_{22}}\right)}{\left(\frac{z_1}{\delta t_{11}} - \frac{z_3}{\delta t_{33}}\right)\left(\frac{x_1}{\delta t_{11}} - \frac{x_2}{\delta t_{22}}\right) - \left(\frac{z_1}{\delta t_{11}} - \frac{z_2}{\delta t_{22}}\right)\left(\frac{x_1}{\delta t_{11}} - \frac{x_3}{\delta t_{33}}\right)} \quad (2.32)$$

$$\tan\alpha = \frac{\left(\frac{z_2}{\delta t_{22}} - \frac{z_1}{\delta t_{11}}\right)}{\left(\frac{x_1}{\delta t_{11}} - \frac{x_2}{\delta t_{22}}\right)\sin\beta + \left(\frac{y_1}{\delta t_{11}} - \frac{y_2}{\delta t_{22}}\right)\cos\beta} \quad (2.33)$$

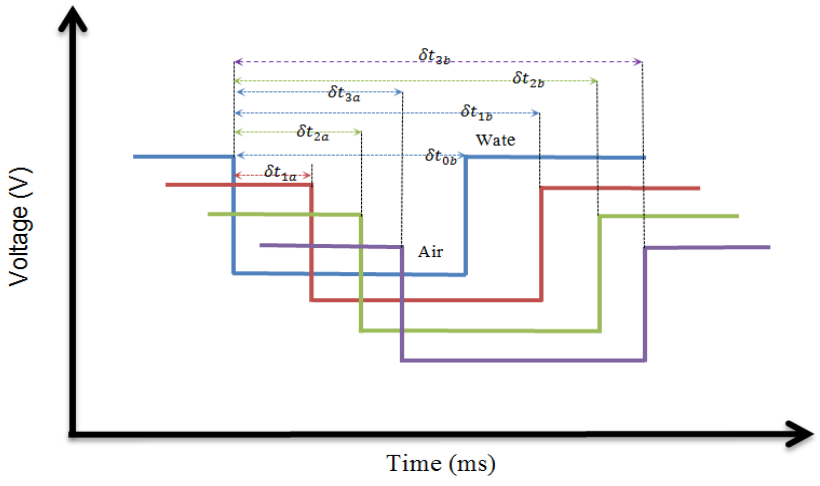

Figure 2.39. Ideal signals generated from the 4-sensor probe.

The authors have found that this technique has been relatively insensitive to the assumptions made regarding the exact time of contact of the sensors and the surface of the bubble. The authors have also found that the presence of the four-sensor probe in the flow stream could cause the magnitude of bubble velocity vector, v, to be reduced by up to about 20%.

Pradhan, et al. [140] have validated the four-sensor probe by using two high speed cameras. The experimental setup has consisted of a vertical PVC pipe of 80 mm internal diameter with and without the presence of a swirler. Two cases have been investigated, for the first case, water superficial velocity of 0.76 m/s and superficial velocity 0.04 m/s gas have been used, whereas for the second case water superficial velocity of 0.57 m/s and superficial velocity 0.02 m/s gas have been used.

From the comparison between the probe measurement and the high-speed cameras measurement, a reasonably good agreement has been observed. The authors have claimed that the development of a unique digital signal processing schemes has enabled the accurate computation of different flow characteristics and forwarded this as a novel feature of their work. From the experiments, the authors have established that the increase of probe's frontal area would reduce the possibility of bubble to be touched by all the sensors. Therefore, probes with smaller frontal area have been preferable for the time delays' measurement in air-water bubbly flow. The authors have recommended applying the sampling rate of 1e^5 Hz or above for the data collection to minimize the measurements' errors.

Cobo, et al. [141] have carried out experimental and numerical studies on bubbly, cap and slug air-water two-phase flow in a vertical pipe. A four-sensor probe has been utilized in their study for investigating the dispersed phase properties in a 3 m height and 52 mm of inner diameter Plexiglas pipe, as shown in Figure 2.40. A purified water has been used as a primary phase, whilst air has been used as a secondary phase that has been supplied by an air compressor through a porous sinter element with an average pore size of 40. Furthermore, both phases' temperature has been kept constant during the experiments.
For the experimental part, Laser Doppler Anemometry (LDA) has been used to measure the liquid velocity, whereas a four-sensor conductivity probe has been used as a dispersed phase detector.

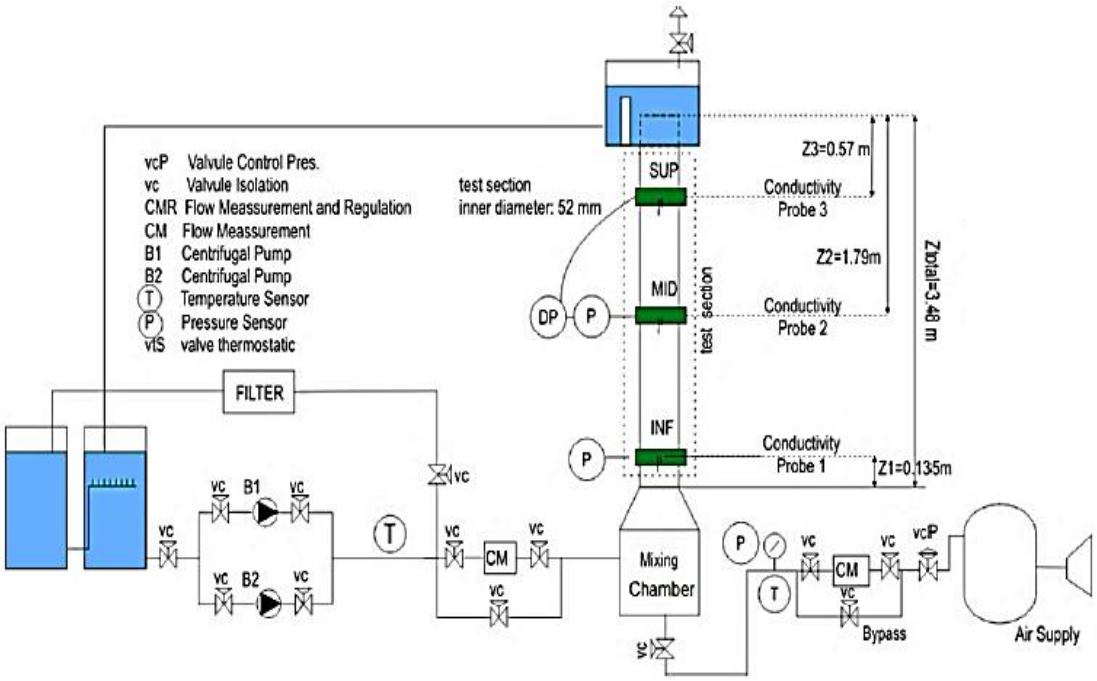

Figure 2.40. Schematic diagram of experimental loop [141].

The four-sensor probe has comprised of four gold coated stainless-steel sensors of 0.26 mm in diameter. where the axial, SL, and radial, x, dimension is presented in Figure 2.41.

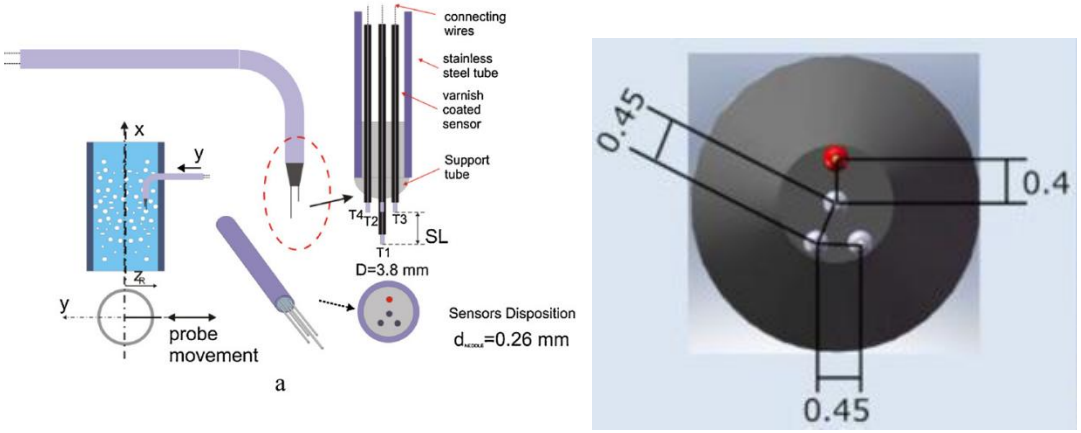

Figure 2.41. The dimensions of the four-sensor probe [141].

For the numerical part, the Lagrangian–Eulerian model combined with a 3D random walk model has been established. A good agreement of the void fraction profile has been obtained between the model

prediction and the four-sensor probe measurements for the bubbly flow case. The results have been compared with the results from the literature, very good agreement has been observed.

Shen and Nakamura [142] have conducted experimental studies of air-water two-phase flows in a vertical pipe utilizing a four-sensor conductivity probe, as shown in Figure 2.42.

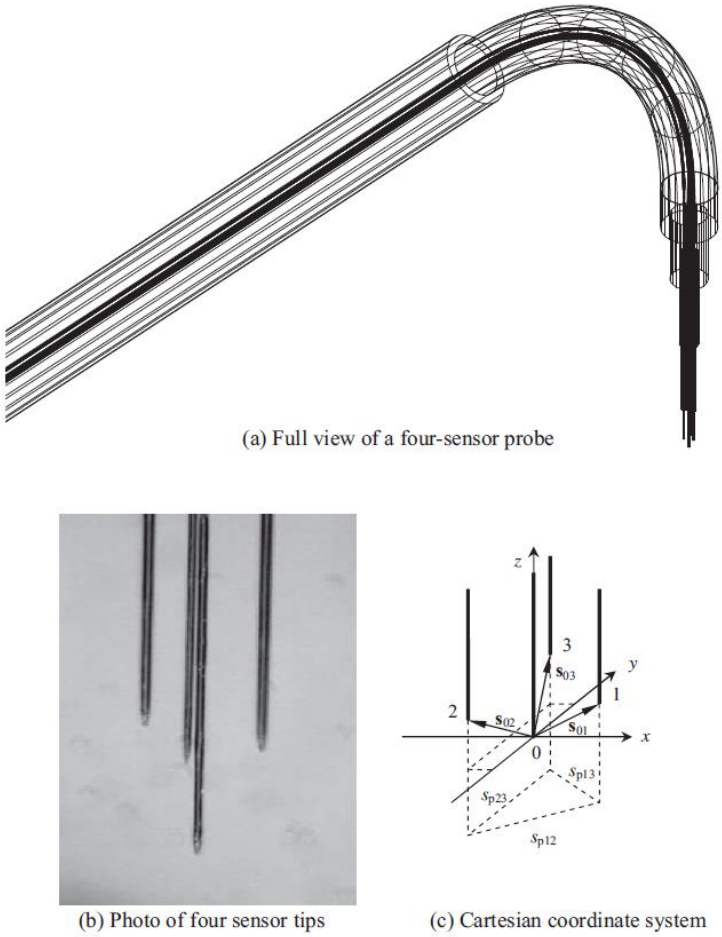

Figure 2.42. Four-sensor probe [142].

The multiphase phase flows experiment has been carried out in a vertical 200 mm inner diameter pipe, as shown in

Figure *2.43* . A pressure gage and orifice flow meters have been used for the gas pressure and inlet gas flow rate measurements respectively. Differential pressure (DP) gages have been used for obtaining the pressure distribution along the flow, consequently the cross-sectional area-averaged void fractions along the flow. The local dispersed phase flow measurements have been obtained from the optical four-sensor probes that have been installed at z/ D = 41.5, 82.8 and 113 axial locations. Each

probe measured the flow properties at 11 radial locations with a sampling frequency of 10 kHz for 3 x 100 sec.

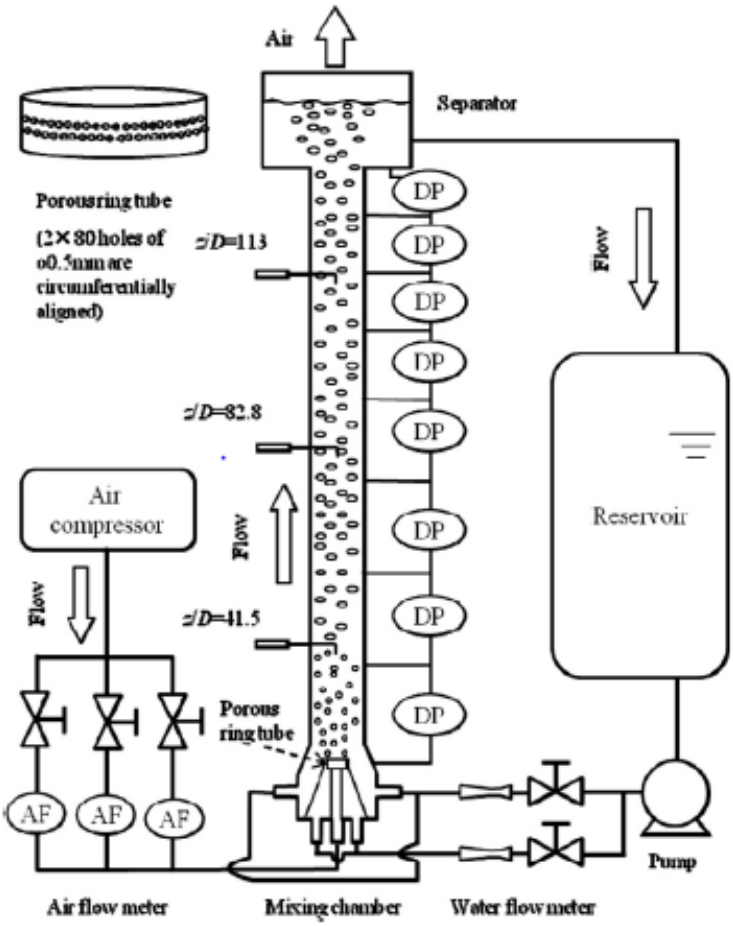

Figure 2.43. Schematic diagram of experimental loop [142].

Their investigations have focused on a theoretical establishment of the measurement approaches of the time-averaged local interfacial area concentration and the local interfacial velocity vector.

In this study, the four-sensor probe limitations have been reported as:

1. The finite size, the invasiveness of the multi-sensor probe and the difference between the assumed and real interfaces around the probe. All these may force some of the bubbles to escape from touching the front sensor tip.
2. The bubbles' shapes are subject to deform of and /or bubble velocity slows down due to the effect of the probe's wall shear stress. Therefore, the authors were advised to not using the four-sensor probe for multi-phase properties measurements where the liquid phase velocity is very low.

3. The axial separation distance, S, between the lead and the trailer sensors has a direct effect on the increase of the number of the missing bubbles.

The multi-sensor probes have been found to measure the large bubble size's properties with a reasonable accuracy. Whilst, certain deviations in the measurement have been obtained when small bubbles have presented. The signal-processing scheme has been based on the interface–pairing signal processing and combined the missing and escaped bubbles into the dispersed phase calculation. The flow chart shown in Figure 2.44 explains the signal-processing process.

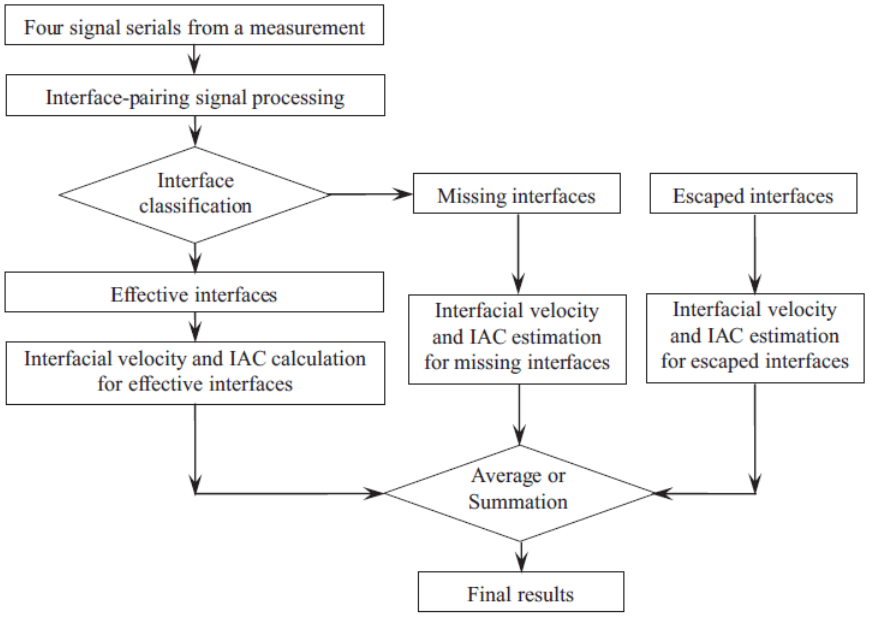

Figure 2.44. Flow chart of signal processing use by [142].

Smith et al. [143] have employed four-sensor probes to investigate the flow properties in large pipes experimentally.The experiment has consisted of two large vertical pipes of 102 mm and 152 mm ID, as shown in Figure 2.45. The system pressure has been of 500 kPa, 20 m/s of gas superficial velocitie, 10 m/s of liquid superficial velocitie and in the test section have been of 0.102 m ID, whilst 9 m/s gas superficial velocity and 4 m/s liquid superficial velocity have been used in the test section of 0.152 m ID.

The main reason for their investigations has been to provide a wider database for the interfacial area transport equation, IATE, source and sink term models for understanding the two-phase flow structure in large pipe and evaluating the current flow regime transition criteria for large pipes.

In their study, the authors have stated the capability of the multi-sensor conductivity probe in measuring the flow properties, with some measurement uncertainty, using the four-sensor probe that is similar to the one used by Kim et al. [138].

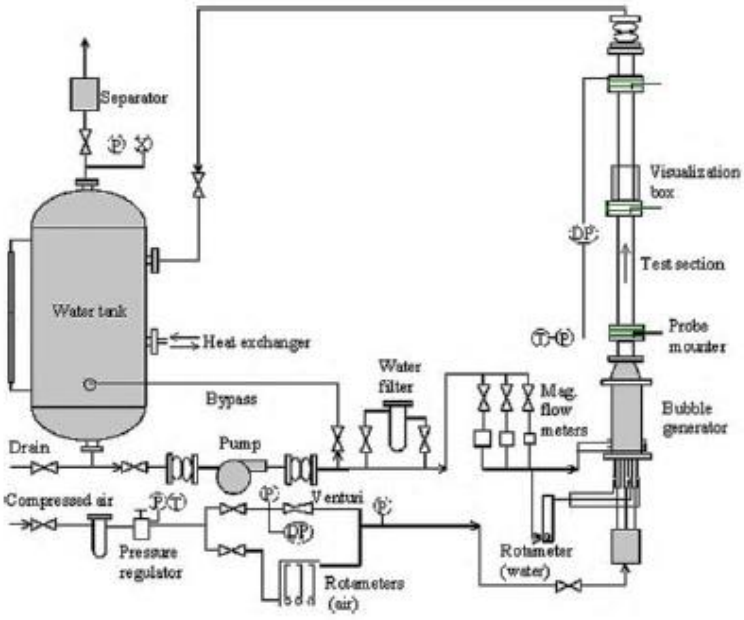

Figure 2.45. Experimental test rig [143].

The measurement uncertainty of the conductivity probe has been identified into two sources as given below:

1. The probe structure, this has been connected to the probe geometry, interface velocity, and frequency rate. This source affects the uncertainty of the velocity of a single bubble interface. This source has been evaluated to produce 9.8% of uncertainty in measurement. Furthermore, the experiments have been conducted on 20 kHz of measurement rate.

2. Large bubbles shape deformation due to the bubble-sensor interactions, this source has been reported to cause 6% uncertainty approximately.

Further, a magnetic flow meter with an accuracy of ±1% for the water flow rate measurement has been used, whilst a rotometer or Venturi mass flow meter has been used for the air flow rate measurement with an accuracy of ±1%. Moreover, a high-speed camera has been used to verify the classification of flow conditions in flow regime identification. No repeatability has been reported.

2.3.2.4 Five-sensor conductivity probes

Burgess and Calderbank [74] have established an improved multipoint conductive probe to eliminate the uncertainties, which have been associated with previous techniques for measuring bubble velocity and size in air-water two-phase flow. The probe consisted of five sensors made of nickel wire with 0.22 mm diameter. Each sensor has been coated with PTFE coating, except at the tips, and is enclosed within a stainless steel tube, as shown in Figure 2.46.

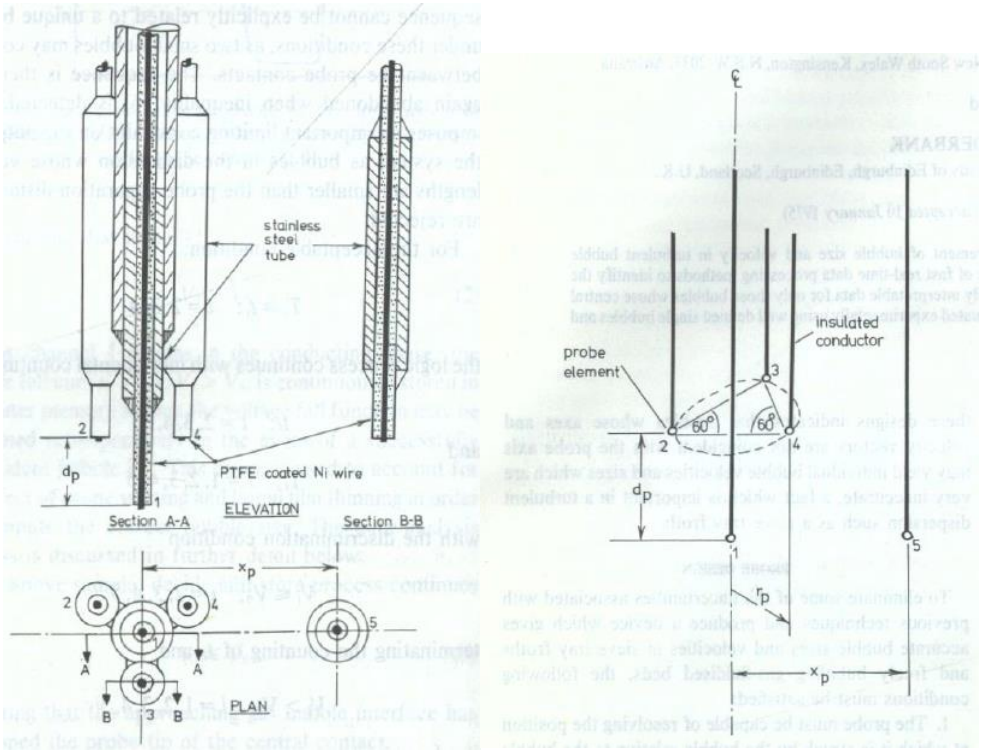

Figure 2.46. Five-sensor probe [74].

The probe has been designed in such a way in which three of the five sensors have been placed around the central sensor creating an equal sided triangle. The transverse distance between sensors 2, 3, 4 and the central sensor 1 has been 1.52 mm; whereas, the fifth sensor has been positioned at the same axial distance as the middle sensor with a radial distant of Xp between them, where Xp was approximately 5.86 mm. The bubble velocity, U_B, has been calculated using equation 2.34,

$$U_B = \frac{3d_p}{\sum_{i=2}^{4} t_i} \tag{2.34}$$

where, d_p is axial separation distance, t_i is the time delay measured by sensors 2, 3 and 4.

whilst, the bubble size has been measured from calculating chord length using equation 2.35,

$$L_{C=}U_B t_{1c} \tag{2.35}$$

where, t_{1c} is the time between the start and end of the interval time as shown in Figure 2.47.

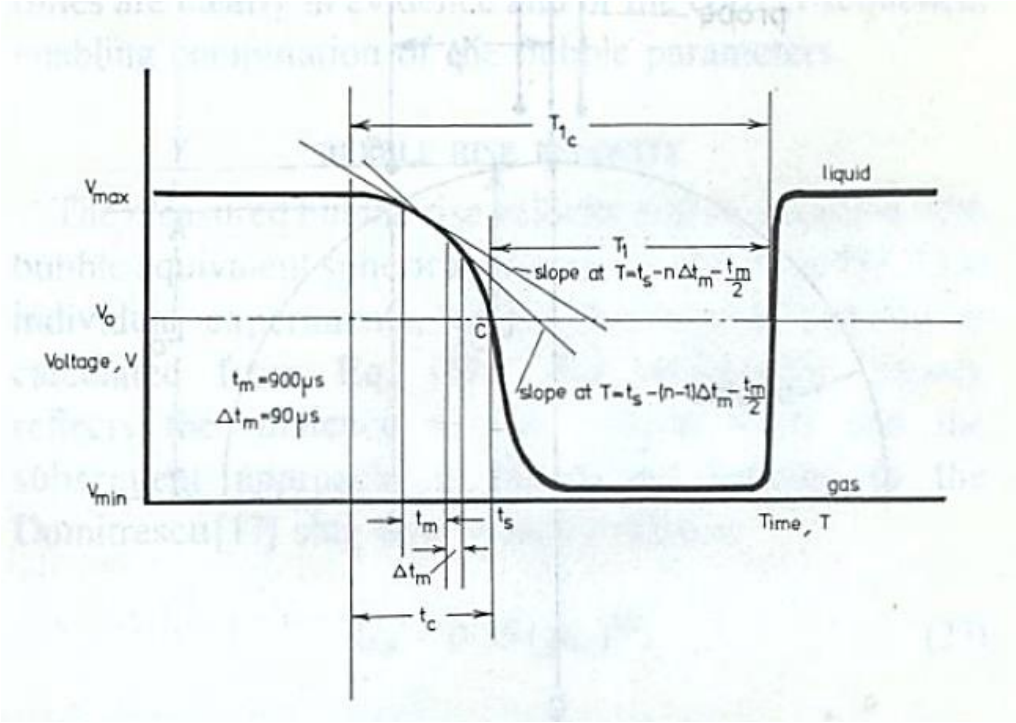

Figure 2.47. The Ideal signal for the time response of the wetted element [74].

The experimental test has been carried out in a 0.13m internal diameter glass pipe. The primary phase, water, has been stagnant, whilst the secondary phase, air or argon, has been injected from the bottom of the pipe.

The drawback of the probe operation is that the probe operates at limited conditions. It operates only when the bubble velocity and bubble vertical axis are coincident with the probe axis within fine limits, and where the bubble size is at least 6 mm. The response of the fifth sensor has been used for the determination of horizontal dimension of the bubble, with the assumption that bubbles have ellipsoidal shape.

Euh, et al. [144] have developed a five-sensor conductivity probe system for the measurement of the interfacial area concentration (IAC) in multiphase flows. The investigation has included some numerical simulations for three bubble shapes, namely cap, ellipsoidal and spherical bubbles for the new system

evaluations. The five-sensor conductivity probe has comprised of a central front sensor, a central rear sensor, and three peripheral rear sensors, as shown in Figure 2.48.

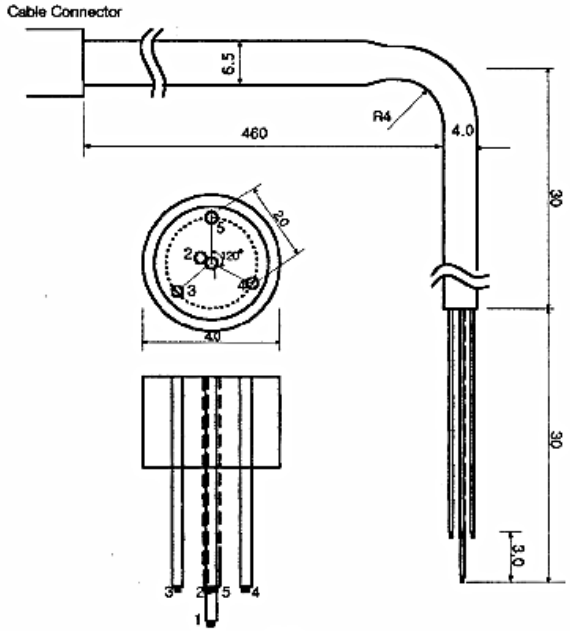

Figure 2.48. Prototype of the five-sensor conductivity probe [144].

Three different length scales of the probe have been applied to the simulations in order to study the effect of the probe size on the accuracy of IAC measurement.

From the numerical simulations, the authors have reported that the five-sensor probe has provided reasonably better results as compared to a four-sensor probe measurement.

Conclusion remarks

It is apparent from the literature review that:

1. the real-life bubble shape and size have not been measured yet, and all attempts have been limited on providing mean Sauter dimeter as a size and spherical or ellipsoidal shape.
2. Many factors have limited the researchers from extending their research area using multi-sensor probes, such as the effect of flow field around the probe and sensor. To overcome this effect, authors tend to use rigid materials or sensor-support materials to strength the sensors against deflection; however, this method increases the bubble-sensor interactions. Furthermore, none of the researchers attempted to overcome this issue using an embedded code instead of physical treatments. As the finite size and the intrusiveness of the multi-sensor probe is inevitable and the difference between the real and assumed interfaces around the sensors is relatively large, therefore, it is essential to evaluate, reduce and correct the errors associate with the measurement when the multi-sensor probe is used in the real-world applications.

3. Limited dispersed phase properties available, especially bubble shape and size, in large pipe diameters.

2.4 Bubble size measurement

Bubble-size distributions have a significant influence on the performance of multiphase systems, nonetheless, this property has not been readily measured directly using probes [145]. Most of the researches have obtained bubble sizes by obtaining the bubble size from the chord lengths by modelling the bubble shape as an ellipsoid.

Many attempts have been made to measure the bubble size, such as capturing bubbles in bubble column using high speed cameras. This method can effectively capture the bubble-size distribution, [146] and [147]. However, the X-ray method, has been used to measure the bubble sizes in three-dimensional flow fields [148]. Using the X-ray method is limited to the width of the bed that limits the ray intensities application. Therefore, at a dense bubbly flow, individual bubbles cannot be recognised clearly. Locally measuring probes usually measure chord lengths that can be used to characterize bubble sizes [145]. The chord length is the product of the bubble velocity and the time delay of the corresponding pulse of the probe signal. The method of extracting bubble size from the chord-length data is not straightforward. Werther and Molerus [149] have investigated the multiphase flows properties of fluidization in random sizes of beds . The measurement system has been comprised of a miniaturized capacitance probe shaped specifically, to reduce the interference between the probe the flow field. The authors have used ellipsoidal bubble shapes as a base of providing the initial investigation of the association between the bubble size and the chord length. Clark and Turton [150] have investigated the relations between the chord lengths distribution and the bubble sizes distribution for a variety of bubble shapes, Based on their investigations, the authors have proposed a numerical backward transform for deducing the chord-length distribution from the bubble size distribution. Later, Turton and Clark [38], based on bubble's size, have extended these techniques to include the spherical-cap bubbles that have been observed in fluid beds with bubble velocity.

Steinemann and Buchholz [136] have developed the particle surface formula based on the bubble parameters of motion, which are velocity, the polar angle and the direction of ascent. However, these equations depict the bubble size and shape only when the bubble shape is ellipsoid. Furthermore, the authors assumed that the bubble does change neither its form nor its direction of movement before all probe points have left the bubble.

2.5 Summary of Literature

Based on the literature review presented above, the needle probe has been considered to be one of the best intrusive tools for dispersed phase properties detection in multiphase flows, however, many factors affect the accuracy of the secondary phase properties detection. These factors can be classified as the probe geometry, intrusiveness nature of the probe and the signal processing.

The size of the probe, especially the probe frontal area, and the invasiveness of the probe body in the flow stream generates turbulence around the probe and interrupts the flow stream lines, consequently this leads the bubbles to escape from touching the sensors tip this, in turn increases the number of the missing bubbles. The sensor diameter and the insulation material have a direct effect on the deformation of the bubbles shape and /or slowing down the bubble velocity. However, smaller sensor diameter is not always the solution, since it exposes the sensors to the risk of deflections. A correct axial separation distance selection, S, between the lead and trailer sensors is vital to measure the dispersed phase flow properties accurately. Side by side, the accurate threshold selection, sampling frequency and sampling period in the signal processing stage is promptly affects the measurement accuracy of the dispersed phase properties. In these regards, extensive work has been conducted to minimize the effect of these factors. However, precise solutions have not been proposed.

The real-life bubble shape and size have not been measured yet, and all attempts have been limited on providing mean Sauter dimeter as a size and spherical or ellipsoidal shape.

2.6 Scope of Research

Currently, the accuracy of dispersed phase properties measurement using multi-sensor probes is relatively low; sometimes the uncertainty reaches 30% [137] due to the bubble-sensor interactions. Based on the review of published literature, key areas of research for multi-sensor conductivity probes in the area of probe manufacturing and signal processing have been found:

1. The bubbles shape and size: these parameters are important for many engineering aspects such as void fraction profile and the drag forces on bubbles. The methodology for measuring these parameters has been limited on bubble chord length for bubble diameter measurement, which did not take the bubble deformation due to the bubble-sensor interaction into account.
2. The mathematical models that have been used for dispersed phase properties measurement are based on the time between the first and last contact of the bubble with the front sensor.
3. The dispersed phase velocity has not been measured accurately yet due to the fact that bubble slows down as the sensors immerse into the bubble.
4. The volume fraction measurement depends on double bubble-sensor contacts. Therefore, inaccuracy could occur in the volume fraction measurement-process due to bubble deformation.

5. The previous studies have not investigated the effect of the sensor and the probe deflection on the measurement accuracy. Since they have used sensor support materials, which it increases the bubble-sensor interactions.
6. Generally, there is lack of queries related to the interfacial area concentration, which needs the measurement of surface area of bubbles and droplets to be well established, there is also lack of actual bubble shape and size information in cases of regular/irregular bubbles shapes.

2.7 Specific Research Objectives

The main research objectives are:

- To develop a novel mathematical model that can be used to quantify the dispersed phase properties from the measured time corresponding to the first bubble-sensor contact.
- To develop a novel mathematical model for irregular bubble shape, which can be used to quantify the dispersed phase properties from the measured time corresponding to the first bubble-sensor contact.
- To design, development and manufacture the novel multi-sensor needle probe system, for the measurement of the dispersed phase properties.
- To quantify the flow field effect around the probe body.
- To establish the quantitative flow-sensor interaction over a wide range of flow variations.
- To develop novel mathematical expressions for each sensor that can be used to correct the measurement error due to the sensors deflection.
- To develop an image processing code that can measure the dispersed phase properties including the volume fraction.
- To investigate the accuracy of the novel probe with a high-speed camera in single-bubble experiments.
- To achieve deeper understanding of the bubble hydrodynamics by analysing the obtained data and introducing bubble size distribution across the test section.

After specifying the project aims and objectives clearly, it is the time to achieve these objectives. Therefore, experimental and numerical investigations are required to be carried out. Consequently, a detailed description of the experimental and numerical setups incorporated in this study are presented in the following chapter.

Chapter 3.

Methodology

Based on the research objectives of this study, which have been presented in the previous chapter, rigorous experimental and numerical investigations are required to be carried out. Therefore, an appropriate flow loop should be developed for this purpose. The flow loop construction comprised of pipelines, flow meters and test-section and traverse system have been presented in this chapter. Furthermore, the electronic circuit and data acquisition system have also been discussed critically in this chapter.

3.1 Flow loop setup

The purpose of this study, is to improve the multi-sensor conductivity probe measurement accuracy and consequently using this probe to produce valuable data that can be used to develop the knowledge about hydrodynamic bubble interactions. A suitable flow loop, therefore, is essential for the required flow field production that is relevant to the present study. The flow loop consists of 1160 mm x 1200 mm x 1000 mm MBN 1000-litre water tank with opened top to the atmosphere, and 4" PVC Schedule 40 connecting pipes. The main phase, which is water, has been supplied by a single-stage glanded centrifugal pump (Wilo CronoLine-IL 65/170-11/2), which has been in turn connected to the axial helix-type turbine water flow meter. The test section has been made of a transparent acrylic resin to observe the flow pattern, as shown in Figure 3.1. The compressed air has been fed into the flow loop via a mass flow meter, Omega FMA 1700/1800 series, through the air injection taps.

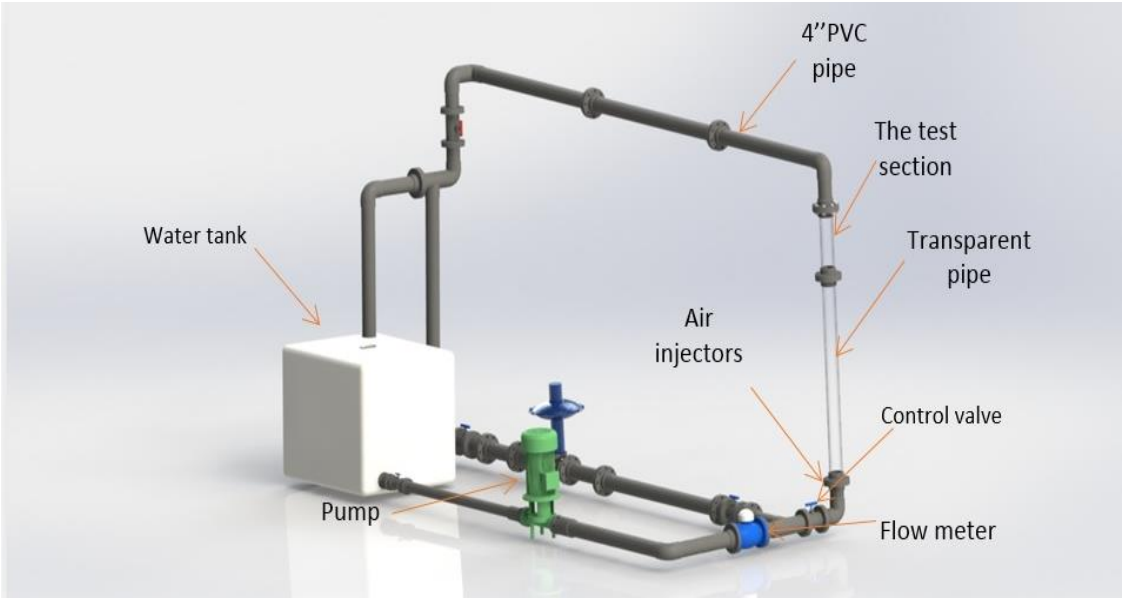

Figure 3.1. The outline of the experimental rig used in this study.

3.1.1 The water flow meter

For the water flow-rate measurement, Woltmann axial helix-type turbine water flow meter, MID MI-001 model, has been used. This flow meter measures the flow rate with an accuracy of ∓5%.

Principle of operation

The axial turbine flow meter converts the fluid flow motion, into an electrical signal, in form of AC sine wave pulse. In general, the bodies of turbine meter are usually made of bronze, cast Iron, or ductile iron materials. Whilst plastic or non-corrosive metal alloys is used for the internal turbine components.

The axial turbine flow meter measures flow rate accurately in normal working conditions. However, it is greatly affected by the flow profile and fluid conditions.

3.1.2 Air mass flow meter

In this study, the mass flow rate of the compressed air has been measured using an Omega FMA 1700/1800 series, as shown in Figure 3.2. This Mass Flow Meter is designed to work with clean gases only. Therefore, this mass flow meter has been connected to the flow loop via a pressure regulator, which has a filter to keep the air quality high. Moreover, it has been connected to non-return valves to keep the water away from the mass flow meter since the presence of water in the air flow meter could damage it.

Principle of operation

As the air stream enters into the transducer it is split by pushing a small percentage of the air flow through a stainless-steel capillary tube, which is the sensor. Whilst the remain fraction of the air flows through the main pipe. Both of the geometries of capillary tube and the main pipe are designed to ensure that the flow is kept laminar in each section. Based on the fluid dynamics principles the air flow rates in the two-laminar flow tubes are proportional to one another. Hence, the total flow through the transducer is directly proportional to the measured flow rates by the capillary tube. For sensing the flow in the capillary tube, at two sections of the capillary tube heat flux is introduced by means of precision wound heater-sensor coils. Thereafter the generated heat is transferred through the thin wall of the sensor tube to the inside flowing air. When the air flows through the tube, the transferred heat is carried by the air stream from the beginning of the coil to the end of coil windings. At the end, electronic control circuit is designed to detect the generated temperature. From the electronic control circuit, a generated output signal is obtained which is function of the carried heat by the air to indicate mass-molecular based flow rates. The maximum air mass flow meter can measured up to 50 L/min in this setup.

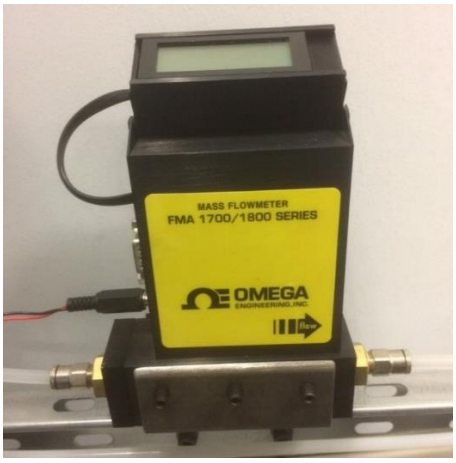

Figure 3.2. Air mass flow meter.

3.1.3 Differential Pressure Transmitter

Pressure and differential pressure measurements have been conducted by using IMPRESS Differential Pressure Transmitter pressure gauge, as shown in Figure 3.3. Two DP taps have been located down and up stream of the test section with a separated distance of 1 m between the two taps. The DP Transmitter measuring rate is 0 – 0.25 Bar.

Figure 3.3. Differential pressure transmitter.

Principle of operation

The Principle of operation of any differential pressure transmitter is based on sensing the difference of pressure between the two different points and then a signal is produced which corresponds to the range of pressures. Usually this operation requires the transmitter to be built from two separated cases. One of these cases combines the pressure-sensing element, whilst the other case holds the electronic circuits that produces the signals that represents the calibrated pressure amount, in form of either voltages or current.

The Transmitter Strain Sensor accuracy that has been used in this study, and according to IEC 60770, is 0.5 % FSO.

3.1.4 The Location of the multi-sensor probe

As multiphase flows enter the test pipe, boundary layers continue growing until they meet after some distance downstream from the entrance region. From this distance onwards, the velocity distribution pattern remains same. This flow is called a fully developed flow. Moreover, fully developed turbulent flows are the basis for most of flow meter usage and calibrations [151]. Therefore, a CFD simulation has been conducted to quantify the entering distance in which the flow gets fully developed. At that distance and onward the multi-sensor probe can be located.

The test section has been modelled for this investigation comprises of 2 m long pipe with 100 mm inner diameter. The pipe has been considered relatively smooth having a wall roughness constant of zero. A single-phase flow water at 20 ºC has been tested at 1 m/s. The mesh density of $1x10^6$ elements have been used in this investigation, according to a CFD simulations had been conducted to justify the number of elements required for this investigation.

Four length ratios, L/D, namely 10, 13, 15, 17 and 18 have been examined along the test-section, as shown in Figure 3.4. It has been found that the flow gets fully developed at L/D =13. Therefore, the test section has been located at 1300 mm from the air injection points, as shown in Figure 3.4.

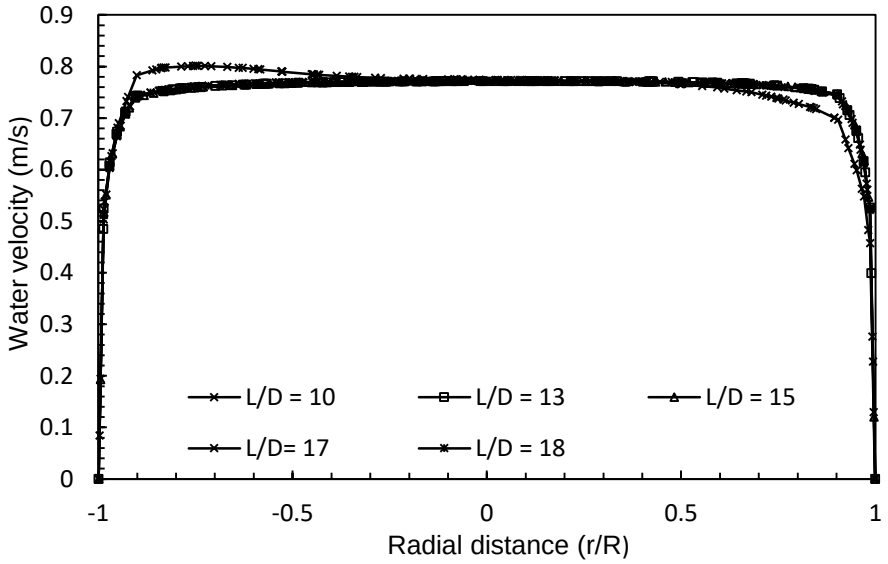

Figure 3.4. The flow development investigation at different L/D.

3.1.5 Traverse design

Multiphase flow properties vary in their magnitudes and distribution patterns at any cross-sectional plane location in a pipe or a duct. Therefore, a traverse mechanism is necessary to be used to reposition the probe in the pipe's cross-section (r and θ) as this enables the probe to measure the multiphase flow properties at each location. A traverse system has been designed and fabricated, as shown in Figure 3.5. This traverse mechanism comprises of linear and rotary probe traversing systems that enables the probe to cover the test pipe cross section.

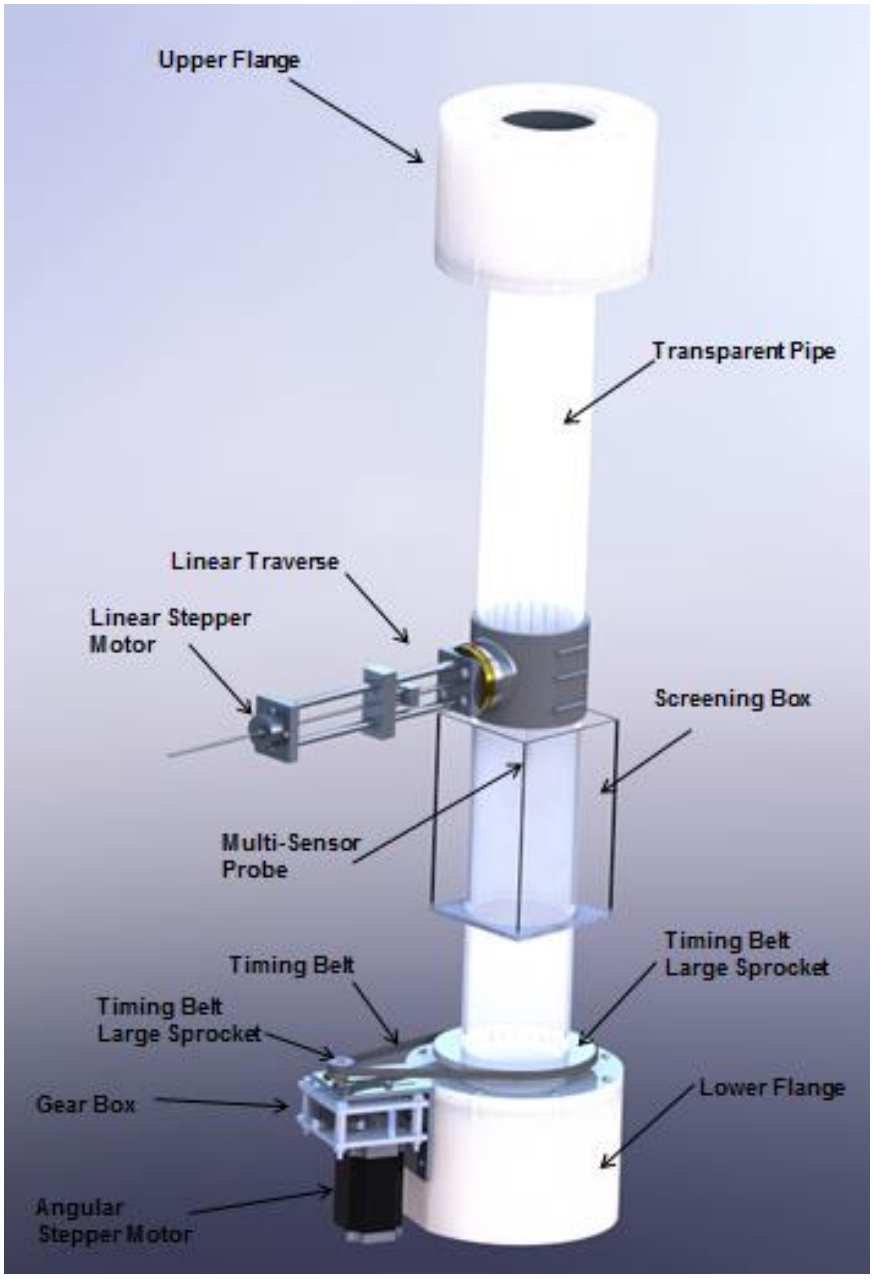

Figure 3.5. The traverse mechanism system.

3.1.5.1 The Linear Traverse Mechanism (r)

To enable the probe to translate linearly and cover the radial distance of the pipe, a linear traverse mechanism has been introduced, as illustrated in Figure 3.6.

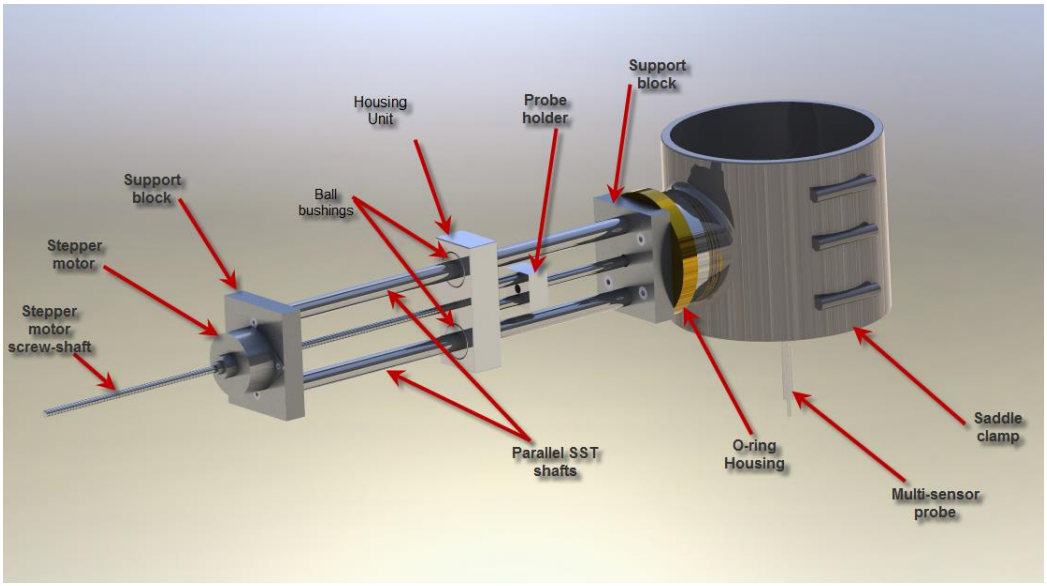

Figure 3.6. Linear traverse mechanism.

The main factors that have been taken into consideration for designing this mechanism are durable linear traverse components, which are light in weight, and are not prone to corrosion. The linear traverse mechanism comprises of:

1. Two off 10 x 250 mm stainless steel, Cf53, and tolerance h6 shafts with M 5 x 12 drilled & tapped both ends. These two shafts have been used as a probe guider to insure that the probe translates linearly and smoothly. Moreover, these two shafts have been used for carrying the other linear components as discussed below.
2. Two of standard ball bushings for holding the probe fixing components, as shown in Figure 3.7.

Figure 3.7. Standard ball bushings.

3. O-ring housing, as shown in Figure 3.8, comprises of a brass housing that has been connected to a saddle clamp at one end and to the support block at the other end. Moreover, it works as a dynamic sealant since it encloses a NBR gasket that has been chosen as a sealant substance and a PVC plug that gives enough pressure to prevent any possible leakage during the linear translation. O-ring housing has been designed to be the first barrier to repel water pressure and leakage instead of using sealant mechanism attached to the traverse pipe. This in turn allows the pipe to have bigger drilled hole; thus, extra entering space for the multi-sensor probe to enter the test pipe without causing any damage to the multi-sensor probe.

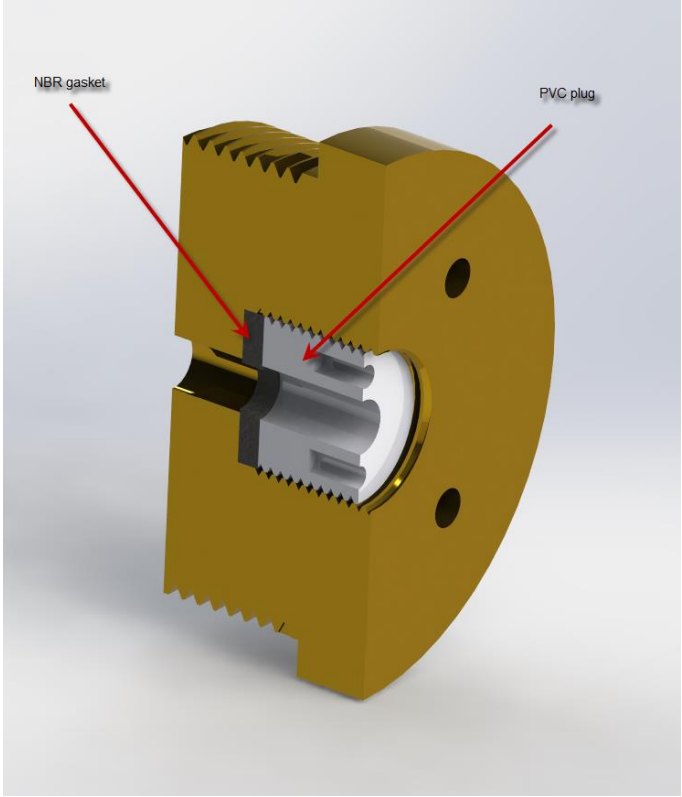

Figure 3.8. Section view of the O-ring housing.

4. Non-Captive Linear Stepper Motor.

   There are three designs available for the linear stepper motor actuators: external linear, non-captive and captive, as shown in Figure 3.9. Non-Captive stepper motor has been selected since the Non-Captive Linear Stepper Motor has small motor shaft. The selection of the Non-Captive linear motor has been made according to the axial thrust force required. This force is the force required to overcome friction force between the NBR sealant and the stainless steel, SST, probe body. From an experiment measurement that has been conducted to measure the

induced friction force from the sealant, it has been found that the friction force has been equal to 25 N. Therefore, a 55 N thrust and pull stepper motor have been chosen with a linear stroke of 100 mm, as shown in Figure 3.10.

Figure 3.9. The three designs of stepper motor linear actuator.

Figure 3.10. Non-captive linear stepper motor [152].

Each stepper motor needs a micro stepping driver that can feed the motor with a desired voltage and current from the pulse signals sent from the main micro-controller. Therefore, a MSD542-V2.0 Micro-stepping driver has been assigned for this purpose as shown in Figure 3.11.

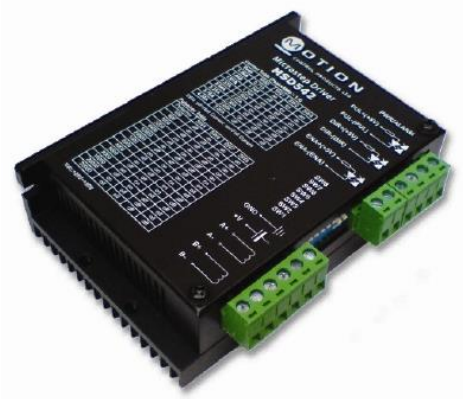

Figure 3.11. MSD542-V2.0 Micro-Stepping Driver [152].

5. Two of support blocks made of aluminium have been manufactured to give lighter weight construction and keep the two rail shafts in parallel and stable.
6. The housing unit that is responsible for connecting the multi-sensor probe holder to the linear stepper motor via the screwed-shaft. This unit has been mounted on the two of standard ball bushings.

3.1.5.2 The Rotary Traverse Mechanism (θ)

The main challenge that the designer faces in the rotary part of the traverse mechanism is reducing the rotating torque without producing water leakage, therefore, extra care has been taken whilst designing and manufacturing these components, as shown in Figure 3.12.

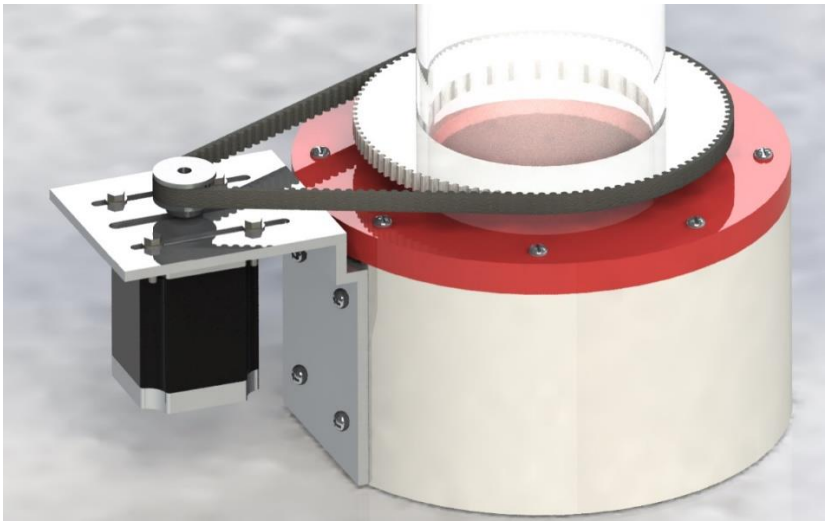

Figure 3.12. The rotary traverse mechanism.

The rotor drive mechanism consists of:

a. Timing belt. A Power Grip High Torque Drive (HTD) Belt has been utilised as a power transmission mean as this type of belt offers an efficient and economic method for high power transmission. The curvilinear tooth shape of the HTD gives more uniform shear stresses distribution; hence, it makes HTD more durable, as shown in Figure 3.13.

Figure 3.13. Contact section view of the power grip HTD belt tooth/groove.

The choice of timing belt, as a means for torque transmission, came from the following considerations.:

- It has minimum vibration effect.
- It almost has no slip as it is engaged.
- It works under a variety of speed magnitudes.
- It does not enlarge during operation.
- It has an effective power transmission.
- It does not need to be lubricated.
- It has low noise.
- It is easy to maintain.
- It has an excellent scratch resistance.
- It has no rust effect.
- It has a light Weight.
- It is safe to be used.
- It is economical as compared to other power transition methods.

b. The PVC driven sprocket, is as shown in Figure 3.14. In this rotary traverse-mechanism component, PVC material has been selected with mechanical properties of tensile modulus 411 kpsi, yield strength 7.5 kpsi, flexural modulus 481 kpsi and yield strength 12.8 kpsi. The main design factor of the driven sprocket to be considered is the outside diameter since it has a direct effect on minimizing the torque generated from the friction force between the sealant components and the traverse pipe. Therefore, a large diameter of 165.97 mm has been assigned for the sprocket outside diameter.

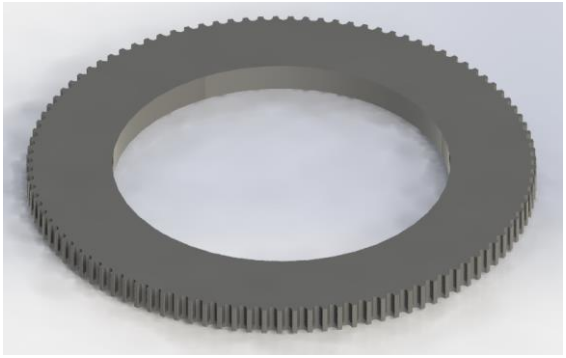

Figure 3.14. The driven timing belt sprocket.

In general, the main parameters in the timing-belt sprocket design process are the Pitch, Belt pitch line, sprocket pitch diameter, sprocket outer diameter and sprocket pitch circle, as shown in Figure 3.15.

The Pitch Diameter (P.D.) of 167.11 mm has been calculated from equation 3.1 [153], whereas the pitch differential (u) is the distance between the pulley outer diameter and the pitch diameter, moreover, it could be obtained from Table 3.1 [153] for HTD5 belts.

$$\text{Outside Diameter O.D.} = \text{P.D.} - 2u \tag{3.1}$$

By using equation 3.2, the number of the driven sprocket's teeth has been calculated to be 105 teeth.

$$\text{Pitch Diameter (P.D.)} = (\text{Pitch} \times \text{Number of teeth}) / \pi \tag{3.2}$$

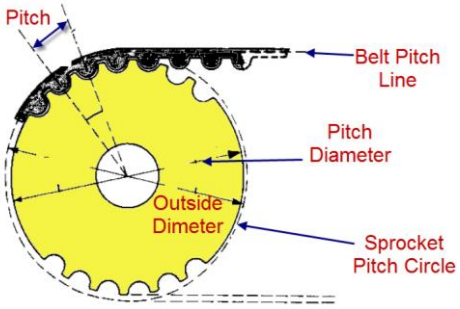

Figure 3.15. Pulley and belt geometry.

Table 3.1: Timing belt dimensions [153]

Belt section		*p - belt pitch*	*H - belt height*	*u - pitch differential*	*h - tooth height*
XL	in	0.200	0.090	0.010	0.050
	mm	5.1	2.3	0.3	1.3
L	in	0.375	0.140	0.015	0.075
	mm	9.5	3.6	0.4	1.9
H	in	0.500	0.160	0.027	0.090
	mm	12.7	4.1	0.7	2.3
XH	in	0.875	0.440	0.055	0.250
	mm	22.2	11.2	1.4	6.4
T5	in	0.197	0.087	0.020	0.047
	mm	5.0	2.2	0.5	1.2
T10	in	0.394	0.177	0.039	0.098
	mm	10.0	4.5	1.0	2.5
T20	in	0.787	0.315	0.059	1.500
	mm	20.0	8.0	1.5	5.0
HTD 5	in	0.197	0.142	0.028	0.83
	mm	5.0	3.6	0.7	2.1
HTD 8	in	0.315	0.220	0.028	0.134
	mm	8.0	5.6	0.7	3.4
HTD 14	in	0.551	0.394	0.055	0.236
	mm	14.0	10.0	1.4	6.0
STD 5	in	0.197	0.134	0.028	0.075
	mm	5.0	3.4	0.7	1.9
STD 8	in	0.315	0.205	0.028	0.11
	mm	8.0	5.2	0.7	3.0
STD 14	in	0.551	0.402	0.055	0.209
	mm	14.0	10.2	1.4	5.3

c. The drive sprocket, is as shown in Figure 3.16. The selection of the drive sprocket was based on keeping the torque ratio of about 1:7. To obtain this ratio, the drive sprocket outside-diameter should be 24.32 mm. From equations 3.1 and 3.2, the pitch diameter and the number of teeth has been obtained to be 25.46 mm and 16 teeth respectively.

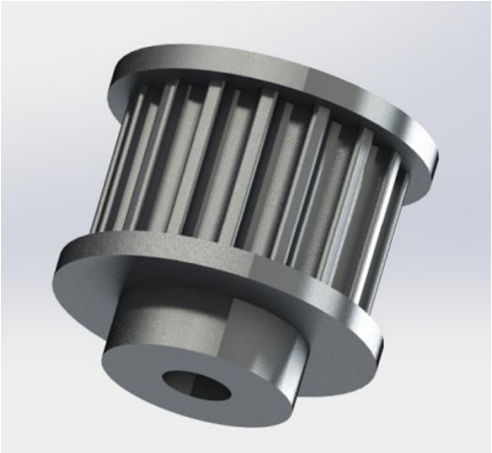

Figure 3.16. The drive sprocket.

d. Stepper motor. Stepper motor selection process depends on the torque required to be overcome. The forces that are involved in generating this torque are one on entering (tight) and one on leaving (slack) sides. The difference between these two forces produces the effective tension force, F_e, as expressed in equation 3.3. This force represents the active force that transmits from the driver sprocket to the driven one.

$$F_e = F_1 - F_2 \tag{3.3}$$

where, F_1 and F_2 are the entering and leaving tension forces, respectively.

Hence, the driving torque T can be calculated as

$$T = F_e \cdot \frac{d}{2} \tag{3.4}$$

where d is the driver sprocket pitch diameter.

The torque that needs to be overcome is generated from the driven sprocket. Therefore, the torque requirement at the stepper motor can be expressed as:

$$T_1 = F_e \cdot \frac{d_1}{2} = \frac{T_2}{\eta} \cdot \frac{d_1}{d_2} \tag{3.5}$$

where, η is the belt efficiency (η = 0.94 − 0.96) and d_1 and d_2 are the driver and driven sprockets pitch diameters respectively.

Therefore, for the present case the driver torque can be expressed as:

$$T_1 = T_2 \cdot 0.16 \tag{3.6}$$

The actual torque, which the sealant produced, has been measured experimentally since there is very limited information regarding the friction coefficient between NBR 70 rubber and machined PVC.

From the experiment, it has been found the sealant produces 10 $N \cdot m$. for each flange. Since the rotary traverse mechanism has two sealants for the both flanges, the required torque to rotate the traverse components can be calculated as

$$T_2 = 10 \cdot 2 = 20\ N \cdot m$$

From equation 3.6, the required torque that the stepper motor should generate is:

$$T_1 = 3.2\ N \cdot m$$

From the above torque calculations, it can be concluded that the required stepper motor specifications should include a torque higher of 3 $N \cdot m$ or more. Therefore, a Nema23 Stepper Motor with 4 Nm torque capability has been selected as a mean of rotational movement generator, as shown in Figure 3.17.

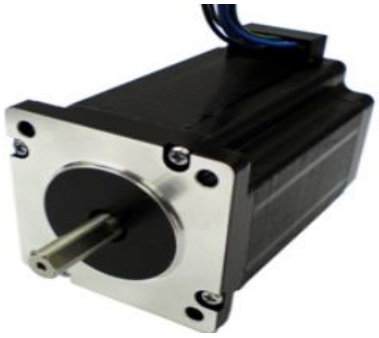

Figure 3.17. NEMA 23 (60 mm) high torque stepper motor [152].

The Stepper driver board role is crucial, especially as it feeds the stepper motor with the desired power to control the motor rotation. Moreover, it provides fractional steps that give smoother motion to the stepper motor. The outcome of the fractional steps of the stepper motors can ensure rotation in smaller angle and furthermore the generated vibrations can be reduced. The typical stepping board can be seen in Figure 3.18.

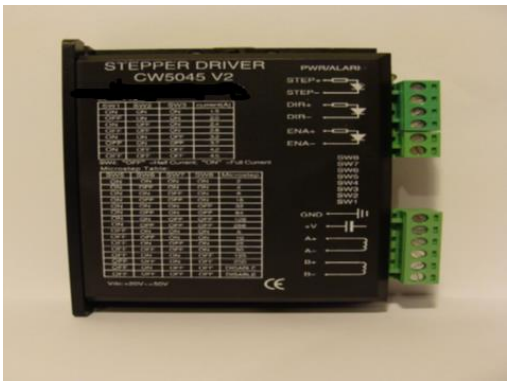

Figure 3.18. Stepper driver CW5045 V2 [152].

The second important part in any stepper motor is the stepper motor controller. The step motor is the device that converts the electric power into mechanical rotational motion, which is in form of precise gradual angular distance per step. Therefore, the full stepper motor shaft revolution is divided into number of steps. This distinctive feature privileged the stepper motors upon the other motor. The micro-controller board can accurately control the stepper motor's angular motion and velocity. This could be achieved from the pulse commands that have been given by the controller. Therefore, the number of the steps, that the stepper motor performs, is equal to the number of the pulses that are sent from the micro-controller board.

Consequently, it is crucial to use stepper motor controller to control the traverse mechanism in both (r and θ) directions. An Arduino Uno ATmega328, as shown in Figure 3.19, has been selected as a micro-controller board that connects the micro-stepping board to the computer via a USB port. Figure 3.20 illustrates the electrical connection between the two-stepper motors, microcontroller board and the micro-stepping board.

Figure 3.19. Arduino Uno ATmega328 microcontroller board [154].

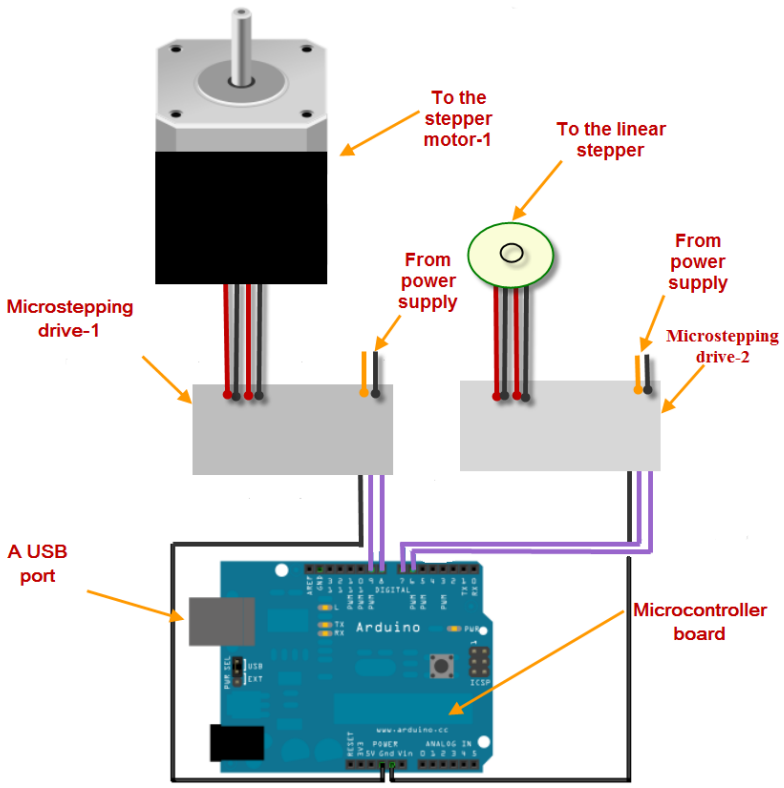

Figure 3.20. A schematic diagram for controlling two stepper motors.

In general, a set of instructions are created by one of the software that has been installed previously in a PC and then these instructions are transferred via a USB cable to the micro-controller board, as illustrated in Figure 3.20. The micro-controller board in turn generates a control command pulse. The motor acceleration, deceleration and break depend on the frequency modification of the pulse sequence. These command pulses then transfer into the micro-stepping board. The micro-stepping board stepper task is to regulate the current flow magnitude and direction. It takes the command pulse and translates it into a desire energy that the stepper motor requires to follow the command. The command eventually reaches the stepper motor, which has two phases. The motor takes a step as the current passes through each phase.

e. Stepper motor support. This support, as shown in Figure 3.21, has been made of aluminium. Since the stepper motor converts the electrical power to mechanical power and heat losses, the stepper motor support, meant to be a good heat dissipation source to prevent the stepper motor from being over heated due to long operation time.

Figure 3.21. Stepper motor support.

3.1.5.3 The rotary flanges

In order to connect the traverse system to the stationary pipes, two rotary flanges have been designed and manufactured, namely upper and lower flanges, as shown in Figure 3.22. Both flanges have the same components apart from that the lower flange has a stepper motor attached to.

The material selection for the traverse mechanism has been based on following requirements:

- It should be durable.
- It should be cheap.
- It should be water proof.
- It should be high strength.
- It should be resistant to cleaning agents.
- It should be stiff.
- It should be high toughness.
- It should be electrically insulated.
- It should has a machinability.
- It should have a good slide and wear properties.

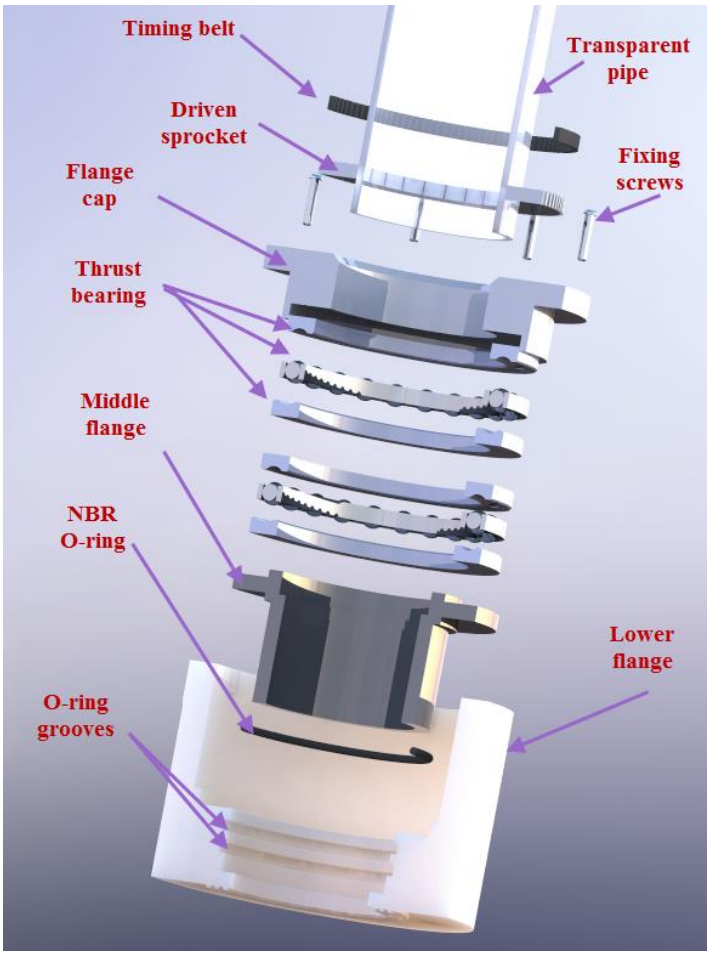

Figure 3.22. The lower rotary flange components.

The rotary flanges, as shown in Figure 3.22, comprises of:

a. Flange cap: This part has been made of Acetyl. It has been attached to the main flange using M5 screws, which make the rotary components replacement and maintenance easy.
b. Two thrust bearings. The idea behind selecting the thrust bearing is to hold the traverse components as they have much lower coefficient of static friction, normally in the range of 0.0008 to 0.0035, than the plastic parts, as a result lower torque will be generated.
c. Middle flange: This part has been made of PVC and not from Acetyl material on purpose, since this part is required to be bonded to the acrylic transparent pipe, whereas Acetyl material cannot be bonded. The main role of the middle flange is to hold the two thrust bearings. Moreover, it is considered as an O-ring rod for the sealing process.
d. The main flange, lower, or upper has been made of Acetyl: The main role of this part is to combine all rotary parts. Moreover, it has the O-ring grooves that are part of the sealant mechanism. Furthermore, it connects the rotary parts to the fixed pipe flange.

e. Transparent pipe, the traverse test section pipe has been made of an acrylic pipe, to allow visual investigations of the multiphase flow properties. The maximum flow loop pressure is well below 6 bars. Hence, using acrylic pipe with a thickness of 5 mm, which bears maximum pressure up to 6 bars, is assumed to be safe to be used.

f. O-ring. An O-Ring is the component that is frequently used for sealing in static and dynamic applications; as it has low cost. It can be also used to block any potential pressure drops that are caused by fluid leakage. As the O-Ring is installed between two closely spaced surfaces, it can bear a high fluid pressure. The O-ring friction force, that prevents the pressure drop, comes from the friction force between the O-ring material and the rod material. The normal force depends on the O-ring squeezing distance. This distance depends on the clearance between the O-ring housing and the shaft or the rod and the groove diameter. The O-Ring cross-sectional deformation is shown in Figure 3.23.

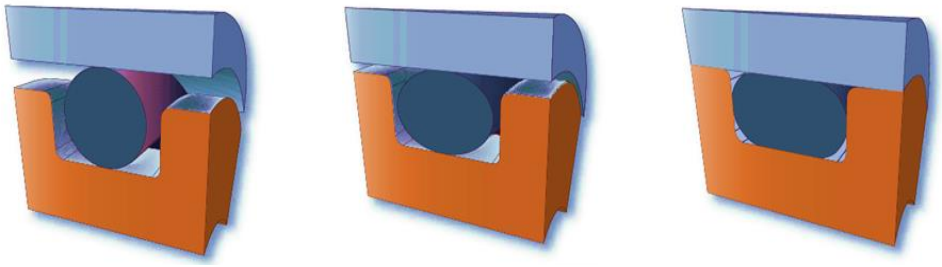

Figure 3.23. O-ring deformation.

The Advantages of using O-ring as a sealant material [155] are:

- It is easily replaceable.
- It has the ability to seal under sever boundary conditions such a high pressure and temperature.
- It has a lightweight.
- It can be reused.
- It has a long operational life.
- It does not fail suddenly.
- It can be used in dynamic and static sealing.
- It is low cost component.

To measure the O-rings and groves sizes, an online calculator [156] has been employed as a tool for calculating the groove (gland) fillet radius, width and groove (gland) diameter, as shown in Figure 3.24. In case of the radial dynamic sealing, the calculation accuracy is quite crucial.

When the O-ring is over compressed, extra torque is required for rotating the traverse system. On the other hand, when the O-ring is under compressed a pressure leakage occurs.

By using the online calculator, it has been calculated that for 5mm cross-sectional diameter and 120mm inner diameter; the groove fillet radius, width, and groove diameter are: 0 .3 ,7.13 and 128.4mm respectively.

As per ISO 3601, the O-ring cross-sectional compression should be 27% for radial static applications and 35-36% for radial dynamic applications of the O-ring cross-section.

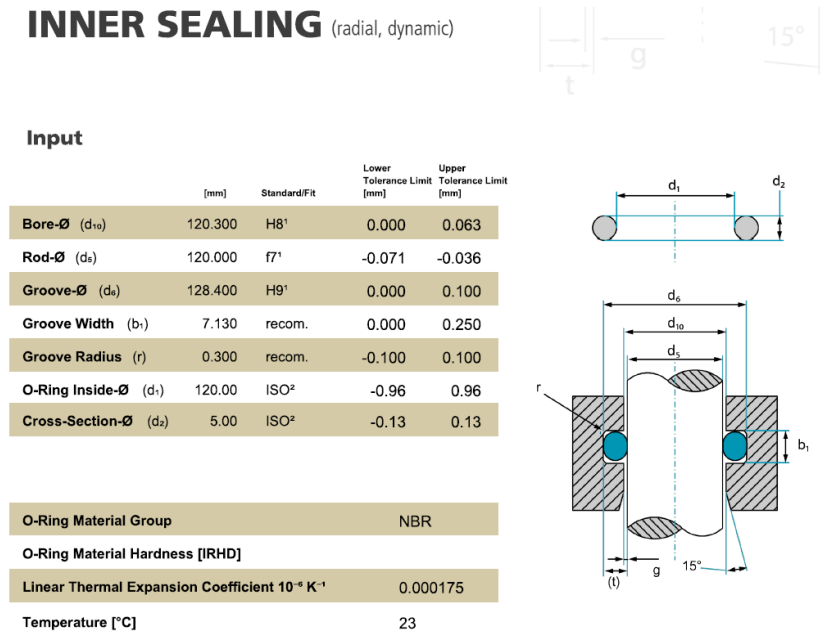

Figure 3.24. The O-ring calculator [156].

Friction force

One of the main concerns in the traverse mechanism design is decreasing the required rotational torque. High torque requires more powerful stepper motor; thus, the stepper motor needs higher current in that situation. Which in turn will need larger driver and power supply should be provided for this. Since the traverse, system components are made of plastics, Acetyl and PVC, the static coefficient of friction is in range of 0.3-0.4. The maximum friction force can be computed from equation 3.7.

$$F_{max} = \mu_s N \tag{3.7}$$

where, F_{max} is the maximum friction force, N is normal load and μ_s is coefficient of static friction.

However, the normal load can be calculated from

$$\sigma = P = \frac{N}{A} \tag{3.8}$$

$$N = P * A \tag{3.9}$$

Rubber may demonstrate uncommon sliding friction. This happens when rubber slides on a hard surface, this surface applies fluctuating forces on the rubber surface causing an internal friction force to the rubber, which in turn leads to energy “dissipation” [157].

3.2 Electronic circuits

Multi-sensor probes produce several raw analogue signals. These signals can be processed with a data-acquisition device, DAQ. Moreover, the DAQ operates on certain voltage magnitudes. Therefore, the raw signals should be adopted before any connection to the DAQ. For the signal adoption, electronic circuits are needed. The electronic circuit consists of operational amplifiers, OP AMP LM741 8 DIP. The LM741 series are general-purpose operational amplifiers. They are intended for a wide range of analogue applications. The high gain and wide range of operating voltage provides superior performance in integrator, summing amplifier, and general feedback applications. The LM741 series have the following features,

- Short circuit protection.
- Excellent temperature stability.
- Internal frequency compensation.
- High Input voltage range.
- Null offset.

The operational amplifier is widely used in many electronic boards. However, its primary limitation is that it is not fast. The typical performance degrades rapidly for frequencies greater than 1 MHz, although some models are designed specially to handle higher frequencies. The typical OP-AMP diagram can be seen in Figure 3.25.

The electronic circuit also consists of variable and fixed resistances. The simple circuit internal block diagram is shown in Figure 3.26. The complete circuit is based on a non-inverting amplifier and a regulated DC voltage source.

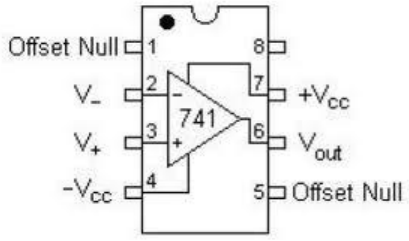

Figure 3.25. Internal block diagram for OP AMP LM741.

where, V_{cc} is Supply Voltage V_{out} is the amplified Voltage and V is the input voltage.

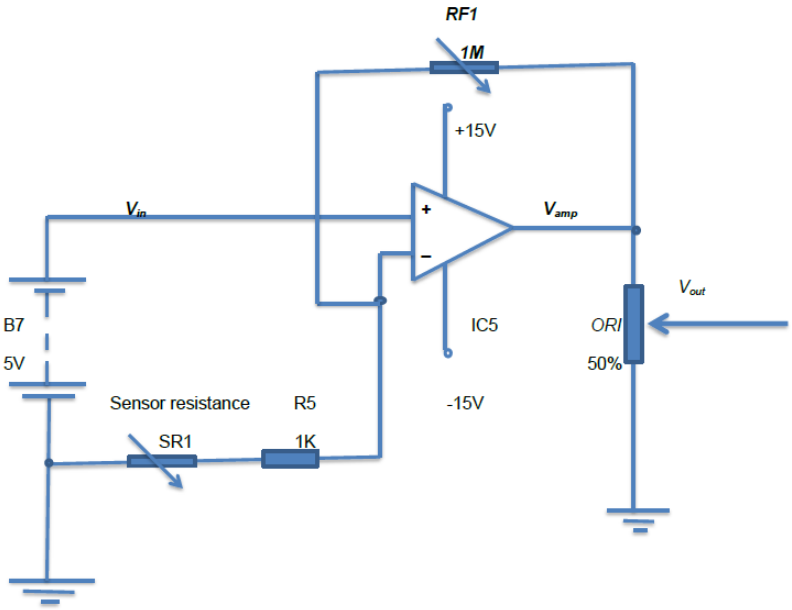

Figure 3.26. DC circuit for a single sensor.

The gain of the non-inverting amplifier circuit (A_G) is

$$A_G = \frac{V_{amp}}{V_{in}} = \frac{(SR_1 + R_5) + RF_1}{(SR_1 + R_5)} \quad (3.10)$$

$V_{amp} = V_{in} * A_G$

Therefore, the amplifying part of the circuit has been based on equation 3.11

$$V_{amp} = V_{in}(1 + \frac{RF_1}{SR_1 + R_5}) \quad (3.11)$$

where, $SR1$ is the resistance between the relevant sensor tip and the probe body (common electrode), V_{amp} is the output voltage that is acquired by the DAQ, V_{in} is the inlet voltage which has been normally supplied from power supply. The numbers of amplifier circuits depend on number of the signals that is generated from the multi-sensor probe. Therefore, a complete circuit has been built for this purpose, as shown in Figure 3.27 and Figure 3.28.

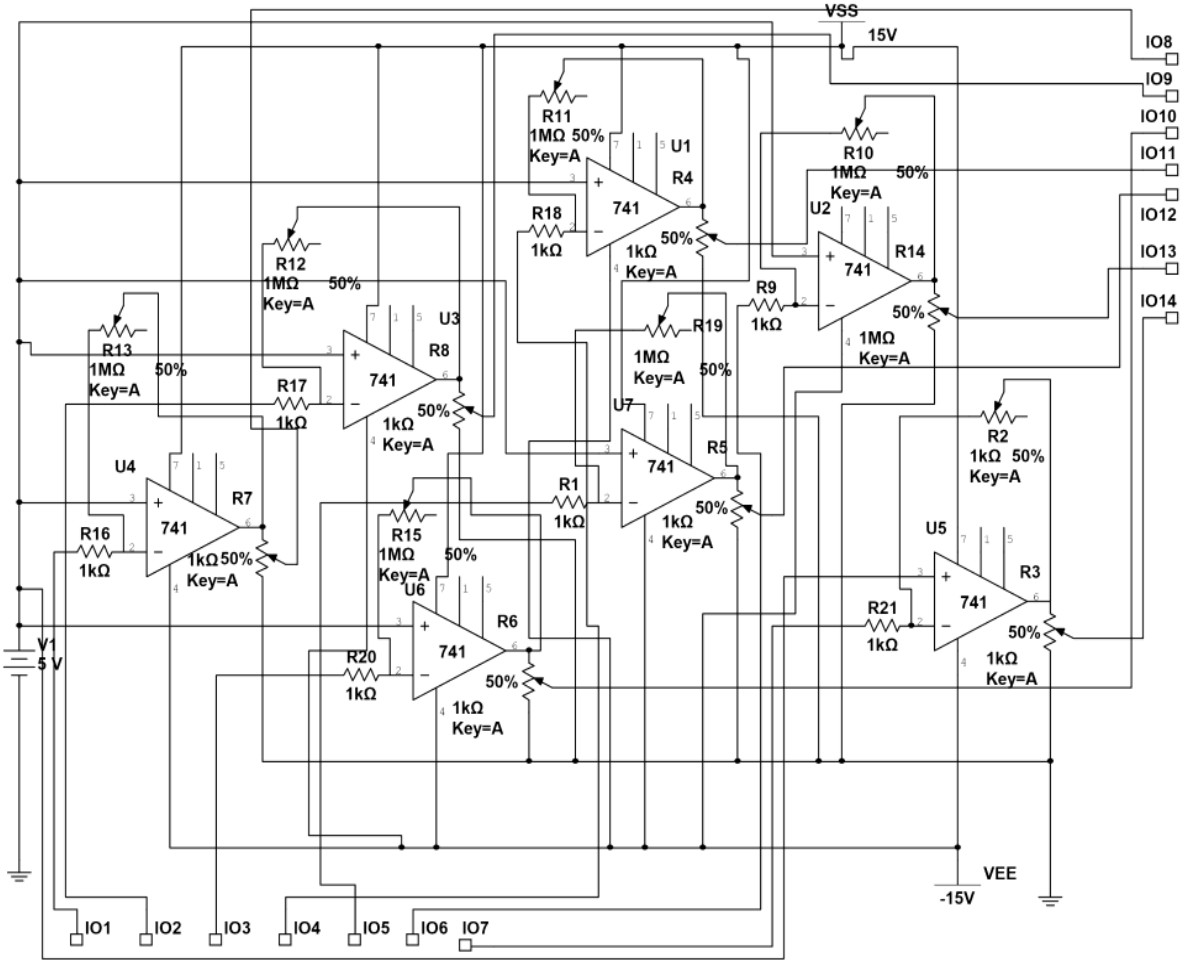

Figure 3.27. DC circuit for the seven sensors.

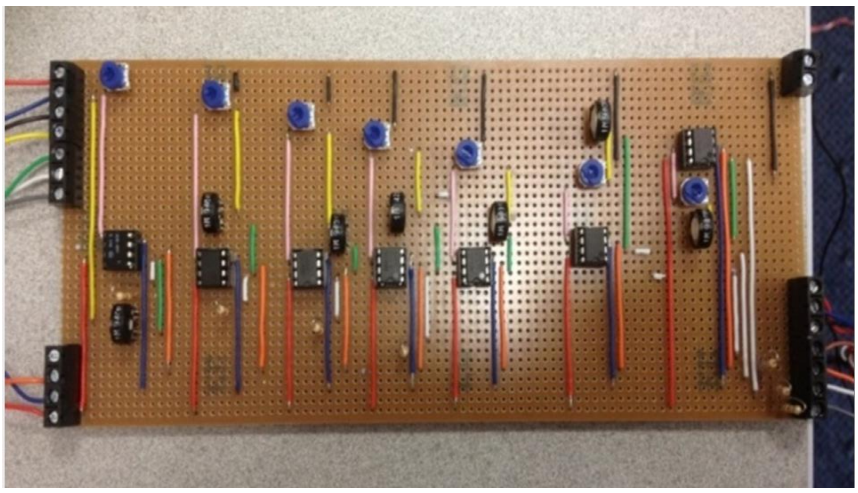

Figure 3.28. Signal amplifier circuit board for the seven sensors.

Basically, the circuit working principle depends on the difference in conductivity of two substances. As the all seven sensors immerse into the continuous phase, water for instance, the value of $SR1$ is very insignificant compared to the feedback resistor, normally $RF1$ > 1.5 MΩ. Thus, V_{amp} value is almost equal to the positive supply voltage of the operational amplifier, +15 V.

When the tip of a sensor touches an air bubble in the flow stream, the circuit becomes as an open loop due to the low conductivity of air making the value of $SR1$ very high. Therefore, $\left(\frac{RF_1}{SR_1+R_5}\right)$ gets almost zero value. Consequently, V_{amp} approaches to V_{in} value, which is +5 volts.

The reason behind using a variable resistor OR1 in the circuit is to fine tune the output voltage V_{out}, which controls the output voltage, see Figure 3.28.

This electronic board circuit is a DC source circuit. As AC source produces more noise than DC source.

3.3 Controlling the traverse system movements

The traverse system has been designed to enable the multi-sensor probe to collect data across the test-pipe cross-section. This system allows data to be collected at any cross-sectional area of the test pipe. This system is essential to be used as the flow in a pipe is not always symmetrical, such as flow after bend, examining swirled flow etc. 90 locations have been assigned across the test pipe to cover the test plane, as shown in Figure 3.39. This will provide nine reading points at each pipe's radial positions (r/R) at angle of 18˚ between each other.

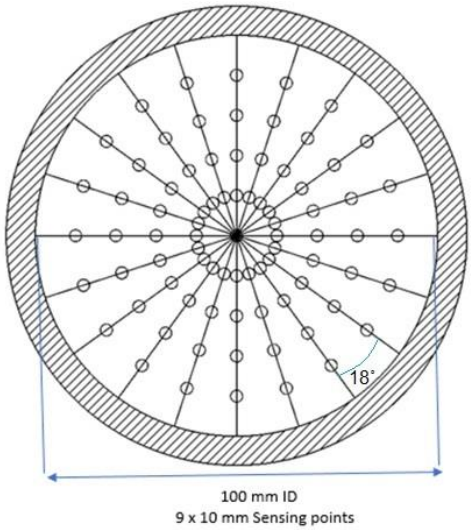

Figure 3.29. Data collection points across the test pipe.

The data acquiring process requires 60 secs to obtain valuable data at each of the 90 sensing points; this consecutively requires 1.5hrs to carry out a full test. Therefore, an automatic control process is required to control the two-stepper motors that provide axial and rotational motions, and to collect data for 60 secs at each sensing point. A LabVIEW (Laboratory Virtual Instrument Engineering Workbench) code has been developed to collect data from the DAQ device and drive the two-stepper motors using Arduino micro-controller. Arduino is an open-source micro-controller used to develop interactive objects. It receives inputs from a variety of switches or sensors and controls a variety of lights, motors and other physical outputs. The advantage of using Arduino is that it can be controlled either by compiling code of instructions into its chip or by using a software installed in a computer system.

3.4 Controlling stepper motors

For controlling the two-stepper motors a LabVIEW code has been developed to send the required commands in forms of signal packages, this code consisted of:

1. LabVIEW interface for Arduino VI, whereas VI is an embedded written program that allows controlling Arduino IO and directing analogue input feedback via USB interface. As shown in Figure 3.30, this VI initialises the connection to an Arduino. In this study, Arduino Uno has been utilised.

   The input setups for this VI are:

   - VISA resource, this input is a PC I/O port source such as COM2, COM3 etc.
   - Baud rate, this input refers to the symbol rate by which the microcontrollers communicate to the computer. This rate must match the baud rate defined by default baud rate in the Arduino firmware. The default baud rate for Arduino is 115200.

- The type of the Arduino used such as Uno, Mega etc.
- Bytes per Packet, is the maximum transmission bytes allowed per packet .This input must match the command length specified in the Arduino firmware. Therefore, it has assigned to 15 bytes.
- Connection types, such as USB or serial port.
- Error feedback.

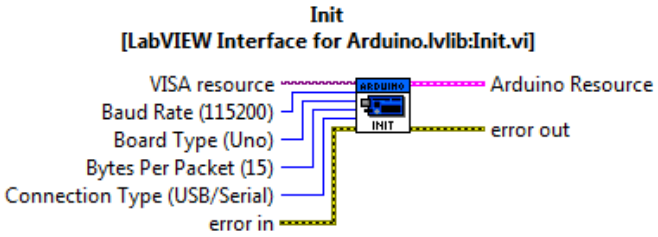

Figure 3.30. LabVIEW interface for Arduino.

2. Two-stepper motor configures VI, as shown in Figure 3.31, each VI responsible for configuring method for controlling each stepper motor and assigning the type of digital pin for the Arduino micro-controller board.

   The input setups for this VI are:

   - The stepper motor number.
   - Arduino resource.
   - Stepper pin.
   - Error feedback.
   - Control method, such as two wires (pulse and direction).

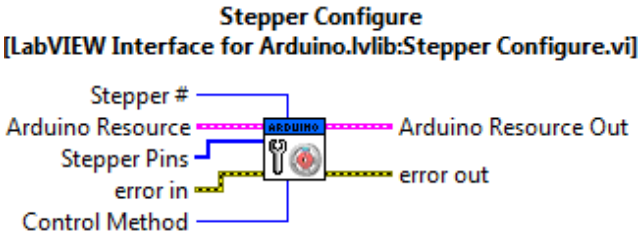

Figure 3.31. Stepper configure VI.

3. Stepper write VI, as shown in Figure 3.32. For each stepper motor a stepper write VI is required. This VI is responsible for the motor speed and the number of steps to rotate.

   The input setups for this VI are:

   - The stepper motor number.
   - Arduino resource.

- The number of steps to go.
- The motor speed in term of steps per second.
- Motor acceleration
- Error feedback.

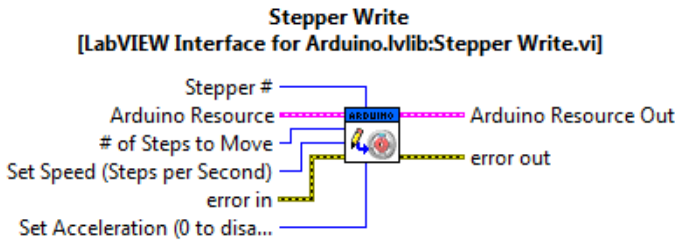

Figure 3.32. Stepper Write VI.

4. Stepper to go VI, as shown in Figure 3.33. This VI checks if Arduino is still processing the previous step command or not. If it is still in processing status, it delays the execution process until the remaining steps are executed. On the other hand, if it is not, it ensures that the step commands are not overwritten.

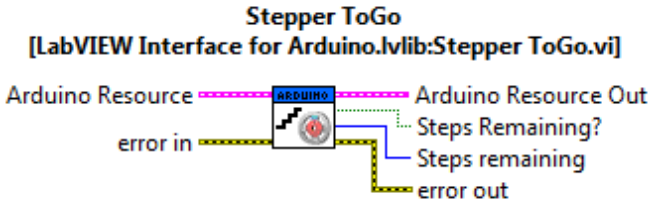

Figure 3.33. Stepper ToGo VI.

5. Stepper close VI, as shown in Figure 3.34. This VI responsible for setting the stepper control pins' power to low.

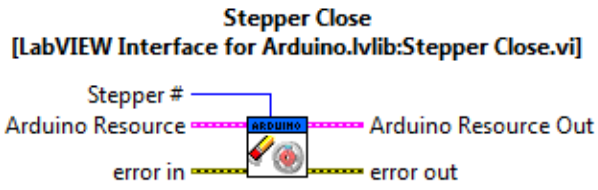

Figure 3.34. Stepper Close VI.

The input setups for this VI are:

- The stepper motor number.
- Arduino resource.
- Error feedback.

6. Two For-loops. The traverse mechanism system is based on repositioning the test section 10 times at 18˚ along 180˚ path. At each angular reposition, 9 linear probe translations occur to get 90 sensing points across the test pipe. To apply this automatically, two For-loops have been used to carry out these processes. The first loop is responsible for sending command to the stepper motor to rotate the test section by 18˚. The code has been designed in such way that the angular movement occurs whenever the loop counter is even number. Alternatively, the command will be transferred to the axial stepper driver for the axial probe translation and data acquisition.
7. Three Case Structures. In general, a case structure is a LabVIEW primitive that dynamically selects which part of the code should be executed. Therefore, this VI has been utilized as a code flow control for cases:

a. Controlling the changing over between the two stepper motors operation.
b. Controlling the direction movement of the rotational stepper motor. This is to return the test section to the initial position after data acquisition process accomplished.
c. Controlling the distance movement of the axial stepper motor.

8. A Flat Sequence Structure, this structure is a frame / multi-frames structure that let the events executed sequentially. This VI has been used to let the program to acquire data after each axial movement.
9. Close VI, as shown in Figure 3.35. This VI closes the active connection to the Arduino.

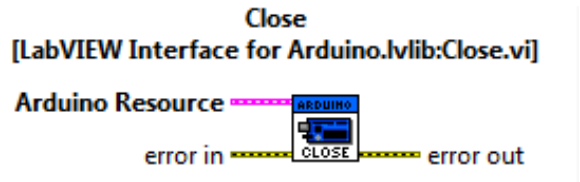

Figure 3.35. Arduino Close VI.

3.5 Stepping number calculation

The theory of controlling stepper motors based on commands sent from the controlling code to the stepper motor in form of pulses, each pulse represents a step movement for the stepper motor. Therefore, for accurate the two stepper motors movement; careful calculations for these steps are needed.

3.5.1 In case of rotational movement:

According to the stepper motor specification, 200 steps generate one motor revolution. The ratio between the two sprockets is 0.1465. Therefore, for each 18˚ large sprocket revolution, 1.365 rev are required for the small sprocket. As the motor is attached to a gearbox, which increases the amount of torque 3 times, the number of 819 steps is required at speed of 1000 steps/s to rotate the test section at an angle of 18˚.

At the end of the test, where the test section has already rotated 180˚, the test section is needed to go back to the initial position to be ready for the next test, therefore, 8190 steps are required from the stepper motor to rotate in reversed direction at 1000 step/s to rotate.

3.5.2 In case of axial translation:

According to the stepper motor manufacturing specification, the sum of 24 motor revolution steps generates one motor revolution. Consequently, each motor shaft revolution generates 1 mm axial probe movement. Therefore, for each axial probe movement of 8.8 mm, 211 steps are required for the motor to rotate at 500 step/s speed.

At the end of the of the probe collection data at a given radial distance, the probe should return back to the initial position for it to be ready for the next test, therefore, 2110 steps required from the stepper motor at a speed of 750 step/s to rotate.

3.6 Data acquisition method

The bubbly two-phase flow data have been acquired via the multi-sensor conductivity probe using DAQ assistant VI, which is available within the LabVIEW code that had been installed in the PC. The USB X Series Multifunction DAQ from NI has been employed as the means of data conversion from analogue to binary data, as shown in Figure 3.36.

Figure 3.36. The acquired data path.

The input setups for the DAQ assistant VI, as shown in Figure 3.37 are:

- Sampling rate. How many samples to read per second?
- Number of samples. The number of samples to be read at each sampling time.
- Error feedback.
- Stop. When to stop acquiring the samples.
- Device name. The device that is acquiring the samples.

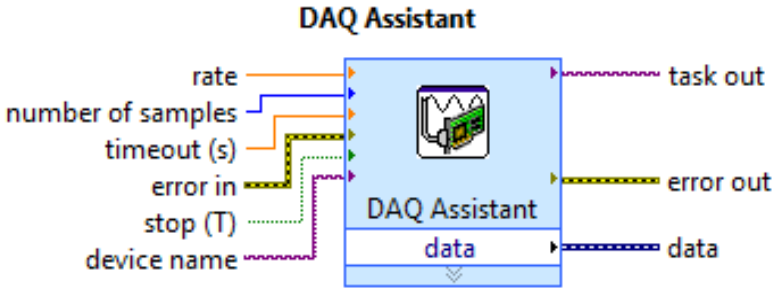

Figure 3.37. DAQ Assistant VI.

The output data line eventually has been connected to (Write to Measurement) VI, as shown in Figure 3.38, that is responsible to save the data in excel sheet.

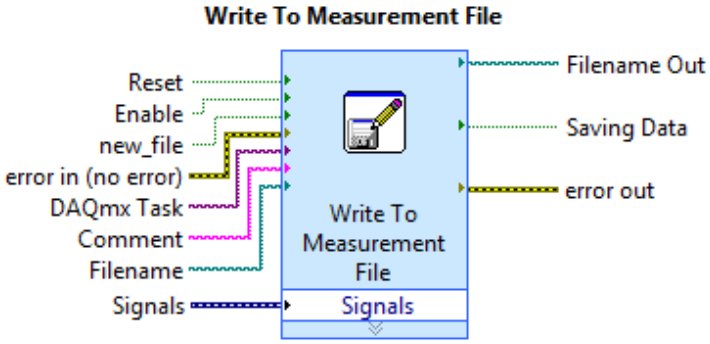

Figure 3.38. Write To Measurement VI.

3.7 DAQ assistant connection

In this project, the seven-sensor probe system has been used to measure the time interval that has been generated due to its translation through the sensors. This process depends on the voltage drop due to the variation in electrical conductivity values between air and water. Therefore, DAQ system is used to capture this variation within the measurement time. In general, there are two main categories of signal sources; as shown in Figure 3.39 [158]:

- Grounded signal source. A grounded source is one in which the voltage signals are referenced to the system ground, such as earth or building ground.
- Floating signal source is not connected in any way to the building ground system, but it has an isolated ground-reference point.

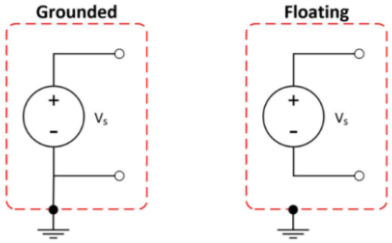

Figure 3.39. Types of signal sources [158].

3.7.1 DAQ assistant configuration

The DAQ instrument can be configured to one of the three modes [158] and these are typically presented in Figure 3.40:

1. Differential (DIFF). In this method, the differential voltage does not have any reference to ground. The measurement process occurs by measuring the voltage difference between the two wires attached to the sensor. Noise elimination is considered to be the main advantage of a differential measurement. Since the noise is added to the both wires; any common filtration can eliminate this noise from the data acquisition system. Differential measurement is recommended to be utilised in cases where the data is expected to accompany by a high rate of the noise, as the surrounding noise affects the data quality.

The differential mode can be used:

- At low level input signals, normally less than one volte.
- The connecting wires between the sensors and DAQ length are greater than three meters.
- A separate ground-reference point or return signal are required for the input signals.
- The test environment is a noisy environment that affects the signals while traveling through the connecting wires.

2. Referenced single-ended (RSE). This is the method where the voltage difference between a wire and ground is taken as a single measurement process. This method is commonly used in an amplified signal, where only a single wire is needed to transfer the data. This process measures the signals along with the output voltage from the sensor. In this project, for the seven-sensor conductivity probe each sensor has only one output signal, therefore, each of this output must be wired into a single-ended channel in the DAQ device. One of the advantages of adopting this approach is the reduction of the number of channels that are needed to measure the sensors.

In general, the Referenced Single-Ended mode can be used when:

- A high level of the input signal is required normally, higher than one volt.
- The connecting wires between the sensors and the DAQ system are less than 3 m in length.
- A floating input signal is used.

3. Nonreferenced single-ended, NRSE, is a signal measurement type which uses one channel and a common reference point only, which is not ground; the drawback of using this type of measurement is that this system is more susceptible to noise compared to differential measurements.

The NRSE mode can be used when:

- A high level of the input signal is required normally, higher than one volt.
- The connecting wires between the sensors and the DAQ system are less than 3 m.
- The input signal is referenced to ground

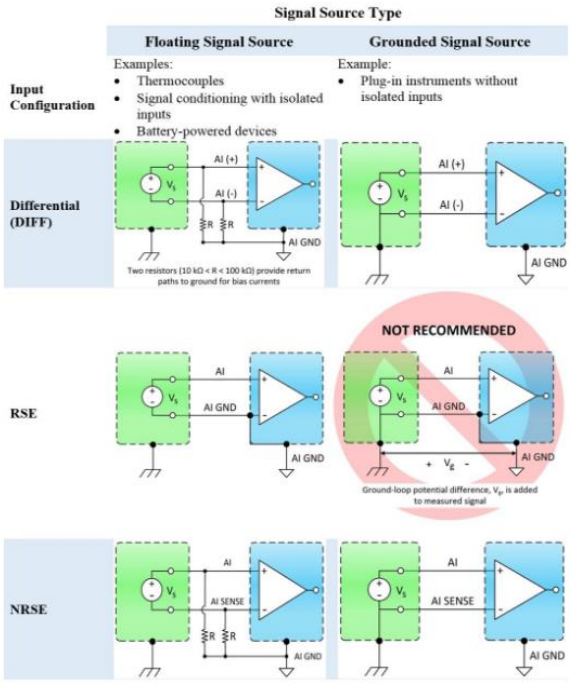

Figure 3.40. DAQ configuration depending on the signal source type [158].

For configuring the DAQ assistant, the following steps have been used:

1. Acquire Signals.
2. Set the input to analogue input.
3. From the analogue input, the voltage measurement is selected since the multi-sensor probe uses voltage-based measurement.
4. From the supported physical channels for the device, the number of channels should be assigned depending on the number of the sensors, form Voltage 0 to Voltage number of the sensors, as shown in Figure 3.40.
5. Terminal configuration Referenced Single-Ended, RSE, has been nominated for each channel as mentioned previously.
6. Data acquisition timing setting:

- Acquisition mode. When performing an acquisition with DAQmx, the acquired data is transferred into an installed software (LabVIEW, SignalExpress, C-code, etc.) in two important transfer steps:

1. Data is transferred from the DAQ device into the memory (RAM) of the computer. There is a finite amount of space in the RAM, called the buffer that is reserved for that transfer.
2. Data is read from the buffer and transferred into the installed software memory in chunks.

a. Continuous samples acquisition. Continuous samples acquisition mode is one of the DAQ modes that acquires samples continuously. The advantage of using this method arises from the fact that it is instantaneous acquisition method and; it runs continuously from the acquisition process has starts. It takes samples at a specified rate (e.g. 1 kHz) and fills FIFO buffer constantly, whereas FIFO is First In First Out memory.

b. N samples acquisition. The N samples acquisition mode is slightly more complicated as compared to the Continuous samples acquisition mode. In this method, the NI-DAQmx allocates a buffer equal in size to the value of the samples per channel attribute / property and the Samples per Channel is used to determine the size of the buffer. The acquisition mode is set to finite (sample mode on the Timing function/VI set to Finite Samples), for instance, if 1 kS at 1 kHz is specified to be sampled and then placed in a while loop, 1000 of samples would be generated for each iteration during a second. Consequently, whenever each iteration of the loop is invoked, 1000 of samples, at a rate of 1000 Hz, 0.001 s between samples, will be collected. This process is hardware timed with an oscillator, so it gives more accurate sampling. This process occurs whenever the VI is called, it reads several data points out of the buffered data (samples to read, e.g. 1000 samples).

   The only difference between the N samples acquisition mode and continuous mode is the while loop. If it is removed from the above example, only 1000 samples will be acquired.

Reading data depends on two features, namely the speed of digitizing the real-world signals, and the size of retrieved data by software at a time from the hardware FIFO.

The DAQ assistant timing vi, from the hardware side, is responsible for determining the transferred data rate from the sensor to the FIFO hardware that is located on the data acquisition board. Whereas, the DAQ assistant read VI, the software side, is responsible for determining the transferring rate of data from the PC buffer into the software. For the buffering size calculation NI-DAQmx uses the value in the Table 3.2.

Table 3.2 DAQmx use buffering size calculation

Sample Rate	Buffer Size
No rate specified	10 kS
0-100 S/s	1 kS
101-10,000 S/s	10 kS
10,001-1,000,000 S/s	100 kS
>1,000,000 S/s	1 MS

- Samples to read. The number of samples to be read at each sample rate.
- Sample rate (Hz) is the frequency of sampling per second.

The data acquisition device that has been utilised in this project is NI USB-6341 model; Table 3.3 represents the DAQ specification.

Table 3.3 The DAQ specification

Model	Analogue Inputs	Max Sampling Rate	Aggregate Throughput (All channels)	Analogue Outputs	Digital I/O	Max Clock Rate
NI USB-6341	16	500 kS/s	500 kS/s	2	24	1 MHz

3.8 The sampling rate and number

If 10 samples required to be read at sampling rate of 100 (Hz), it will take one tenth of the second to read all of the voltages . In turn, 1000 Hz of data will be provided. The interval between each sample will be 0.001 sec (1/1000).

In this project, the data has been acquired using LabVIEW code for 1 min of sampling time, Pradhan [159] has reported that 30 sec and over to be a sufficient acquiring time to obtain a useful data especially in cases where low bubble frequencies are existed.

After setting up the flow loop, the test elements have been identified along with a proper electronic circuit populated and the method of data acquisition illustrated. The next step is to design and manufacture the novel sensor that will fill part of the knowledge gaps that have been found earlier in chapter 2. Detailed description about the novel probe will be presented in the next chapter.

3.9 Experimental design, procedure and test condition

3.9.1 Experimental design

Generally, multi-sensor conductivity probes are used for measuring the dispersed phase flow in the continue phase flow depending on the difference in rate of conductivity between the two phases.
The experimental design has been carried out for two types of experiments, namely bubble column and flow loop.
The experimental design criteria for bubble column have been:

1. The continuous phase, water, is stagnant.
2. The air volume flow rate should be so low in order to produce one bubble a time.
3. Each test should be carried out at least three times.
4. The halogen lights should be located in a way where minimal bubble reflections occur.
5. Both cameras should capture the images spontaneously.
6. Exact distances between both cameras and the seven-sensor should be maintained.

Whilst the experimental design criteria for flow loop have been:

1. The volume fraction should not exceed 0.1, in order to keep the secondary flow, which is air, as a bubbly flow.
2. The water superficial velocity has been used as 1 m/s, controlled by variable speed drive, VSD, water pump.
3. Three values of air superficial velocities have been used, namely 0.05, 0.07 and 0.1 m/s, that have been controlled by a ball valve.
4. The test section allocated at 1.3 m above the air injection points, where the flow has been fully developed.
5. The air injection points have been designed in a way that producing bubble with minimum diameter exceeding the seven-sensor frontal area, which has been 2mm in this project.
6. The reference pressure, for the threshold selection process, has been obtained from two pressure taps that have been located up/downstream of the teste section with 1 m distance between the two taps.

7. As it is unknown if the flow is symmetrical or not before carrying out the experiment; it is important to use the designed traverse for relocating the seven-sensor plot across the pipe cross-sectional area to cover the sensing points.
8. Lab view code has been prepared to control the treverse system and collect data.
9. The sensing time at each point has been 1 min at sampling frequency of 30k, because of the DAQ limitation, which will be discussed in chapter 5.
10. Each test has been carried out at least three times at each sensing point.
11. The experimental environment has been kept the same for the all tests.

3.9.2 Experimental procedure

As it has been mentioned previously, two methods of experimental have been carried out in this project, namely bubble column and flow loop. Therefore, the experimental procedure for each test will be illustrated separately.

A. Bubble column test.

In order to carry out this test, the following tasks are required:

1. Filling the glass water tank with water.
2. Leave the water for certain time until its temperature equals the room temperature.
3. Place the seven-sensor probe at the centre of the water tank.
4. Place the two high-speed cameras perpendicular to each other and at the same distance from the seven-sensor probe.
5. Place grey background for each camera.
6. Direct the halogen lights to the grey backgrounds.
7. Connect the water tank to the power supply negative port.
8. Connect the both 12V and 5V terminals to the amplifier board.
9. Connect the seven-sensor probe to the amplifier board.
10. Ensure the output seven signal voltages are below 10V.
11. Connect the seven-sensor probe to the DAQ via the amplifier board.
12. Operate both cameras and the seven-sensor system simultaneously.
13. Collect the data and save it.
14. Repeat steps 12 and 13 for three times or more, for the repeatability check.

B. Flow loop test

In order to carry out this test, the following tasks are required:

1. Filling the water tank with water.

2. Connect the air flow meter to power supply and turn it on half an hour before the test time.
3. Run the water pump for 15 min before conducting the test, to ensure no air left in the flow loop.
4. Adjust the water velocity to 1m/s.
5. Supply the compressed air through the air regulator and adjust the air superficial velocity to the desired velocities, 0.05, 0.07 and 0.1m/s.
6. Collect the data from the seven-sensor probe using the prepared LabView code at the sensing point.
7. Repeat step 6 several times for repeatability check.
8. Repeat the testing process for each air superficial velocity
9. Save the obtained data

3.9.3 The test conditions

The flow loop experimental test has been carried out under the boundary condition as shown in Table 3.4.

Table 3.4 The experimental boundary condition.

Pressure (Pa)	101325
Temperature (°C)	20
Water superficial velocity	1 m/s
Air superficial velocities	0.05, 0.07 and 0.1 m/s

The bubble column tests have been carried out under the same flow loop test boundary conditions apart from the superficial velocities.

The water has been stagnant, 0 m/s, and the air has been 1.1-1.3 m/s.

Both tests have had the same material properties as shown in Table 3.5.

Table 3.5. the experimental material properties.

	density	viscosity
water	998.2 Kg/m3	100.3e-05 Kg/m-sec
air	1.225 Kg/m3	1.7894e-05 Kg/m-sec

Chapter 4.

The Results

Based on the critically reviewed literature, some gaps have been identified in literature regarding multiphase flows properties and measurement instrumentation. In order to fill these gaps, nine objectives, therefore, have been created. These objectives have been achieved and presented in the following chapters. In this chapter, the design of a novel multi-sensor probe has been introduced with both theoretical and physical aspects. The design of the novel probe has been based on the developing of the existing probes. In addition, it has taken into consideration most of the factors that caused discrepancy in the multiphase measurement due to the bubble-sensor interactions.

4.1 The mathematical model

The measurement principle of the multi-sensor probe is to obtain time-delays that are generated as the bubbles touch the sensors one after the other in a multi-sensor probe system, as shown in Figure 4.1. The seven-sensor probe system also works on the same principle. However, this system differs to the previous systems, from collecting the data from the first bubble sensor contact, whilst the previous systems have collected the data when the sensor immersed and exited the bubble.

In order to enable the novel probe to measure three-dimensional bubble velocity and bubble shape and size, six variables well generate namely, the thee velocity components, which are Vx, Vy and Vz, and the bubble axes Rx, Ry, and Rz. Therefore, six equations are needed for the six variables determination. Consequently, six time-delays required for providing enough information to solve these equations.

In this probe system, the contact time between each sensor and the bubble surface has been recorded to achieve 6 time-delays, which have been generated between the leading and each of the trailer sensors. The typical generated 6 time-delays from the seven-sensor probe have been shown in Figure 4.2. However, these signals are not in square shapes due to the sensors' poor-wettability [105].

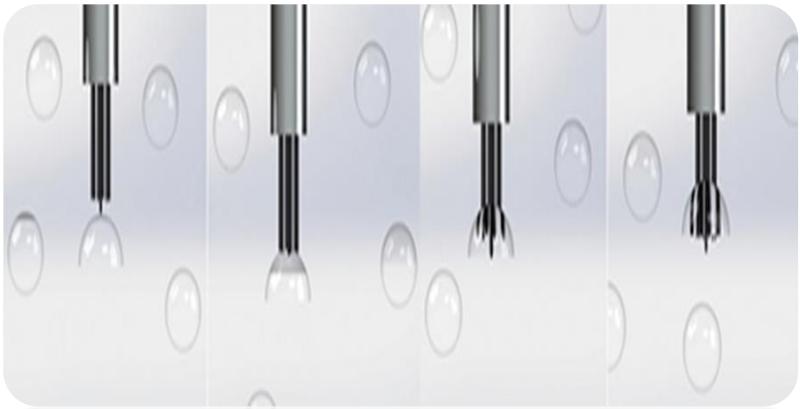

Figure 4.1 The process of immersing and exiting the seven sensors through a bubble

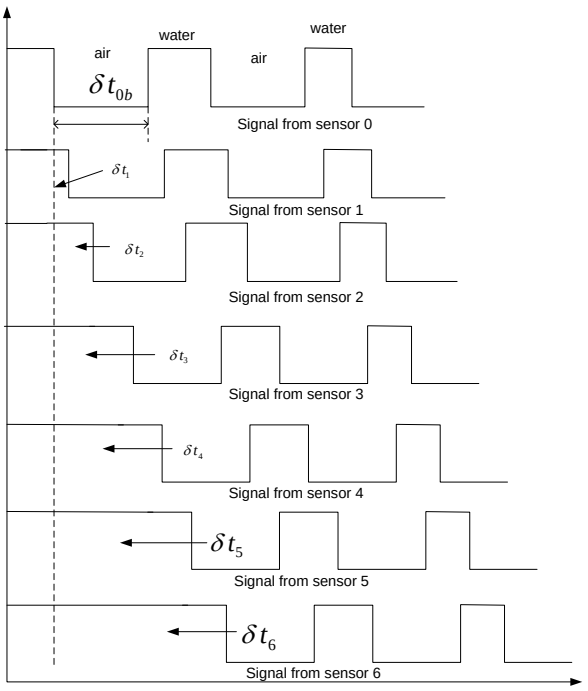

Figure 4.2. Ideal signals from a seven-sensor probe.

The time values used in the computations have corresponded to the first contact of the bubble with the seven sensors, this will eliminate any measurement discrepancy due to bubble slowing down or bubble deformation due to the interaction between the bubble and the sensors especially in large bubbles. Each of the seven sensors measures the local conductance at its tip. The output-signals from the seven-sensor probe, as the bubble moves across the probe, are almost like the idealized signal shown in Figure 4.2.The lead sensor, sensor 0, is located at the centre and ahead of the other six sensors. Each rear sensor has been placed in such a way that they make 60° angle with each other and represented by x_i , y_i and z_i coordinates with respect to the front sensor, sensor 0, where (*i= 1,2,3,4,5 and 6*)

Whilst the seven sensors immerse in and out the bubbles, seven signals are generated. These signals represent the time intervals between the first touch of the bubble or droplet to the front sensor 0, and the first and last touch of the bubble to each of the rear sensors. These processes have been clearly illustrated in Figure 4.1 and Figure 4.2, which show the idealized signals from the seven sensors. For deriving the mathematical model, the following assumptions have been considered:

- All the rear sensors touch the droplet surface.
- The front sensor, $S_{0,}$ immerses into all the passing droplets prior the rear sensors.
- The bubble and the probe interactions do not affect the velocity vector and the bubble shape.

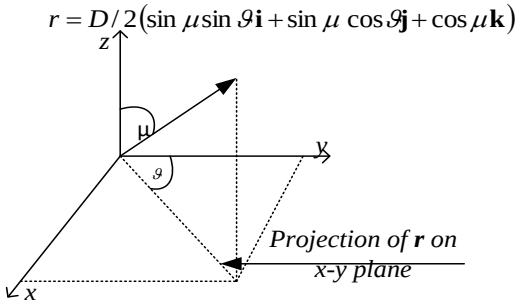

Figure 4.3. Symbolic representation of position vector of the point of first contact of droplet with the lead sensor S_0.

Concerning to Figure 4.3, the point of first contact of the droplet surface and sensor 0, with respect to the droplet centre, is denoted by the vector r

where

$$r = \frac{D}{2}\hat{\cap}_i \tag{4.1}$$

where, *D* is the diameter of the droplet. $\hat{\cap}_i$ is a unit vector given by

$$\hat{\cap}_i = sin\mu sin\vartheta\ \mathrm{i} + sin\ \mu\ cos\vartheta \mathrm{j} + cos\ \mu\ \mathrm{k} \tag{4.2}$$

In equation 4.2, μ is a polar angle and ν is an azimuthal angle, as defined in Figure 4.4.

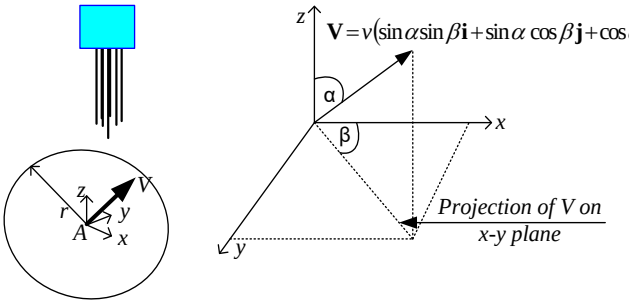

Figure 4.4. Symbolic representation of velocity vector as bubble touches seven-sensor probe.

Concerning Figure 4.4, it has been assumed that the bubble with a velocity V moves across the probe. Based on the assumptions mentioned above, the magnitude and the direction of the bubble velocity vector remain unchanged as the bubble moves across the sensors, therefore, the velocity vector can be written:

$$V = v(sin\alpha sin\beta\ \mathrm{i} + sin\ \alpha\ cos\beta \mathrm{j} + cos\ \alpha\ \mathrm{k}) \quad (4.3)$$

where, $V = v\ \widehat{\cap}_v$

where, v is the magnitude of the bubble, $\widehat{\cap}_v$ is the unit vector in the direction of V, α is angle between V and probe axis and β is the azimuthal angle, as shown in Figure 4.4. After time δt_1 bubble comes into the contact with sensor 1 located at x_1 , y_1 , z_1 with respect to the front sensor S0, as shown in Figure 4.5.

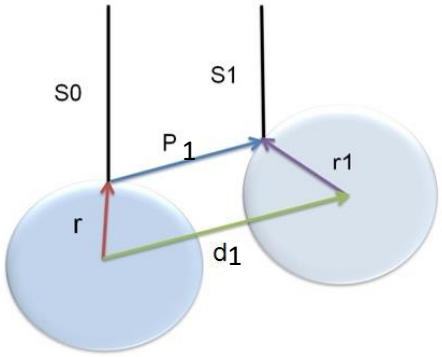

Figure 4.5. The bubble connection after time δt_1.

The vector resultant, $\overrightarrow{d_1}$, can be calculated from equation 4.4.

$$\overrightarrow{d_1} = \vec{r} + \vec{P}_1 - \vec{r}_1 \quad (4.4)$$

The position vector r_1 of this point of contact of sensor 1 on the bubble surface with respect to the centre of gravity of the bubble can be written as

$$\vec{r}_1 = \vec{r} + \vec{P}_1 - \overrightarrow{d_1} \quad (4.5)$$

where,

$\vec{P}_1 = x_1\mathrm{i} + y_1\mathrm{j} + z_1\mathrm{k}$, and $\overrightarrow{d_1} = V\delta\mathrm{t}_1$.

$$r_1 = (r + x_1\mathrm{i} + y_1\mathrm{j} + z_1\mathrm{k} - V\delta\mathrm{t}_1) \quad (4.6)$$

By squaring 4.6 equation, the following:

$$r_1^2 = (r + x_1\mathrm{i} + y_1\mathrm{j} + z_1\mathrm{k} - V\delta\mathrm{t}_1).(r + x_1\mathrm{i} + y_1\mathrm{j} + z_1\mathrm{k} - V\delta\mathrm{t}_1) \quad (4.7)$$

Expanding equation, 4.7, and substituting $V = v\,\hat{\cap}_v$ and $r = r\,\hat{\cap}_i$ we get

$$\begin{aligned} r_1^2 = {} & r^2 + rx_1(\hat{\cap}_i.\mathrm{i}) + ry_1(\hat{\cap}_i.\mathrm{j}) + rz_1(\hat{\cap}_i.\mathrm{k}) - rv\delta t_1(\hat{\cap}_v.\hat{\cap}_i) + rx_1(\hat{\cap}_i.\mathrm{i}) + x_1^2 \\ & - x_1 v\delta t_1(\hat{\cap}_v.\mathrm{i}) + ry_1(\hat{\cap}_i.\mathrm{j}) + y_1^2 - y_1 v\delta t_1(\hat{\cap}_v.\mathrm{j}) + rz_1(\hat{\cap}_i.\mathrm{k}) \\ & + z_1^2 - z_1 v\delta t_1(\hat{\cap}_v.\mathrm{k}) - rv\delta t_1(\hat{\cap}_v.\hat{\cap}_i) - x_1 v\delta t_1(\hat{\cap}_v.\mathrm{i}) \\ & - y_1 v\delta t_1(\hat{\cap}_v.\mathrm{j}) - z_1 v\delta t_1(\hat{\cap}_v.\mathrm{k}) + v^2\delta t_1^2 \end{aligned} \tag{4.8}$$

Rearranging equation, 4.8, we get

$$\begin{aligned} & v^2\delta t_1^2 - v\delta t_1\big(2r(\hat{\cap}_i.\hat{\cap}_v) + 2x_1(\hat{\cap}_v.i) + 2y_1(\hat{\cap}_v.j) + 2z_1(\hat{\cap}_v.k)\big) \\ & \quad + [x_1^2 + y_1^2 + z_1^2 + 2rx_1(\hat{\cap}_i.i) + 2ry_1(\hat{\cap}_i.j) + 2rz_1(\hat{\cap}_i.k) - r_1^2 \\ & \quad + r^2] = 0 \end{aligned} \tag{4.9}$$

The bubble has been assumed to be sphere between the sensors, therefore, $r_1^2 = r^2$

By analogy with the arguments given above, the following equation is valid for the times δt_2 when the droplets encounter sensor 2.

$$r_2^2 = (r + x_2\mathrm{i} + y_2\mathrm{j} + z_2\mathrm{k} - V\delta\mathrm{t}_2)(r + x_2\mathrm{i} + y_2\mathrm{j} + z_2\mathrm{k} - V\delta\mathrm{t}_2) \tag{4.10}$$

Again, expanding equation, 4.10, and substituting $V = v\,\hat{\cap}_v$ and $r = r\,\hat{\cap}_i$ we get

$$\begin{aligned} & v^2\delta t_2^2 - v\delta t_2\big(2r(\hat{\cap}_i.\hat{\cap}_v) + 2x_2(\hat{\cap}_v.i) + 2y_2(\hat{\cap}_v.j) + 2z_2(\hat{\cap}_v.k)\big) \\ & \quad + [x_2^2 + y_2^2 + z_2^2 + 2rx_2(\hat{\cap}_i.i) + 2ry_2(\hat{\cap}_i.j) + 2rz_2(\hat{\cap}_i.k) - r_2^2 \\ & \quad + r^2] = 0 \end{aligned} \tag{4.11}$$

Thus, the equation, 4.11, can be simplified as equation, 4.12, for each sensor as a bubble passes through it:

$$\begin{aligned} & v^2\delta t_i^2 - v\delta t_i\big(2r(\hat{\cap}_i.\hat{\cap}_v) + 2x_i(\hat{\cap}_v.i) + 2y_i(\hat{\cap}_v.j) + 2z_i(\hat{\cap}_v.k)\big) + [x_i^2 + y_i^2 + \\ & \quad z_i^2 + 2rx_i(\hat{\cap}_i.i) + 2ry_i(\hat{\cap}_i.j) + 2rz_i(\hat{\cap}_i.k)\,] = 0 \end{aligned} \tag{4.12}$$

$$\begin{aligned} & \big(v_x + v_y + v_z\big)^2\delta t_i^2 - 2\delta t_i\big(v_x r_x + v_y r_y + v_z r_z + x_i v_x + y_i v_y + z_i v_z\big) \\ & \quad + \big[x_i^2 + y_i^2 + z_i^2 + 2x_i r_x + 2y_i r_y + 2z_i r_z\,\big] = 0 \end{aligned} \tag{4.13}$$

where *i= 1, 2, 3, 4, 5 and 6*

In equation, 4.13, there are 6 unknown parameters v_x, v_y, v_z, r_x, r_y *and* r_z and by replacing *i* with *1, 2, 3, 4, 5 and 6*, representing each rear sensor, we can achieve 6 different equations. Therefore, seven sensors are needed to provide six-time delays between the reference sensor and the six trailer sensors to solve

these set of equations. Finally, by using an iterative method, the six unknown parameters $v_x, v_y, v_z, r_x, r_y \; and \; r_z$ of a bubble in air-water multiphase flow can be computed.

4.2 Irregular shape bubbles

As bubbles are subject to coalescence and break up whilst flowing in the flow stream; bubble shapes, therefore, are subject to deformation. Moreover, there is no recognised mathematical model available in literature to be used for this purpose. Thus, a mathematical model is required to quantify the dispersed phase properties from the measured time corresponded to the first bubble-sensor contact. In the next part of this chapter a mathematical model has been introduced that has the ability of measuring the size and the shape of the bubbles of irregular shape.

When two spherical bubbles of diameter of d_1 and d_2 coalescence and intersect each other at point k and k', they form an intersection length $a\,(a = a_1 + a_2)$. Hence, p is the distance between B and A', see Figure 4.6.

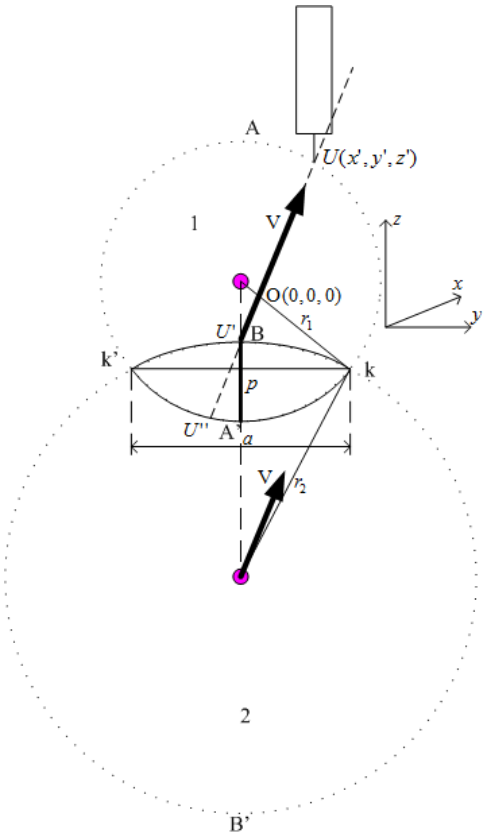

Figure 4.6. Symbolic representation of bubble probe interaction.

According to Intersecting Chord Theorem, which states, “When two chords intersect each other inside a circle, the products of their segments are equal” [160] therefore, for circle 1, it can be written:

$$p_2\,(d_1 - p_2\,) = a_1 a_2$$

$$p_2\,d_1 - p_2^2 - C = 0 \tag{4.14}$$

where $C = a_1 a_2,\ a_1 = a_2$

$$p_2^2 - p_2\,d_1 + C = 0$$

$$p_2 = \frac{d_1 \mp \sqrt{d_1^2 - 4C}}{2} \tag{4.15}$$

Similarly, for circle 2

$$p_1 = \frac{d_2 \mp \sqrt{d_2^2 - 4C}}{2} \tag{4.16}$$

By using equation, 4.15, and 4.16, it is possible to calculate the vertical axis of the given bubble. Let us assume that both bubbles are rising with velocity vector, V, as shown in Figure 4.6, the probe makes the first contact with the bubble at the point $U\ (x', y', z')$. After Δt time probe makes first contact with bubble 2 with centre $(0,0,D)$ at a point U', which is given by

$$\left((x' - v_x\Delta t), (y' - v_y\Delta t\,), (z' - v_z\Delta t)\right) \tag{4.17}$$

where,

$v_x = v\sin\alpha\sin\beta$, $v_y = v\sin\alpha\cos\beta$ and $v_z = vcos\alpha$

hence,

$$\left((x' - v_x\Delta t)^2 + \left(y' - v_y\Delta t\,\right)^2 + (z' - v_z\Delta t - D)^2\right) = r_2^2$$

$$\begin{aligned}\Big(\left(x'^2 - 2x'v_x\Delta t + (v_x\Delta t)^2\right) + \left(y'^2 - 2y'v_y\Delta t + \left(v_y\Delta t\right)^2\right) \\ + \left(z'^2 - 2v_z\Delta t z' + (v_z\Delta t)^2 - 2z'D + 2\Delta t D + D^2\right)\Big) = r_2^2\end{aligned} \tag{4.18}$$

The equation can be rearranged into the following quadratic form:

$$\left[\Delta t^2\left(v_x^2 + v_y^2 + v_z^2\right) - \Delta t\left(2x'v_x + 2y'\,v_y + 2z'v_z + 2D\right) + (x^2 + y^2 + z^2 + D^2 - r_2^2 - 2z'D)\right] = 0$$

The solution of the equation can be written as

$$\Delta t = \frac{-b \pm \sqrt{b^2 - 4ac}}{2a} \quad (4.19)$$

where

$a = \left(v_x^2 + v_y^2 + v_z^2\right)$, $b = -\left(2x'v_x + 2y'\,v_y + 2z'v_z + 2D\right)$ and $c = (x^2 + y^2 + z^2 + D^2 - r_2^2 - 2z'D)$

By using equation 4.19, and determining the six unknown parameters $v_x, v_y, v_z, r_x, r_y\ and\ r_z$ of a bubble in air-water multiphase flow, it is possible to predict the contact time between the coalescence bubbles at points $U'and\ U''$.

4.3 Probe fabrication

As a part of building the novel seven-sensor probe system, manufacturing the seven sensors probe is required. The accuracy of data measurement depends directly on many factors, such as the probe fabrication, the sensors' size, dimensions, insulation, and the probe limitations. In this section, all the above limitations are going to be discussed thoroughly.

4.3.1 The sensor (pin) Selection

One of the fabricating challenges of any conductive sensors is selecting the right size of a pin to be used as a sensor. To obtain accurate dispersed phase property measurements, the sensor's frontal area should be as small as possible. Since the bubble strikes each sensor twice, it is important that each probe have a minimal effect on the bubble shape and the velocity vector. The smallest tip-size of a sensor minimizes the interaction between the sensor and the bubble, moreover, reduces the sensor tip wettability consequently increases the sensor measuring accuracy. The rigidity and the uniform shape of the needles provide a fix sensors tip location consequently increases the sensor measuring accuracy. The sensor's thickness is one of the significant variables that should be taken into consideration, as thicker sensors give more rigidity, but it increases the bubble-sensor interaction and the bubble shape deformation; moreover, it generates wakes around the sensors preventing the bubble to reach the sensors. On the other hand, the use of very thin pins causes the sensor to be less rigid, thus, it becomes subject to deflection due to flow effect. The other important parameter in sensor's fabrication is the pin's material. There is a direct contact between the sensor and flow domain as the seven-sensor probe operates internally. Therefore, the pin's material selection should be based on the knowledge of the chemical reaction that may occur during the measurement process. For instance, the choice of a stainless-steel pin can be considered as a good choice in case of bubbly flow air-water two-phase flow.

For all above reasons, a 0.25 mm body diameter, and 0.03 mm tip diameter of a stainless-steel pin with electrical resistivity of $6.90 \times 10^{-7}\ \Omega \cdot m$ at 20°C and electrical conductivity of $1.45 \times 10^{6}\ \ Siemens/m$ at 20 °C, have been utilised in this work to represent the conductive sensor.

Seven different colours of 30 AWG Wire Solid Copper Core Teflon Coated have been used as a mean for transferring the signals that have been generated by the bubbles hitting the sensor tip to the electrical board. One of the exposed ends of each wire has been twisted around each of the exposed pin's end as shown in Figure 4.7. Moreover, it has been coated with a conductive glue, to ensure no gap left between the sensor and the wire.

Figure 4.7. The exposed wire twisted around a conductive sensor.

The needles and the attached exposed wire have been painted using waterproof paint to insulate the sensors from any electrical interference that may occur during the measurement process, as shown in Figure 4.8.

Figure 4.8.The conductive sensor with attached wire that is insulated by waterproof paint.

As the seven-sensor probe measures the properties of the bubble, using the first contacts only, it is important to keep the sensor body insulated apart from its tip that is exposed to the attacking bubbles. For this reason, the very end of the painted needle's tip has been cleaned by using a fine emery paper, as illustrated in Figure 4.9.

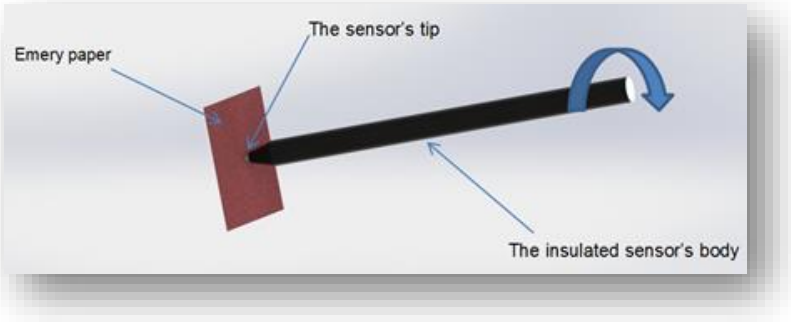

Figure 4.9. A fine Emery paper used to remove the insulation from the tips of a sensor.

All seven sensors have been aligned in parallel using an acrylic guide-disc that has been manufactured accurately using one of the laser machines, provided by the University of Huddersfield, since laser cut can generate accurate dimensions that can reduce the gap between the sensors and the guide holes. This reduction causes all seven sensors to stay in parallel position facing the flow stream. This, in turn, reduces the effect of flow field on probe's measurement. The guider comprises of seven holes of 0.25 mm arranged in circular shape, one in the middle and the other six holes away from it for a distance of 1 mm, as shown in Figure 4.10.

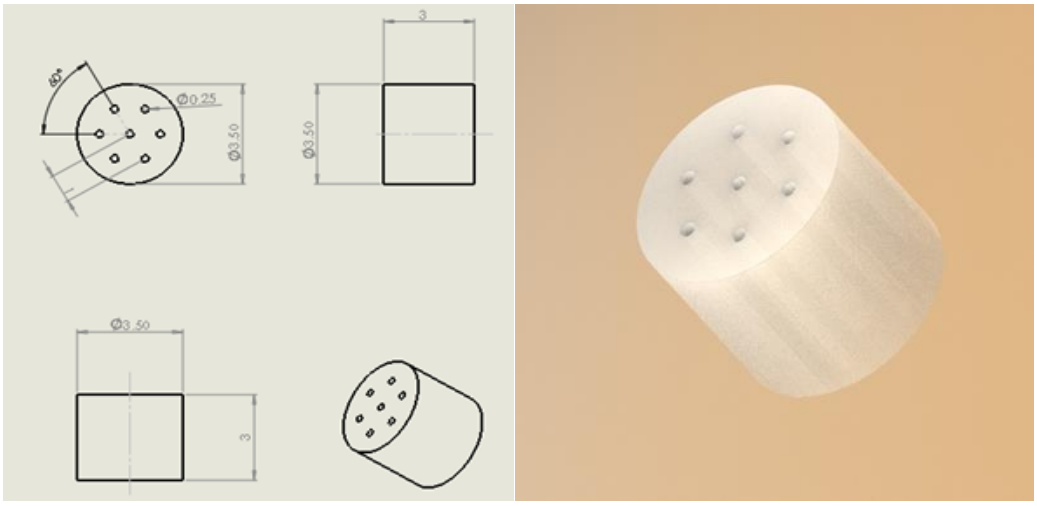

Figure 4.10. The acrylic guider.

For the sensors' housing two stainless steel tubes with of 6 x 4.5 mm and 4 x 3.3 mm, outer and inner diameter respectively have been used. The tubes have been bent in such a way that the inner profile has been kept circular as much as possible to ensure that the wires that have been embedded do not cause any contact with the housing tube, as shown in Figure 4.11.

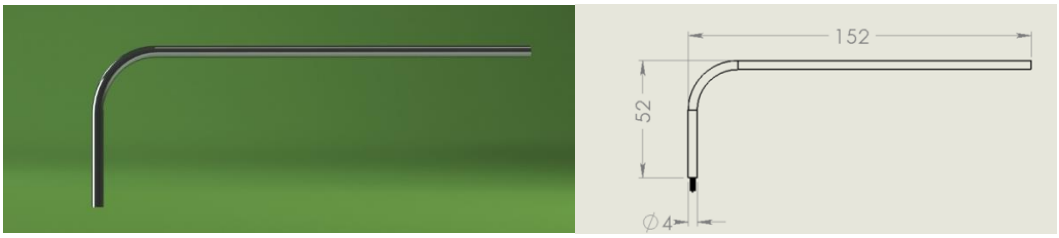

Figure 4.11. The L-shape stainless steel tube that has been used as probe housing.

All seven sensors have been aligned in such a way; the middle sensor, with 12.5 mm length, precedes the trailer sensors, 10 mm in length, by a distance (S) of 2.5 as shown in fFigure 4.12.

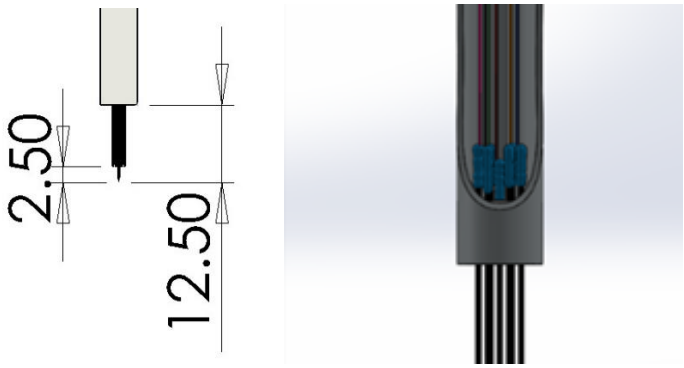

Figure 4.12. The seven-sensor alignment.

The observation made by Wu, et al. [61] for the vertical upward air–water flows has been taken into consideration. This observation has revealed the fact that the air-bubbles velocity vectors are not always purely axial, but they are also accompanied with small lateral velocity vectors. Therefore, these lateral velocity vectors could cause the bubble surface to strike both the front and rear sensors nearly simultaneously. This, in turn, the makes the time interval, δt, to be zero consequently the mean local axial bubble velocity, U_{gl}, will be infinite. To minimize the effects of this problem in the vertically upward, bubbly air–water flows; Wu et al. [61] have suggested that the axial separation, S, of the sensors should be in the range of 0.5d ≤ S≤ 2d; where d is the mean bubble diameter.

4.3.2 CFD based analysis of the effect of probe geometry on the flow field interference

The performance of seven-sensor probes for measuring the conductance of gas–liquid mixtures in vertical pipes has been investigated in this section using CFD simulations, to quantify the effect of the interference between the flow field and the probe. There is a strong requirement to avoid the disturbance of the flow as much as possible, to minimize the effect of the probe intrusiveness using CFD as a tool for designing and optimization probes that have been used for measuring the flow parameters has been done successfully by researchers such as [161], [162], [163] and [164].

In this study, the effect of the length of the sensor needle, Z_n, the probe's diameter D_p and the axial probe length, L_p, have been investigated to analyse and predict, the effective of changing these variables on the probe-flow field interactions.The simulations have been conducted using a 4" pipe model, this pipe size has been selected to mimic the flow loop experimental that has been used in this project. Moreover, three probe diameters of 4, 5 and 6 mm, where 4 mm tube is the minimum probe diameter that can combine seven sensors with seven wires attached to, have been used at different axial lengths of 50,60,70,80 and 100 mm. Stainless steel needles with 0.25 mm diameter have been used, this is the smallest diameter that has been found in the market. A bubbly two-phase flow of air-water has been considered with water superficial velocity of 0.74 m/s, the minimum velocity that the flow loop can handle, and air of 0.04 m/s, to keep the flow as a bubbly flow, at ambient conditions.

4.3.2.1 The effect of the probe diameter, D_p

To find the effect of the probe diameter on the flow structure, CFD analysis has been carried out with various probe diameters. The minimum probe diameter has been limited to 4 mm due to the limitation of the working space for 7 sensors that require to be connected with the wires and insulated them. Result from the CFD analysis for probe diameter 4 mm and 6 mm has been presented in Figure 4.36, which indicates that the probe's diameter D_p has a direct effect on velocity profile. In Figure 4.13a, in which the probe diameter is 4 mm, the velocity profiles appear to be symmetric across the test section of the pipe. Figure 4.13b represents the results for 6 mm probe diameter. From Figure 4.13, it appears as the probe diameter increases the flow structure tends to be asymmetric, due to the increase of flow-probe interaction.

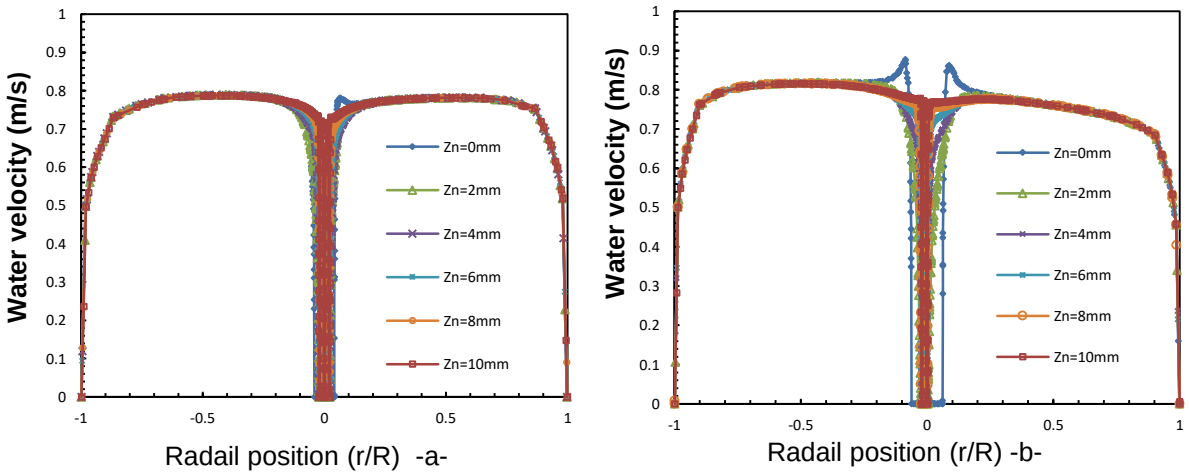

Figure 4.13. *The effect of probe diameter on the water velocity distributions a) D_p=4 mm, b) D_p=6 mm.*

4.3.2.2 The effect of the probe's axial length (L_p)

The CFD analysis has been also carried out for investigating the effect of the probe's axial length (L_p) on the flow structure. From the contour visualisation presented in Figure 4.14, it appears that the probes stem at axial length (L_p) of 50mm has a minimum or no effect on the bubble's velocity distribution i.e. the axial stem length of 50 mm or above produces less flow-probe interactions in the area close to the sensors.

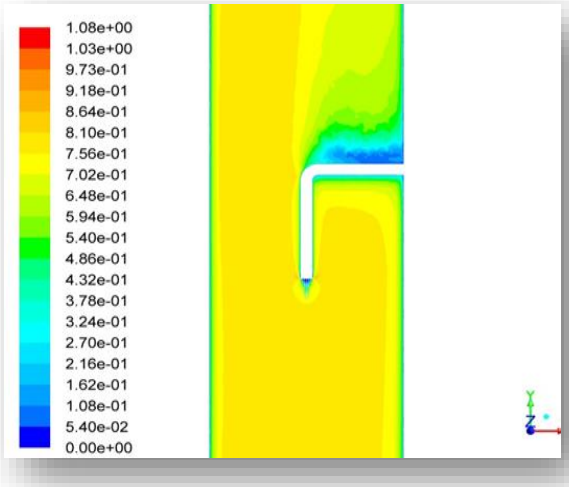

Figure 4.14. Contour plot of water velocity (ID=97.18, D_p =6mm, L_p=50mm).

4.3.2.3 The effect of the sensor length, Z_n

The other parameter that has been taken into consideration in this analysis is the sensor (needle) length. According to Figure 4.15, it appears that the probe's frontal area disturbs the stream and its disturbance is gradually decreased by moving, upstream, away from the probe's frontal area.

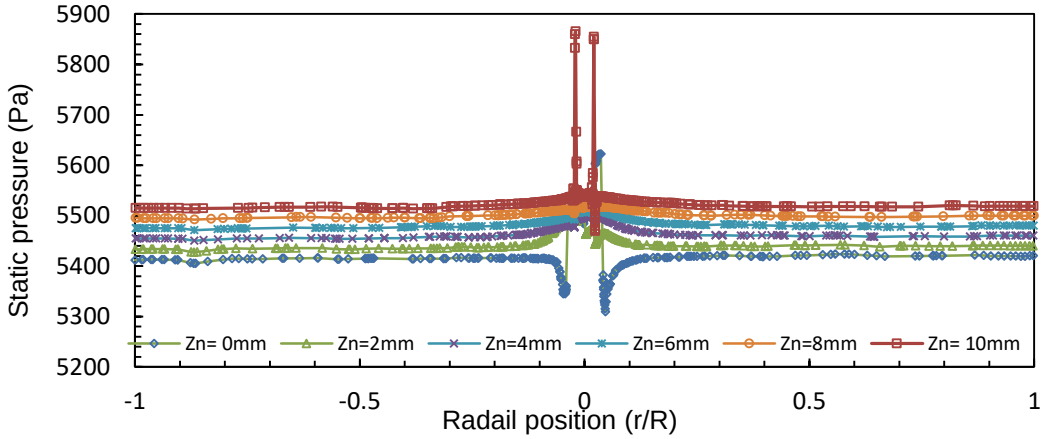

Figure 4.15. The effect of sensor length, Z_n, on the static pressure distributions around the seven-sensor probe (ID=97.18, D_p=4mm, L_p =50mm).

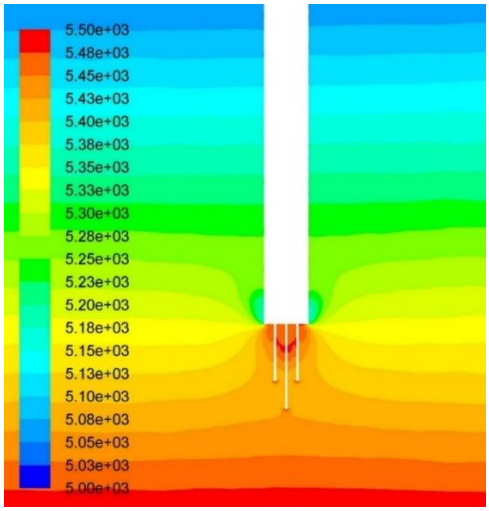

Figure 4.16. Contour plot of the static pressure around the seven-sensor probe

Figure 4.16 depicts the contour plot of the static pressure around the probe sensors, it can be clearly seen that static pressure between the lead sensor and the trailer sensors is the same, this in turn reveals that sensors with about 8 mm and above is the right choice to reduce the missing bubbles due to the intrusiveness of the seven-sensor probe.

From the CFD investigation the following points have been concluded:

1. Using smaller probe diameter , D_p, reduces the effect of the probe intrusvness on the measurement accuracy. However, in case of seven-sensor probe, we cannot use tubes less than 4 mm diameter due to the number of wires that need to be combined.
2. The probe's axial length, L_p, has been found to be 50 mm and above to eliminate the effect of the probe stems on the measurement accuracy.
3. The sensors length has been found to be 8 mm and above to reduce the number of the missing bubbles.

4.3.3 The probe dimensions

The seven-sensor probe theory is based on the six time-delays generating from the seven sensors that are separated by fixed radial distances, moreover, the lead sensor, S_0, is heading the rear sensors by an axial distance, S. Therefore, as a part of the probe manufacturing, these distances need to be measured accurately for obtaining accurate measurement of the dispersed phase properties. This process includes assigning each sensor with an x, y and z coordinate. The most useful method for the probe dimension measurement is by using a digital microscope as shown in Figure 4.17, which can capture the sensor's tips whilst magnified as shown in Figure 4.18.

Figure 4.17. Digital microscope camera.

Figure 4.18. The sensor tips captured by the digital microscope camera.

For the sensor's axial coordinate (Z_n) measurement, the probe should lay down perpendicularly, as shown in Figure 4.19.

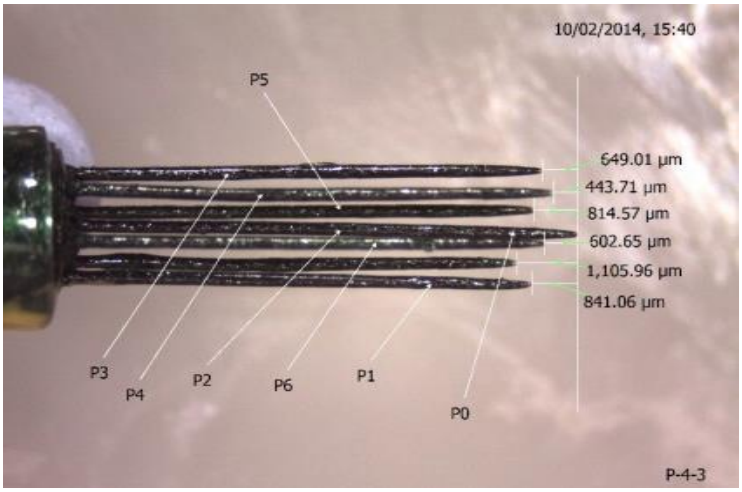

Figure 4.19. The measuring process of the axial sensors' length Z_n using a microscope camera.

For the sensor's radial and azimuthal, x and y coordinates measurement respectively, the sensors should be aligned with the digital camera's horizontal position. This can be done by align the axes of the microscope Xc and Yc with the axes of the probe x and y. Figure 4.20 depicts the sensors' x and y coordinates.

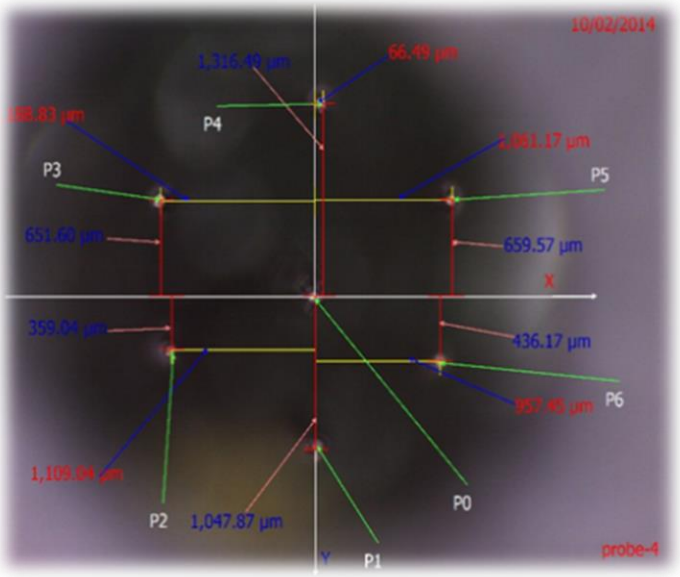

Figure 4.20. The sensors' x, in red colour and y, in blue colour, coordinates.

From the probe measurement process, Table 4.1 has been developed to be used later in the mathematical model for predicting the velocity vectors.

Table 4.1: The probe coordinates

#	X (mm)	Y(mm)	Z(mm)
Sensor 0	0	0	0
Sensor 1	0	-1.04787	0.84106
Sensor 2	-1.10904	-0.35904	0.60265
Sensor 3	-1.18883	0.65160	0.44371
Sensor 4	0.06649	1.31649	0.64901
Sensor 5	1.06117	0.65957	0.81457
Sensor 6	0.94745	-0.43617	1.10596

4.4 Data processing

The core task of data processing of the seven-sensor probe system is to recognise the signal parts representing the bubble in the raw signal. This recognition occurs when the sensors enter and exit through each bubble. The bubble recognition process based on distinguishing between the different levels in the raw signals, i.e. the gas level, the liquid level and the noise level. The data processing is considered to be one of the main sources for measurement uncertainty. Therefore, a high consideration has been undertaken whilst conducting this process. The data processing is comprised of conditioning the raw data using appropriate filter, processing the conditioned signals, and calculating the dispersed flow properties.

4.5 Data conditioning

In this process, the raw signals have been filtered using one of the filtering methods provided by MATLAB code to distinguish the noise signals from the desired signals. A low-pass filter has been used in this process, since it lets signals with a frequency lower than a certain cut-off frequency pass and reduces signals with frequencies higher than the cut-off frequency. Based on the literature, two filtration methods have been found to be used effectively to reduce the accompanying noise, namely Butterworth [165] and median filters. Therefore, both methods have been examined, as shown in Figure 4.21 and Figure 4.22. From Figure 4.21 and Figure *4.22*, it can be clearly seen that the median filter can provide much better results, less fluctuations and higher low frequency cut off, compared to the one from Butterworth filtration. Therefore, the median filtration has been used in the signal condition process.

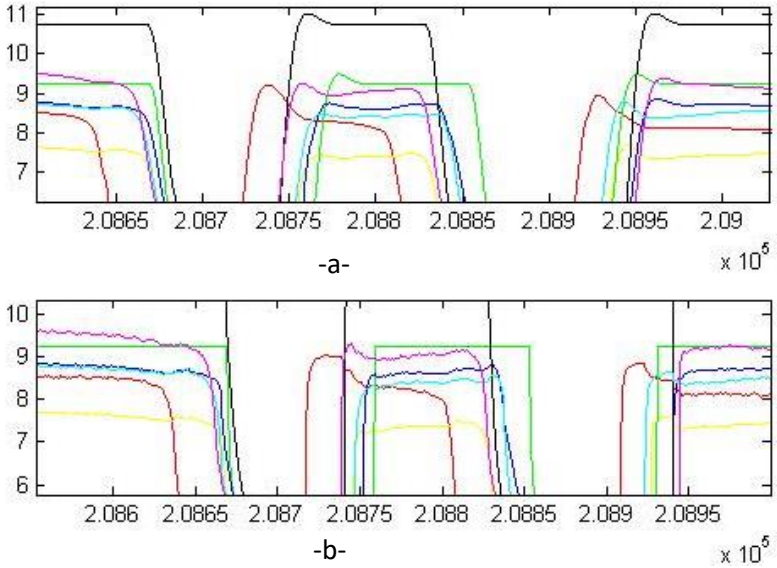

Figure 4.21. Butterworth filter (a) Filtered signals (b) Raw signals.

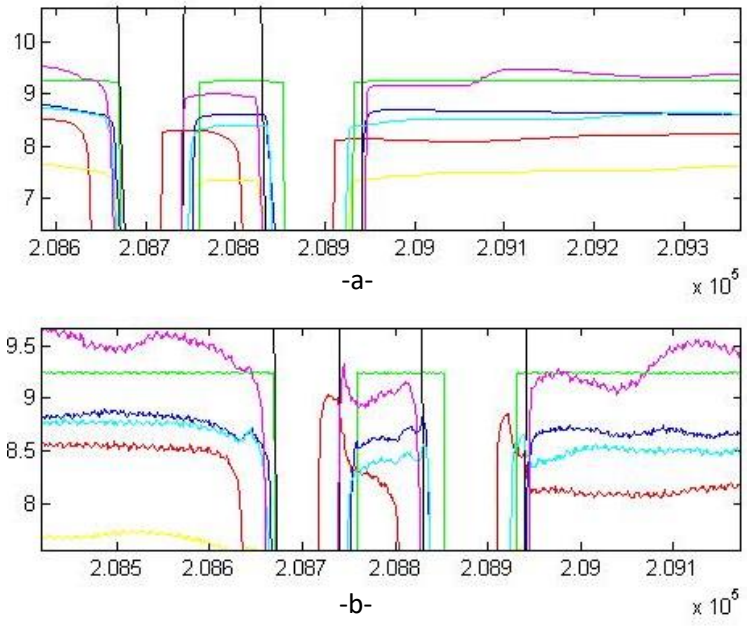

Figure 4.22. Median filter (a) Filtered signals (b) Raw signals.

4.5.1 Processing the conditioned signals

After removing the undesired noise signals from the raw data, an appropriate threshold value is required to be coupled with the filtering procedure to eliminate the effect of the remained noise. Voltage threshold is the minimum voltage value that is required to distinguish the gas and liquid phases.

In this research, the threshold voltage value selection is based on how this value affects the volume fraction measurement. When the threshold magnitude is increased the residence-time will be decreased for each given sensor in a bubble. In turn, the measured volume fraction will be underestimated. Therefore, in order to overcome this discrepancy, the similar process of threshold voltage identification as had been reported by Pradhan et al. [140] has been applied. This method ensures that the mass conservation law is fulfilled at any measurement point within the flow field. Therefore, all seven sensors must produce the same volume fraction. This process is based on iterations process implementation where different threshold values will be applied to measure the volume fraction from each sensor. The obtained volume fraction is then compared with the reference volume fraction which has been calculated using equation 4.20, [166].

$$\alpha = \frac{\Delta p + F}{(\rho_w + \rho_g) g h \cos\theta} \tag{4.20}$$

where Δp is the pressure drop between two pressure sensing points, ρ_w and ρ_g represent water and air densities respectively, h is the separation distance between two pressure sensing points, g is gravitational acceleration, θ is the pipe inclination angle and F is the pressure loss due to the friction.

As the dominant phase is water which has density of several times higher than the dispersed phase air density, moreover, the dispersed phase fraction is less 0.1 i e, bubbly flows; therefore, Darcy equation that is used for the single-phase flow can be successfully used for friction losses calculation:

$$F = \frac{f h \rho_w (U_h)^2}{2M} \tag{4.21}$$

where f is the friction factor for the single-phase, M is the hydraulic radius and U_h is the homogenous velocity that can be obtained from

$$U\_h = U\_W + U\_G \tag{4.22}$$

$U_W \; and \; U_G$ are water and air superficial velocities respectively.

The threshold voltage magnitude will be considered only when the measured volume fraction is equal to the calculated reference volume fraction or has less than 0.0001 in difference.

After the raw data is conditioned and accurate threshold is applied, conducting a scheme for the time interval assessment within the code will be the next step. This scheme is based on following assumptions:

1. The signal processing does not account the missing bubbles, the bubbles that touch the main sensor, S_0, and miss to touch at least one of the auxiliary sensors, S_i,.
2. The signal processing does not account signals with small time intervals. This process will ignore any bubble that contacts one or two sensors at their edge, causing misperception during the signal processing. Such small time intervals will result in an abnormally higher velocity, eventually resulting in over-estimating the velocity magnitude [159].
3. All bubbles should first touch the main sensor then the rear sensors. Any bubble that contravenes this law will be considered as a missing bubble.

4.6 Calculating the dispersed flow properties

After the signals had been conditioned and after applying a proper threshold, six-time delays have been calculated. Six equations, therefore, needed to be solved to obtain six unknowns

In fact, there are two methods available for solving Quadratic Equation namely, iteration method, trial and error, and the f-solve method, where initial guess is used to reduce the amount of the iterative process, this function is provided by the MATLAB code. Because iteration method is very expensive, high computing time consumer, to run and needs a very large computer RAM size, therefore, f-solve method has been used to obtain the velocity and bubble diameter components in this project.

Typically, Figure 4.23 represents a block diagram of the signal processing method that has been used to capture the signals from the seven-sensor probe and to obtain the desired flow properties.

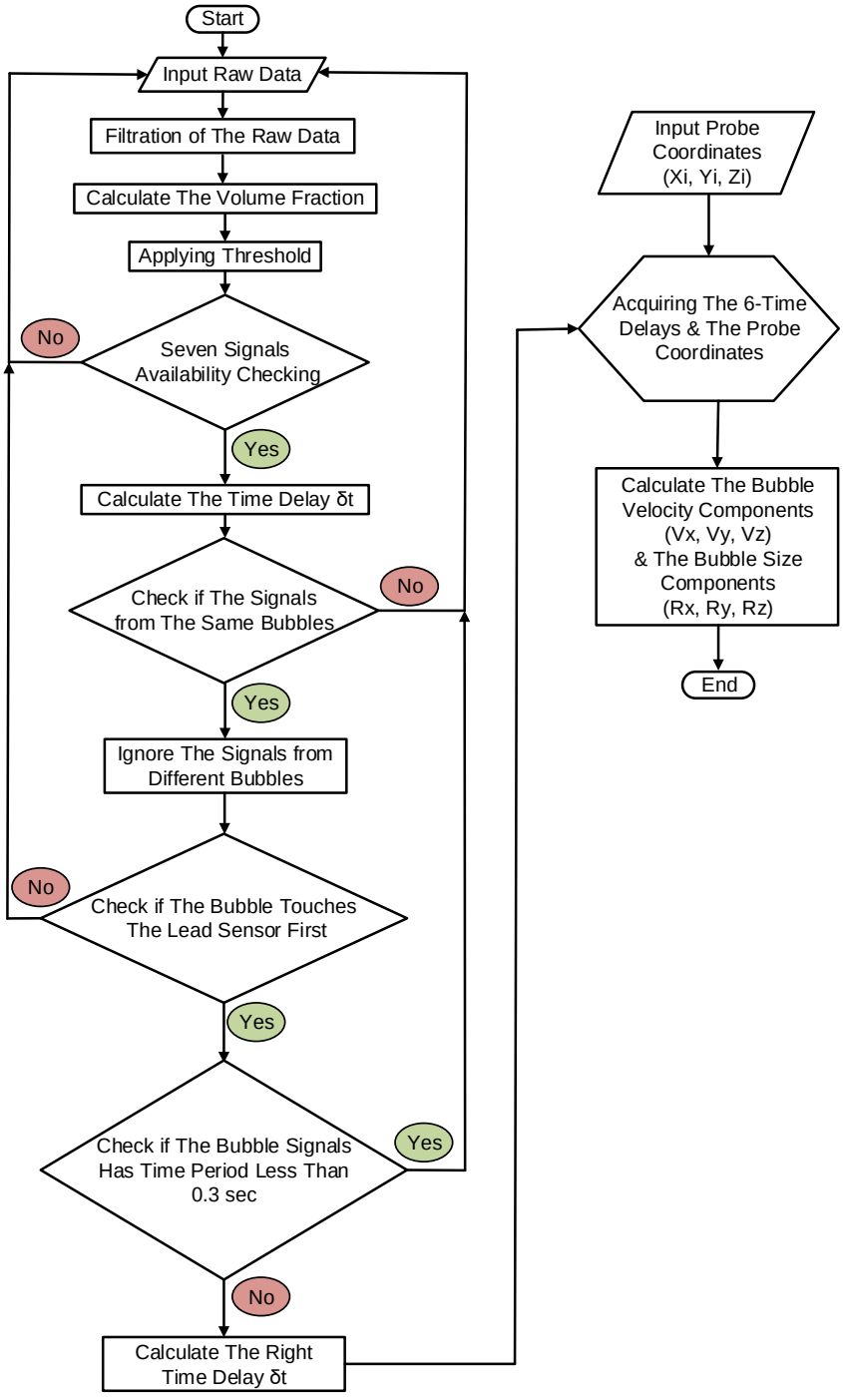

Figure 4.23. Block diagram for signal conditioning and processing that is used in the seven-sensor probe system.

In general, f-solve has three algorithms:

- trust-region-dogleg
- trust-region
- levenberg-marquardt

In this project the trust-region-dogleg has been used for solving the quadric equations as the algorithm is the only algorithm that is specially designed to solve nonlinear equations [167].

4.7 Uncertainty Source

The uncertainty can be defined as a factor related to any measurement that describes the scattering of the values, which could realistically be attributed to the measurement. The uncertainty cannot be defined as an error in measurement, since error is defined as the difference between an individual result and the true value of the measurement. In practice, an observed measurement error is the difference between observed values and reference values. As such, error whether theoretical or observed is a single value. In principle, the value of a known error can be applied as a correction to the result. Whilst uncertainty takes the form of a range or an interval, and, if estimated for an analytical procedure and defined sample type, may apply to all determinations so described. In general, the value of the uncertainty cannot be used to correct a measurement result.

The main source of uncertainty in the present work can be illustrated as:

1. At the image processing stage, the uncertainty arises when the local bubble velocity related to the frame rates and the geometrical properties determination (i.e. centre of mass of the bubble) and applied magnification factor.
2. The pixel-mm conversion aspect has been obtained by taking the probe head length as a reference length. The MATLAB code has been used to acquire the images and the time interval between sequential images, which has been reasonable accurate. The accuracy of geometrical properties of the bubble, such as, the bubble's centre of mass, bubble major and minor axes etc., depends on the image segmentation performance and the contrast between background and the bubble.
3. As the probe has been manufactured in house; it is not very accurate in terms of the probe, the length of the six of the trailer sensors of the probe may not be the same. The distances between the middle sensor's tip and the other six trailer tips differ slightly. Furthermore, the six-time intervals used to calculate the bubble velocity also varied because of unpredictable
4. Due to inaccuracies in measuring instruments (water flow meter, air low meter and DP cell).

This chapter has provided a detailed overview of the design of the novel seven-sensor probe that is going to be used for measuring the dispersed phase properties in the proceeding chapters. The novelty of the probe is based on the fact that the seven sensors identify the second phase properties from the first

bubble-sensor contact. Moreover, this probe can measure the real bubble diameter component, x, y and z.

In this chapter, three objectives have been achieved, namely the development of a novel mathematical model that calculates the dispersed phase flow properties from the first bubble sensor contact, the development of a novel mathematical model that calculates the dispersed phase flow properties from the first bubble sensor contact for irregular bubble shape, i.e. when bubbles coalescence, and finally, design, development and manufacture of the novel seven-sensor needle probe system that will be used to measure the dispersed phase properties including actual bubble shape and size. Moreover, CFD based investigation has been conducted to quantify the optimal probe geometry that reduces the effect of probe intrusive to minimal.

The next chapter will shed light on the knowledge gaps regarding the flow-sensor interaction over a wide range of flow variation.

4.8 Multi-sensor probe's measurement- error reduction

The principle of needle probes operation is based on obtaining data from the needles' tip. These tips are fixed at a certain axial and radial distances. The accuracy of the dispersed phase properties measurement depends on how accurate these distances are measured. Therefore, any relocation of these tips causes measurement uncertainty. The main source causing the sensor's tip to be relocated is sensors deflection. In this chapter, extensive numerical investigations have been carried out to quantify the flow field variables that affect the sensor deflection. Thereafter, these factors have been transferred as form of pressure magnitude and have been applied to the sensors and probe body surfaces. By using FEA technique, the amount of the transferred pressure will be translated into displacement. Finally, mathematical equations have been developed, based on regression analysis, to measure the sensor displacements values depending on the flow field variables that have been investigated. Currently, the availability of instruments for measuring the sensor displacement are very limited. Therefore, a CFD code has been used to predict the sensors' tip relocations.

4.8.1 CFD Model and Simulation

Due to the advance development of CFD, it can be a useful tool to be used for assessing the flow field effect on the multi-sensor probe, therefore, this tool has been utilized to predict the flow field variables that affect the sensor deflection. In these investigations, set of three-dimensional computational domains of vertical straight pipes have been created for simulations. These domains have comprised of three pipes of 60, 80 and 100 mm internal diameters and 2000 mm in length using the Design Modeller software, which is provided in ANSYS software. These geometries have been separated into three sections to represent the test pipe boundaries. These boundaries have been the Inlet, Test section and the Outlet.

The distance between the Inlet pipe and the location, where the seven-sensor probe has been located, has been at 1300 mm, which corresponds to L/D =13, as shown in Figure 4.24. The selection of the entrance distance has been based on the CFD simulation that had been conducted previously in chapter 3. That simulation had been carried out to quantify the entrance distance where the flow reaches fully developed condition. The test section that has been used in this study had a smooth wall i.e. the absolute roughness value of the pipe has been zero.

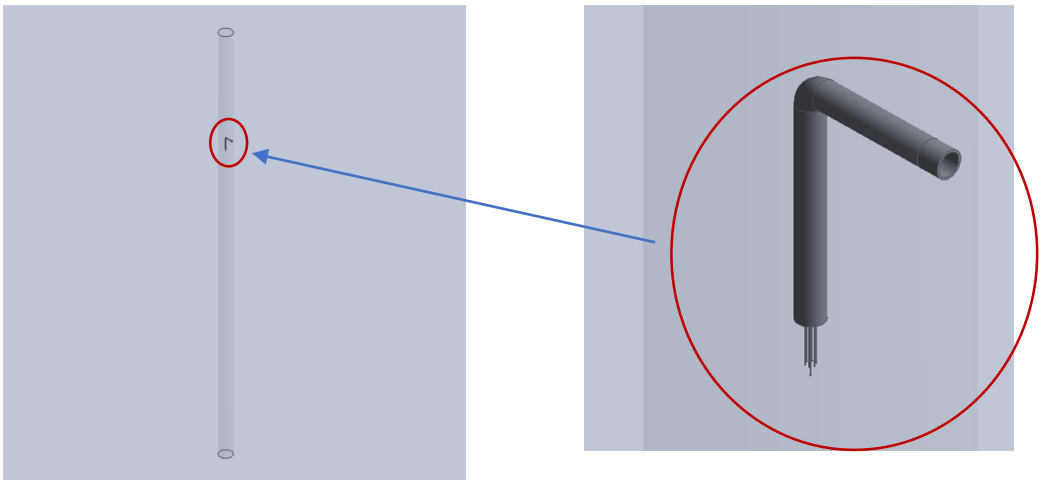

Figure 4.24. The location of the seven-sensor probe in the test pipe geometry.

The probe has been located at three radial positions, namely 10, 50 and 90% of the internal test pipe diameter where the sections that have most flow effect on the probe. Therefore, for each simulation, three models are needed to be created, as shown in Figure 4.25.

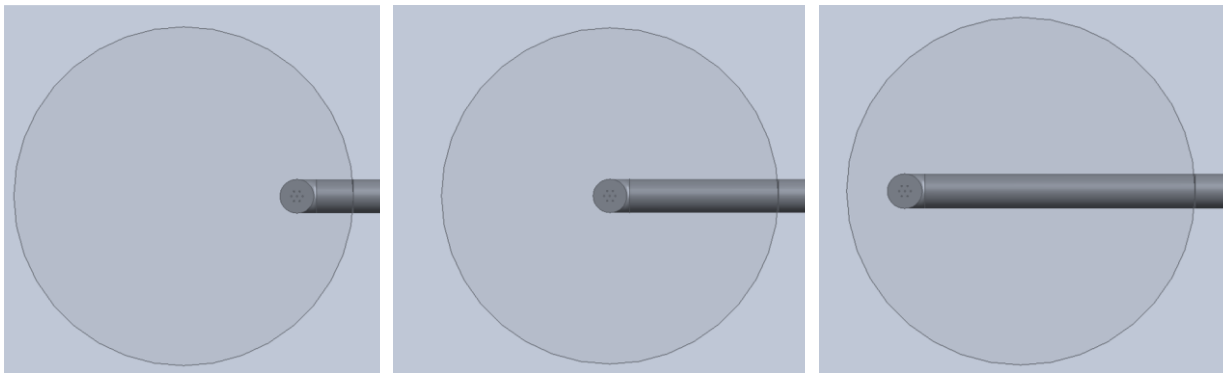

10% 50% 90%

Figure 4.25. The geometries of seven-sensor probe position in the 60 mm test pipe.

4.8.1.1 Meshing process

All the geometries have been meshed using tetrahedron meshing method due to the complexity of the geometry. Generally, it is important for any CFD simulation to capture the large variation in velocity profile in the near-wall region correctly. Therefore, it is necessary to use inflation mesh layers for accurately capturing the boundary layer region for any wall-bounded turbulent flows. In this study, five inflation layers have been used, as shown in Figure 4.26 - Figure 5.28.

It is important in turbulence modelling to determine the proper size of the cells near the domain's walls. Therefore, the turbulence model wall laws have restrictions on the y^+ value at the wall, where y^+ is a non-dimensional distance at wall region. $y^+ \approx 30$ is most desirable for wall functions [103]. Therefore, the y^+ value has been examined for each case to make sure that it is close to 30.

Figure 4.26 - Figure 4.28 depict the mesh distribution in flow domain for mesh density of 766168,1045397 and 2589548 elements. A grid independency test has been carried out on three different grid sizes to check the effect of these sizes on the air velocity distribution across the test pipe, the air velocity has been used in this test as the novel sensor can measure the air velocity only not the water.

According to Figure 4.29, the air velocity distribution for the different grid sizes has indicated that there is no significant change in air velocity distribution with the change in number of elements between 1045397 and 2589548 elements. Accordingly, the mesh density of 1045397 elements has been used for the numerical investigations.

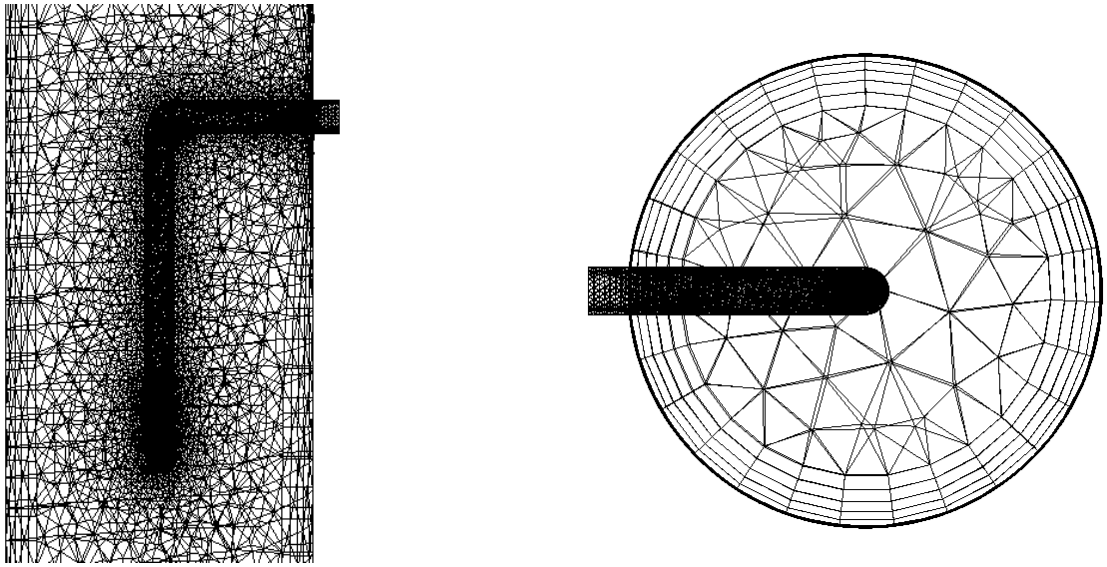

Figure 4.26. The mesh distribution of the flow domain with 766168 elements.

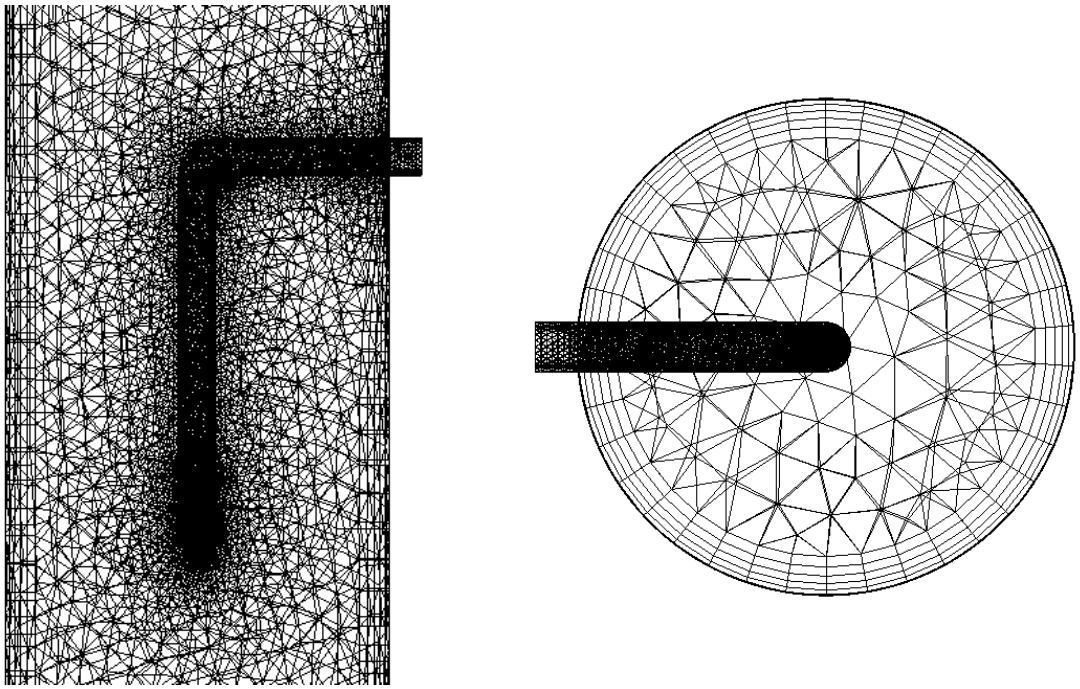

Figure 4.27. The mesh distribution of the flow domain with 1045397 elements.

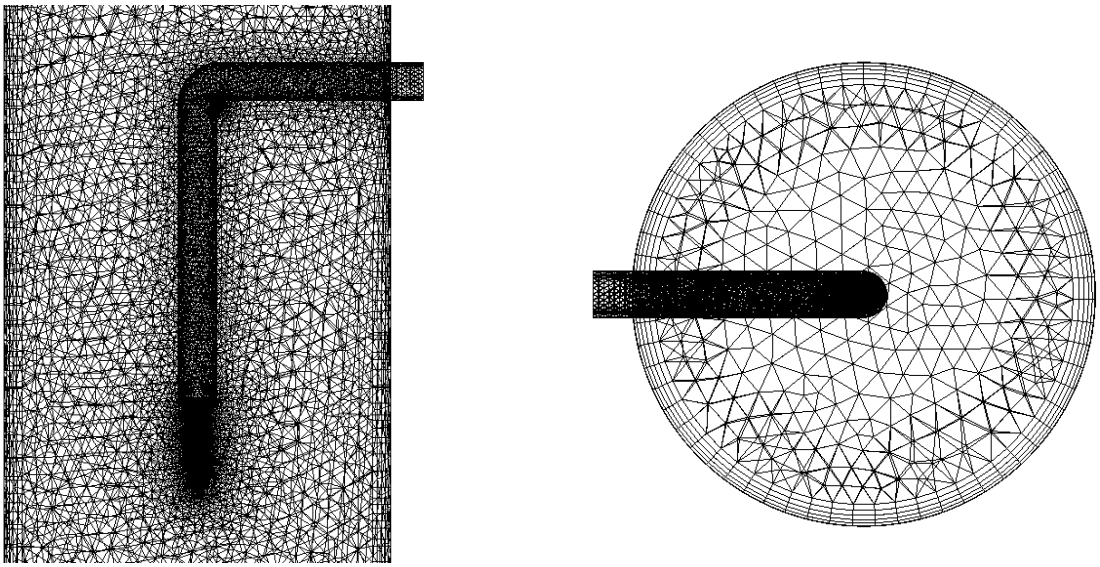

Figure 4.28. The mesh distribution of the flow domain with 2589548 elements.

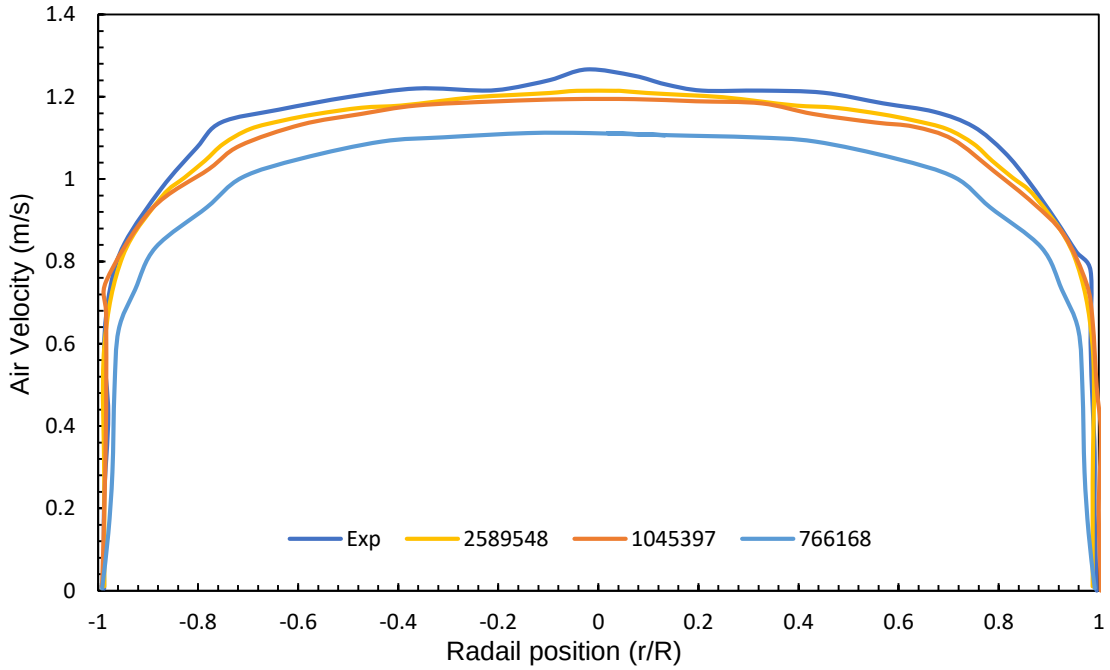

Figure 4.29. Radial velocity distributions for different number of mesh elements.

4.8.1.2 Boundary Conditions

In these investigations, three values of mixture velocities have been used namely, 0.5, 1 and 4 m/sec. The reason for choosing these velocities is that many researchers have used these mixed flow velocities during their investigation of the secondary phase properties. The initial volume fraction, volumetric quality, of 0.01 has been used during the numerical investigations with a bubble size of 6 mm. The pressure at the outlet of the pipe has been kept at atmospheric pressure, i.e. 0Pa gauge. As have been discussed earlier, the pipe has been considered relatively smooth having a wall roughness constant of zero.

4.8.1.3 Defining Material Properties and Operating Conditions

In the present study, investigations have been undertaken in vertical and relatively large pipelines to quantify the effect of the surrounding flow field on the probe body. The two-phase flows within the pipe have been defined as the liquid-water, with density of 998.2 Kg/m3 and dynamic viscosity of 100.3e-05 Kg/m-sec, as a primary phase and gas air, with density of 1.225 Kg/m3 and dynamic viscosity of 1.7894e-05 Kg/m-sec, as the secondary phase. The operating conditions that have been given to the solver are the operating pressure of 101325 Pa (i.e. atmospheric pressure) and turning the gravitational acceleration of 9.81 m/sec^2 on for the investigations.

4.8.1.4 Solver Settings

The upward bubbly gas-liquid flows have been modelled using the Euler-Euler approach. This model solves the continuity and momentum equations for each phase separately for low volume fractions of approximately 1%. The following time averaged governing equations of mass and momentum transport for each phase is the basis of the Eulerian model, which have been used in ANSYS Fluent:

$$\nabla.(\alpha_k \rho_k \overline{v_k}) = 0 \tag{5.1}$$

$$(\alpha_k \rho_k \overline{v_k}\ \overline{v_k}) = -\alpha_k \nabla p + \nabla.\alpha_k \mu_k (\nabla v_k + \nabla. v_K^T) + \alpha_k \rho_k g + M_k \tag{5.2}$$

where the subscript k refers to the phase (k = 1, 2), $\overline{v_k}$ is the average velocity vector, α_k is the volume fraction, ρ_k is the density, μ_k is the shear viscosity, p is the static pressure, g is the gravitational acceleration, and M_k is the net interfacial force on the phase. The Shear-Stress Transport (SST) $k-\omega$ Model has been selected as a turbulent model to capture the turbulence phenomenon and the flow separation that occurs due to the excessive of the four-sensor probe [168]. Moreover, this model can be calculated from [169]:

$$\frac{\partial}{\partial t}(\rho k) + \frac{\partial}{\partial x_i}(\rho k u_i) = \frac{\partial}{\partial x_j}\left(\Gamma_k \frac{\partial k}{\partial x_j}\right) + G_k - Y_k + S_k \tag{5.3}$$

and

$$\frac{\partial}{\partial t}(\rho \omega) + \frac{\partial}{\partial x_j}(\rho \omega u_i) = \frac{\partial}{\partial x_j}\left(\Gamma_\omega \frac{\partial \omega}{\partial x_j}\right) + G_\omega - Y_\omega + D_\omega + S_\alpha \tag{5.4}$$

where S_k, and S_ω , are user-defined source terms. $Y_k\ and\ Y_\omega$ represent the dissipation of $k\ and\ \omega$ due to turbulence. α_k and α_ε are the generation of turbulence kinetic energy due to the mean velocity gradient. G_k represents the production of turbulence kinetic energy, and G_ω denotes the generation of turbulence kinetic energy and is defined in the same manner as in the standard $k-\omega$. In addition, $\Gamma_k\ and\ \Gamma_\omega$ represent the effective diffusivity of k and ω , respectively and finally, D_ω represents the cross-diffusion term.

4.8.1.5 Model validation

The radial velocity and volume fraction distributions of the air have been employed as a criterion comparing the CFD calculations with the experiments. For the geometry validation, the inlet conditions have been assumed to be homogeneous in terms of superficial liquid and gas velocities and volume fractions for both phases in accordance with the experimental setup conditions [159].

Figure 4.30 and Figure 4.31 depict the comparison between the experimental results [159] and the CFD predictions in term of bubble velocity and air volume fraction respectively. From the figures, the numerical simulations have reproduced the radial volume fraction and the bubble velocity profiles with a good agreement to the experimental measurements. It has been observed that the non-drag forces, which act perpendicular to the flow direction, have mainly influenced the volume fraction distribution.

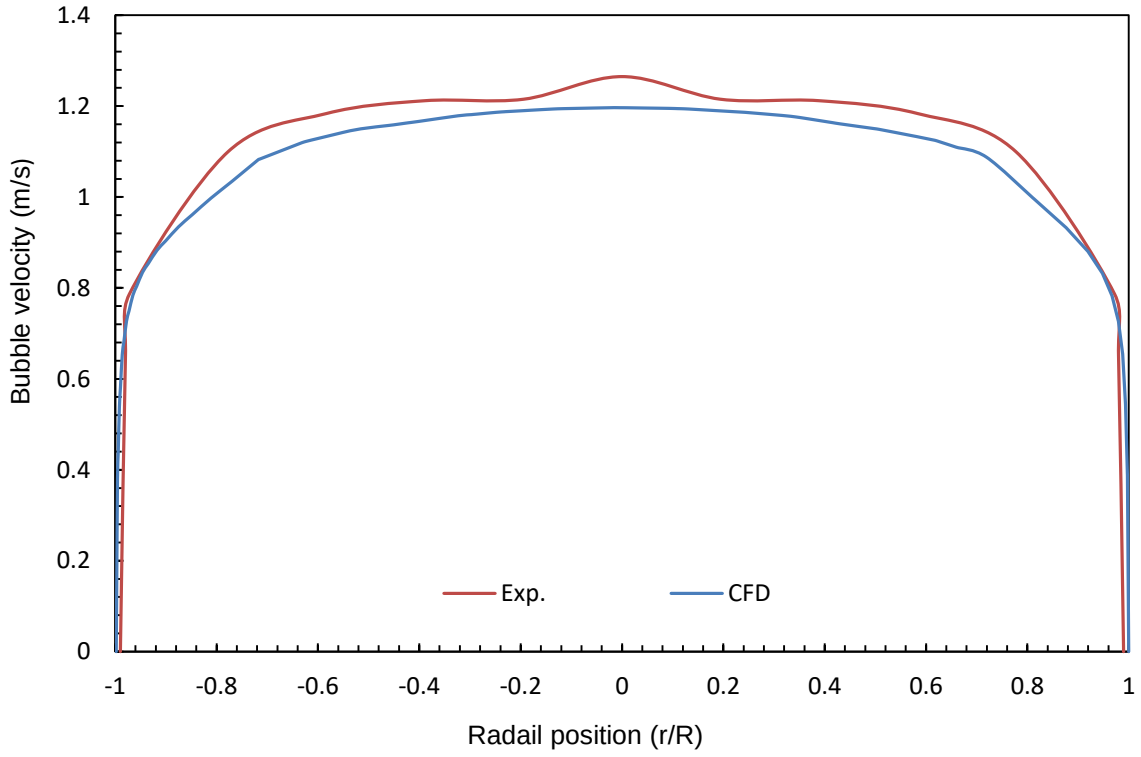

Figure 4.30. The comparison of the bubble velocity distribution between the experimental results (Exp.) and the CFD prediction (CFD), $\alpha = 0.038, U_{GS} = 0.041 ms^{-1},\ U_{LS} = 0.763 ms^{-1}$.

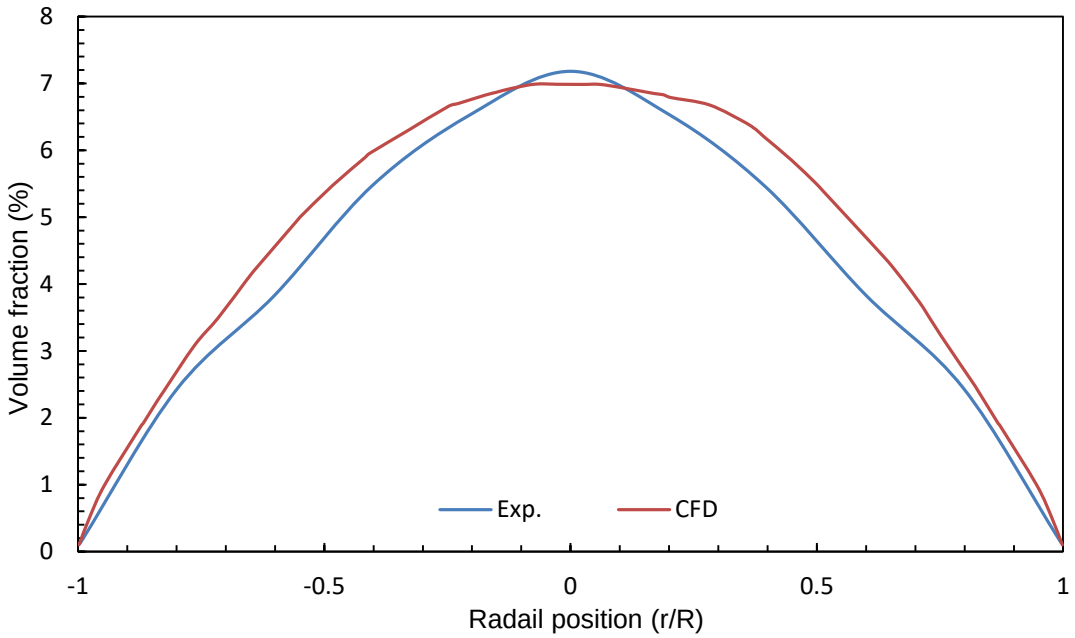

Figure 4.31. A comparison of volume fraction distribution between the experimental results (Exp.) and the CFD prediction (CFD), $\alpha = 0.038, U_{GS} = 0.041 ms^{-1},\ U_{LS} = 0.763 ms^{-1}$

4.8.1.6 The results

Several simulations have been carried out to investigate and predict the flow field variables around the probe and sensor bodies. In this study, the effect of probe location, the test pipe internal diameter and the inlet mixture velocity have been taken into consideration during the investigations. In order to conduct these investigations, 27 simulations have been carried out. The following section has illustrated some of the results depending on each cause.

4.8.1.6.1 The effect of probe location

Figure 4.32 depicts Contour plots of the static pressure distributions around the probe where the seven-sensor probe is placed at 3 radial positions i.e. 90, 50 and 10% of the pipe diameter, with water superficial velocity of 4 m/s, within 60 mm pipe diameter. From Figure 4.32, it can be clearly observed that pipe walls have significant effects on the static pressure distribution around the probe and sensors bodies. Maximum uneven pressure distributions around the sensors have been found when the probe has been close to the pipe wall, whilst almost equal pressure distributions around the sensors have been found at the pipe centre-line.

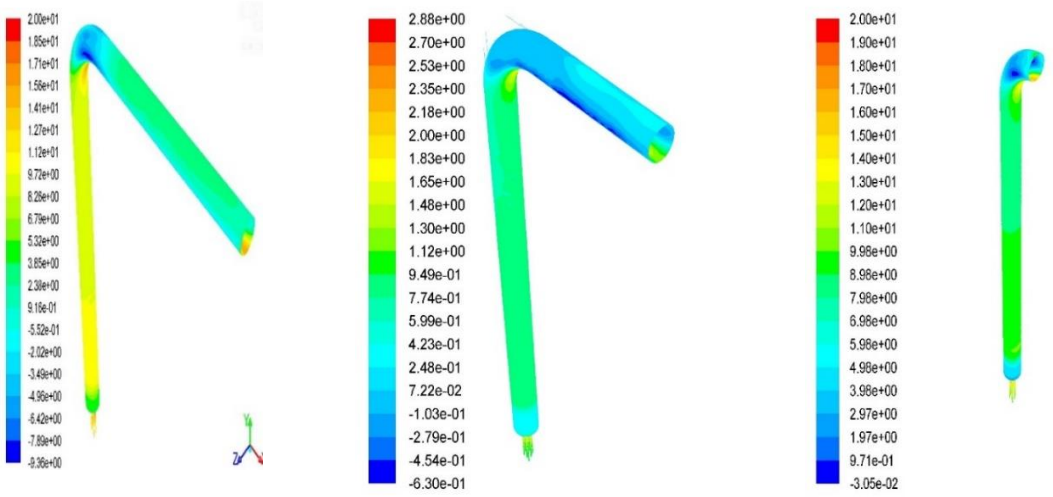

Figure 4.32. Contour plots of the static pressure distributions around the probe where the seven-sensor probe at 3 radial positions, 90, 50 and 10% of the pipe diameter (water superficial velocity of 4 m/s, 60 mm pipe diameter).

4.8.1.6.2 The effect of increasing the mixture velocity

Figure 4.33 depicts Contour plots of the static pressure distributions around the probe at 3 different mixed superficial velocity of 4, 1 and 0.5 m/s at radial position of 50 % of the pipe diameter (60 mm pipe diameter). From this figure, it can be clearly observed that the increase in flow velocity from 0.5 to 4 m/s increases the static pressure by 37%. This process occurs because of the increase of friction losses around the probe due to the high velocity.

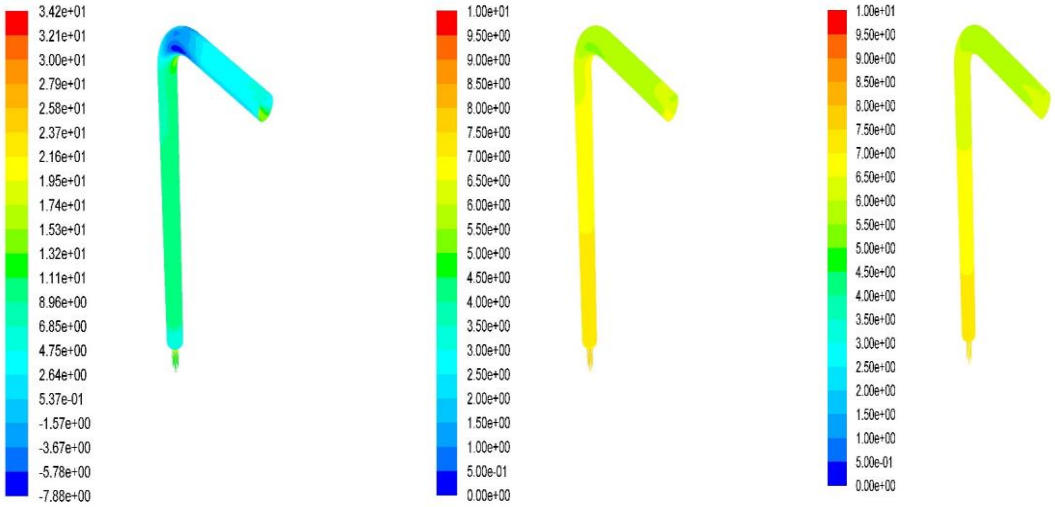

Figure 4.33. Contour plots of the static pressure distributions around the probe at 3 different mixed superficial velocities of 4, 1 and 0.5 m/s at radial position of 50 % of the pipe diameter (60 mm pipe diameter).

4.8.1.6.3 The effect of increasing pipe diameter

In this study, the effect of pipe diameter has also been investigated. Figure 4.34 depicts the contour plots of the static pressure distributions around the probe at 3 different pipe diameters of 100, 80 and 60 mm at radial position of 50 % of pipe diameter and mixed superficial velocity of the 4 m/s. It has been concluded that as the pipe diameter increases the static pressure decreases by 6%.

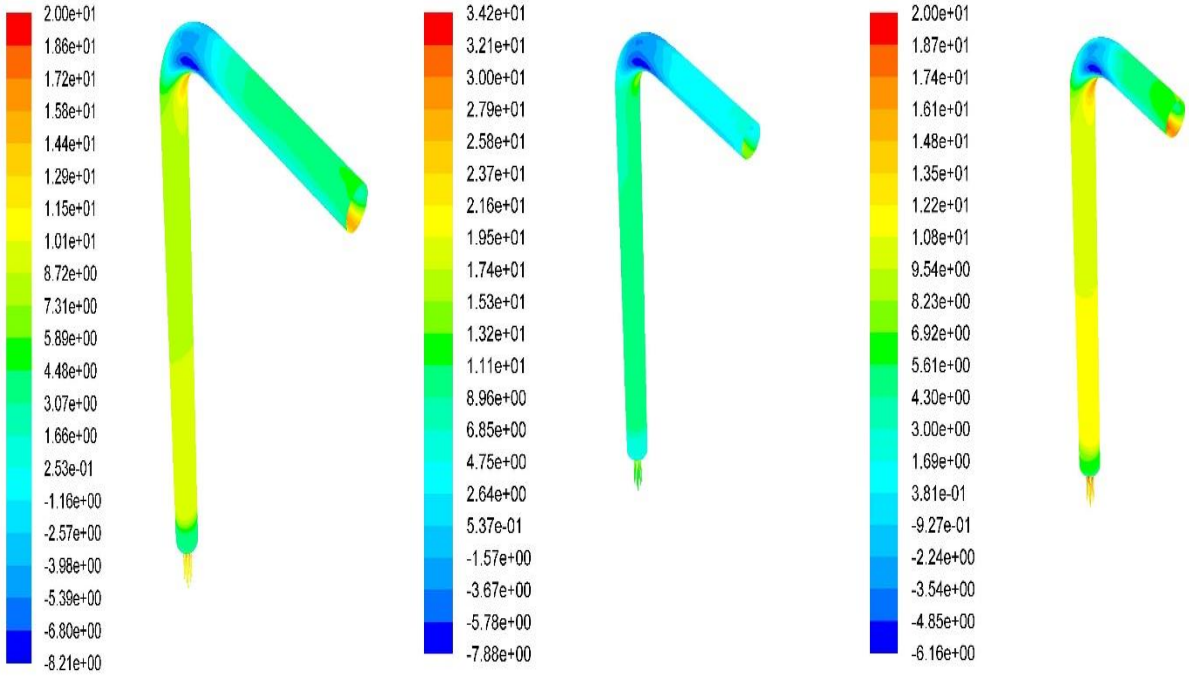

Figure 4.34. Contour plots of the static pressure distributions around the probe at 3 different pipe diameters of 100, 80 and 60 mm at radial position of 50 % *of* pipe diameter and mixed superficial velocity of the 4 m/s.

The obtained results from the 27 simulations have been transferred to the FEA code to obtain the sensor deflections as it has been discussed in the next part.

4.8.2 FEA simulation

The Finite Element Analysis (FEA) is a computational approach that is used to predict solutions for complicated engineering problems. This approach is a handful technique used by the engineers for solving problems that have complicated geometries, loadings, and material properties where conventional analytical solutions cannot be obtained. This method has broad applications, such as mechanical, aerospace, civil and automotive engineering, structural and stress analysis etc.

In this part, the displacement evaluations have been performed using a finite-element analysis software, which is used to effectively calculate the linear displacement of the sensors and the probe body. Three-dimensional finite-element models have been developed to quantify the maximum displacement that each sensor could experience in x, y and z directions. These models comprise of 3D probe geometries modelled for three different stem lengths, (corresponding to the lengths for the CFD simulations), as shown in Figure 4.35, at different positions in the pipe namely, at 10, 50 and 90% of each pipe internal diameters. The internal diameters were 60, 80 and 100 mm for each test pipe, similar to CFD simulations. Each probe and sensor body surfaces have been separated into four perpendicular surfaces where the predicted pressure from the CFD simulations will be applied.

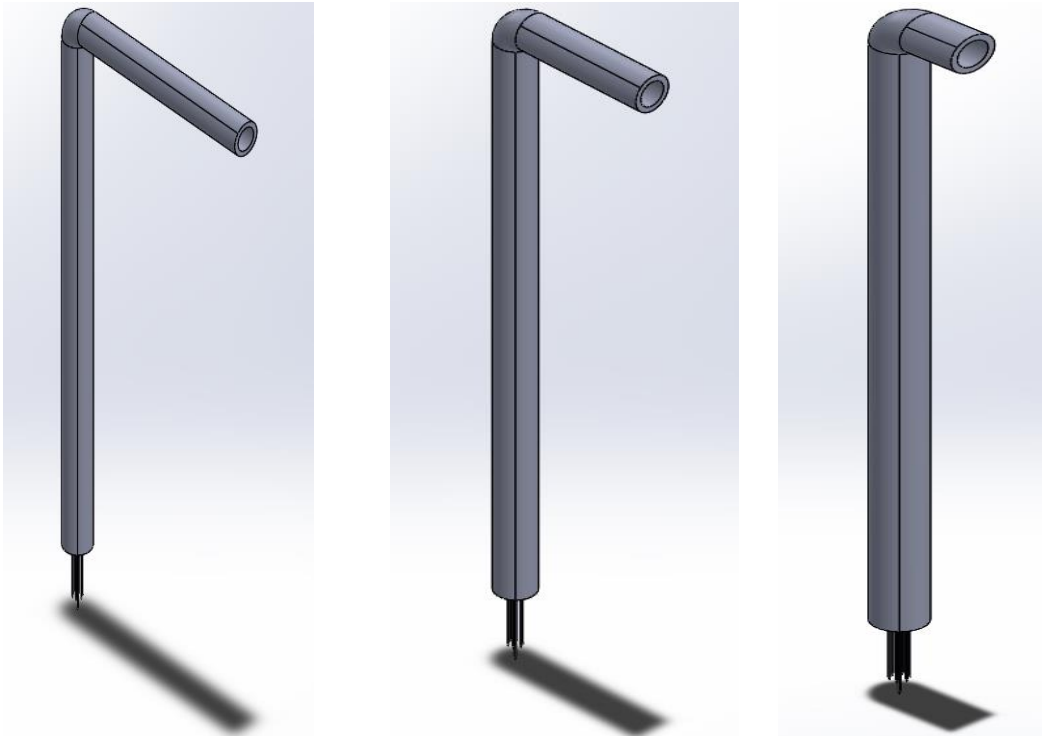

Figure 4.35. 3D probe geometries modelled at three different stem lengths of 90, 50 and 10% of the test pipe diameter.

4.8.2.1 Meshing process

The models have been meshed globally and locally as shown in Figure 4.36. A local mesh has been applied around the sensors with high mesh density to capture the amount of deflection accurately, whilst a coarse mesh applied around the rest of the probe geometry to reduce the computational time.

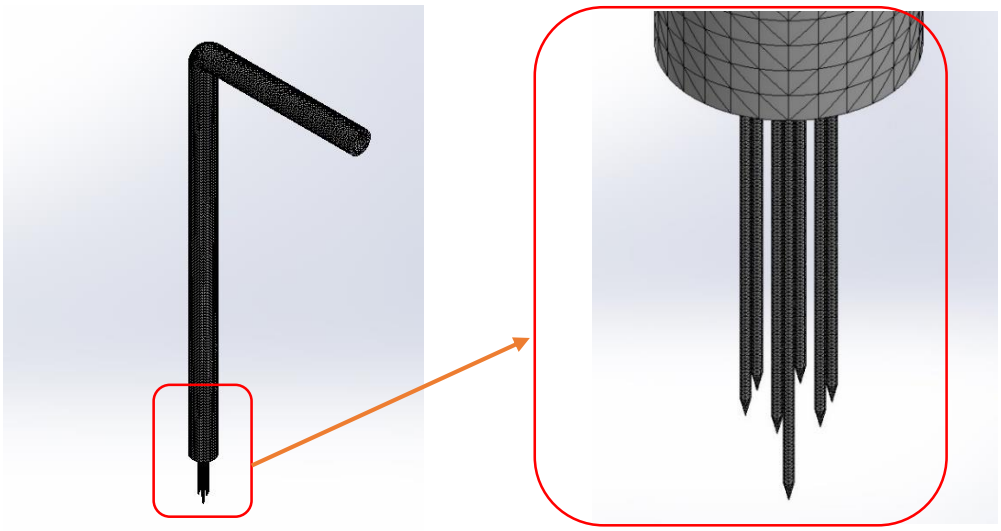

Figure 4.36. The global and local mesh application on the seven-sensor probe.

4.8.2.2 Converges analysis

One of the important steps to be conducted whilst carrying out the FEA is implementing converges analysis. Converges analysis in FEA is the process of evaluating the effect of grid size on the results' accuracy; it is similar to mesh independence test in CFD. In this process, four simulations have been carried out to quantify the right size of the mesh elements, using four mesh sizes of 39614, 47398, 56373 and 68046 elements.

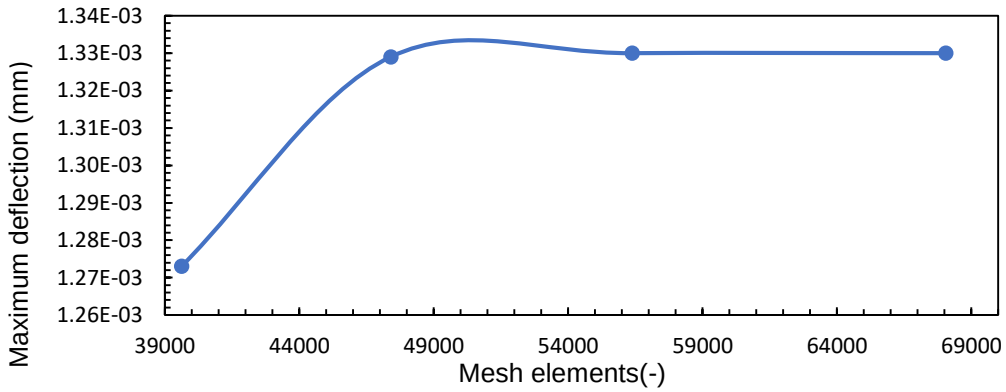

Figure 4.37. The effect of the number of mesh elements on the maximum sensor, S_1, deflection.

Figure 5.14 depicts the effect of mesh size on the maximum deflection. From this figure, it can be seen that mesh size of 56373 elements and above does not make a significant difference in the maximum sensor deflection. Therefore, 56373 elements have been adopted for the sensor displacement investigations.

4.8.2.3 Pressure application process

The static pressure, which is predicted from the CFD simulations, has been applied at each sensor and the probe body surfaces, moreover, the probe has been fully restrained at the top end of the probe body, as shown in Figure 4.38.

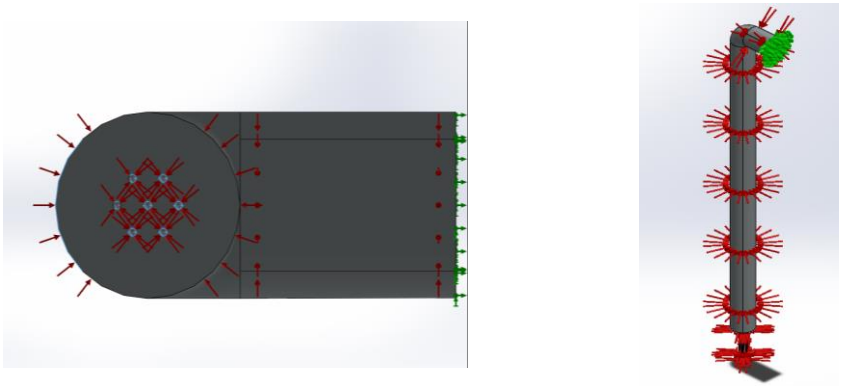

Figure 4.38. Static pressure distribution around both the seven sensors and the probe body.

The outer diameter of 6 mm chrome hollow stainless-steel tube has been used to represent the probe body that has been exposed to the fluid flow with an inner diameter of 4.2 mm, as this tube is the minimal size that can be used for the probe body. The probe has been assumed to be immersed in the flow domain by 10, 50 and 90 % of the test pipe diameter with 50 mm of probe stem downstream axial distance. Chrome stainless steel has also designated to be the material for the seven sensors, with specifications as shown in Table 4.2, the sensor diameter of 0.25 mm has been used. The reference sensor length has been 12.5 mm whereas the surrounding sensors have been of 10 mm length, to mimic the actual seven-sensor probe.

Table 4.2. The probe and the seven-sensor material specification.

Property	Value	Units
Elastic Modulus	200	GPa
Poisson's Ratio	0.28	
Shear Modulus	770	GPa
Density	7.85	Mg/m^3
Tensile Strength	413613	KPa
Yield Strength	172339	KPa
Thermal Expansion Coefficient	1.10 e-05	/K
Thermal Conductivity	18	W/(m•K)
Specific Heat	460	J/(kg•K)

After conducting the FEA, linear displacements have been predicted with reasonable accuracy. From the predicted results, the following parameters have been observed affecting the sensor deflection:

4.8.2.4 The effect of pipe diameter on sensor deflection

One of the important parameters that affect sensor deflection is the use of the conductivity probe in different pipe diameters. It can be clearly seen in Figure 4.39, that by using a conductivity probe in a larger pipe, whilst keeping the mixture velocity magnitude constant, the sensor deflection decreases, this can be concluded due to the reduction in local static pressure around the sensors with the increase of pipe diameter.

It is noticeably worth to mention here, that all figures that represent the effect of flow field variables on sensor deflection have been used sensor 1, S_1, since similar trend has been found for each flow field variables but at different values.

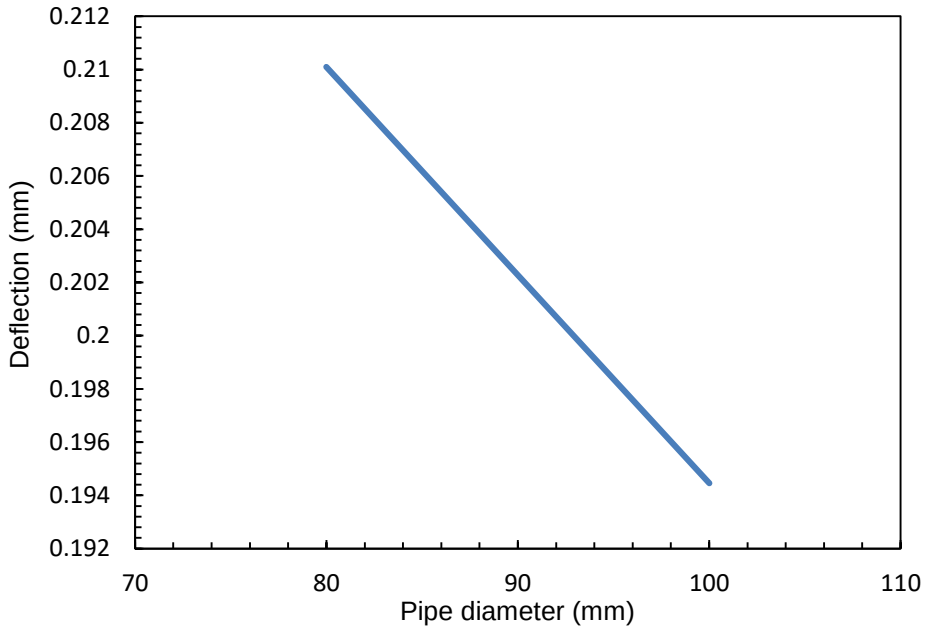

Figure 4.39. The effect of the change in pipe diameter on the sensor, S_1, deflection.

4.8.2.5 The effect of probe's radial location on sensor deflection

The effect of the probe location within the pipe has been considered in this study. From Figure 4.40, it can be clearly observed that pipe walls have significant effect on the sensor deflection. Maximum deflection can be found when the probe is close to the pipe wall, whilst almost no deflection can be found at the pipe centre-line.

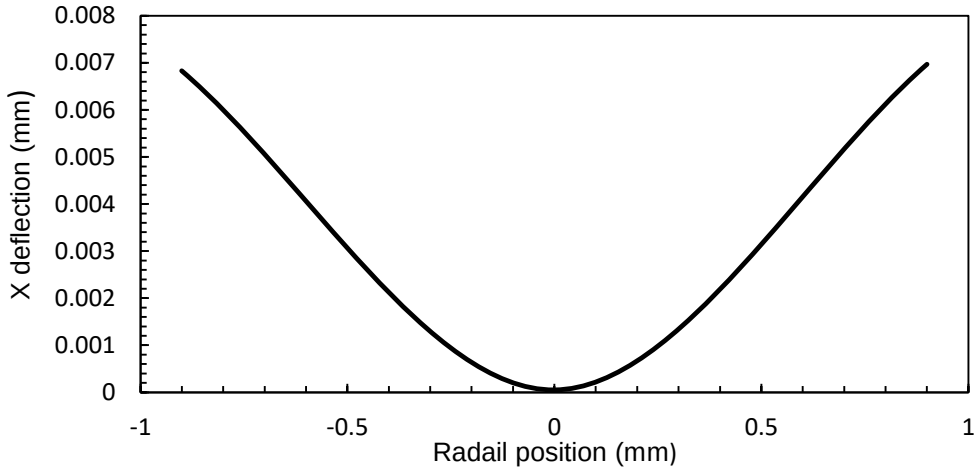

Figure 4.40. The effect of the change in radial location on the sensor, S_1, deflection, at 0.76 m/s.

However, Figure 4.40 is applicable for cases when the flow velocity is relatively low i.e. 0.76 m/s. Figure 4.41 depicts the amount of the deflection that is affected by the change in probe's radial location at high velocity of 6 m/s. It can be seen that the amount of deflection increases as the probe's stem exposed to the high-flow velocity length increases because maximum probe deflection depends on the perpendicular distance between the applied force and the probe support.

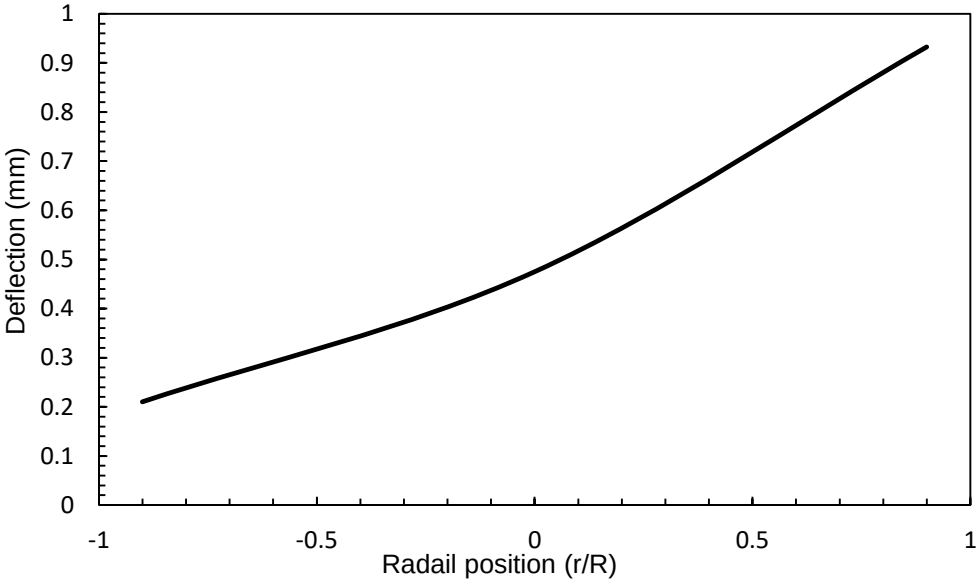

Figure 4.41. The effect of the change in radial location on the sensor, S_1, deflection, at 6 m/s.

4.8.2.6 The effect of mixture velocity on sensor deflection

Figure 4.42, depicts sensor deflection due to the increase in mixture velocity. It can be clearly observed that the increase in flow velocity increases the sensor deflection. This process occurs because of the increase in static pressure that is induced from the frictional sheer force at the sensor surface due to the high velocity.

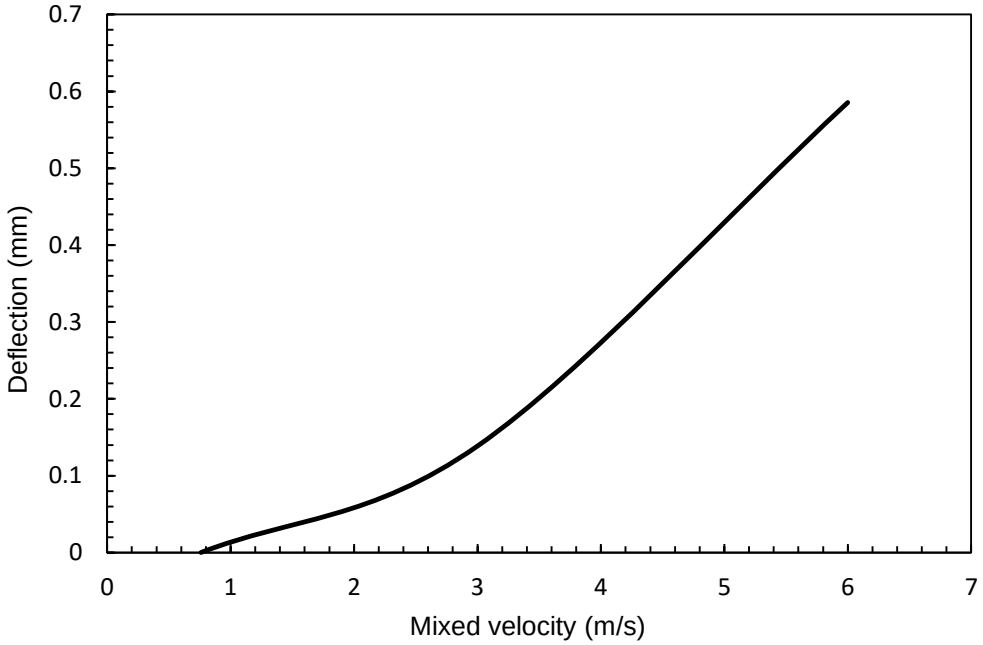

Figure 4.42. The impact of the flow mixed velocity on the sensor deflection.

From Figure 4.42, the slope of sensor deflection can be found to be higher as the conductivity probe is exposed to higher velocities. The higher velocity increases the static pressure around the sensor, in turn, increases the sensor deflection.

From the FEA results, using the nonlinear regression analysis, three-dimensional equations, x, y and z, have been developed for measuring the amount of sensors' displacement due to the variation of the flow field variables. These equations have been set in terms of Re and the radial probe location, r, within the test pipe, the variables which have been investigated. Then they have been compiled within the signal processing code to be used as a deflection-error reduction minimiser for more accurate results production. For instance, if the user provides the probe location within the test pipe, r, the flow velocity, V_{mix} , and the pipe internal diameter ID, the code automatically detects the sensor deflection at this point and retrieves the results to reduce the induced error due to the sensors deflection.

Equations from 5.5-5.22 have been prepared for the seven-sensor probe. The equations for the lead sensor have not been developed since this sensor has been considered as a reference sensor. Therefore, the deflection that has been produced by this sensor has been distributed among the auxiliary-sensors.

Sensor 1

$$S_{1x} = -0.3612 + Re * 10^{-9} + 0.0053r \quad (5.5)$$

$$S_{1y} = -3 * 10^{-6} - 8Re * 10^{-14} + 2.42r * 10^{-7} \quad (5.6)$$

$$S_{1z} = 0.0026222 - 4.4457Re * 10^{-11} + 1.1257r * 10^{-05} \quad (5.7)$$

Sensor 2

$$S_{2x} = -0.17866225 + 6.64975Re * 10^{-10} + 0.0017776r \quad (5.8)$$

$$S_{2y} = -0.000411 - 1.5Re * 10^{-12} - 6r * 10^{-06} \quad (5.9)$$

$$S_{2z} = -0.00364 + 4.17Re * 10^{-11} + 1.86r * 10^{-05} \quad (5.10)$$

Sensor 3

$$S_{3x} = -0.34975 + 9.96Re * 10^{-10} + 0.0059336r \quad (5.11)$$

$$S_{3y} = -0.0004 - 1.57Re * 10^{-12} - 5.53r * 10^{-06} \quad (5.12)$$

$$S_{3z} = -0.00375 + 4.09Re * 10^{-11} + 2.2r * 10^{-05} \quad (5.13)$$

Sensor 4

$$S_{4x} = -0.3612 + Re * 10^{-9} + 0.0053r \quad (5.14)$$

$$S_{4y} = -3 * 10^{-6} - 8Re * 10^{-14} + 2.42r * 10^{-7} \quad (5.15)$$

$$S_{4z} = 0.0026222 - 4.4457Re * 10^{-11} + 1.1257r * 10^{-05} \quad (5.16)$$

Sensor 5

$$S_{5x} = -0.17866225 + 6.64975Re * 10^{-10} + 0.0017776r \quad (5.17)$$

$$S_{5y} = -0.000411 - 1.5Re * 10^{-12} - 6r * 10^{-06} \quad (5.18)$$

$$S_{5z} = -0.00364 + 4.17Re * 10^{-11} + 1.86r * 10^{-05} \quad (5.19)$$

Sensor 6

$$S_{6x} = -0.34975 + 9.96Re * 10^{-10} + 0.0059336r \quad (5.20)$$

$$S_{6y} = -0.0004 - 1.57Re * 10^{-12} - 5.53r * 10^{-06} \quad (5.21)$$

$$S_{6z} = -0.00375 + 4.09Re * 10^{-11} + 2.2r * 10^{-05} \quad (5.22)$$

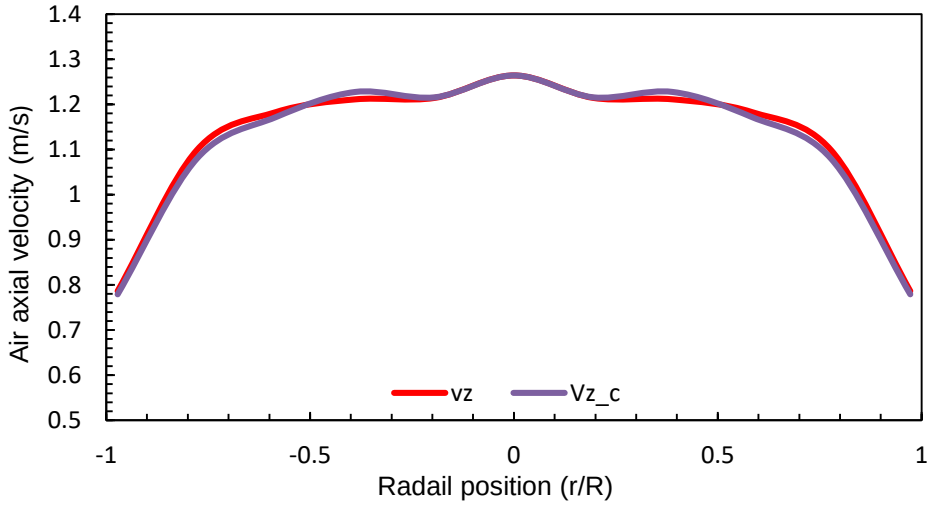

Figure 4.43. The air axial velocity without correction (vz) and with correction (vz_c).

Figure 4.43 depicts the effect of the new technique on the bubble velocity distribution. As the mixture velocity magnitude is relatively low; the effect of the sensors' deflection on the probe measurement is quite trivial. The maximum discrepancy can be found in the regions where the sensors are close to the pipe wall, whereas almost no compensation is found at the pipe central line.

4.8.3 Multi-sensor geometry factors

There are many factors that can limit the ability of multi-sensor probes to measure dispersed phase properties accurately. These factors include: the axial length, S, between the leading sensor, S_0, and the trailer sensors, the radial distance between the sensors, x, the sensor material, the sensor diameter and the mixed flow velocity. Limited publications have been found in this area; such as [130] [131] [137] [135] [140]. Mishra, et al. [135] have concluded that for 5 mm diameter droplets, when the sensors separation distances X1, X2 and X3 equal to 1 mm, the four-sensor probe can measure bubble velocity components for a maximum polar angle, α_{max}, up to about 27º. Pradhan, et al. [140] have conducted an investigation to find a relationship between the required axial separation of the sensors and the flow field characteristics. This investigation has adopted the development of a mathematical model that can be used to determine the optimum axial separation of the front sensor with respect to three rear sensors of a four-sensor probe system. The authors have concluded that the values of the axial distance increase as bubble diameter increases.

As shown above, advanced work has been carried out in this field. However, there is not a mathematical expression available in literature that helps the probe designer to quantify the relation between the bubble diameter, D_{min}, the radial distance, x, the axial distance, S; and the maximum azimuthal angle, θ. Therefore, mathematical expressions between the above-mentioned factors are required to enable the probe designer to carefully select the sensors' separation distances, axial and radial, depending on the bubble diameter and the azimuthal bubble velocity angle.

From the trigonometry relationship, as shown in Figure 4.44, between the bubble diameter, D_{min}, the radial distance, x, and the axial distance, S; the maximum azimuthal angle, θ, that the probe can be functional has been founded in terms of $\frac{S}{D_{min}}$ and $\frac{S}{X}$ as, $\theta_{Max} < \sin^{-1}\frac{S}{D_{min}}$ or $\theta_{Max} < \tan^{-1}\frac{S}{X}$

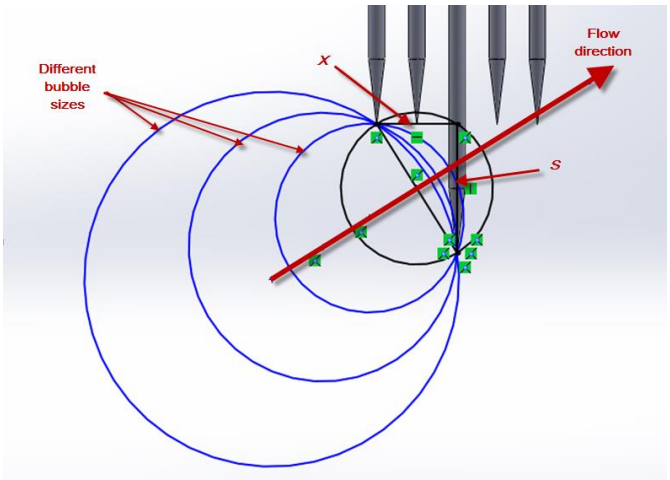

Figure 4.44. The relationship between the bubble diameter, D_{min}, the radial distance, x, and the axial distance, S between the six sensors and the reference sensor

whereas, the minimum bubble D_{min},

$$D_{min} > \begin{cases} 2x & For\ 90 - \tan^{-1}\frac{S}{X} \geq \theta \geq 0° \\ \sqrt{S^2 + X^2} & FOR\ \tan^{-1}\frac{S}{X} > \theta > 90 - \tan^{-1}\frac{S}{X} \end{cases}$$

However, S should be $\geq 0.866 D_{min}$

For instance, if we have a flowing bubble diameter which is 5 mm then the axial separation distance will be $S = 4.33$ and the radial distance can be calculated as x =1.83 mm. From the probe dimension calculation, the designer can estimate that the probe that can be used in bubbly flow with an azimuthal bubble velocity angle up to 67˚.

4.8.4 Accuracy and repeatability

4.8.4.1 The Accuracy

In order to quantify the predicted results accuracy from the CFD simulations; a comparison has been carried out between the published data of air velocity that has been measured by 4-sensor conductivity probe [140] and the CFD results, at the same boundary conditions, as shown in Figure 4.30 and Figure 4.31. The mesh number of 1045397 elements, that has been used in the CFD simulations, has produced an accuracy of 14.4353 %, which represents the accuracy of the error corrections equations.

4.8.4.2 The repeatability

The repeatability in general, is the assessing process of the variation in measurement results that is obtained from independent measurement tests under the same boundary test conditions with the same measurement method, i.e. identical test items, test rig, and the operator within a short period of time. Therefore, the repeatability of the equations has been found to be 0%; because the CFD solves the similar equations for the flow problem under the identical boundary conditions.

Chapter 5.

Discussions

The movement of the multi-dimensional interface between one phase and another is considered to be the characteristic feature of multiphase flows that makes the flow parameters predictions theoretically more difficult comparing to the single-phase flow. Therefore, experimental investigations are the key factors for providing required information for supporting and designing multiphase flows system.

There are no effective ways for measuring the bubble size and shape in two-phase flow up to now using intrusive probe, therefore, it is vital to use the novel seven-sensor probe to measure the true bubble size, and to understand the effect of this parameter on the flow regime distribution in a large pipe. In this chapter, a series of experimental tests have been carried out to quantify the effectiveness of using the novel seven sensor probe for measuring the bubble size and shape. Further, the effect of bubble size distribution on the flow regime has been investigated. Finally, the effect of gas superficial velocity on the two-phase flow properties has also been investigated.

5. Discussion

Conventionally, for designing any multiphase flows system empirical correlations are used. As it has been mentioned earlier, these empirical correlations and their assumptions have been based on the experimental measurements and observations. Therefore, in order to enrich the available characteristics of bubbly flow properties data; a variety of experimental techniques have been developed and utilized in this study, namely bubble column test, where water has been stagnant, and the air bubbles has been rising in a rectangular cross-section tank, and flow loop test, where both air and water have been flowing at a certain volume fraction and superficial velocities.

5.1 Bubble column test

The first step of using the seven-sensor probe is by assessing the measured data and validating it against an approved method. This process is essential as the seven-sensor probe uses newer system comparing to the existing conductivity probes system, which includes increasing the number of the sensors, having a new mathematical model and a new signal processing scheme. A high-speed camera method is the approved method that has been used in this study. The reason behind selecting the high-speed camera will be discussed hereafter.

For the above-mentioned reasons, three sets of flat bubble column test have been performed. Each test set has comprised of a glass water tank that has had a cross section of 210 x 210 mm, with a liquid level height of 750 mm, as shown in Figure 5.3. The air has been pressurised into the tank using an aquarium pump with maximum flow rate of 130 L/hr, through a stainless-steel tube of 4.2 mm inner diameter. The airflow rate has been controlled using a screw valve that has been attached to the air injection line. A pre-test, prior to the three tests, has been conducted to check whether seven-sensor probe is functioning, as shown in Figure 5.1.

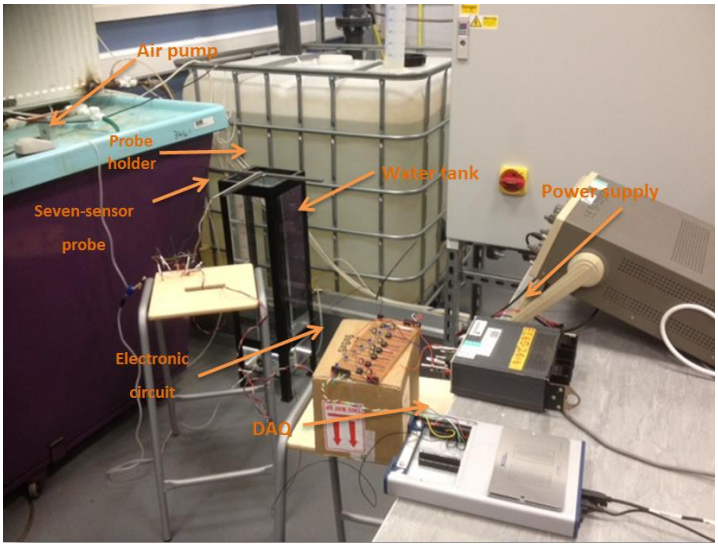

Figure 5.1. The flat bubble column test apparatus

From the pre-test, the seven-sensor probe has measured the dispersed phase properties in form of raw signals, as shown in Figure 5.2.

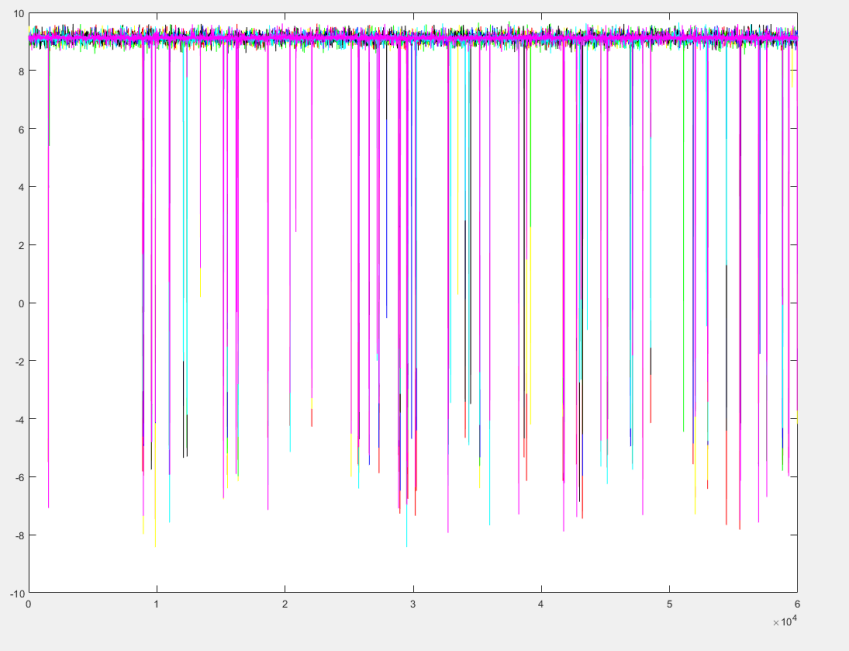

Figure 5.2. Raw signals produced by the seven-sensor probe.

From the raw signal, the dispersed flow properties have been calculated using a MATLAB code that has been developed as described earlier.

The flow field, as shown in Figure 5.3, has been described in, x, y and z, coordinate system, where the z axis is pointing upwards and the y axis is pointing to the right in the bottom horizontal plane of the front view of the tank. The fluid properties that have been used in the three tests are shown in Table 5.1

Table 5.1. Fluid properties.

At 20 ˚C	Viscosity (kg/m.s)	Density (kg/m3)
Water	0.001003	998.2
Air	1.7894e-05	1.225

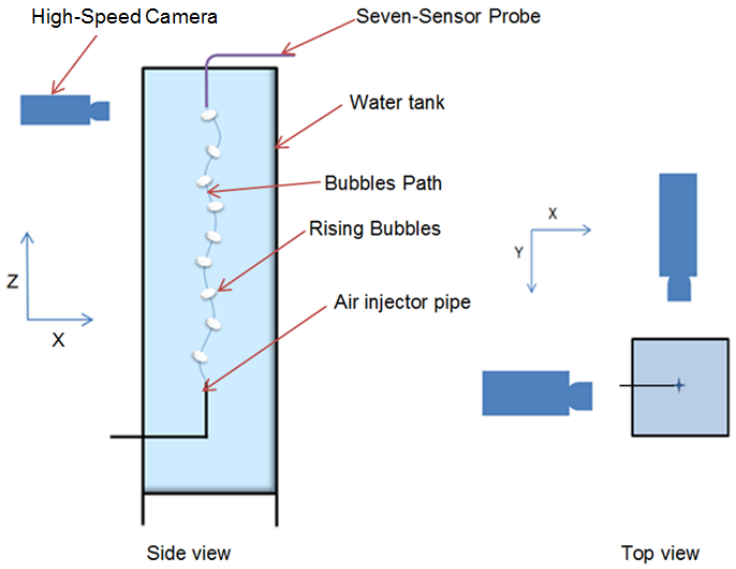

Figure 5.3. The side and top view of the test apparatus.

As it has been mentioned previously, two high-speed cameras have been employed in these tests, as shown in Figure 5.3. The two cameras have been situated perpendicularly to each other, furthermore, they have been connected and synchronised to each other, so they could capture any single bubble at the same time. One of the cameras has been denoted as a master camera, whereas the second camera has been denoted as a slave camera. Whenever the master camera starts recording, the slave camera is triggered and automatically starts recording spontaneously.

5.1.1 High-speed cameras

The novelty of the seven-sensor probe based on the bubble properties measurement from the first bubble-sensor contacts. These properties include the bubble velocity vectors, bubble size and shape and dispersed phase volume fraction. Since this probe is used for the first time, it is essential to validate and calibrate the probe against a proofed validation instrument. Therefore, a decision of using a high-speed camera as a validation means in a rectangular flat bubble column has been taken, as it has been used in most of bubble size measurement in bubble column tests by the researchers. One of the advantages of implementing high-speed camera is its ability to detect moving objects and track motion-based objects. However, for the tracking and object detection process, an appropriate code should be developed.

There are two main factors required to be taken into consideration while tracing an object in each frame, detecting the moving entity and associating the detected corresponding to the same entity over the detection time.

For the segmentation and detection of moving entity, different methods have been used. Bugeau and Pérez [170] have classified these methods into: Thresholding methods, such as Canny, log, Prewitt, Roberts and el zero-cross method, Background modelling and subtraction methods, Layer approaches methods and Saliency-based methods.

The seven-sensor probe validation and calibration process has utilised fixed cameras with a stationary background, therefore, Background Modelling and Subtraction methods have been used for the segmentation and detection of the moving bubbles, as these two methods are the most convenient method for stationary background.

The Background Modelling algorithm is based on Gaussian mixture models. For eliminating noises that are accompanied with the moving bubbles, Morphological operations have been applied to the foreground mask. Thereafter, for detecting the connected pixels groups; blob analysis has been used. The bubble detections process in each frame has been established merely on the motion of each bubble. A Kalman filter has been used to estimate the motion of each bubble path. The use of the Kalman filter function is to trace bubbles' location in each frame, and to determine the likelihood of detecting the same bubble in each frame.

5.1.2 Video processing

In general, a video clip can be defined as a sequence of still images, which captures any instance of change. Therefore, the higher number of the captured still images within a second, which is known as a frame rate, increases the chance of observing the changes occurring in the subject status more accurately. Video acquisition can be defined as the process of converting an analogue video to digital video and then saving it as one of the video file formats, such as AVI, MPEG, etc. using a high-speed camera.

The image processing process is comprised of three major steps. Firstly, recording image sequences using two off digital High-Speed Camera (Model: TS250). The use of two cameras is to capture bubble properties in two perpendicular planes, one of the planes represents the z-x coordinates, and the second plane represents z-y coordinates. Therefore, 3D shape, size and velocity components of the moving bubbles can be formulated. Both high speed cameras could capture images with frame rate up to 250 frames-per-second with a maximum image size of 640 x 480 pixel. Secondly, transferring the recorded images digitally from the high-speed camera to the PC system for the image processing using SD card. Finally, analysing and evaluating the images by using an in-house developed MATLAB code.

This code is based on image segmentation and feature extraction. In the first image processing step, the images have been transformed from the cameras' 24-bit format to an 8-bit format grey value image. The grey value image then has been converted to a matrix of 0 and 1 digits; where all dark pixels are denoted to 1 and all other pixels are 0. The Foreground Detector System object has been used to compare a colour or grayscale video frame to the background model to determine whether individual pixels are part of the background or the foreground. The code then computes a foreground mask. By using background subtraction, foreground objects can be detected in an image taken from a stationary camera. Figure 5.4 typically illustrates this process.

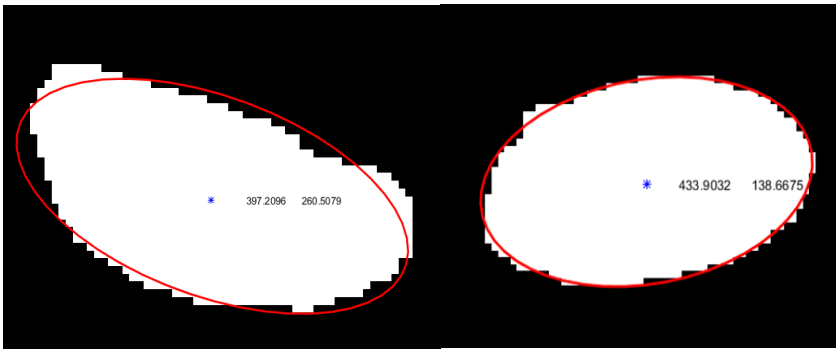

Figure 5.4. Segmented bubbles.

Thereafter, the code creates structural elements for each bubble, in the current work, a square structure has been chosen with side length of 1. For the image filtration, all connected pixels that forms components, objects, that have fewer connected pixels than N pixels, which considered as undesired objects, will be removed from the binary image using breakopen MATLAB function. NumObjects MATLAB functions have been employed for detecting and counting the connected objects within the binary image. Then, the connected pixels together form holes in the binary images; these holes, thereafter are filled using imfill function to represent the bubbles, so bubbles now are ready and prepared for their properties measurement.

From the filled objects, the properties of the desired objects have been measured within the binary image using region props function; these properties include (Area, Perimeter, Major Axis Length, Minor Axis Length, Centroid, and Orientation). With the knowledge of the bubbles centroid positions and frame rate, it is possible to measure the bubble velocity vectors.

For velocity vector calculation in y-direction V_y the following equations have been used:

$$V_y = \frac{y_b}{t_b} \tag{5.1}$$

where V_y is bubble velocity vector in y direction, y_b is the y-direction displacement of the bubble centre of gravity, this has been calculated from:

$$y_b = (y_5 - y_1) * C \tag{5.2}$$

where y_5 and y_1 are the fifth and first pixel y coordinates, whereas C is the correction factor that can be calculated as:

$$C = \frac{C_R}{C_P} \tag{5.3}$$

where C_R is the actual probe head measurement, in addition, C_P is the equivalent of C_R in pixels. The correction factor is not a constant value as it depends on many factors such as the camera resolution, the distance between the measurement field and the camera's lens, etc.

t_b is the time that needed to travel the bubble in y_b distance and can be calculated from

$$t_b = f_r / N_f \tag{5.4}$$

whereas, f_r is the video frame rate and N_f is the number of the frames.

The above equations have been used for the V_z, bubble velocity vector in the vertical direction, while using similar method has been conducted for the V_x, bubble velocity vector in the x direction, calculations.

One of the major problems that face any researcher, who is using image processing, is the light reflection phenomenon, since the reflection at a bubble surface breaks the connecting pixels that form the bubble shape. To minimise this reflection effect, a grey background has been placed at the back of each water tank side, and a halogen light has been projected at each grey background in a position that had a minimal effect on both the camera and the moving bubbles, as shown in Figure 5.5.

Figure 5.5. The bubble column test set up.

After preparing all test setups, three tests have been performed using the seven-sensor probe spontaneously with the two high-speed cameras, as shown in Figure 5.5.

5.1.3 Bubble column test 1

Before carrying out the image processing, the first frame has been taken from the test video-clip for the result accuracy inspection. With the aid of Leica Application Suite software, bubbles' major and minor axes have been measured as shown in Figure 5.6.

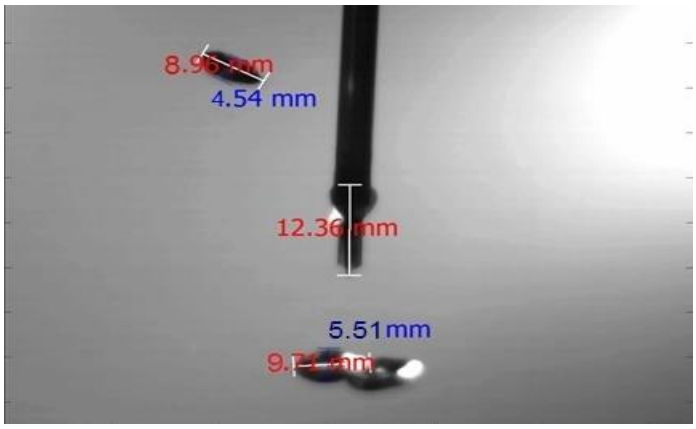

Figure 5.6. Major and minor bubble axes measurement using Leica Application Suite.

Afterward, a comparison has been made between the achieved results, regarding the major and minor axes, from the Leica software and the one, which have been obtained by the image processing code, as presented in Table 5.2. Fairly good agreement has been found between the two results. Whereas, the discrepancy in the results has been related to the image processing code; since this process measures the mean length, not the exact length, of both the major and minor axes.

Table 5.2. The test 1 results of both seven-sensor probe and high-speed cameras.

Test 1	Vx	Vy	Vz	Major Axis	Minor Axis	θ to the x-Axis	vf
Seven-Sensor	-0.02526	0.034101	0.11635	12.52	6.4313	20.04	0.00405
Speed Camera	-0.02669	0.008673	0.11386	9.9584	5.791	22.476	-

From Table 5.2, the air volume fraction of 0.405 % has been measured for 1 min running test time. The bubble inclination to the x-axis has been measured of 22.5˚ using the high-speed cameras, this generates 10.8% error in measurement comparing to same angle measured by the seven-sensor probe system.

In case of the Major Axis and Minor Axis measurement, 20.46 and 9.95 % discrepancy has been found between the probe and high-speed camera for the major and minor axis respectively. These discrepancies can be explained due to the probe coordinate measurement, as the digital microscope accuracy that has been used for probe coordinate measurement was not so high. Furthermore, the effect of the backlight, as appears in Figure 5.6, had a direct effect on the camera results, since it had caused a reflection at the edge of each bubble. In turn, the image processing code has considered the bubble size smaller than the expected size. It is clearly noticeable, from Figure 5.6, that the reflection affects the major axis measurement more than the minor axis measurement .

In case of bubble velocity in x- direction measurement, Vx, good agreement has been found between the seven-sensor probe and high-speed camera. The percentage error between the two measurements has been found so low.

In case of bubble velocity in y- direction measurement, Vy, a high discrepancy has been found between the probe and high-speed camera in case of bubble velocity vector in y direction; this can be concluded due to the inaccuracy of the probe coordinate measurement especially in y-direction. In case of bubble velocity in z- direction measurement, Vz, a good agreement has been found between the probe and high-speed camera when measuring bubble velocity vector in the axial direction. It is noteworthy, that the sensor wettability has a direct effect on the all properties measurements using the novel seven sensor probe, therefore, part of the measurement discrepancy between the high-speed camera and the seven-sensor probe can be connected to this phenomenon.

5.1.4 Bubble column test 2

In the second water test, slightly higher air fraction has been used with different light-projection angles. The results for both high-speed cameras and the seven-sensor probe have been illustrated in Table 5.3.

Table 5.3 The test 2 results of both seven-sensor probe and high-speed cameras.

Test 2	Vx	Vy	Vz	Major Axis	Minor Axis	θ to the x-Axis	vf
Seven-Sensor	-0.0076	0.0283	0.13201	7.4082	4.749	12.5	0.00565
Speed Camera	-0.0066	0.04134	0.12121	7.5367	4.2975	19.898	-

From Table 5.3, the air volume fraction of 0.565 % has been measured for 1 min running test time. The bubble inclination to the x-axis has been found to be 19.9˚ by the high-speed cameras, herein 37% error has been found comparing to the seven-sensor probe system.

In case of Major and Minor axes: 1.7 and 9.5 % measurement discrepancy has been found between the probe and high-speed cameras respectively. This has been explained due to the inaccuracy of the probe coordinate measurement. Furthermore, the effect of the backlight, as appears in Figure 5.7, had less effect on the camera's results comparing to test 1; since the halogen lights had been relocated to minimise the reflection effect at edge of each bubble. Moreover, this relocation of the halogen lights reveals that the 9.5 %discrepancy for the minor axis is kept unaffected.

In case of the Vx measurement, a high discrepancy has been found between the probe and high-speed cameras especially for bubble velocity vector in x direction. This can be explained as the water tank had been contaminated, which affected the high speed cameras' measurement for the small property values.

In case of the Vy measurement, less discrepancy has been found between the probe and high-speed cameras in case of bubble velocity vector in y direction.

In case of the Vz measurement, a good agreement has been found between the probe and high-speed cameras in case of measuring bubble velocity vector in the axial direction. This can be explained because the effect of probe coordinate measurement accuracy and the light reflection on the axial velocity measurement were so small. However, the discrepancy has increased comparing to test 1 due to the flow field contamination effect.

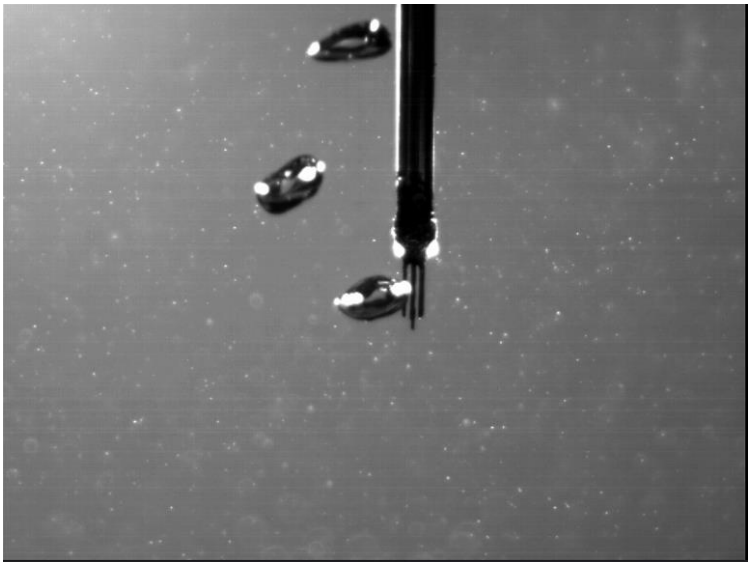

Figure 5.7. Bubble properties measurements process in test 2.

5.1.5 Bubble column test 3

In the third water test, again higher air fraction has been used with different light-projection angles. The results for both high-speed cameras and the seven-sensor probe have been illustrated in Table 5.4.

Table 5.4. The test 3 results of both seven-sensor probe and high-speed cameras.

Test 3	Vx	Vy	Vz	Major Axis	Minor Axis	θ to the x-Axis	vf
Seven-Sensor	0.06245	0.01227	0.1154	13.657	10.31	18.4	0.00564
Speed Camera	0.03087	0.03837	0.1174	11.991	6.556	19.988	-

From Table 5.4, the air volume fraction of 0.564 % has been measured for 1 min running test time. The bubble inclination to the x-axis has been found to be 19.9˚, herein 7.94% error has been found comparing to the seven-sensor probe system measurement.

In case of Major Axis and Minor Axis measurements, 12.2 and 36.4 %measurement discrepancy has been found between the probe and high-speed cameras respectively. After enhancing the test medium regarding the light reflection and water contamination, as appears in Figure 5.8; the discrepancy has increased. This can be explained due to the probe coordinate measurement accuracy and the high-speed cameras resolution, as the high-speed cameras that have been used in this test were 640 x 460 pixels.

In case of Vx and Vy measurements, a high discrepancy has been found between the probe and high-speed cameras in case of bubble velocity vector in x and y direction, however, it was lower than test 2. In case of Vz measurement, despite the inaccuracy that has been found in the other bubble properties; a good agreement has been found between the probe and high-speed cameras in case of measuring bubble velocity vector in the axial direction, which was 1.768 %.

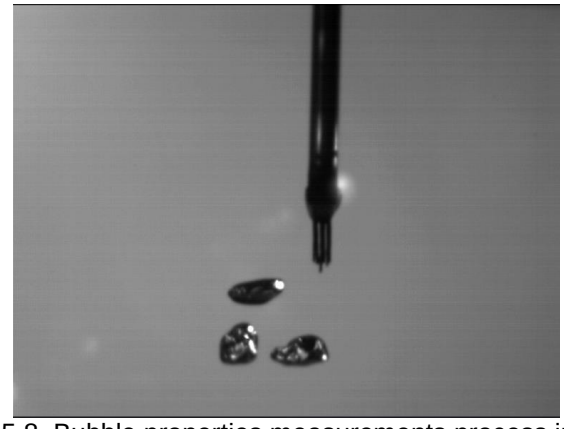

Figure 5.8. Bubble properties measurements process in test 3.

5.2 Flow loop Experiments

The local dispersed phase properties in vertical upward bubbly air–water flows measurements have been carried out. Seven-sensor probe has been used in these measurements in a vertical transparent, test section of 2000 mm long, 100 mm inner diameter, as shown in Figure 5.9. Tap water has been pumped into the test pipe from the upstream through a turbine meter that is used to measure the volumetric flow rate of water, Qw. consequently, the water phase superficial velocity, U_w, has been calculated from the obtained Qw. by

$$U_w = \frac{Q_W}{A} \tag{5.5}$$

where, A is the pipe cross-sectional area. The gas phase, which is air, has been compressed into the test section via a series of holes with diameter of 4.5 mm equally spaced distributed around the circumference of the base of the rest section. A thermal mass flow meter has been used to measure the air mass flow rate before the entering the test section. The air superficial velocity, $U_{g,}$ has been calculated using

$$U_g = \frac{Q_g}{A} \tag{5.6}$$

The reference air volume fraction α_{ref} has been obtained using a differential pressure measurement between two pressure taps, this method based on pressure compensation for the effects of frictional pressure loss. The two pressure taps have been separated axially, by a distance *h* in this study this distance has been equal to 1 m, these taps have been connected via water-filled lines, to a differential pressure transducer. As the test section in this study has been situated vertically, as mentioned previously, the magnitude of the angle θ is zero, therefore, the mean air volume fraction α_{ref} has been obtained using the following relationship

$$\alpha_{ref} = \frac{\Delta p + F}{(\rho_w - \rho_g) g h \cos\theta} \tag{5.7}$$

where, ρ_g and ρ_w represent the densities of gas and water respectively, Δp is the differential pressure, g is the acceleration due to gravity. For each flow condition investigated the frictional pressure loss, F, has been calculated using the single-phase relationship based on the Darcy formula

$$F = \frac{f\, h \rho_w (U_h)^2}{2D} \tag{5.8}$$

where, U_h is the homogeneous velocity f is a single-phase friction factor and *D* is the hydraulic diameter of the flow loop.

A fully automated two-axes traversing mechanism has been designed to mount the seven-sensor probe in. This mechanism enables the probe to be moved to any desired measurement points in a plane at a distance of 13 pipe diameters from the test section's inlet. The traverse system, allows the probe to traverse across 9 equally spaced diameters in the flow cross-section, in which data has been obtained, giving a total of 90 distinct measurement locations. Data has been acquired from the seven-sensor probe for a period of 60 sec at each measurement point. It has been not possible to obtain data at distances of less than 6 mm from the internal pipe wall; Because of probe body thickness. The volumetric flow rate has been recorded continuously during the experiments with an uncertainty of ±0.3%, as previously mentioned in chapter 4. Signal processing has been executed for interpreting the raw electrical signals into a valuable data using MATLAB code that had been prepared earlier as described in chapter 4.

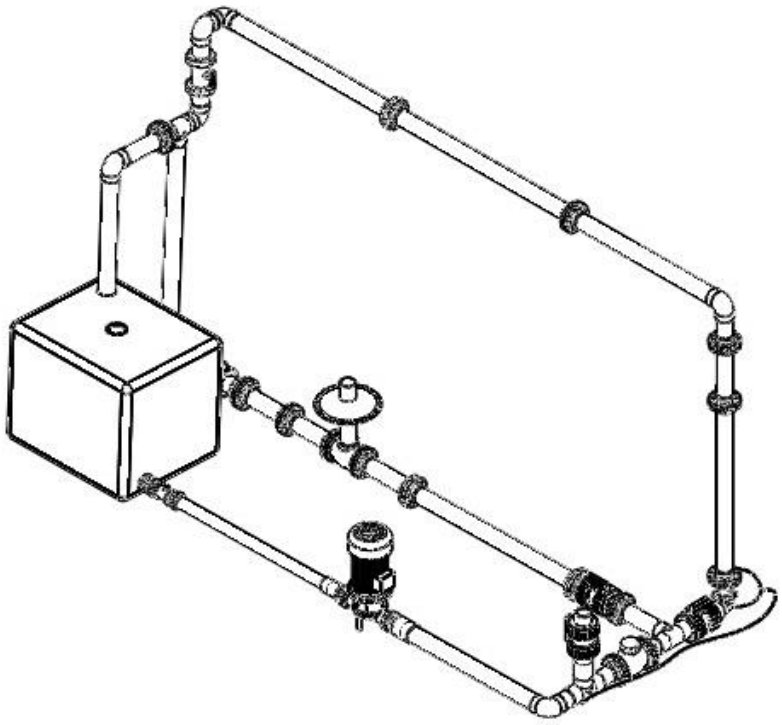

Figure 5.9. Schematic of flow loop setup.

5.2.1 The effect of sampling frequency on flow properties measurements

The seven-sensor probe has been used to collect data with a sampling frequency varying between 10-40 KHz at two sampling periods namely 30 sec and one minute to quantify the best sampling frequency that can be used for the data collection process. Wu et al. [146] proposed, for the spherical shaped bubble, a sampling rate greater than 20 KHz.

Generally, longer sampling time is required during collecting date to overcome the missing bubbles. Based on sampling frequency, the speed that is necessary to read the signal is applied. Based on the DAQ system used in the experiments limitation, the maximum sampling frequency of 280 kHz, has been used to collect the data from the seven channels simultaneously. Many factors affect the sampling frequency selection process such as the separation distance between sensors and the bubbles-sensors contact frequency. The denser the bubbles flow; the higher the sampling frequency is required. On the other hand, smaller separation distance between the sensors requires higher sampling frequency.

Sampling time-period, the time of acquiring the samples, governs the time length for which samples are collected. From the literature, 180 seconds has been found to be the appropriate sampling time-period, if the bubble frequency is low; higher sampling time-period is required. In signal processing code that has been used in this study, the sampling time-period has been chosen in such a way to ensure that at least 30 or more bubbles touch all seven sensors of the probe simultaneously.

Figure 5.10 depicts the effect of sampling frequency on the volume fraction measurement. In this investigation, four bands of frequency have been used at the same flow field conditions to quantify the effect of sampling frequency on the volume fraction measurement namely, 10, 20, 30 and 40 kHz.

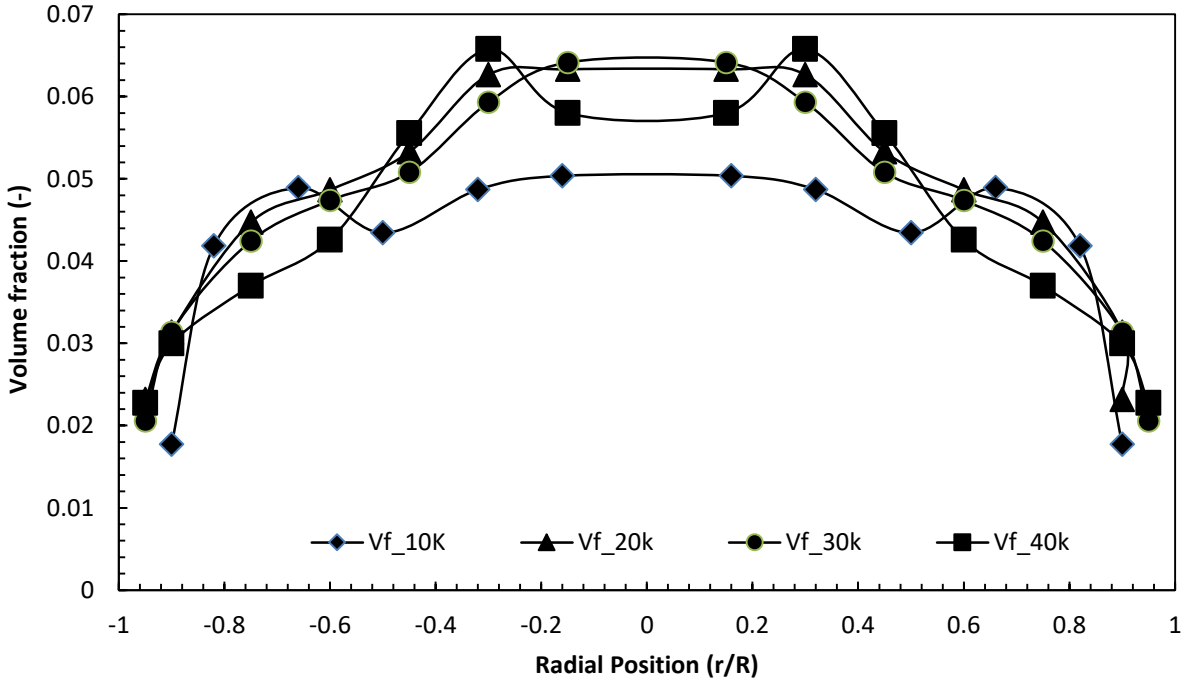

Figure 5.10. The effect of sampling frequency on the volume fraction measurement.

The first three volume fraction measurement experiments have been carried out at sampling time-period of 60 sec, whereas the latter experiment, 40 kHz, has been carried out at sampling time-period of 30 sec, due to the DAQ limitation. These investigations have been carried out, as mentioned earlier in this chapter, in a vertical riser with initial bubble diameter of 5 mm or more, the expected local gas volume fraction to be distributed in the test pipe as centre line peak, or so-call core peak pattern [50]. Therefore, it can be noticed, from the figure, that at 30 kHz data has been collected more accurately comparing to the other frequency bands. However, the 40 kHz band has been expected to present more accurate results, but this measurement has been carried out at 30 sec, this period of time in turn has not provided enough time to collect the desired data.

5.2.2 The Effect of Superficial Gas Velocity on the dispersed phase properties

The superficial gas velocity, U_g, is known as one of the significant operational variables that affects the bubbles flow dynamics of bubbly flow. Therefore, the effects of U_g on bubbles property in a vertical upward test pipe has been investigated in this study and presented.

5.2.2.1 The effect of gas superficial velocity variation on the volume fraction distribution

Valuable information on the general multiphase flows structure is based on the local volume fraction pattern knowledge. However, the internal structure of the multiphase flows is not fully reflected by the local volume fraction pattern. In bubbly flow, either a large number of small bubbles or a small number of large bubbles may obtain the same void fraction. The two cases differ from each other regarding the flow characteristics The bubble size distributions mainly depend on the operating conditions, gas and liquid phase properties and the sparger configuration [171]. Therefore, in this study, the effect of increasing air superficial velocity, which increases the number of the small bubbles, on the air volume fraction profile has been investigated experimentally.

A number of experiments has been carried out to quantify the effect of gas superficial velocity variation on the volume fraction distribution that is obtained using the seven-sensor probe as described previously. These experiments have been carried out using gas superficial velocity U_g of 0.05, 0.07 and 0.1 m/s at a fixed water superficial velocity U_w of 1 m/s, this is the maximum water velocity can be achieved from the flow loop. The mean gas volume fraction has been kept less than 0.1, to ensure bubbly flow regime during the investigations. The mean volume fraction that had been obtained from the seven-sensor has been compared with reference volume fraction for the threshold selection accuracy, as shown in Table 5.5.

Table 5.5. The comparison between the α_{mean} and the α_{ref} of each gas superficial velocity

Ug (m/s)	mean vf (-)	ref vf (-)
0.05	0.047027	0.04712
0.07	0.060117	0.06153
0.1	0.082132	0.082083

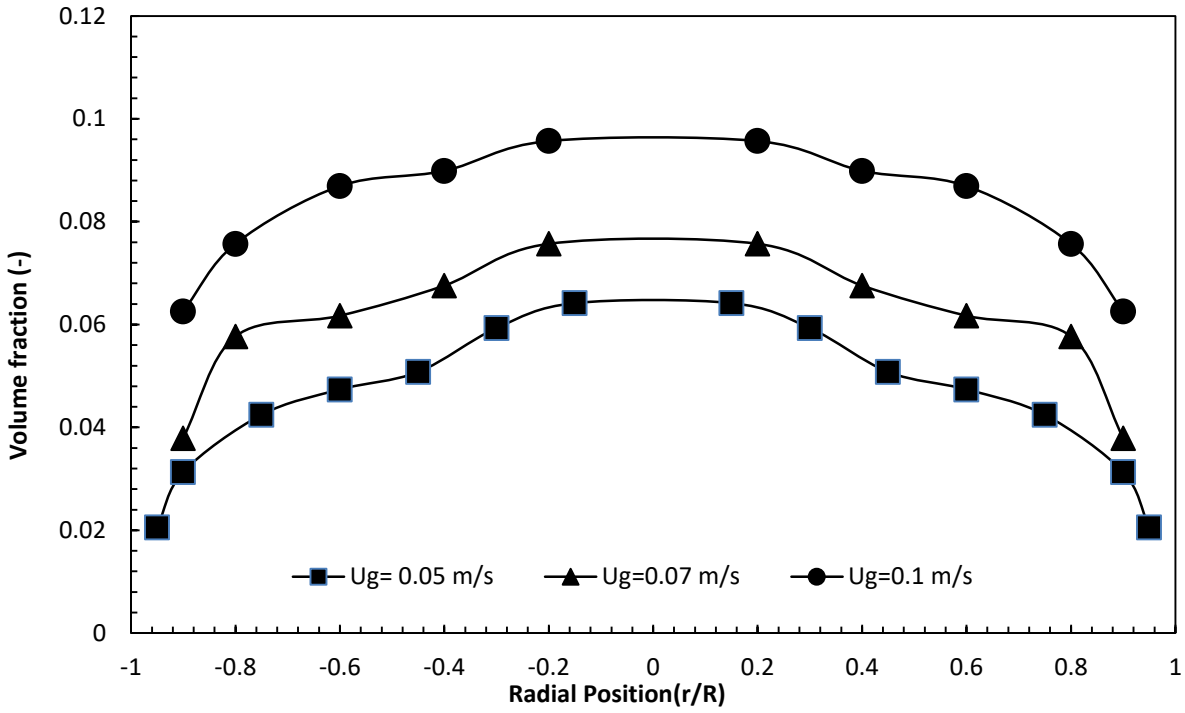

Figure 5.11. The effect of variation of air superficial velocity on the air volume fraction pattern at a constant water velocity of 1 m/s.

Figure 5.11 depicts the effect of air superficial velocity variation on the air volume-fraction pattern at a constant water velocity of 1 m/s. It has been reported that no significant wall peak is observed in these flow condition, whilst only core peak volume fraction profiles have been observed in vertical upward gas liquid two-phase flows. Similar trend has been reported by [172], for 51.2 mm internal pipe dimeter, 1 m/s water velocity and 1.2 m/s air velocity. The gradually radial changes of these profiles have also been observed in the present experiment. It has been further found that the core peak shape has been maintained in all of the cases, which means that the air volume friction core peak pattern does not change with the increase in the air superficial velocity when the flow is bubbly. These volume fraction profiles have been expected since the initial bubble diameters have been 6 mm or above.

5.2.2.2 The effect of gas superficial velocity on bubble size distribution

The gas superficial velocity has a great influence on bubble distribution across the test pipes [173]. Increasing the gas superficial velocity increases the turbulence intensity, which consequently increases bubbles coalescence and breakup rates. In case where the bubbles coalescence takes place, bubble size grows up and hence due to the wall lift force effect, bubbles tend to move towards the pipe centreline and form a centreline peak pattern. Whilst in case where bubbles breakup due to the impact of turbulent eddies and interfacial instabilities, bubbles tend to shearing-off into small bubbles from larger cap bubbles. Therefore, bubbles tend to move toward the pipe wall and form wall peak pattern.

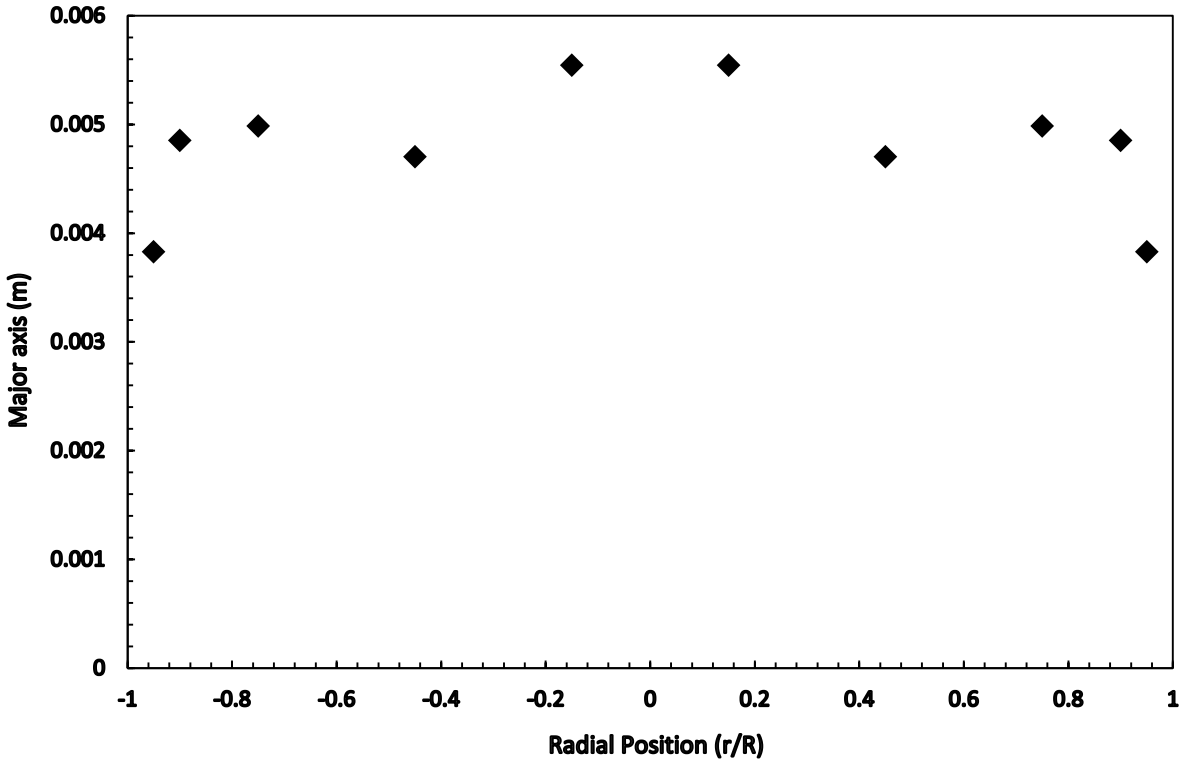

Figure.5.12. The average bubble major axis distribution along the radial position, U_g=0.05 m/s and U_l=1m/s.

Figure.5.12 depicts the average bubble major axes distribution across the test pipe, U_g=0.05 m/s and U_l=1 m/s. It can be seen that at low air superficial velocity the average bubble major-axes have been relatively small, depending on the bubble injector's orifice size, which has been almost equal to 5.8 mm which leads the effect of wall lubrication force, and turbulent force to be almost equal to the drag force. Consequently, the bubble distribution across the pipe has been nearly flat. These are in line with Tomiyama [50] finding for single bubbles, which the lift force has an inversion of the direction of at a certain critical bubble diameter of 5.8 mm [174].

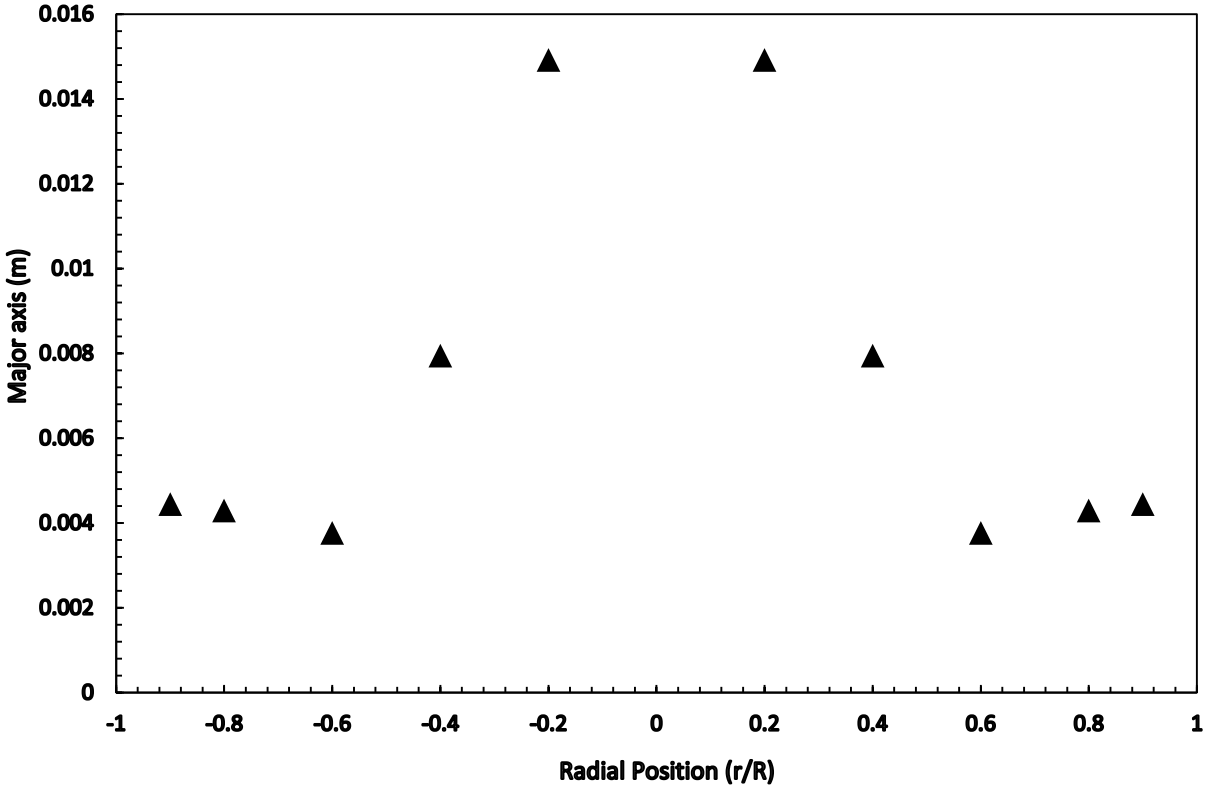

Figure 5.13. The average bubble major axes distribution along the radial position, U_g=0.07 m/s and U_l=1m/s.

Figure 5.13 depicts the average bubble major axes distribution across the test pipe, U_g=0.07 m/s and U_l=1 m/s. It is apparent from Figure 5.13 that when the air superficial velocity has increased, the average bubble major axes have increased too. The increase of bubble major axes may be the result of bubble coalescence process due to the increase of the turbulent intensity and bubble movement towards the pipe centre line and similar conclusion was obtained by [171]. Moreover, as the bubbles have flown toward higher level in the test pipe the pressure drop has decreased, which then has increased the bubble size. This in turn has enabled the lateral drag forces, wall lubrication force and turbulent force to overcome the drag force. Consequently, these lateral forces drive the bubbles with larger major axes from the wall vicinity towards the pipe centre line vicinity whilst smaller bubbles, with major axes of 5.8 mm or smaller, have maintained their position at the wall peak vicinity.

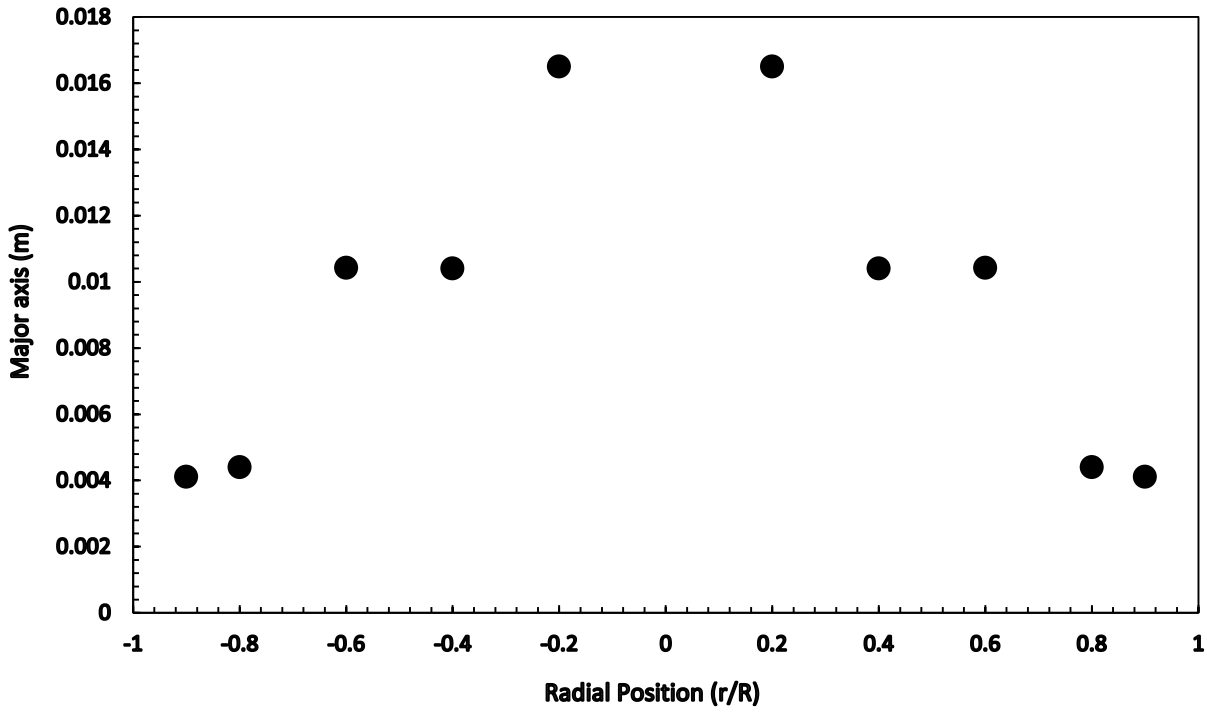

Figure 5.14. The average bubble major axes distribution along the radial position, U_g=0.1 m/s and U_l=1m/s.

Figure 5.14 depicts the *average* bubble major axes radial distribution, for U_g= 0.1 m/s and U_l =1m/s. Figure 5.14 shows by increasing the air superficial velocity, the average bubble major axes have increased. As the air superficial velocity has further increased, the turbulent intensity has further increased too in the test pipe [175]. This in turn has increased the average bubble major axes due to the increase in the bubble coalescence rate. Therefore, bubbles with larger major axes have travelled from the wall vicinity towards the pipe centre- as explained earlier. Whilst smaller bubbles, with major axes of 5.8 mm or smaller, have maintained their position at the wall peak vicinity.

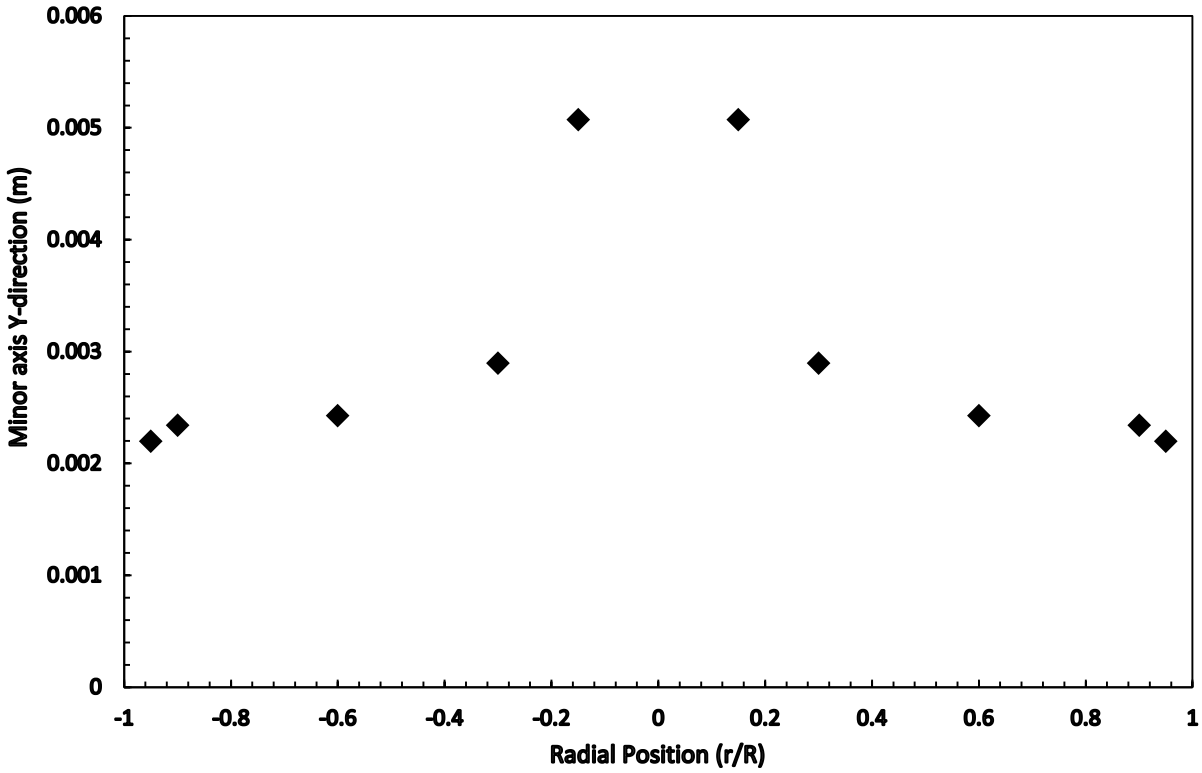

Figure 5.15. The average bubble minor axes y-direction distribution along the radial position, U_g=0.05 m/s and U_l=1m/s.

Figure 5.15 depicts the average bubble minor axes y-direction radial distribution, for U_g=0.05 m/s and U_l=1m/s. It can be seen that at low air superficial velocity the average bubble minor-axes have been relatively small. Therefore, the effects of the lateral drag forces, which are wall lubrication force, and turbulent force, have been larger than drag force. Consequently, the bubble distribution across the pipe has been centre line peaked.

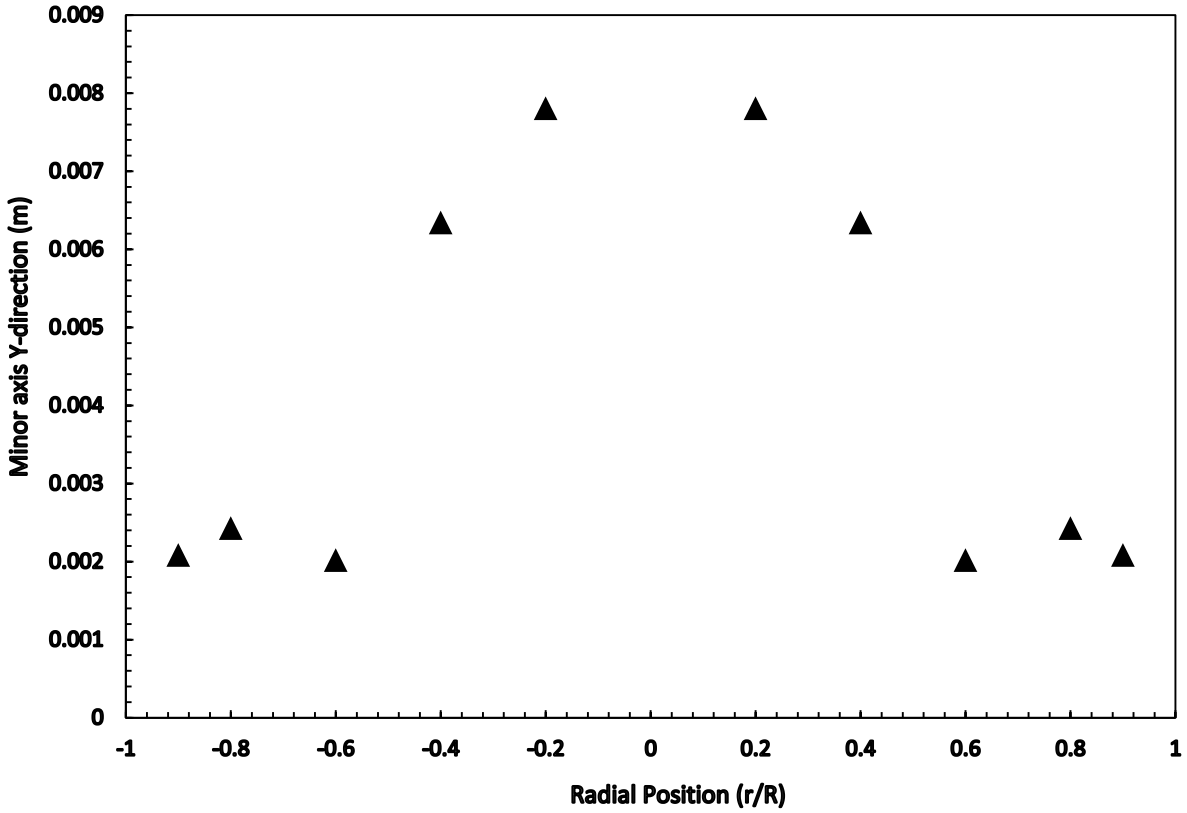

Figure 5.16. The average bubble minor axes y- direction distribution along the radial position, U_g=0.07 m/s and U_l=1 m/s.

Figure 5.16 depicts the average bubble minor axes distribution across the test pipe, U_g=0.07 m/s and U_l=1 m/s. It is apparent from Figure 5.16 that by increasing the air superficial velocity the average bubble minor axes have increased. The increase in average bubble minor axes has been referred to bubble coalescence process due to the increase of the turbulent intensity. In this figure, small bubbles, less than 5 mm major axis, have been observed to be away from the wall vicinity.

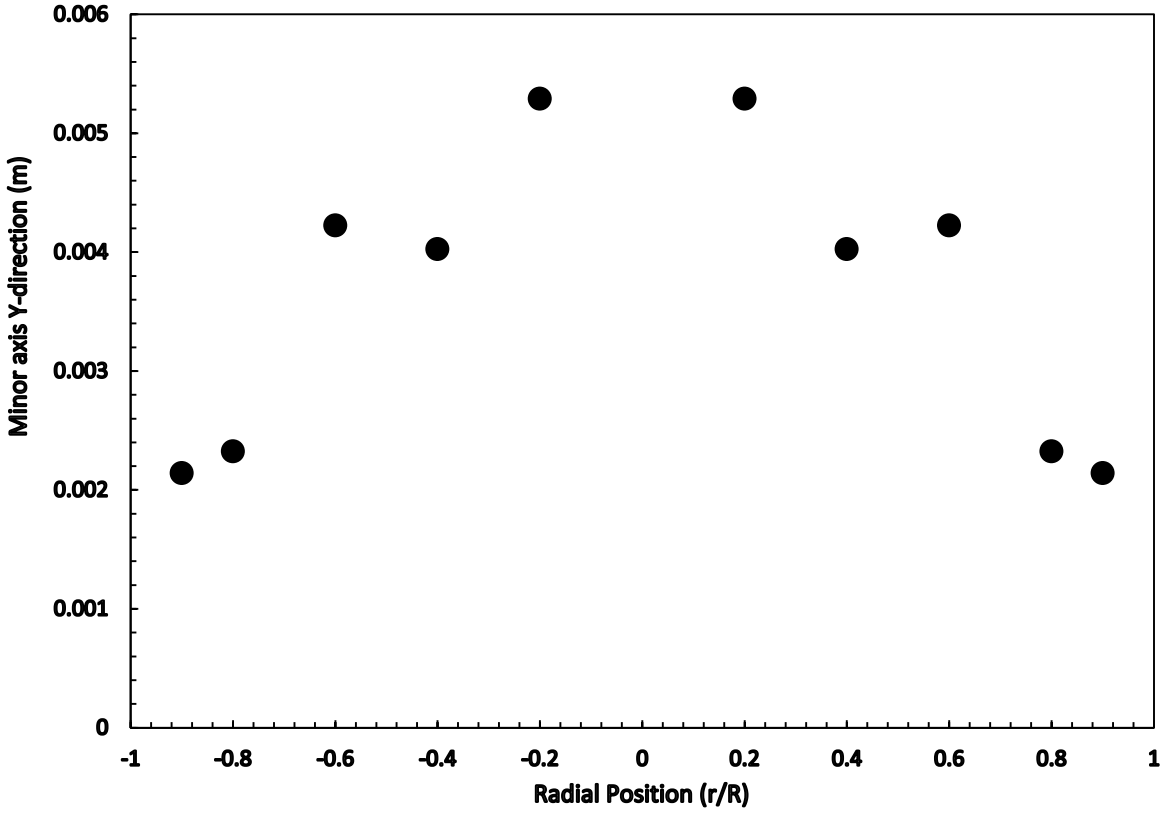

Figure 5.17. The average bubble minor axes y- direction distribution along the radial position, U_g=0.1 m/s and U_l=1m/s.

Figure 5.17 depicts the average bubble minor axes in y- direction radial distribution along the radial pipe position, for U_g=0.1 m/s and U_l=1 m/s. It is apparent from Figure 5.17 that by increasing air superficial velocity; the average bubble minor axes have further increased. As the air superficial has further increased, the turbulent intensity around the bubble has increased in the test pipe, which in turn has increased the bubble coalescence rate consequently the bubble minor axes increased. Therefore, the bubbles with larger minor axes have travelled from the wall vicinity towards the pipe centre-line as explained earlier, whilst smaller bubbles have maintained in their position at the wall peak vicinity.

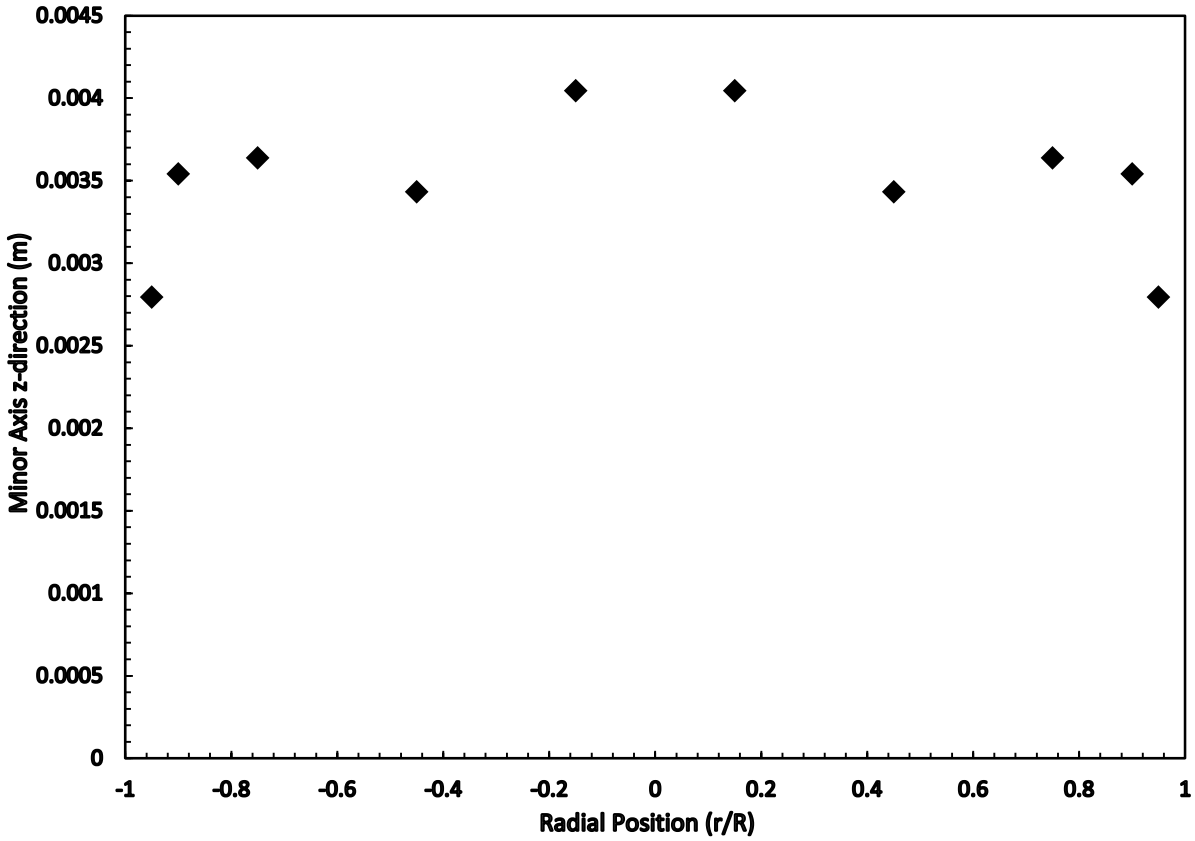

Figure 5.18. The average bubble minor axes Z-direction distribution along the radial position, U_g=0.05 m/s and U_l=1m/s.

Figure 5.18 depicts the average bubble minor axes in Z-direction along the radial pipe position, U_g=0.05 m/s and U_l=1m/s. It can be seen that at low air superficial velocity the average bubble minor-axes have been relatively small. This in turn leads the lateral drag forces, which are wall lubrication force, and turbulent force, to overcome the drag force. Consequently, the bubble distribution across the pipe became centre line peaked. Finally, similar trend to major axis has been found with smaller value due to the effect of virtual mass force and the static pressure.

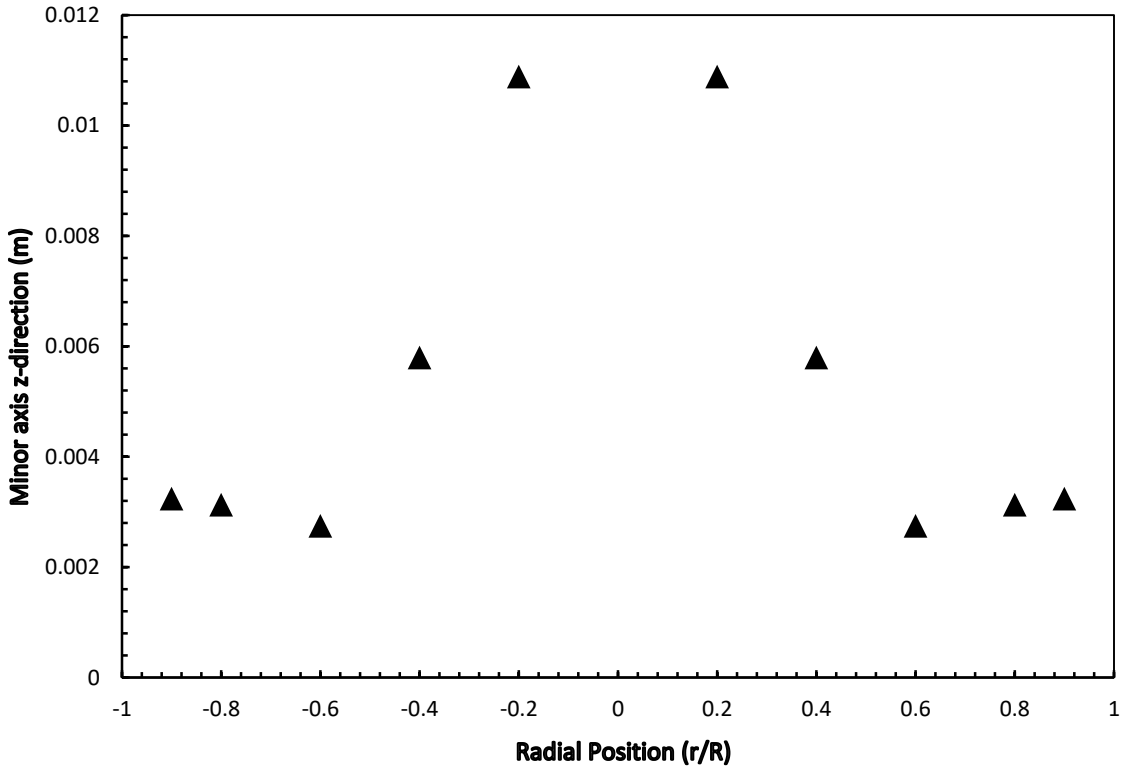

Figure 5.19. The average bubble minor axes z- direction distribution along the radial position, U_g=0.07 m/s and U_l=1 m/s.

Figure 5.19 predicts the average bubble minor axes z- direction distribution along the radial pipe position, U_g=0.07 m/s and U_l=1 m/s. It is clearly noticed from Figure 5.19 that by increasing the air superficial velocity the average bubble minor axes along z- direction increases. The increase in average bubble minor axes along z- direction referrers to the bubble coalescence process due to the increase of the turbulent intensity.

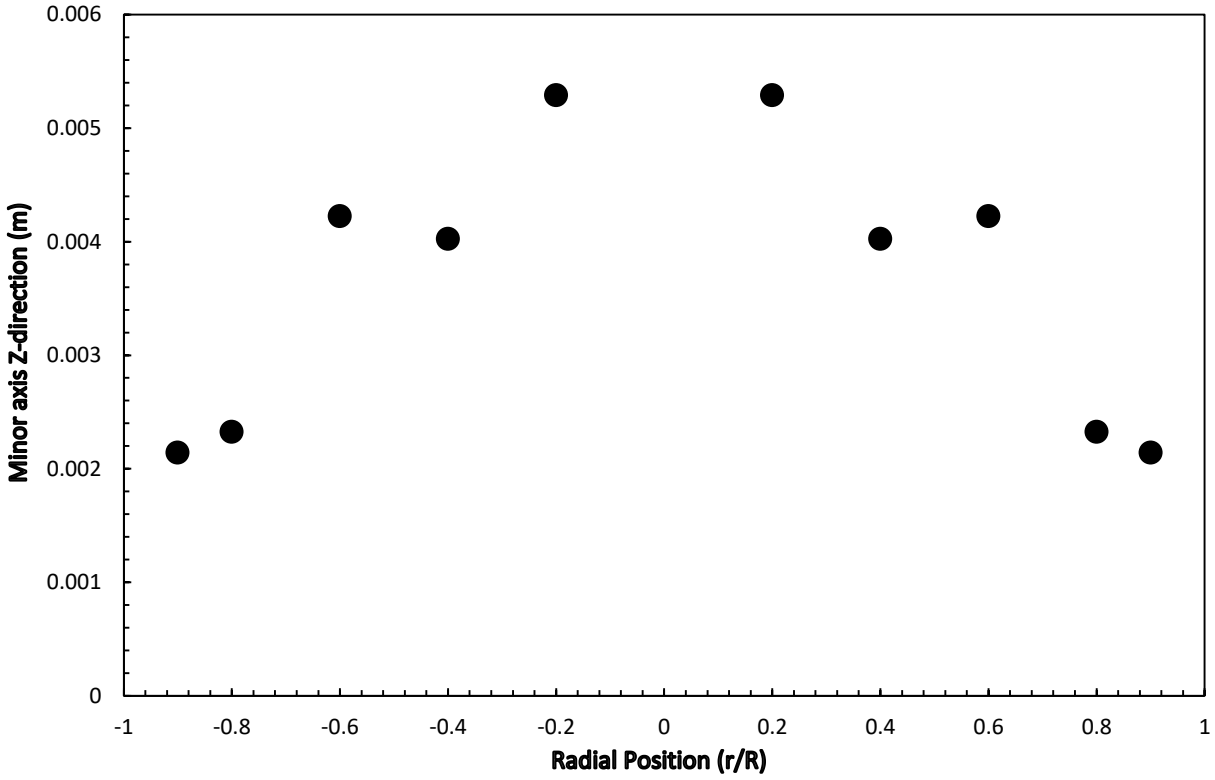

Figure 5.20. The average bubble minor axes z- direction distribution along the radial position, U_g=0.1 m/s and U_l=1m/s.

Figure 5.20 depicts the average bubble minor axes in z- direction radial distribution, for U_g=0.1 m/s and U_l=1 m/s. It is apparent from Figure 5.20 that by increasing air superficial velocity; the average bubble minor axes have further increased. As the air superficial has further increased, the turbulent intensity around the bubble has increased in the test pipe, which in turn has increased the bubble coalescence rate consequently the bubble minor axes increased. Therefore, the bubbles with larger minor axes have travelled from the wall vicinity towards the pipe centre-line vicinity as explained earlier, whilst smaller bubbles have maintained in their position at the wall peak vicinity. Finally, similar trend to major axis has been found, however, the bubble minor axes in Z-direction value is smaller due to the effect of virtual mass force and the static pressure.

5.2.2.3 The effect of gas superficial velocity on the local gas velocity distribution

The gas superficial velocity has a direct effect on the local air velocity profile. This is true, due to the effect of the air superficial velocity on the bubble size, as mentioned in the previous part in this chapter; this in turn increases the bubble velocity.

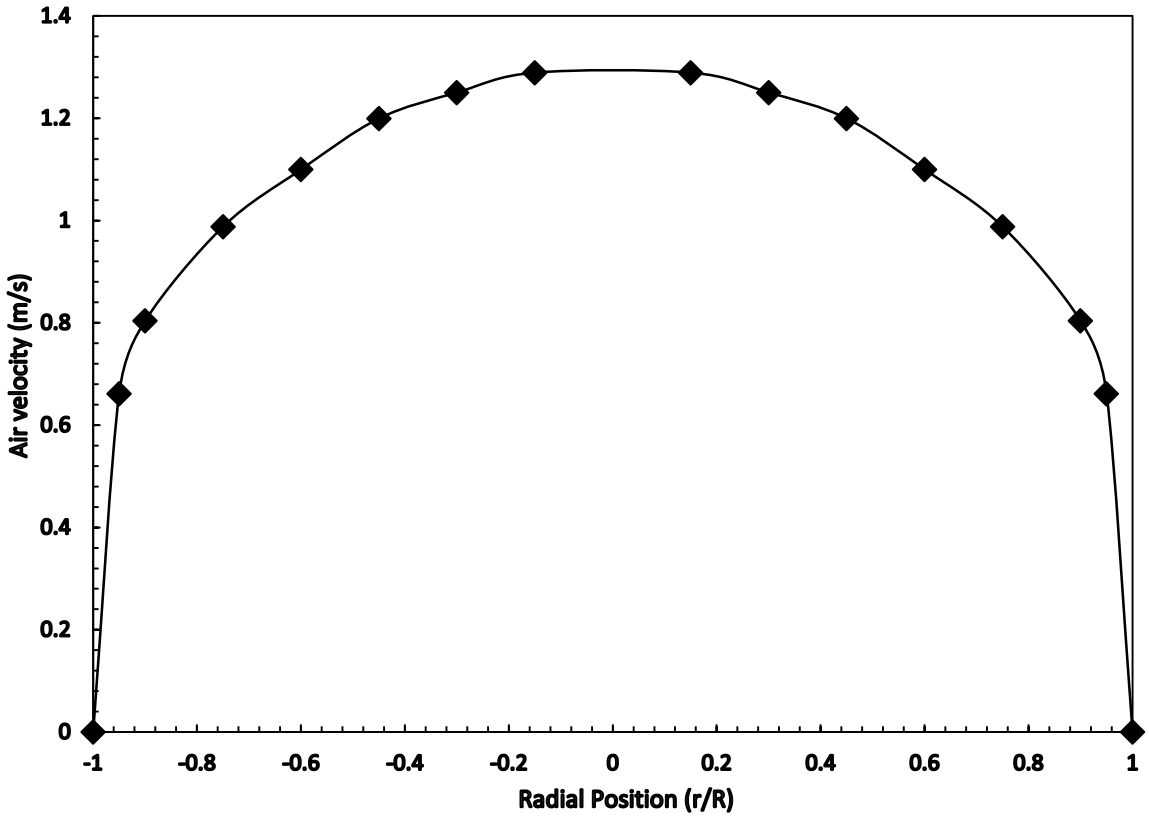

Figure 5.21. The bubble velocity distribution along the radial position, U_g=0.05 m/s and U_l=1m/s.

Figure 5.21 depicts the bubble velocity radial distribution, at U_g=0.05 m/s and U_l=1 m/s. It is apparent from Figure 5.21, that the measured axial air velocity profiles are much flatter than the volume fraction profiles shown in Figure 5.21. It is also apparent that higher bubble local velocity has been found at the pipe centre.

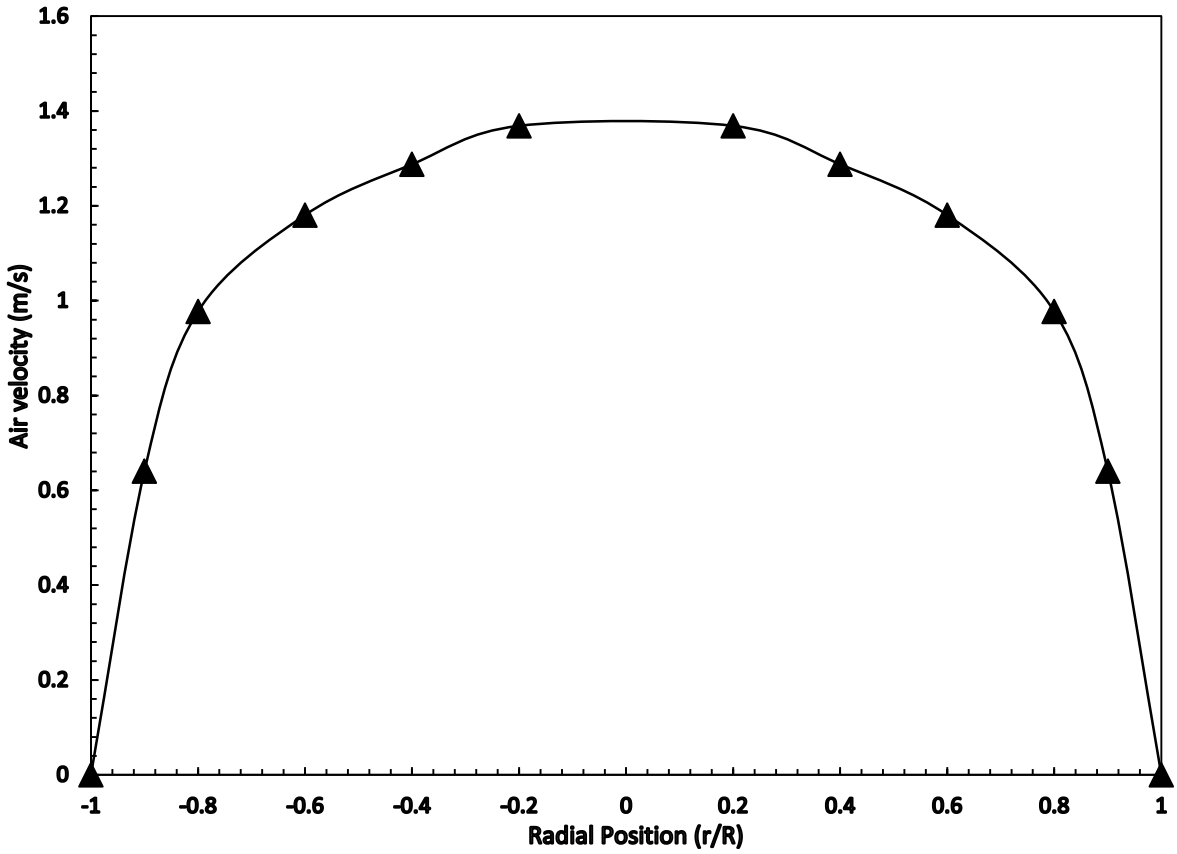

Figure 5.22. The bubble velocity distribution along the radial position, U_g=0.07 m/s and U_l=1m/s.

Figure 5.22 depicts the bubble velocity radial distribution across the test pipe, U_g=0.07 m/s and U_l=1 m/s. It can be seen that by increasing the air superficial velocity the local bubble velocity has increased. As it has been mentioned previously, that the higher bubble velocity has been found at the pipe centre line vicinity, this can be concluded due to location of the large bubble in the centre line vicinity.

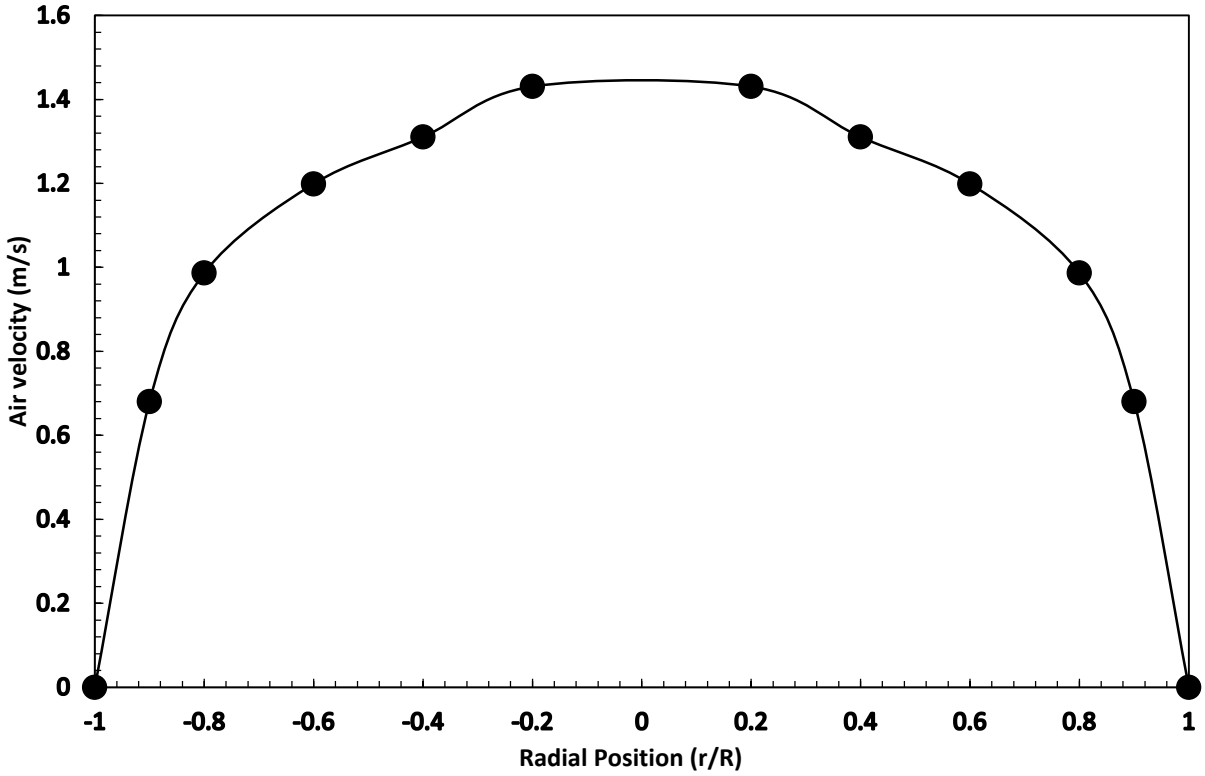

Figure 5.23. The bubble velocity distribution along the radial position, U_g=0.1 m/s and U_l=1m/s.

Figure 5.23 depicts the bubble velocity radial distribution across the test pipe, U_g=0.1 m/s and U_l=1 m/s. It can be noticed that by further increasing the air superficial velocity the local bubble velocity has increased. In addition, the local bubble velocity tends to form parabolic shape with steeper gradient. This can be concluded due to the high difference between the bubble size at the pipe centre and the bubbles close to the pipe wall.

5.2.2.4 The effect of gas superficial velocity on the local Azimuthal bubble velocity

Generally, the bubbles do not move in axial-direction only due to several factors, such as the drag force, wall effect, turbulent effect etc. Therefore, bubble in motion has three velocity vector components, namely axial, radial and azimuthal velocity components.

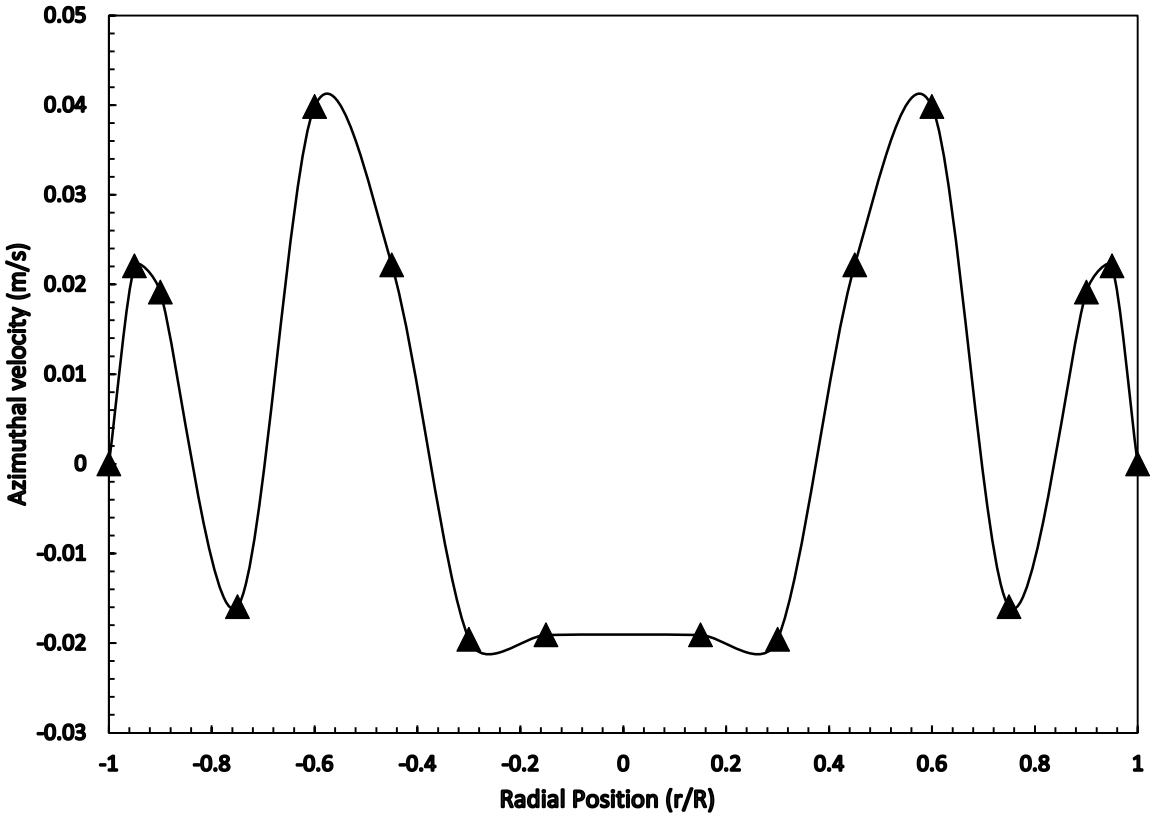

Figure 5.24. The bubble azimuthal velocity distribution along the radial position, U_g=0.05 m/s and U_l=1 m/s.

Figure 5.24 depicts the bubble azimuthal velocity distribution across the test pipe, at U_g=0.05 m/s and U_l=1m/s. It can be noticed that the azimuthal velocity value is quite small; it ranges between -0.03 to 0.05 m/s. In addition, it can be noticed that the peak azimuthal velocity of 0.04 m/s has located in the vicinity close to the pipe wall. It is apparent that the azimuthal velocity has symmetrical distributed across the test pipe section and fluctuated around zero magnitude.

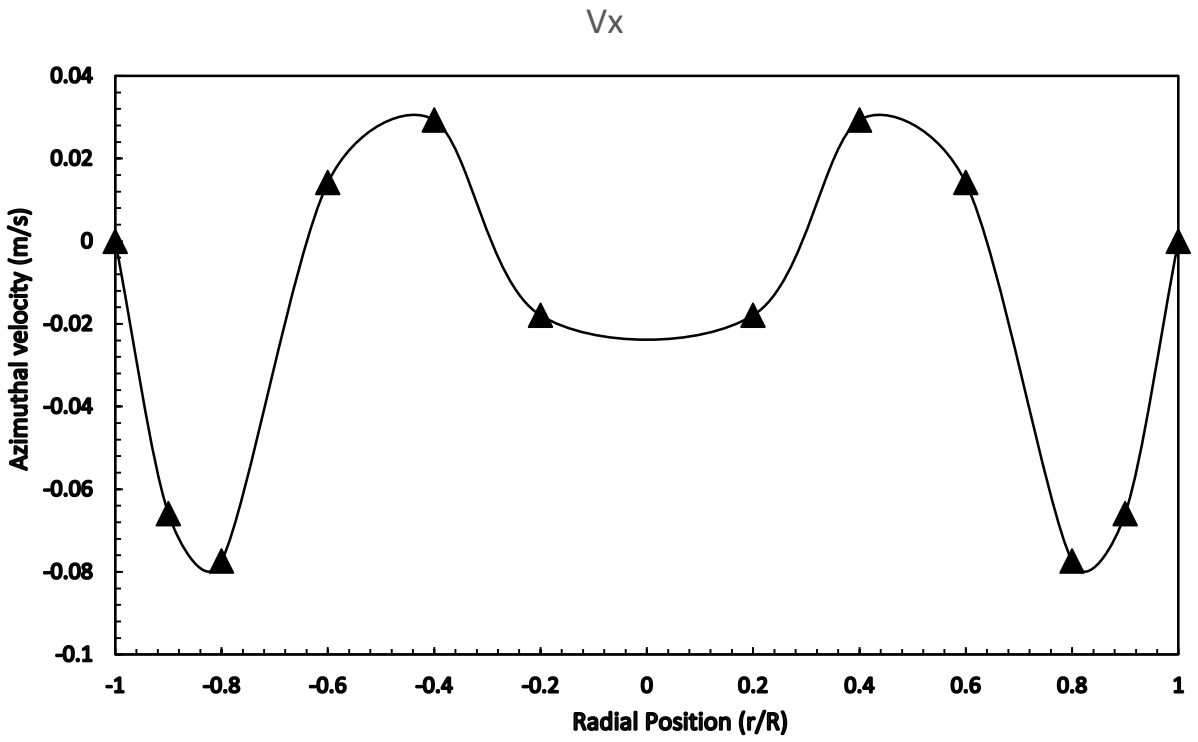

Figure 5.25. The bubble azimuthal velocity distribution along the radial position, U_g=0.07 m/s and U_l=1 m/s.

Figure 5.25 depicts the bubble azimuthal velocity radial distribution across the test pipe, U_g=0.07 m/s and U_l=1 m/s. It can be seen that by increasing the air superficial velocity the azimuthal velocity has increased in the wall vicinity whilst decreased in the vicinity of pipe centre. It can also be seen that the azimuthal velocity fluctuation has decreased when the air superficial velocity increased.

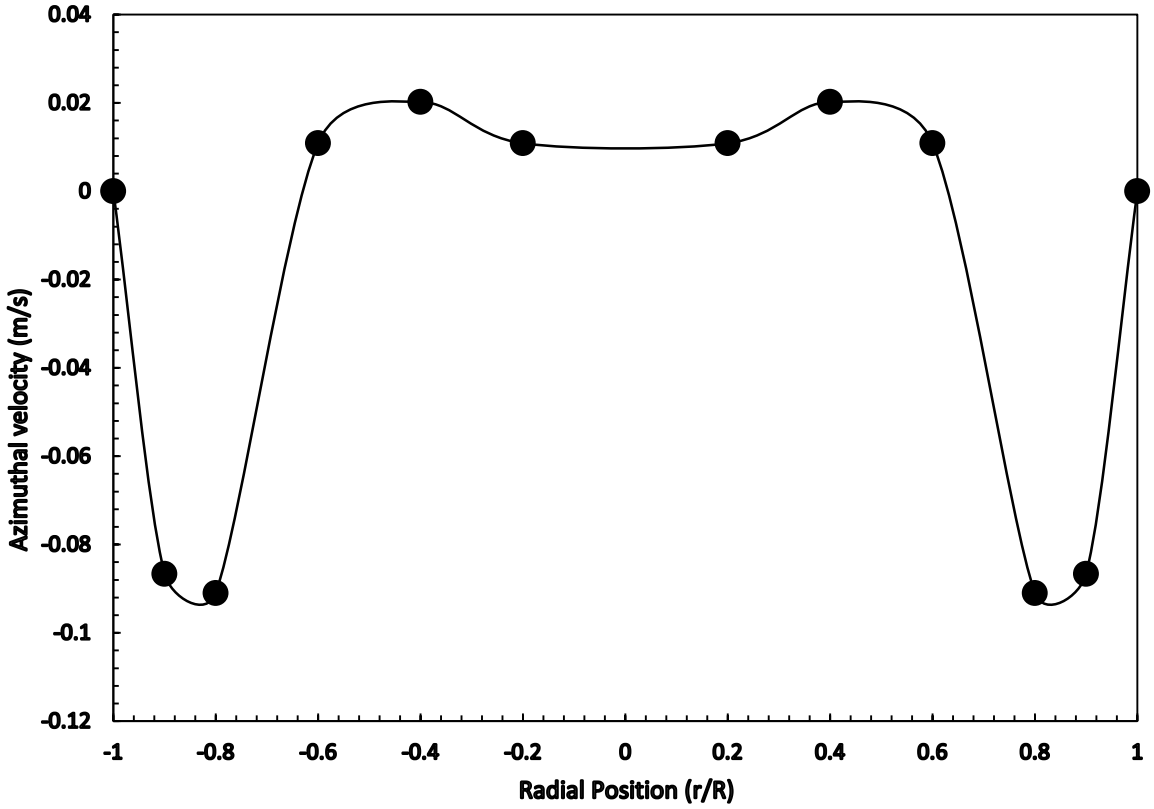

Figure 5.26. The bubble azimuthal velocity distribution along the radial position, U_g=0.1 m/s and U_l=1 m/s.

Figure 5.26 depicts the bubble azimuthal velocity distribution across the test pipe, for U_g=0.1 m/s and U_l=1 m/s. It is apparent that by further increasing the air superficial velocity the azimuthal velocity has further increased in the wall vicinity, whilst it has decreased in the pipe centre vicinity. It is also apparent that the azimuthal velocity profile has been flatter at the pipe centre vicinity. From the three experimental tests, it can be concluded that the magnitude of the azimuthal velocity has been relatively small. Moreover, by increasing the air superficial velocity the bubble azimuthal velocity has increased and the peak velocity has migrated from the pipe centre- line vicinity towards the wall zone. Furthermore, the azimuthal velocity fluctuation has been decreased with the increase in air superficial velocity.

5.2.2.5 The effect of gas superficial velocity on the local radial bubble velocity distribution

The bubble radial velocity vector is the velocity that directs the bubble motion radially. This velocity vector is directly related to the bubble size [50], i.e. bubble diameter; as the bubble diameter increases the lateral forces such as wall lubrication force and turbulent dissipation force increase and direct the radial velocity vector towards the pipe centre line. Whilst as the bubble diameter decreases the lateral forces decrease, consequently the bubble vector directs towards the pipe wall.

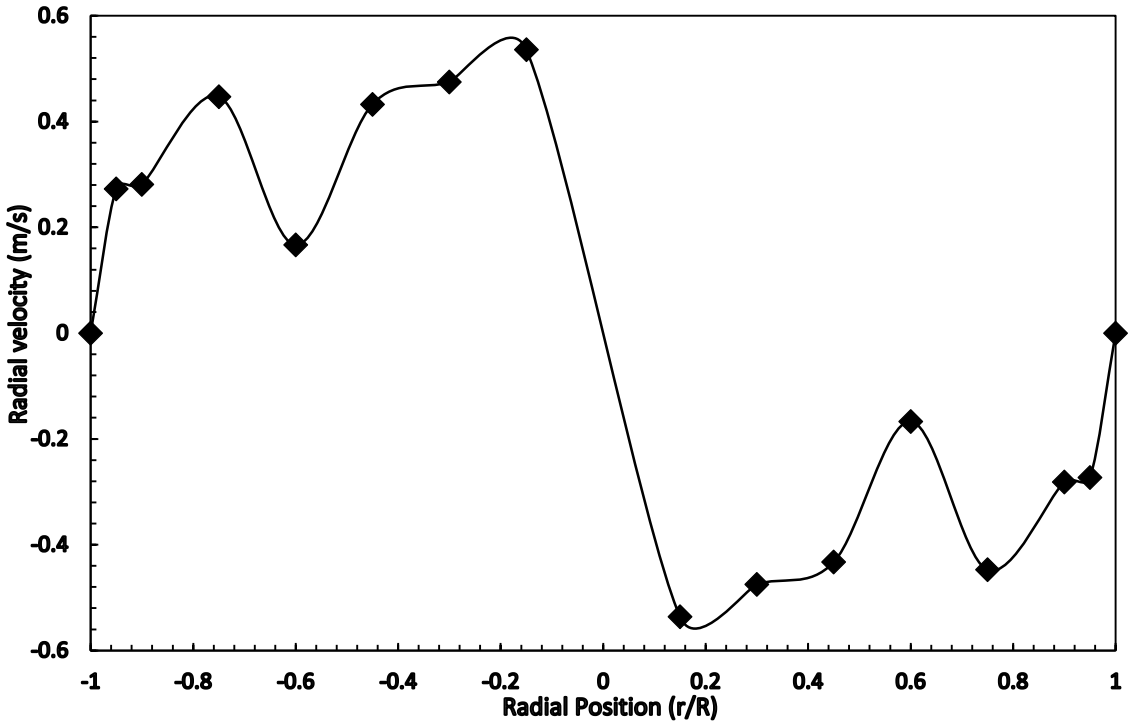

Figure 5.27. The bubble radial-velocity distribution along the radial position, U_g=0.05 m/s and U_l=1m/s.

Figure 5.27 depicts the bubble radial velocity distribution across the test pipe, for U_g=0.05 m/s and U_l=1m/s. It can be seen that the radial velocity has larger effect on the bubble trajectory than the azimuthal velocity. Furthermore, the bubble radial velocity has been found to be higher in the vicinity close to the pipe wall. This can be concluded due to the bubble tendency to move from the wall region towards the pipe centre line. It can also be seen that the radial velocity has been symmetrical distributed in value but in opposite sign, since the bubbles direction has been towards the pipe centreline.

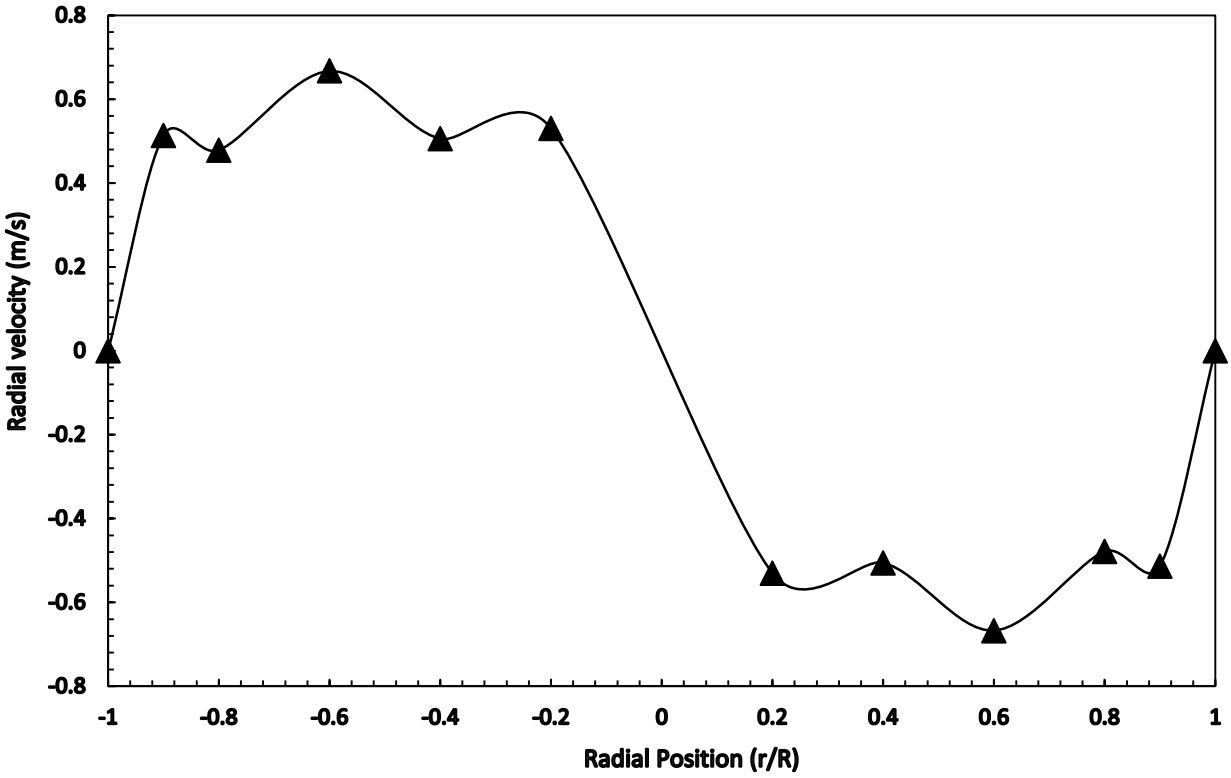

Figure 5.28. The bubble radial velocity distribution along the radial position, U_g=0.07 m/s and U_l=1m/s.

Figure 5.28 depicts the bubble radial velocity distribution across the test pipe, for U_g=0.07 m/s and U_l=1m/s. It is apparent that by increasing the air superficial velocity the bubble radial velocity in the near wall region has increased whilst the radial velocity in pipe centre region has not increased. It is also obvious that by increasing the air superficial velocity near the wall region the bubble radial velocity tends to take flatter distribution comparing to Figure 5.27. The interesting phenomenon that can be observed is the peak radial velocity profile has been found close to the wall vicinity, which can be the result of the transition of the bubble diameter from small diameter to larger than 5.8 mm [50].

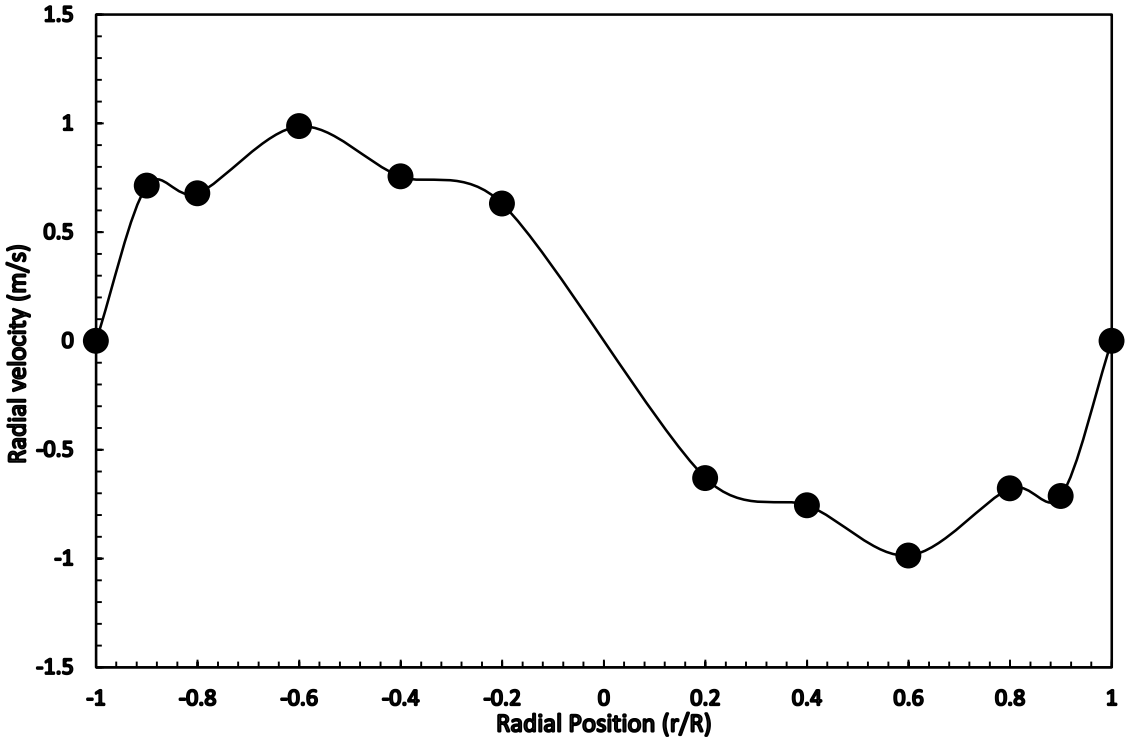

Figure 5.29. The bubble radial velocity distribution along the radial position, U_g=0.1 m/s and U_l=1 m/s.

Figure 5.29 depicts the bubble radial velocity distribution across the test pipe, for U_g=0.1 m/s and U_l=1 m/s. It can be seen that by further increasing the air superficial velocity the bubble radial velocity in the near wall region has increased too, whilst the radial velocity in pipe centre region has reduced. It is also apparent that by increasing the air superficial velocity, at near the wall region, the bubble radial velocity tends to take flatter distribution as comparing to Figure 5.28. The peak radial velocity profile close to the wall vicinity also has been observed. However, the magnitude of the peak velocity has been found higher than the case of 0.07 m/s of air superficial velocity.

5.2.2.6 The effect of gas superficial velocity on the bubble inclination angles, α, distribution across the test pipe

Bubble inclination angle, α, is the polar angle between the z-axis and the bubble axial velocity vector. This angle represents bubble direction with reference to the reference sensor S_0. It has been found that α has a proportional relation with the air superficial velocity whilst keeping the water velocity constant. This will be discussed in depth in each figure below.

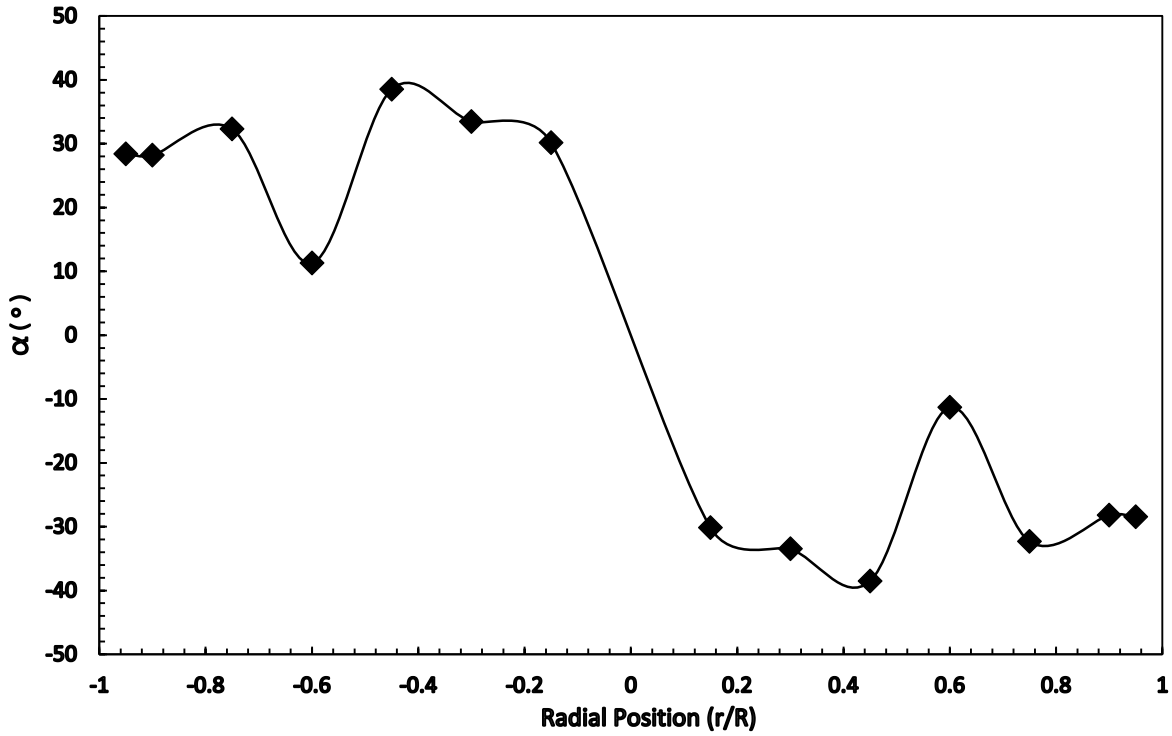

Figure 5.30. The bubble polar angles, α, distribution along the radial position, U_g=0.05 m/s and U_l=1 m/s.

Figure 5.30 depicts the polar angles distribution across the test pipe, U_g=0.05 m/s and U_l=1 m/s. It can be seen that the polar angle, α, value fluctuating in the near wall region. This has been concluded due to the effect of the imbalanced wall lubrication, wall lift force, and the drag force on the small bubbles, which forces the bubbles that have had a critical diameter, 5 mm, to fluctuate in their movement toward the pipe wall and the pipe centre-line vicinity. The maximum peak angle has been found close to the pipe wall region.

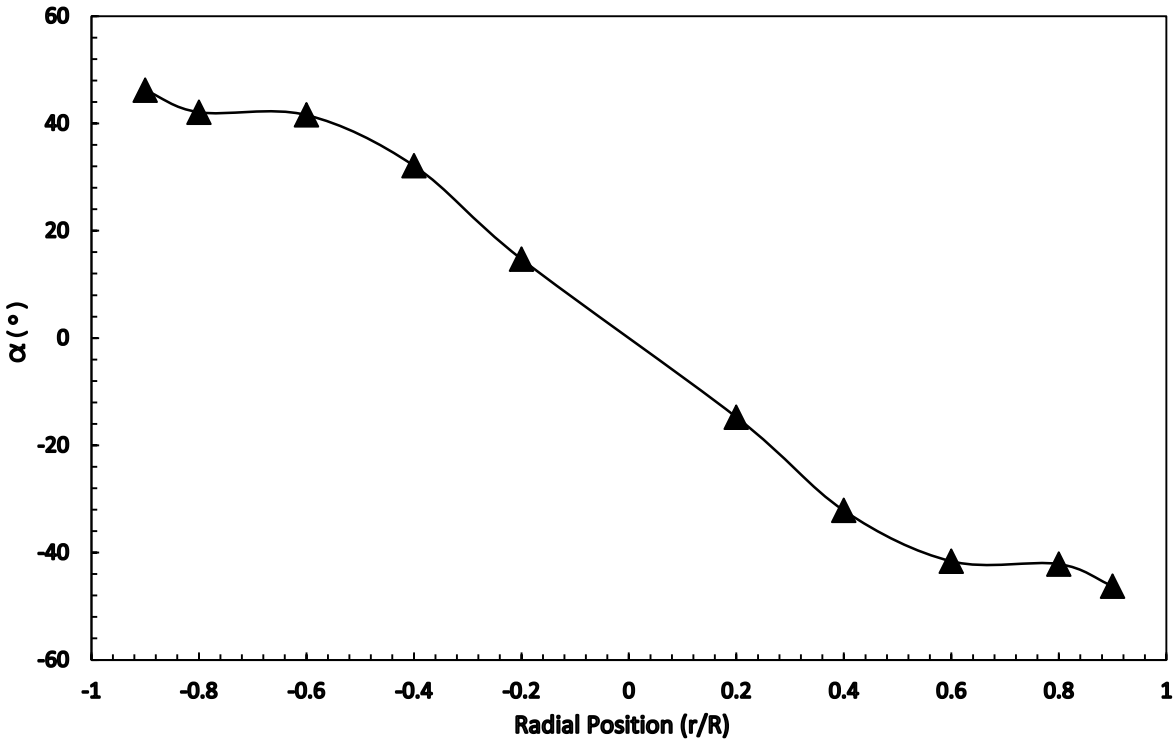

Figure 5.31. The bubble polar angles, α, distribution along the radial position, U_g=0.07 m/s and U_l=1 m/s.

Figure 5.31 depicts the bubble inclination angles distribution across the test pipe to the axial-axis, U_g=0.07 m/s and U_l=1 m/s. It is apparent that by increasing the air superficial velocity the polar angle in wall region has increased. The polar angle gradually decreased as the bubble has moved toward the pipe centre line. It is also apparent that the bubble polar angles have distributed symmetrical with opposite sings, the negative sign refers to the bubble movement in opposite direction. It has been concluded that as the air superficial velocity increases the bubble size increases, consequently bubble tends to move toward the pipe centre region.

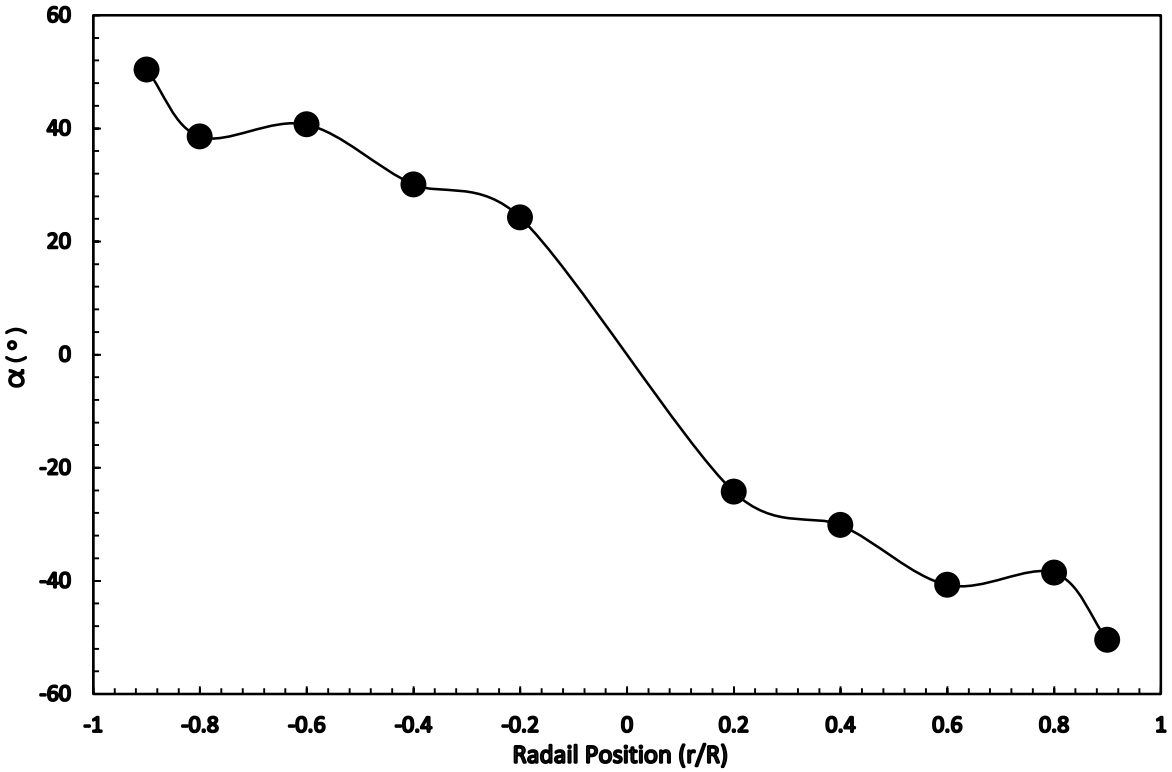

Figure 5.32. The bubble polar angles, α, distribution along the radial position, U_g=0.1m/s and U_l=1m/s.

Figure 5.32 depicts the bubble inclination angles distribution across the test pipe to the axial-axis, U_g =0.1 m/s and U_l =1 m/s. It is apparent that by further increasing the air superficial velocity the polar angle, in wall region, has increased too. This has similar trend to the 0.07 m/s case. It has been concluded that as bubble size increases to larger diameter the polar angle become steeper. The bubble polar angle profile remains symmetrical distributed whilst the air superficial velocity increases.

5.2.2.7 The effect of gas superficial velocity on bubble shape distribution

The effect of gas superficial velocity on the bubble shape distribution has been investigated experimentally using the novel seven-sensor probe. The investigations have been carried out at three gas superficial velocities namely, 0.05, 0.07 and 0.1 m/s at a constant water superficial velocity of 1 m/s.

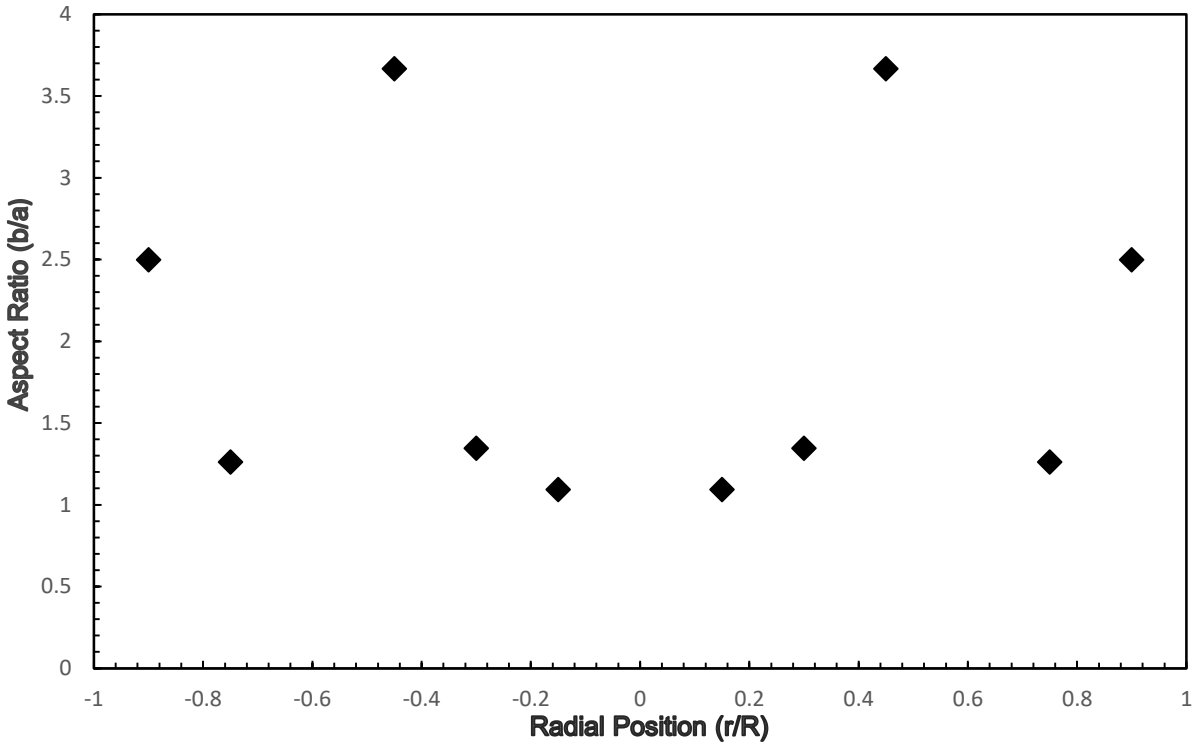

Figure 5.33. The average bubble aspect ratio distribution along the radial position, U_g=0.05 m/s and U_l=1m/s.

Figure 5.33 depicts the average bubble aspect ratio distribution along the radial position, U_g=0.05 m/s and U_l=1 m/s. It can be seen that at this gas superficial velocity, bubbles tend to get spherical shape, aspect ratio=1, at the pipe centre line region, whilst they take ellipsoidal shape close to the pipe wall region. The highest average aspect ratio, where the average major axis larger than the average minor axis, has been found in the transition area between the pipe centre line region and the pipe wall region.

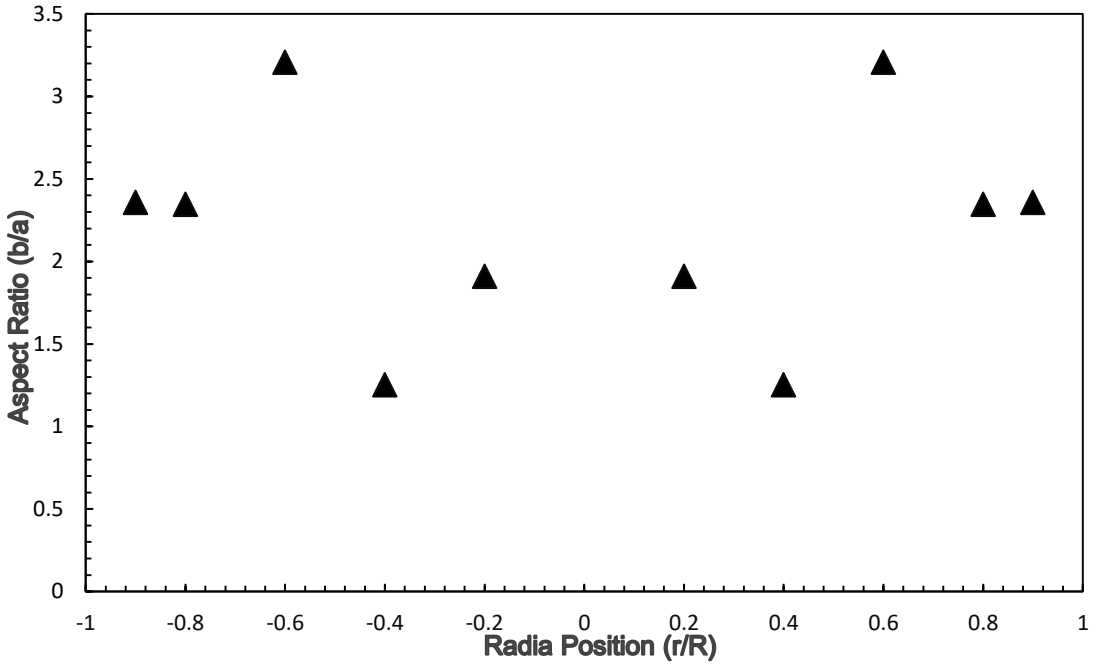

Figure 5.34. The average bubble aspect ratio distribution along the radial position, U_g=0.07 m/s and U_l=1m/s.

Figure 5.34 depicts the average bubble aspect ratio distribution along the radial position, U_g=0.07 m/s and U_l=1m/s. It can be seen that by increasing gas superficial velocity; bubbles' shape tends to change from spherical shape to ellipsoidal shape at the pipe centre line region. The majority bubbles shape at this gas superficial velocity has been found to be ellipsoidal shape, however, a trace of spherical bubbles has been observed in the region between the pipe centre line and the wall region. The highest average aspect ratio, similarly to the case of 0.05 m/s gas superficial velocity, has been found in the transition area between the pipe centre line region and the pipe wall region.

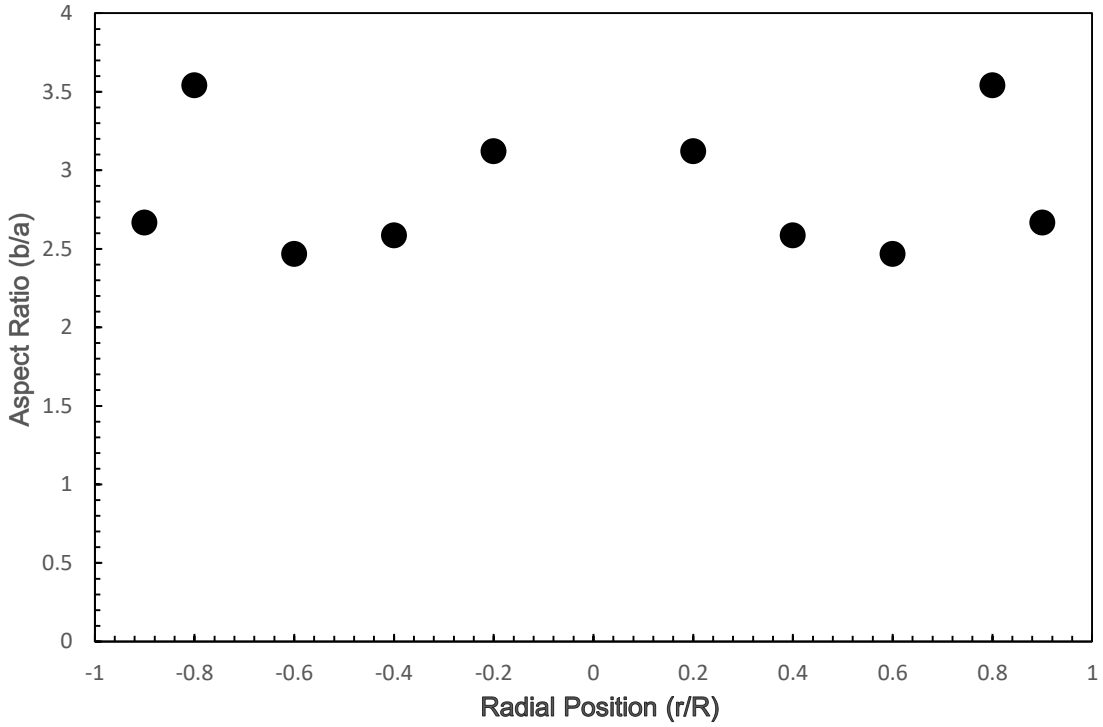

Figure 5.35. The average bubble aspect ratio distribution along the radial position, U_g=0.1 m/s and U_l=1m/s.

Figure 5.35 depicts the average bubble aspect ratio distribution along the radial position, U_g=0.1 m/s and U_l=1 m/s. It can be noticed from this figure that by increasing more gas superficial velocity; bubbles' shape tends to change from spherical shape to ellipsoidal shape across the test pipe. This can be justified as the gas superficial velocity increases the effect of the surrounding forces that overcome the effect of bubble surface tension force. The highest average aspect ratio has been found in the pipe centre line region and the pipe wall region.

5.3 The accuracy and the repeatability

5.3.1 The seven-sensor measurement accuracy

Generally, measurement accuracy denotes to how the measured data is close to a known or standard data. To determine the high-speed cameras measurement accuracy, the results that have been obtained from the high-speed cameras have been compared with the still image from Leica Application Suite, as shown in figure 5.6. It has been found that high-speed cameras have produced measurement error of 2.5%.

In this project, the novel seven-sensor conductivity probe measurements have been validated against the high-speed video cameras, therefore, the overall probe accuracy has taken the high-speed camera accuracy into account as:

1. The measurement error of 7.94% has been recorded for the bubble inclination angle, this in turn has produced the overall measurement error of 10.44%.
2. The measurement error of 10.5% has been recorded for the Minor Axis, this in turn has produced the overall measurement error of 13%.
3. The measurement error of 1.7% has been recorded for the Minor Axis, this in turn has produced the overall measurement error of 4.2%.
4. The measurement error of 1.7% has been recorded for the velocity component in z-direction, this in turn has produced the overall measurement error of 4.2%.
5. The measurement error of 23% has been recorded for the velocity component in y-direction, this in turn has produced the overall measurement error of 25.5%.
6. The measurement error of 5.32% has been recorded for the velocity component in x-direction, this in turn has produced the overall measurement error of 7.82%.

5.3.2 Measurement repeatability of the seven-sensor probe

In order to check the repeatability of the seven-sensor probe, it is necessary to perform several measurements of the dispersed phase properties at each sensing point under repeatability conditions which are:

- Identical measurement procedure.
- Identical witness, i.e. the measurements should be carried out by the same person.
- Identical measuring instrument under the identical conditions.
- Over a short period of time the measurement should be repeated. Therefore, three runs have been carried out for gas superficial velocities of 0.05m/s, with a constant water superficial velocity of 1 m/s.

Figures 5.36 – 5.39 depicts the measurement repeatability of bubble velocity, major and minor axes and the bubble polar angles, α, distribution along the radial position, U_g=0.05 m/s and U_l=1m/s respectively.

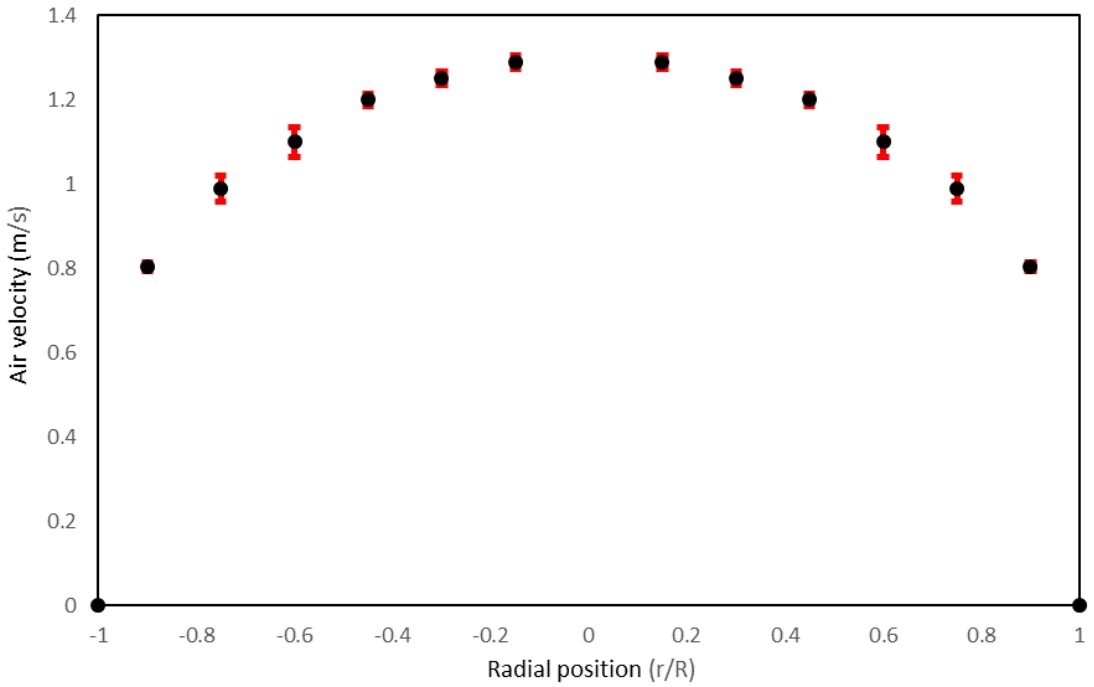

Figure 5.36. Measurement repeatability of the bubble velocity distribution along the radial position, U_g=0.05 m/s and U_l=1m/s.

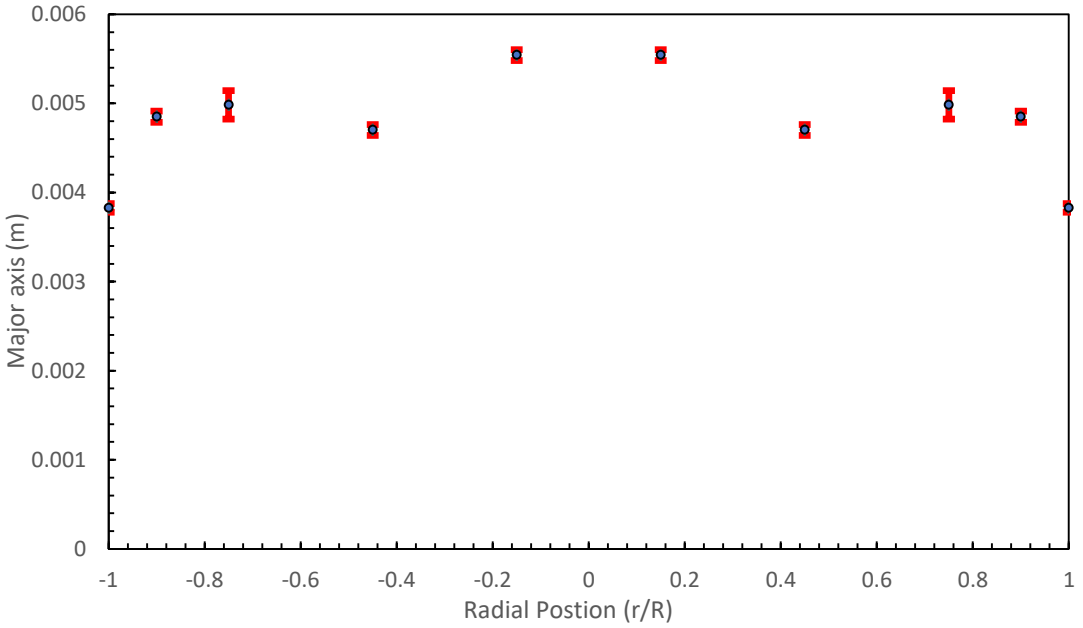

Figure 5.37. Measurement repeatability of the major axis distribution along the radial position, U_g=0.05 m/s and U_l=1m/s.

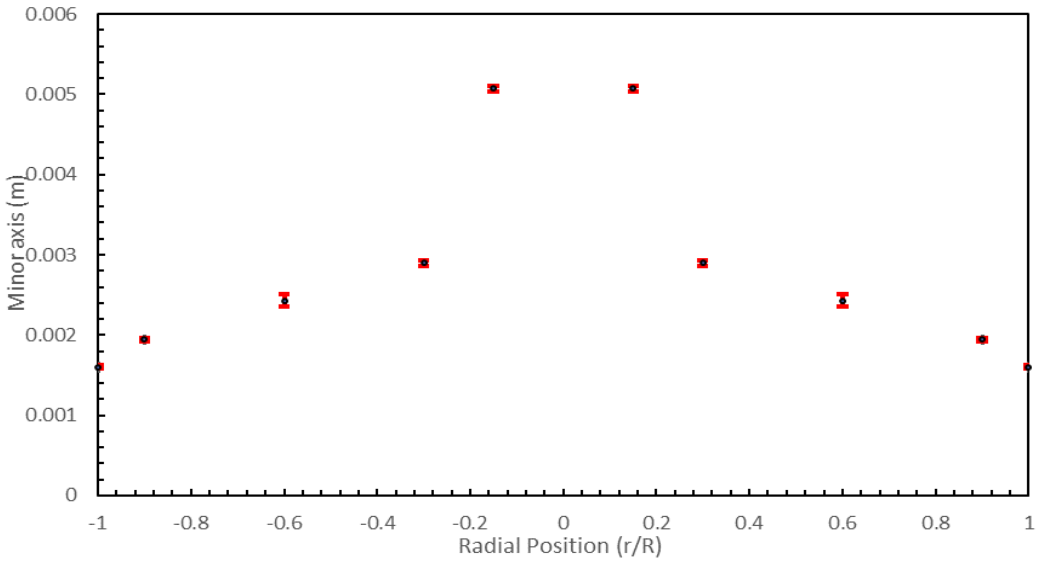

Figure 5.38. Measurement repeatability of the minor axis distribution along the radial position, U_g=0.05 m/s and U_l=1m/s.

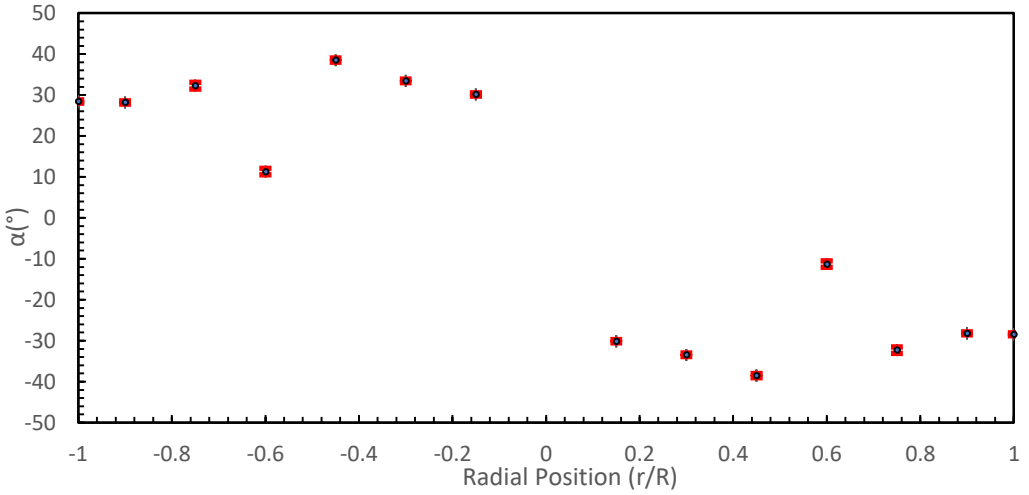

Figure 5.39. Measurement repeatability of the bubble polar angles, α, distribution along the radial position, U_g=0.05 m/s and U_l=1m/s.

From the measurement repeatability tests, it has been found that the seven-sensor probe measures the dispersed phase properties with an error margin of ±1.3%. This percentage has been expected because the seven-sensor probe system is fully automated, and the testes have been carried out under identical boundary conditions. However, an error margin of ±3.32% has been found in pipe's transition area, i.e. the zone between the pipe's wall zone and the centre line zones. This can be explained due to the bubble shape and size transitions which produce the instability in measurements.

5.4 Summary

In this chapter, the novel seven-sensor has been used to measure the air-water two-phase flow properties experimentally. The experiments comprised of two methods, namely bubble column and flow loop.

In the bubble column experiments, the water phase has been stationary, $U_l = 0$, whereas the gas has been compressed into the domain to produce single bubbly flow. In this experiment two of high-speed cameras have been used as a source for validating and calibrating the novel seven sensor probe. A new image processing code has been developed for capturing the dispersed phase properties, including the void fraction from the images that have been captured by the high-speed cameras. From the comparison between both methods, the seven-sensor probe and the high-speed camera measurements, good agreement has been found.

In the flow loop experiments, the novel seven-sensor probe system has been used for measuring the dispersed phase properties from the first bubble sensor contact. Primarily, the effect of sampling frequency on flow properties measurements has been investigated to quantify the precise sampling period and frequency to be used later in the flow loop experiments. It was found that by using the 30 kHz sampling frequency for a period of 60 sec, for measuring the volume fraction, has produced accurate results.

Thereafter, the effect of variation of gas superficial velocity, with the values being .05, 0.07 and 0.1 m/s, on the dispersed phase properties has been investigated. Regarding the effect of gas superficial velocity variation on the volume fraction distribution, it was found that by increasing the gas superficial velocity the peak value of the void fraction increases. However, the void fraction trend kept unchanged for the all three investigations. In case of the effect of gas superficial velocity on bubble size distribution, it was found that bubbles with larger diameter than 5.8 mm travels toward the pipe centre region, whereas bubbles with smaller diameter have been observed in the vicinity of the wall vicinity, this matches [50] earlier observations. Moreover, for the bubble size has been found to increase as the gas superficial velocity increases The increase of bubble size has referred to the bubble coalescence process due to the increase of the turbulent intensity and bubble movement towards the pipe centre line, similar conclusion was obtained by [171].

The main contribution of this chapter is obtaining the average bubble shape and size for the first time as measured from the first bubble-sensor contact.

Chapter 6.

Conclusions

Depending on the important achievements in the previous chapters concerning introducing and manufacturing a novel seven-sensor probe system and obtaining new data regarding the dispersed phase properties in large diameter pipelines, detailed conclusions have been illustrated in this chapter. The major achievements and contributions to the existing knowledge has been summarised and wherever possible referenced back to the initial aims and the objectives of this study. Finally, the works that have been performed in this study have been evaluated and requirements for future work in the area of using multi-sensor conductivity probe in pipelines have been defined.

6.1 Conclusions

6.1.1 Research Problem Synopsis

Multi-sensor conductivity probe systems are being widely utilised for measuring the secondary phase properties in multiphase flows, and these systems are considered to be one of the best intrusive techniques for the multiphase flows properties measurements. However, the measurement accuracy in this system needs to be further improved. Therefore, extensive works have been carried out in this regard to improve the multi-sensor probe accuracy over decades.

From an extensive review of the published literature, a number of limitations have been observed concerning the measurement accuracy using Multi-sensor conductivity probes system measurement. Therefore, to improve this system, set of aims and objectives have been identified in this study to reflect and define the scope of this work.

6.1.2 Research Aims and Major Achievements

The main aims of the study have been deduced from the extensive reviewed literature of the pioneer works that had been carried out in this field, these aims and the achievement of each aim in this study have been summarised.

1. Introducing a novel intrusive measuring system that has the ability to measure bubbles size and shape in addition to the other dispersed phase properties.

Achievement: This study has introduced the design and manufacturing process for a novel seven-sensor probe system that can be used to measure the local properties of the dispersed phase as well as the shape and size of the bubbles in bubbly multiphase flows from the first bubble-sensor contact. This system comprises of two novel mathematical models that calculate the dispersed flow properties from the first contact between the bubble-sensor, for regular and irregular bubble shapes. It also comprises of an improved signal processing scheme that treats and removes the undesired noise signals from the raw data. Moreover, it distinguished between the liquid and gas phases as well as noise levels and applies an adequate threshold value based on the comparison between the obtained volume fraction, from the probe, and the reference volume fraction, from the pressure transducer.

2. Reducing the bubble-sensor interactions, enhancing the measurement accuracy, and extending the flow-field velocity range application of multi-sensor probes.

Achievement: Extensive numerical investigations have been carried out in this study to quantify the effect of the flow field, such as the probe location, mixture velocity and pipe diameter, on the multi-sensor probe readings. Consequently, these effects have been analysed and related to the 3-dimensional sensor deflection. Accordingly, three-dimensional, x, y and z, equations with aid

of regression analysis, have been developed to represent the deflection of the sensors, based on the flow field variations. Thereafter these equations are integrated within the signal process code to minimize the effect of the sensor and probe deflection on the measurement accuracy within the signal processing stage i.e. no physical treatment required.

3. Investigating the local dispersed phase property in bubbly multiphase flows experimentally in cases of a stagnant and moving primary phase.

Achievement: Series of experimental investigations have been carried out in this study to obtain valuable data about the dispersed phase behaviour in upward two-phase gas-liquid flow. Throughout the experiments, a valuable data has been obtained from the use of the novel seven-sensor probe, this includes the gas local velocity, the local void fraction and for the first time a real-life bubble shape and size. Two sets of experimental investigations have been carried out namely, bubble column experiments and flow loop experiments. Further, a novel image processing code has been also introduced in this study, which is based on image segmentation, using the Foreground Detector System object, and feature extraction. The significant aspect of this code is the ability to capture most of the bubble properties such as velocity vector components, bubble shape and size and void fraction.

6.1.3 Conclusions

A detailed investigation has been carried out in this study to produce significant contributions to the existing knowledge and filling knowledge gaps in the area of multiphase flow measurements. These investigations are concerned with the enhancement of the multiphase flow's system measurement accuracy and providing novel additions to improve the current understanding of the design process, operational characteristics, and geometry-related effects for the multi-sensor conductivity probe on the secondary phase properties measurement. The main conclusions from each aspect of this report are as given below.:

Objective 1: To develop a novel mathematical model that can be used to quantify the dispersed phase properties from the measured time corresponded to the first bubble-sensor contact.

Conclusion: The mathematical model for seven-sensor probe has been developed to calculate the properties of the bubble droplets in bubbly air-water multiphase flow from the time delays that have been obtained from the seven sensors signals. The mathematical equations have been developed to calculate the dispersed phase properties from the first bubble-sensor contacts only i.e. from the time

interval between the first contact of the bubble with front S_0, which is the reference sensor, and the first contact of the bubble with rear sensor S_i. This reduces the uncertainty of measurement due to the bubble retardation and bubble deformation. It also reduces the effect of bubble slowing down, especially large bubbles, on bubble properties measurement-process during the bubble motion through the sensors. From the results presented in this study, it has been concluded that the developed mathematical model has reasonably calculated the dispersed phase properties such as the bubble velocity components axial, radial, and azimuthal velocities with minimum error.

Objective 2: To develop a novel mathematical model for irregular bubble shape, which can be used to quantify the dispersed phase properties from the measured time corresponded to the first bubble-sensor contact.

Conclusion: Generally, bubbles are subject to coalescence and break-up during their motion. Consequently, this produces an instantaneous irregular bubble shapes and size. Researches have been carried out to investigate the process of coalesces and break up of bubble during their flow; because of the relation between this phenomenon and the rate of the heat and mass transfer. Therefore, there is a strong demand for a mathematical model that can calculate the bubble shape and size of the moment that the bubble has an irregular shape and size.
In this study, mathematical model has been developed to calculate the dispersed phase properties including the bubble size and shape at the moment when bubble has an irregular shape and size to fulfil the gap in literature.

Objective 3: To design, develop and manufacture the novel seven-sensor needle probe system for the measurement of the dispersed phase properties.

Conclusion: From the investigations regarding the design factors that affect the multi-sensor measurement accuracy using the CFD tool, it has been noticed that the probe axial distance has a direct effect on the measurement accuracy. Since the probe stem disturbs the flow stream, the flowing bubbles are affected by the presence of the probe radial stem when the axial probe length is 100 mm or shorter. Furthermore, reducing the probe diameter by 2 mm, from 6 to 4 mm, will decrease the effect of presence of the probe in flow stream on the measurement accuracy.

Regarding the signal processing, it has been found that better conditioned signals can be obtained by using the median signal filter compared to the one produced from Butterworth method. Moreover, the threshold selection has a great influence on the obtained results. Therefore, using the reference volume

fraction as a reference to quantify the threshold magnitude has been found to be the best method. Finally, since the seven-sensor probe system operates in different flow conditions such as in high-pressure medium, the designing process and material selection have taken into consideration these effects. Moreover, using timing belt has been found to be the most cost-effective way to rotate the probe system with low noise. Furthermore, the traverse system has been designed in such a way that could cover the entire test pipe cross-sectional area at 90 inspection points.

Objective 4: To quantify the flow field effect around the probe body.

Conclusion: The accuracy of the dispersed phase properties measurement using multi-sensor probe depends on the accuracy of measuring the sensor coordinates, the sensor's tip location. Therefore, any relocation of these tips causes measurement error. The main source causing the sensor's tip to be relocated is sensors deflection. In this study, a series of numerical investigations have been carried out to quantify the effect of the flow field variables on the deflection rates of the sensors. From the numerical investigations, the following points have been concluded:

a. **The effect of probe positions**.
   It can be concluded that the position of the seven-sensor probe near the pipe walls have a significant effect on the static pressure distribution around the probe and sensors bodies. In case of low mixture velocity of 0.07 m/s, maximum uneven pressure distribution on the sensors' surface has been found when the probe has been close to the pipe wall, whilst almost equal pressure distribution has been found at the pipe centre-line. Whereas in case of high mixture velocity of 6 m/s the sensor deflection rate increases with the increase of immersing the probe stem in the pipe.
b. **The effect of increasing the mixture velocity**.
   It can be concluded that the increase in flow velocity increases the static pressure around the sensors and the probe body. This process occurs because of the increase of friction losses due to the high velocity and the amount of the dynamic pressure that transferred into static pressure around the sensors and probe body.
c. **The effect of increasing pipe diameter**.
   It has been concluded that as the pipe diameter increases the static pressure around the sensors and probe body decreases.

Objective 5: To establish the quantitative flow-sensor interaction over a wide range of flow variation.

Conclusion: From the numerical investigations, the following points have been concluded:

a. **The effect of probe location**.

   It has been concluded that the pipe walls have significant effect on the sensor deflection. In case of low mixture velocity, maximum deflection has been found when the probe has been close to the pipe wall, while almost no deflection has been found at the pipe centre-line. Whilst in case of high mixture velocity, the amount of deflection has been increased as the probe's stem length that has been exposed to the high-flow; this occur because the maximum probe deflection depends on the perpendicular distance between the applied force and the probe support .

b. **The effect of increasing the mixture velocity**.

   It has been concluded that by increasing the flow velocity the sensor deflection increases. This occurs because of the static pressure has increased due to the fractional shear force has increased at the sensor surface.

c. **The effect of increasing pipe diameter**.

   It has been concluded that by using a conductivity probe in larger pipelines, whilst keeping the mixture velocity constant, the sensor deflection decreases. It has been concluded that as the pipe diameter increases the pressure drop decreases, hence the amount of the deflection decreases.

Objective 6: To develop novel mathematical expressions for each sensor that adjusts the measurement error due to the sensors deflection.

Conclusion: From the investigations regarding the effect of the mixture flow-stream velocity, the probe radial location, and the test pipe internal diameter, it has been concluded that these factors have a direct effect on both the probe body's and sensors' deflection consequently affecting the measurement accuracy. Therefore, appropriate mathematical expressions have been developed to overcome the errors that have been produced from above factors and thereafter compiling these equations into the signal processing code. From the application of these equations, it has been concluded that this process has modified the measured velocity profile, however, it can be noticed that the importance of using this process being on when the probe is used in high velocity field flow.

Objective 7: To develop an image processing code that can measure the dispersed phase properties including the volume fraction.

Conclusion: In this study, high-speed cameras have been used as a means of the probe calibration and validation, therefore, a proper image processing code is required to interpret the images to multiphase flow properties. Since the seven-sensor probe validation and calibration experimental utilises fixed cameras with a stationary background, it has been concluded that using the Background

Modelling and Subtraction methods are the most suitable methods for the segmentation and detection of the moving bubbles. The new image processing code have been validated by measuring both the major and minor axes, using the Leica software and the image processing code; fairly good agreement has been obtained between the two results. Whereas the discrepancy in the results have been explained due to the fact that the image processing code measures the mean length of both the major and minor axes for all tracked bubbles during the video clipping period. Finally, this image processing code can be used effectively for measuring the dispersed phase properties in bubble column investigations.

Objective 8: To investigate the accuracy of the novel probe with a high-speed camera in single-bubble experiments

Conclusion: This calibrating and validating of the novel seven-sensor probe process is essential, for the reason that the seven-sensor probe has a completely new form comparing to the previous conductivity probes, which includes the increase in the number of the sensors, a new mathematical model methodology and new signal processing aspects. By validation the seven-sensor probe against video imaging, it has been proved that measuring the bubble properties by the novel probe system is reliable. From the experimental data for validating the seven-sensor probe, it has also been concluded that:

a. In case of the Major Axis and Minor Axis, 20.46 and 9.95 % discrepancies have been found between the probe and the high-speed camera for the major and minor axes respectively. These discrepancies can be referred to the digital microscope's accuracy that has been used for probe coordinate measurement, which has not been so high. Furthermore, the backlight effect on the camera results has been found to be a significant effect, since it generates a reflection at the edge of each bubble, in turn, affects the bubble size measurement, the bubble size be smaller than the actual size. It is clearly noticeable that the reflection affects the major axis measurement more than the minor axis measurement .
b. In the case of bubble velocity in x- direction, Vx, good agreement has been found between the results from seven-sensor probe and high-speed camera. The percentage error between the two measurements was low.
c. In the case of bubble velocity in y- direction, Vy, a high discrepancy has been found between the probe and high-speed camera; this can be referred to the inaccuracy of the probe coordinate measurement especially in y-direction and the sensors' wettability.
d. In the case of bubble velocity in z- direction, Vz, a good agreement has been found between the probe and high-speed cameras measurements.

Objective 9: To achieve deeper understanding of the bubble hydrodynamics by analysing the obtained data and introducing bubble size distribution across the test section.

Conclusion: The novel seven-sensor probe system has been utilized in series of flow loop experiments under specified operating conditions of interest to quantify the effect of gas superficial velocity variation on the measured bubble properties. Primarily, the effect of sampling frequency on flow properties measurements has been investigated. In these investigations, four values of sampling frequencies namely, 10, 20, 30 and 40 kHz have been used, at identical flow conditions, to quantify the effect of sampling frequency on the volume fraction measurement. The first three investigations, where the sampling frequencies have been 10, 20 and 30 kHz, have been carried out at a sampling time-period of 60 sec, whereas the last investigation utilised 40 kHz sampling frequency at sampling time-period of 30 sec. It has been concluded that investigation results that utilised the 30 kHz sampling frequency has provided more accurate data compared to the other frequency bands. However, 40 kHz band has been expected to present more accurate results, but this measurement has been carried out at 30 sec, this in turn has led the probe to miss more bubbles in low bubble frequency flow. Therefore, for all experimental investigations in this study the data has been collected at 30 kHz for one minute. Furthermore, the effect of gas superficial velocity variation on the measured bubble properties has also been concluded as:

a. **The effect of gas superficial velocity on the volume fraction distribution**.
   It has been noticed that no significant wall peak has been observed in these flow conditions, whilst only core peak volume fraction profiles have been observed in vertical upward gas liquid two-phase flows. The gradually radial changes of these profiles have also been observed in the present experiment. It has also been observed that the core peak shape has maintained the same characteristics in the all cases, which means that the air volume fraction core peak pattern does not change with the increase in the air superficial velocity when the flow is bubbly in the range of velocities considered. These volume fraction profiles have been expected since the initial bubble diameters have been expected to be 6 mm or above.
b. **The effect of gas superficial velocity on bubble size distribution**.
   It has been observed that by increasing the air superficial velocity the bubble size increases more. As the air superficial velocity increases further the turbulent intensity increases more in the test pipe, which is in turn increases the a bubble size due to the increase in bubble coalescence rate, similar conclusion was obtained by [171]. Therefore, the bubbles with larger size than 5.8 travel from the wall vicinity towards the pipe centre-line vicinity, the similar phenomenon has been observed by [50], as explained earlier whilst smaller bubbles maintain in their position in the vicinity of the wall.

c. **The effect of gas superficial velocity on the local bubble Azimuthal velocity**.

It has been noticed that by increasing the air superficial velocity the azimuthal velocity increases in the near wall whilst it decreases in the pipe centre vicinity. It has also been noticed that the azimuthal velocity profile tends to be flatter at the pipe centre. From the three experimental tests, it has been concluded that the magnitude of the azimuthal velocity is relatively small. Moreover, the azimuthal velocity fluctuation reduces with the increase in air superficial velocity.

d. **The effect of gas superficial velocity on the local radial bubble velocity distribution**.

It has been observed that by increasing the air superficial velocity the bubble radial velocity in the near wall region has increased too, whilst the radial velocity in pipe centre region has reduced. It is also apparent that by increasing the air superficial velocity, at near the wall region, the bubble radial velocity tends to take flatter distribution. The peak radial velocity profile close to the wall vicinity also has been observed.

e. **The effect of gas superficial velocity on the distribution of bubble polar angles, α, across the test pipe**.

It has been observed that by increasing the air superficial velocity the polar angle in the wall region increases. This increase gradually decreases as the bubble moves toward the pipe centre line. It has also been observed that the bubble polar angles have been symmetrically distributed. Moreover, bubbles at the pipe centre-line have zero angle i.e. these bubbles travel axially. It has also been concluded that as the air superficial velocity increases; bubble size increases consequently, and bubbles tend to move toward the pipe centre.

f. The effect of gas superficial velocity on bubble shape distribution

It has been concluded that by increasing the air superficial velocity; bubbles' shape tends to change from spherical shape to ellipsoidal shape across the pipe. This can be justified because the gas superficial velocity increases the effect of the surrounding forces overcome the effect of bubble surface tension force. The highest average aspect ratio has been found in the pipe centre line region and the pipe wall region at the highest gas superficial velocity.

6.1.4 Thesis Contributions

The major novelties and contributions of this research study are summarized below in which they are described:

Contribution 1:

Inaccuracy in needle probes measurement due to several factors have been found in literature. Bubble slowing down, missing bubbles, bubble deformation and bubble retardation due to bubble-sensor interaction are counted to be among these factors

Therefore, one of the major novelties of this study is introducing a novel mathematical model that calculates the dispersed phase flow properties such as bubble size and shape, volume fraction and velocity vector components, from the first bubble–sensor contact. which reduces the measurement error that may occur due to bubble–sensor interactions.

Contribution 2:

Another major novelty of this study is introducing a novel mathematical model that calculates the dispersed phase flow properties such as bubble size and shape, volume fraction and velocity vector components for irregular bubble shape, from the first bubble-sensor contact. This is the first time that this type of equation is introduced. The benefit of using this model is its use for investigating the dispersed phase properties including the bubble shape and size whilst it is in the process of coalescence and break-up.

Contribution 3:

From the literature, limited image processing codes have been found that used by researchers for the dispersed phase properties investigation in including volume fraction measurement, since many of them used commercial codes that come with the high-speed camera. From literature, conventionally the volume fraction has been measured by using a transparent tube in the flow domain that drives the bubbles through it forming a single bubble flow and then measure the volume fraction from it. This process does not measure the volume fraction accurately and freely. Therefore, in this study a novel image processing code has been developed, which can measure the dispersed phase properties including the volume freely at any point within the flow domain.

Contribution 4:

As the dispersed phase properties measurement using multi-sensor probe depends on a fixed location of the sensors' tip; any relocation of these tips, because of sensor deflection, while measuring these properties affect the measurement accuracy. Therefore, in this study, mathematical expression for the deflection of each sensor has been developed, based on CFD, and FEA simulations, to compensate the measurement error due to the sensors' tip relocation within the signal processing stage i.e. no physical treatment required to overcome this error.

Contribution 5:

There are many factors that can limit the ability of multi-sensor probes to measure dispersed phase properties. These factors include: the axial length, S, between the leading sensor, S_0, and the trailer sensors, S_i, the radial distance between the sensors, x, the sensor material, the sensor diameter and the mixture flow velocity. Limited publications have been found in this area. Therefore, a novel mathematical expression has been developed in this study that relates the bubble diameter to the sensors separation distance selections. These expressions are quite useful tool to be used whilst designing any multi-sensor conductivity probe.

6.2 Recommendations for Future Work

The design, manufacturing and application of the novel seven-sensor probe system have been introduced in this study, to fill the gaps that have been identified in literature. In the light of the concluding remarks provided in the previous sections, the following further works are required:

1. Investigating the effect of flow field vibration on conductivity multi-sensor probe measurement accuracy
2. Improving the image processing code in such a way that can be used to measure the bubbly flow properties in a heavy dense flow.
3. Expanding the probe displacement equations to include different probe materials and dimensions that can be used globally.
4. Applying water repellent materials to the sensors surface to reduce the bubble slowing down process due to the adhesion effect between the bubble–water film and the sensors body
5. Using sensors with a smaller frontal area.
6. Investigating the effect of the pressure variation on the bubble size distribution using this novel seven-sensor probe.
7. Investigating the effect of ambient temperature on the bubble size distribution using the novel seven-sensor probe.
8. Investigating the dispersed phase properties in the larger pipelines at a high mixture velocity.

References

1. Zavareh, F., A. Hill, and A. Podio. *Flow regimes in vertical and inclined oil/water flow in pipes*. in *SPE Annual Technical Conference and Exhibition*. 1988. Society of Petroleum Engineers.

2. Falcone, G., G. Hewitt, and C. Alimonti, *Multiphase flow metering: principles and applications*. Vol. 54. 2009: Elsevier.

3. Boyer, C., A.-M. Duquenne, and G. Wild, *Measuring techniques in gas–liquid and gas–liquid–solid reactors.* Chemical engineering science, 2002. **57**(16): p. 3185-3215.

4. Ahmed, W., et al., *On the development of integrated sensor for multiphase measurements.* WIT Transactions on Engineering Sciences, 2013. **79**: p. 523-533.

5. White, F.M., *Fluid Mechanics. 4th*. McGraw-Hill. p. 388.

6. Stravs, A.A., et al., *Development of an ultrasonic pulse reflection method for measuring relative size distributions of air bubbles in aqueous solutions.* Chemical engineering science, 1987. **42**(7): p. 1677-1688.

7. Joshi, J., *Computational flow modelling and design of bubble column reactors.* Chemical engineering science, 2001. **56**(21): p. 5893-5933.

8. Chen, C. and L.S. Fan, *Discrete simulation of gas-liquid bubble columns and gas-liquid-solid fluidized beds.* AIChE journal, 2004. **50**(2): p. 288-301.

9. Joshi, J., et al., *Coherent flow structures in bubble column reactors.* Chemical Engineering Science, 2002. **57**(16): p. 3157-3183.

10. Laın, S., et al., *Modelling hydrodynamics and turbulence in a bubble column using the Euler–Lagrange procedure.* International Journal of Multiphase Flow, 2002. **28**(8): p. 1381-1407.

11. Sokolichin, A., G. Eigenberger, and A. Lapin, *Simulation of buoyancy driven bubbly flow: established simplifications and open questions.* AIChE Journal, 2004. **50**(1): p. 24-45.

12. Burns, L. and R. Rice, *Circulation in bubble columns.* AIChE journal, 1997. **43**(6): p. 1390-1402.

13. Geary, N.W. and R.G. Rice, *Circulation and scale-up in bubble columns.* AIChE journal, 1992. **38**(1): p. 76-82.

14. Rice, R.G. and N.W. Geary, *Prediction of liquid circulation in viscous bubble columns.* AIChE Journal, 1990. **36**(9): p. 1339-1348.

15. Vitankar, V. and J. Joshi, *A comprehensive one-dimensional model for prediction of flow pattern in bubble columns.* Chemical Engineering Research and Design, 2002. **80**(5): p. 499-512.

16. Buscaglia, G.C., F.A. Bombardelli, and M.H. García, *Numerical modeling of large-scale bubble plumes accounting for mass transfer effects.* International journal of multiphase flow, 2002. **28**(11): p. 1763-1785.

17. Sanyal, J., et al., *Numerical simulation of gas–liquid dynamics in cylindrical bubble column reactors.* Chemical Engineering Science, 1999. **54**(21): p. 5071-5083.

18. Sokolichin, A. and G. Eigenberger, *Gas—liquid flow in bubble columns and loop reactors: Part I. Detailed modelling and numerical simulation.* Chemical Engineering Science, 1994. **49**(24): p. 5735-5746.

19. Sokolichin, A. and G. Eigenberger, *Applicability of the standard k–ε turbulence model to the dynamic simulation of bubble columns: Part I. Detailed numerical simulations.* Chemical Engineering Science, 1999. **54**(13): p. 2273-2284.

20. Rigopoulos, S. and A. Jones, *A hybrid CFD—reaction engineering framework for multiphase reactor modelling: basic concept and application to bubble column reactors.* Chemical engineering science, 2003. **58**(14): p. 3077-3089.

21. Behzadi, A., R. Issa, and H. Rusche, *Modelling of dispersed bubble and droplet flow at high phase fractions.* Chemical Engineering Science, 2004. **59**(4): p. 759-770.

22. Buwa, V.V. and V.V. Ranade, *Dynamics of gas–liquid flow in a rectangular bubble column: experiments and single/multi-group CFD simulations.* Chemical Engineering Science, 2002. **57**(22): p. 4715-4736.

23. Delnoij, E., J. Kuipers, and W. Van Swaaij, *Computational fluid dynamics applied to gas-liquid contactors.* Chemical Engineering Science, 1997. **52**(21): p. 3623-3638.

24. Delnoij, E., J. Kuipers, and W. Van Swaaij, *Dynamic simulation of gas-liquid two-phase flow: effect of column aspect ratio on the flow structure.* Chemical Engineering Science, 1997. **52**(21): p. 3759-3772.

25. Delnoij, E., et al., *Dynamic simulation of dispersed gas-liquid two-phase flow using a discrete bubble model.* Chemical Engineering Science, 1997. **52**(9): p. 1429-1458.

26. Grevskott, S., et al., *Liquid circulation, bubble size distributions, and solids movement in two-and three-phase bubble columns.* Chemical Engineering Science, 1996. **51**(10): p. 1703-1713.

27. Lapin, A. and A. Lübbert, *Numerical simulation of the dynamics of two-phase gas—liquid flows in bubble columns.* Chemical Engineering Science, 1994. **49**(21): p. 3661-3674.

28. Lehr, F., M. Millies, and D. Mewes, *Bubble-Size distributions and flow fields in bubble columns.* AIChE Journal, 2002. **48**(11): p. 2426-2443.

29. Michele, V. and D.C. Hempel, *Liquid flow and phase holdup—measurement and CFD modeling for two-and three-phase bubble columns.* Chemical engineering science, 2002. **57**(11): p. 1899-1908.

30. Mudde, R.F. and O. Simonin, *Two-and three-dimensional simulations of a bubble plume using a two-fluid model.* Chemical Engineering Science, 1999. **54**(21): p. 5061-5069.

31. Oey, R., R. Mudde, and H. Van den Akker, *Sensitivity study on interfacial closure laws in two-fluid bubbly flow simulations.* AIChE journal, 2003. **49**(7): p. 1621-1636.

32. Olmos, E., C. Gentric, and N. Midoux, *Numerical description of flow regime transitions in bubble column reactors by a multiple gas phase model.* Chemical Engineering Science, 2003. **58**(10): p. 2113-2121.

33. Pan, Y., M. Dudukovic, and M. Chang, *Dynamic simulation of bubbly flow in bubble columns.* Chemical Engineering Science, 1999. **54**(13): p. 2481-2489.

34. Pan, Y., M. Dudukovic, and M. Chang, *Numerical investigation of gas-driven flow in 2-D bubble columns.* AIChE journal, 2000. **46**(3): p. 434-449.

35. Pfleger, D. and S. Becker, *Modelling and simulation of the dynamic flow behaviour in a bubble column.* Chemical Engineering Science, 2001. **56**(4): p. 1737-1747.

36. Politano, M., P. Carrica, and J. Converti, *A model for turbulent polydisperse two-phase flow in vertical channels.* International Journal of Multiphase Flow, 2003. **29**(7): p. 1153-1182.

37. Schallenberg, J., J.H. Enß, and D.C. Hempel, *The important role of local dispersed phase hold-ups for the calculation of three-phase bubble columns.* Chemical engineering science, 2005. **60**(22): p. 6027-6033.

38. Turton, R. and N. Clark, *Interpreting probe signals from fluidized beds.* Powder technology, 1989. **59**(2): p. 117-123.

39. Wang, T., J. Wang, and Y. Jin, *Theoretical prediction of flow regime transition in bubble columns by the population balance model.* Chemical Engineering Science, 2005. **60**(22): p. 6199-6209.

40. Zhou, L., et al., *On the second-order moment turbulence model for simulating a bubble column.* Chemical engineering science, 2002. **57**(16): p. 3269-3281.

41. Deen, N.G., T. Solberg, and B.r.H. Hjertager, *Large eddy simulation of the gas–liquid flow in a square cross-sectioned bubble column.* Chemical engineering science, 2001. **56**(21): p. 6341-6349.

42. Bove, S., T. Solberg, and B.H. Hjertager, *Numerical aspects of bubble column simulations.* International Journal of Chemical Reactor Engineering, 2004. **2**(A1): p. 1-22.

43. Wörner, M., *A compact introduction to the numerical modeling of multiphase flows*. 2003: Forschungszentrum Karlsruhe.

44. Morel, C., *Mathematical modeling of disperse two-phase flows*. Vol. 114. 2015: Springer.

45. Oesterlé, B., *Ecoulements multiphasiques.* Hermès-Lavoisier, Paris, 2006.

46. Clift, R., J.R. Grace, and M.E. Weber, *Bubbles, drops, and particles*. 2005: Courier Corporation.

47. Ishii, M., *Two-fluid model for two-phase flow.* Multiphase science and technology, 1990. **5**(1-4).

48. Morsi, S. and A. Alexander, *An investigation of particle trajectories in two-phase flow systems.* Journal of Fluid mechanics, 1972. **55**(02): p. 193-208.

49. Schiller, L. and Z. Naumann, *A drag coefficient correlation.* Z. Ver. Deutsch. Ing, 1935. **77**(1): p. 318-320.

50. Tomiyama, A., et al., *Drag coefficients of single bubbles under normal and micro gravity conditions.* JSME International Journal Series B Fluids and Thermal Engineering, 1998. **41**(2): p. 472-479.

51. Saffman, P., *The lift on a small sphere in a slow shear flow.* Journal of Fluid Mechanics, 1965. **22**(02): p. 385-400.

52. Auton, T., *The lift force on a spherical body in a rotational flow.* Journal of Fluid Mechanics, 1987. **183**: p. 199-218.

53. Lucas, D., J.-M. Shi, and E. Krepper, *MODELLING OF NON-DRAG FORCES FOR BUBBLY FLOWS.* Institute of Safety Research: p. 1.

54. Crowe, C.T., et al., *Multiphase flows with droplets and particles*. 2011: CRC press.

55. Johnson, R.W., *Handbook of fluid dynamics*. 2016: Crc Press.

56. Antal, S., R. Lahey, and J. Flaherty, *Analysis of phase distribution in fully developed laminar bubbly two-phase flow.* International Journal of Multiphase Flow, 1991. **17**(5): p. 635-652.

57. Ishii, M. and T. Hibiki, *Thermo-fluid dynamics of two-phase flow*. 2010: Springer Science & Business Media.

58. Yamoah, S., et al., *Numerical investigation of models for drag, lift, wall lubrication and turbulent dispersion forces for the simulation of gas–liquid two-phase flow.* Chemical Engineering Research and Design, 2015. **98**: p. 17-35.

59. Liang-Shih, F. and K. Tsuchiya, *Bubble wake dynamics in liquids and liquid-solid suspensions*. 2013: Butterworth-Heinemann.

60. Bhaga, D. and M. Weber, *Bubbles in viscous liquids: shapes, wakes and velocities.* Journal of Fluid Mechanics, 1981. **105**: p. 61-85.

61. Wu, Q., et al., *One-group interfacial area transport in vertical bubbly flow.* International Journal of Heat and Mass Transfer, 1998. **41**(8): p. 1103-1112.

62. Kocamustafaogullari, G. and M. Ishii, *Foundation of the interfacial area transport equation and its closure relations.* International Journal of Heat and Mass Transfer, 1995. **38**(3): p. 481-493.

63. Palit, S., *Application of bubble column reactor in environmental engineering-future directions, future dimensions, visionary and deep comprehension.* International Journal of Innovation and Applied Studies, 2014. **7**(1): p. 42.

64. Kantarci, N., F. Borak, and K.O. Ulgen, *Bubble column reactors.* Process Biochemistry, 2005. **40**(7): p. 2263-2283.

65. Kulkarni, A.A., *Mass transfer in bubble column reactors: effect of bubble size distribution.* Industrial & Engineering Chemistry Research, 2007. **46**(7): p. 2205-2211.

66. Yang, G., et al., *Heat-transfer characteristics in slurry bubble columns at elevated pressures and temperatures.* Industrial & engineering chemistry research, 2000. **39**(7): p. 2568-2577.

67. Xue, J., *Bubble velocity, size and interfacial area measurements in bubble columns.* PhD diss., Washington University, 2004.

68. Colella, D., et al., *A study on coalescence and breakage mechanisms in three different bubble columns.* chemical Engineering science, 1999. **54**(21): p. 4767-4777.

69. Spicka, P., et al., *Hydrodynamics of gas–liquid flow in 2D packed/unpacked rectangular reactor.* Chemical engineering science, 1999. **54**(21): p. 5127-5137.

70. Krishna, R., P. Wilkinson, and L. Van Dierendonck, *A model for gas holdup in bubble columns incorporating the influence of gas density on flow regime transitions.* Chemical Engineering Science, 1991. **46**(10): p. 2491-2496.

71. Daly, J., S. Patel, and D. Bukur, *Measurement of gas holdups and sauter mean bubble diameters in bubble column reactors by dynamics gas disengagement method.* Chemical engineering science, 1992. **47**(13-14): p. 3647-3654.

72. Deshpande, N., M. Dinkar, and J. Joshi, *Disengagement of the gas phase in bubble columns.* International journal of multiphase flow, 1995. **21**(6): p. 1191-1201.

73. Jordan, U., A.K. Saxena, and A. Schumpe, *Dynamic Gas Disengagement in a High-Pressure Bubble Column.* The Canadian Journal of Chemical Engineering, 2003. **81**(3-4): p. 491-498.

74. Burgess, J. and P. Calderbank, *The measurement of bubble parameters in two-phase dispersions—I: the development of an improved probe technique.* Chemical engineering science, 1975. **30**(7): p. 743-750.

75. Chabot, J., et al., *Interaction between bubbles and fibre optic probes in a bubble column.* The Canadian Journal of Chemical Engineering, 1992. **70**(1): p. 61-68.

76. Farag, H., et al., *Fibre optic and capacitance probes in turbulent fluidized beds.* Chemical Engineering Communications, 1997. **157**(1): p. 73-107.

77. Iguchi, M., et al., *Measurement of bubble characteristics in a molten iron bath at 1600 C using an electroresistivity probe.* Metallurgical and Materials Transactions B, 1995. **26**(1): p. 67-74.

78. Mudde, R.F. and T. Saito, *Hydrodynamical similarities between bubble column and bubbly pipe flow.* Journal of Fluid Mechanics, 2001. **437**: p. 203-228.

79. Sanaullah, K., S. Zaidi, and J. Hills, *A study of bubbly flow using resistivity probes in a novel configuration.* Chemical Engineering Journal, 2001. **83**(1): p. 45-53.

80. Vince, M., et al., *Optical probe for high-temperature local void fraction determination.* Applied optics, 1982. **21**(5): p. 886-892.

81. Wu, Q. and M. Ishii, *Sensitivity study on double-sensor conductivity probe for the measurement of interfacial area concentration in bubbly flow.* International Journal of Multiphase Flow, 1999. **25**(1): p. 155-173.

82. Xue, J., et al., *Bubble Dynamics Measurements Using Four-Point Optical Probe.* The Canadian Journal of Chemical Engineering, 2003. **81**(3-4): p. 375-381.

83. Yu, Y.H. and S.D. Kim, *Bubble characteristics in the radial direction of three-phase fluidized beds.* AIChE journal, 1988. **34**(12): p. 2069-2072.

84. Baker, O. *Design of pipelines for the simultaneous flow of oil and gas*. in *Fall Meeting of the Petroleum Branch of AIME*. 1953. Society of Petroleum Engineers.

85. Russell, T., G. Hodgson, and G. Govier, *Horizontal pipeline flow of mixtures of oil and water.* The Canadian Journal of Chemical Engineering, 1959. **37**(1): p. 9-17.

86. Charles, M.E., G.t. Govier, and G. Hodgson, *The horizontal pipeline flow of equal density oil-water mixtures.* the Canadian Journal of Chemical engineering, 1961. **39**(1): p. 27-36.

87. Mandhane, J., G. Gregory, and K. Aziz, *A flow pattern map for gas—liquid flow in horizontal pipes.* International Journal of Multiphase Flow, 1974. **1**(4): p. 537-553.

88. Taitel, Y. and A. Dukler, *A model for predicting flow regime transitions in horizontal and near horizontal gas-liquid flow.* AIChE Journal, 1976. **22**(1): p. 47-55.

89. Trallero, J., C. Sarica, and J. Brill. *A study of oil-water flow patterns in horizontal pipes*. in *SPE annual technical conference*. 1996.

90. Shi, H., *A study of oil-water flows in large diameter horizontal pipelines*. 2001, Ohio University.

91. Angeli, P. and G. Hewitt, *Flow structure in horizontal oil–water flow.* International journal of multiphase flow, 2000. **26**(7): p. 1117-1140.

92. Xu, J.-y., et al., *Experimental investigation on the slip between oil and water in horizontal pipes.* Experimental Thermal and Fluid Science, 2008. **33**(1): p. 178-183.

93. Al-Yaari, M.A. and B.F. Abu-Sharkh, *CFD prediction of stratified oil-water flow in a horizontal pipe.* Asian Trans. Eng, 2011. **1**(5): p. 68-75.

94. Bottin, M., et al., *Experimental investigation of a developing two-phase bubbly flow in horizontal pipe.* International journal of multiphase flow, 2014. **60**: p. 161-179.

95. Beggs, D.H. and J.P. Brill, *A study of two-phase flow in inclined pipes.* Journal of Petroleum technology, 1973. **25**(05): p. 607-617.

96. Wicks, M. and J. Fraser, *Entrainment of water by flowing oil.* Materials performance, 1975. **14**(5): p. 9-12.

97. Mukherjee, H., J. Brill, and H. Beggs, *Experimental study of oil-water flow in inclined pipes.* Journal of Energy Resources Technology, 1981. **103**(1): p. 56-66.

98. Vigneaux, P., P. Chenais, and J. Hulin, *Liquid-liquid flows in an inclined pipe.* AIChE Journal, 1988. **34**(5): p. 781-789.

99. Spindler, K. and E. Hahne, *An experimental study of the void fraction distribution in adiabatic water-air two-phase flows in an inclined tube.* International journal of thermal sciences, 1999. **38**(4): p. 305-314.

100. Flores, J.G., et al., *Characterization of oil-water flow patterns in vertical and deviated wells.* SPE production & facilities, 1999. **14**(02): p. 94-101.

101. Al-Sarkhi, A., E. Abu-Nada, and M. Batayneh, *Effect of drag reducing polymer on air–water annular flow in an inclined pipe.* International journal of multiphase flow, 2006. **32**(8): p. 926-934.

102. Atmaca, S., et al., *Characterization of oil/water flows in inclined pipes.* SPE Projects Facilities & Construction, 2009. **4**(02): p. 41-46.

103. Hamad, F.A., D. Albarzenji, and P.B. Ganesan, *Study of kerosene–water two-phase flow characteristics in vertical and inclined pipes.* The Canadian Journal of Chemical Engineering, 2014. **92**(5): p. 905-917.

104. Gould, T.L., M.R. Tek, and D.L. Katz, *Two-phase flow through vertical inclined or curved pipe.* Journal of Petroleum Technology, 1974. **26**(08): p. 915-926.

105. Serizawa, A., I. Kataoka, and I. Michiyoshi, *Turbulence structure of air-water bubbly flow—I. Measuring techniques.* International journal of multiphase flow, 1975. **2**(3): p. 221-233.

106. Beyerlein, S.W., R.K. Cossmann, and H.J. Richter, *Prediction of bubble concentration profiles in vertical turbulent two-phase flow.* International journal of multiphase flow, 1985. **11**(5): p. 629-641.

107. Morriss, S. and A. Hill. *Measurement of Velocity Profiles in Upwards Oil/Water Flow Using Ultrasonic Doppler Velocimetry*. in *SPE Annual Technical Conference and Exhibition*. 1991. Society of Petroleum Engineers.

108. Farrar, B. and H. Bruun, *A computer based hot-film technique used for flow measurements in a vertical kerosene-water pipe flow.* International journal of multiphase flow, 1996. **22**(4): p. 733-751.

109. Hasan, A. and C. Kabir, *A simplified model for oil/water flow in vertical and deviated wellbores.* SPE production & facilities, 1999. **14**(01): p. 56-62.

110. Hua, L., et al., *Measurement of oil volume fraction and velocity distributions in vertical oil-in-water flows using ERT and a local probe.* Journal of Zhejiang University Science A, 2005. **6**(12): p. 1412-1415.

111. Zhao, D., et al., *Experimental study on local characteristics of oil–water dispersed flow in a vertical pipe.* International journal of multiphase flow, 2006. **32**(10): p. 1254-1268.

112. Hu, B., et al., *Mean and turbulent fluctuating velocities in oil–water vertical dispersed flows.* Chemical engineering science, 2007. **62**(4): p. 1199-1214.

113. Hamad, F. and S. He, *Evaluation of hot-film, dual optical and Pitot tube probes for liquid–liquid two-phase flow measurements.* Flow Measurement and Instrumentation, 2010. **21**(3): p. 302-311.

114. Rinne, A. and R. Loth, *Development of local two-phase flow parameters for vertical bubbly flow in a pipe with sudden expansion.* Experimental thermal and fluid science, 1996. **13**(2): p. 152-166.

115. Hamad, F., F. Imberton, and H. Bruun, *An optical probe for measurements in liquid-liquid two-phase flow.* Measurement science and technology, 1997. **8**(10): p. 1122.

116. Cartellier, A., *Measurement of gas phase characteristics using new monofiber optical probes and real-time signal processing.* Nuclear engineering and design, 1998. **184**(2): p. 393-408.

117. Barrau, E., et al., *Single and double optical probes in air-water two-phase flows: real time signal processing and sensor performance.* International journal of multiphase flow, 1999. **25**(2): p. 229-256.

118. Hamad, F., B. Pierscionek, and H. Bruun, *A dual optical probe for volume fraction, drop velocity and drop size measurements in liquid-liquid two-phase flow.* Measurement Science and Technology, 2000. **11**(9): p. 1307.

119. Guet, S., S. Luther, and G. Ooms, *Bubble shape and orientation determination with a four-point optical fibre probe.* Experimental thermal and fluid science, 2005. **29**(7): p. 803-812.

120. Xue, J., et al., *Bubble velocity, size, and interfacial area measurements in a bubble column by four-point optical probe.* AIChE Journal, 2008. **54**(2): p. 350-363.

121. Shen, X., et al., *Methodological improvement of an intrusive four-sensor probe for the multi-dimensional two-phase flow measurement.* International journal of multiphase flow, 2005. **31**(5): p. 593-617.

122. Vejražka, J., et al., *Measurement accuracy of a mono-fiber optical probe in a bubbly flow.* International journal of multiphase flow, 2010. **36**(7): p. 533-548.

123. Neal, L. and S. Bankoff, *A high resolution resistivity probe for determination of local void properties in gas-liquid flow.* AIChE Journal, 1963. **9**(4): p. 490-494.

124. Serizawa, A., I. Kataoka, and I. Michiyoshi, *Turbulence structure of air-water bubbly flow—II. Local properties.* International Journal of Multiphase Flow, 1975. **2**(3): p. 235-246.

125. Serizawa, A., I. Kataoka, and I. Michiyoshi, *Turbulence structure of air-water bubbly flow—III. Transport properties.* International journal of multiphase flow, 1975. **2**(3): p. 247-259.

126. Buchholz, R. and K. Schügerl, *Bubble column bioreactors.* European journal of applied microbiology and biotechnology, 1979. **6**(4): p. 301-313.

127. Van Der Welle, R., *Void fraction, bubble velocity and bubble size in two-phase flow.* International journal of multiphase flow, 1985. **11**(3): p. 317-345.

128. Herringe, R.t. and M. Davis, *Structural development of gas-liquid mixture flows.* J. Fluid Mech, 1976. **73**(1): p. 97-123.

129. Liu, T., *Bubble size and entrance length effects on void development in a vertical channel.* International journal of multiphase flow, 1993. **19**(1): p. 99-113.

130. Wu, Q., et al., *Theoretical studies on the design criteria of double-sensor probe for the measurement of bubble velocity.* Flow Measurement and Instrumentation, 2001. **12**(1): p. 43-51.

131. Kataoka, I., M. Ishii, and A. Serizawa, *Sensitivity analysis of bubble size and probe geometry on the measurements of interfacial area concentration in gas-liquid two-phase flow.* Nuclear engineering and design, 1994. **146**(1): p. 53-70.

132. Cheremisinoff, N.P., *Review of experimental methods for studying the hydrodynamics of gas-solid fluidized beds.* Industrial & Engineering Chemistry Process Design and Development, 1986. **25**(2): p. 329-351.

133. Kocamustafaogullari, G. and Z. Wang, *An experimental study on local interfacial parameters in a horizontal bubbly two-phase flow.* International journal of multiphase flow, 1991. **17**(5): p. 553-572.

134. Felder, S. and H. Chanson, *Phase-detection probe measurements in high-velocity free-surface flows including a discussion of key sampling parameters.* Experimental Thermal and Fluid Science, 2015. **61**(0): p. 66-78.

135. Mishra, R., G. Lucas, and H. Kieckhoefer, *A model for obtaining the velocity vectors of spherical droplets in multiphase flows from measurements using an orthogonal four-sensor probe.* Measurement Science and Technology, 2002. **13**(9): p. 1488.

136. Steinemann, J. and R. Buchholz, *Application of an Electrical Conductivity Microprobe for the Characterization of bubble behavior in gas-liquid bubble flow.* Particle & Particle Systems Characterization, 1984. **1**(1-4): p. 102-107.

137. Le Corre, J.-M. and M. Ishii, *Numerical evaluation and correction method for multi-sensor probe measurement techniques in two-phase bubbly flow.* Nuclear engineering and design, 2002. **216**(1): p. 221-238.

138. Kim, S., et al., *Development of the miniaturized four-sensor conductivity probe and the signal processing scheme.* International journal of heat and mass transfer, 2000. **43**(22): p. 4101-4118.

139. Lucas, G. and R. Mishra, *Measurement of bubble velocity components in a swirling gas–liquid pipe flow using a local four-sensor conductance probe.* Measurement Science and Technology, 2005. **16**(3): p. 749.

140. Pradhan, S., et al., *Optimal design of a four-sensor probe system to measure the flow properties of the dispersed phase in bubbly air–water multiphase flows.* Sensors and Actuators A: Physical, 2013. **201**: p. 10-22.

141. Muñoz-Cobo, J.L., et al., *Simulation of bubbly flow in vertical pipes by coupling Lagrangian and Eulerian models with 3D random walks models: Validation with experimental data using*

multi-sensor conductivity probes and Laser Doppler Anemometry. Nuclear Engineering and Design, 2012. **242**: p. 285-299.

142. Shen, X. and H. Nakamura, *Local interfacial velocity measurement method using a four-sensor probe.* International Journal of Heat and Mass Transfer, 2013. **67**: p. 843-852.

143. Smith, T., et al., *Two-phase flow structure in large diameter pipes.* International Journal of Heat and Fluid Flow, 2012. **33**(1): p. 156-167.

144. Euh, D.-J., et al., *Development of the interfacial area concentration measurement method using a five sensor conductivity probe.* JOURNAL-KOREAN NUCLEAR SOCIETY, 2000. **32**(5): p. 433-445.

145. Liu, W., N.N. Clark, and A.I. Karamavruc, *General method for the transformation of chord-length data to a local bubble-size distribution.* AIChE journal, 1996. **42**(10): p. 2713-2720.

146. CHIBA, T., K. TERASHIMA, and H. KOBAYASHI, *Lateral distribution of bubble sizes in two-dimensional gas-fluidized bed.* Journal of Chemical Engineering of Japan, 1975. **8**(2): p. 167-169.

147. Lim, K. and P.K. Agarwal, *Conversion of pierced lengths measured at a probe to bubble size measures: an assessment of the geometrical probability approach and bubble shape models.* Powder technology, 1990. **63**(3): p. 205-219.

148. Rowe, P. and R. Matsuno, *Single bubbles injected into a gas fluidised bed and observed by X-rays.* Chemical Engineering Science, 1971. **26**(6): p. 923-935.

149. Werther, J.t. and O. Molerus, *The local structure of gas fluidized beds—I. A statistically based measuring system.* International Journal of Multiphase Flow, 1973. **1**(1): p. 103-122.

150. Clark, N.N. and R. Turton, *Chord length distributions related to bubble size distributions in multiphase flows.* International Journal of Multiphase Flow, 1988. **14**(4): p. 413-424.

151. Merzkirch, W., et al., *Fluid mechanics of flow metering*. 2005: Springer.

152. Ltd, M.C.P. *Stepper Motors*. [image] 2015 [cited 2015 20/01]; Available from: https://www.motioncontrolproducts.co.uk/sections/2/stepper_motors/.

153. **GATES MECTROL, I.** *Timing Belt Theory*. [Belt Theory] 2006 [cited 2015 01/05]; Available from: http://www.gatesmectrol.com/mectrol/downloads/download_common.cfm?file=Belt_Theory06sm.pdf&folder=brochure.

154. RS. *Arduino Uno SMD Rev3* [Image] [cited 2015 20/05]; Available from: http://uk.rs-online.com/web/p/product/7697409/?grossPrice=Y&cm_mmc=UK%7CShopping-_-Google+PLA-_-Arduino%7CProcessor+%26+Microcontroller+Development+Kits-_-7697409&kpid=&kpid=7697409&istCompanyId=f7e7b05b-2daf-4c0e-8825-3633baf8113b&istItemId=xwirtlxtm&istBid=tzit&gclid=Cj0KEQjwkIurBRDwoZfi1bGCxocBEiQAmcs-eolFB_zOil-c4s3frc6jgcV9PDkP0hgYgiAoKHRPIAkaAqcR8P8HAQ.

155. *Parker O-Ring Handbook ORD 5700*. 2007: Cleveland, OH. p. 292.

156. Solutions, T.S. *O-ring calculator*. [O-ring Calculator] [cited 2015 05/04]; Available from: http://tss-static.com/remotemedia/media/globalformastercontent/servicetools/flash/index.html.

157. Persson, B.N.J., *On the theory of rubber friction.* Surface Science, 1998. **401**(3): p. 445-454.

158. *Grounding Considerations for Improved Measurements*. 2015 [cited 2015 25/07]; Available from: http://www.ni.com/white-paper/3394/en/.

159. Pradhan, S., *Measurement of Bubble Velocity Vectors in Bubbly Air Water Multiphase Flow*. 2010, University of Huddersfield.

160. Glaister, P., *Intersecting Chords Theorem 30 years on.* Mathematics in School, 2007. **36**(1): p. 22-22.

161. Cain, S.A., *Design of a shrouded probe for airborne aerosol sampling*. 1994, State University of New York at Buffalo.

162. Depolt, T. and W. Koschel. *Investigation on optimizing the design process of multi-hole pressure probes for transonic flow with panel methods*. in *Instrumentation in Aerospace Simulation Facilities, 1991. ICIASF'91 Record., International Congress on*. 1991. IEEE.

163. Devia, F. and M. Fossa, *Design and optimisation of impedance probes for void fraction measurements.* Flow Measurement and Instrumentation, 2003. **14**(4): p. 139-149.

164. Dobrowolski, B., M. Kabaciński, and J. Pospolita, *A mathematical model of the self-averaging Pitot tube: A mathematical model of a flow sensor.* Flow Measurement and Instrumentation, 2005. **16**(4): p. 251-265.

165. Gupta, P., et al., *A novel signal filtering methodology for obtaining liquid phase tracer responses from conductivity probes.* Flow Measurement and Instrumentation, 2000. **11**(2): p. 123-131.

166. Lucas, G. and N. Jin, *Measurement of the homogeneous velocity of inclined oil-in-water flows using a resistance cross correlation flow meter.* Measurement Science and Technology, 2001. **12**(9): p. 1529.

167. mathworks. *fsolve Algorithms*. 2017 [cited 2017 12.03]; Available from: http://uk.mathworks.com/help/optim/ug/choosing-the-algorithm.html?requestedDomain=uk.mathworks.com.

168. Menter, F., et al. *The SST turbulence model with improved wall treatment for heat transfer predictions in gas turbines*. in *Proceedings of the international gas turbine congress*. 2003.

169. ANSYSFLUENT14.5, *ANSYS FLUENT Theory Guide*. 2012, ANSYS, Inc.: Canonsburg, PA, USA.

170. Bugeau, A. and P. Pérez, *Detection and segmentation of moving objects in complex scenes.* Computer Vision and Image Understanding, 2009. **113**(4): p. 459-476.

171. Schäfer, R., C. Merten, and G. Eigenberger, *Bubble size distributions in a bubble column reactor under industrial conditions.* Experimental Thermal and Fluid Science, 2002. **26**(6): p. 595-604.

172. Krepper, E., D. Lucas, and H.-M. Prasser, *On the modelling of bubbly flow in vertical pipes.* Nuclear Engineering and Design, 2005. **235**(5): p. 597-611.

173. Chen, Z., et al., *Distributions of flow regimes and phase holdups in three-phase fluidized beds.* Chemical engineering science, 1995. **50**(13): p. 2153-2159.

174. Prasser, H.-M., et al., *Evolution of the structure of a gas–liquid two-phase flow in a large vertical pipe.* Nuclear Engineering and Design, 2007. **237**(15): p. 1848-1861.

175. Hibiki, T., S. Hogsett, and M. Ishii, *Local measurement of interfacial area, interfacial velocity and liquid turbulence in two-phase flow.* Nuclear Engineering and Design, 1998. **184**(2): p. 287-304.

Appendix A. *Signal processing code*

```
%*-*-*-*-*-*-*-*-*-*-*-*-*-*-*-*-*-*-*-*-*-*-*-*-*-*-*-*-*-*-*-*-*-*-*-*-*-*-*%
%                    Data analysing for Seven-sensor probe                    %
%*-*-*-*-*-*-*-*-*-*-*-*-*-*-*-*-*-*-*-*-*-*-*-*-*-*-*-*-*-*-*-*-*-*-*-*-*-*-*%
Close all;
clear all;
clc;
%*-*-*-*-*-*-*-*-*-*-*-*-*-*-*-*-*-*-*-*-*-*-*-*-*-*-*-*-*-*-*-*-*-*-*-*-*-*-*
Fs = 30000;                                          % Sampling frequency %
                                                                 % Sampling time %
Tp = 600000;                                         % Sampling period %
Er=1;
Er1=zeros(250,1);
CC=0.0;
TH=0.2;

%*-*-*-*-*-*-*-*-*-*-*-*-*-*-*-*-*-*-*-*-*-*-*-*-*-*-*-*-*-*-*-*-*-*-*-*-*-*-*
% Load the data file and divide the data to seven data
%*-*-*-*-*-*-*-*-*-*-*-*-*-*-*-*-*-*-*-*-*-*-*-*-*-*-*-*-*-*-*-*-*-*-*-*-*-*-*
cd('C:\Users\U1370250\Desktop\QDQ\19-06-2015');
Data =load('THE_BEST_SIGNAL.txt');
%Data = 7-sensor;
Data_1 = Data(:,1);
Data_2 = Data(:,2);
Data_3 = Data(:,3);
Data_4 = Data(:,4);
Data_5 = Data(:,5);
Data_6 = Data(:,6);
Data_7 = Data(:,7);
plot(Data_1,'r');
hold on;
plot(Data_2,'y');
hold on;
plot(Data_3,'g');
hold on;
```

```
plot(Data_4,'b');
hold on;
plot(Data_5,'k');
hold on;
plot(Data_6,'c');
hold on;
plot(Data_7,'m')
figure(1);
%*-*-*-*-*-*-*-*-*-*-*-*-*-*-*-*-*-*-*-*-*-*-*-*-*-*-*-*-*-%
%                              Finding the threshold voltage
%*-*-*-*-*-*-*-*-*-*-*-*-*-*-*-*-*-*-*-*-*-*-*-*-*-*-*-*-*-%
k=1;
for     TH=0.01:0.01:2
        MAX_DATA1 = max(Data_1);
        MAX_DATA2 = max(Data_2);
        MAX_DATA3 = max(Data_3);
        MAX_DATA4 = max(Data_4);
        MAX_DATA5 = max(Data_5);
        MAX_DATA6 = max(Data_6);
        MAX_DATA7 = max(Data_7);
        THRESH1= MAX_DATA1-TH;
        THRESH2= MAX_DATA2-TH;
        THRESH3= MAX_DATA3-TH;
        THRESH4= MAX_DATA4-TH;
        THRESH5= MAX_DATA5-TH;
        THRESH6= MAX_DATA6-TH;
        THRESH7= MAX_DATA7-TH;
        Data_1 = Data_1-THRESH1;
        Data_2 = Data_2-THRESH2;
        Data_3 = Data_3-THRESH3;
        Data_4 = Data_4-THRESH4;
        Data_5 = Data_5-THRESH5;
        Data_6 = Data_6-THRESH6;
        Data_7 = Data_7-THRESH7;
%-*-*-*-*-*-*-*-*-*-*-*-*-*-*-*-*-*-*-*-*-*-*-*-*-*-*-*-*-*%
```

```
%                    Median Filter                      %
%-*-*-*-*-*-*-*-*-*-*-*-*-*-*-*-*-*-*-*-*-*-*-*-*-*-*-*-*-*%
        figure(2);
        Data_1= medfilt1(Data_1,20);
        plot(Data_1,'r');
        hold on;
        Data_2= medfilt1(Data_2,20);
        plot(Data_2,'y');
        hold on;
        Data_3= medfilt1(Data_3,20);
        plot(Data_3,'g');
        hold on;
        Data_4= medfilt1(Data_4,20);
        plot(Data_4,'b');
        hold on;
        Data_5= medfilt1(Data_5,20);
        plot(Data_5,'k');
        hold on;
        Data_6= medfilt1(Data_6,20);
        plot(Data_6,'c');
        hold on;
        Data_7= medfilt1(Data_7,20);
        plot(Data_7,'m');
        hold on;
%*-*-*-*-*-*-*-*-*-*-*-*-*-*-*-*-*-*-*-*-*-*-*-*-*-*-*-*-*-*-*-*-*-*-*-*-%
% Finding the points that bubble touches the seven sensors %
%*-*-*-*-*-*-*-*-*-*-*-*-*-*-*-*-*-*-*-*-*-*-*-*-*-*-*-*-*-*-*-*-*-*-*-*-%
        touch_1=0;
        touch_2=0;
        touch_3=0;
        touch_4=0;
        touch_5=0;
        touch_6=0;
        touch_7=0;
        j = 1;
```

```
for i=1:(length(Data_1)-1)
  if Data_1(i)>0&&Data_1(i+1)<0
            touch_1(j)=i;
                    j= j+1;
            end
            if Data_1(i)<0&&Data_1(i+1)>0

            touch_1(j)=i;
             j= j+1;
            end
end
j = 1;
for i=1:(length(Data_2)-1)
            if Data_2(i)>0&&Data_2(i+1)<0
            touch_2(j)=i;
            j= j+1;
end
            if Data_2(i)<0&&Data_2(i+1)>0

            touch_2(j)=i;
            j= j+1;
end
end
j = 1;
for i=1:(length(Data_3)-1)
            if Data_3(i)>0&&Data_3(i+1)<0
            touch_3(j)=i;
            j= j+1;
            end
            if Data_3(i)<0&&Data_3(i+1)>0
             touch_3(j)=i;
             j= j+1;
  end
end
j = 1;
```

```
        for i=1:(length(Data_4)-1)
                if Data_4(i)>0&&Data_4(i+1)<0
                touch_4(j)=i;
                  j= j+1;
                end
                if Data_4(i)<0&&Data_4(i+1)>0

                touch_4(j)=i;
       j= j+1;
    end
end
j = 1;
for i=1:(length(Data_5)-1)
    if Data_5(i)>0&&Data_5(i+1)<0
       touch_5(j)=i;
       j= j+1;
    end
    if Data_5(i)<0&&Data_5(i+1)>0

       touch_5(j)=i;
       j= j+1;
    end
end
j = 1;
for i=1:(length(Data_6)-1)
    if Data_6(i)>0&&Data_6(i+1)<0
       touch_6(j)=i;
       j= j+1;
    end
    if Data_6(i)<0&&Data_6(i+1)>0
       touch_6(j)=i;
       j= j+1;
    end
end
j = 1;
```

```
for i=1:(length(Data_7)-1)
    if Data_7(i)>0&&Data_7(i+1)<0
        touch_7(j)=i;
        j= j+1;
    end
    if Data_7(i)<0&&Data_7(i+1)>0

        touch_7(j)=i;
        j= j+1;
    end
end
Int_1s=0.0;
for i=1:(length(touch_1)-1)
    Int_1= touch_1(i+1)-touch_1(i);
    Int_1s=Int_1s+Int_1;
end
Vf_1=Int_1s/Tp;
Int_2s=0.0;
for i=1:(length(touch_2)-1)
    Int_2= touch_2(i+1)-touch_2(i);
    Int_2s=Int_2s+Int_2;
end
Vf_2=Int_2s/Tp;
Int_3s=0.0;
for i=1:(length(touch_3)-1)
    Int_3= touch_3(i+1)-touch_3(i);
    Int_3s=Int_3s+Int_3;
end
Vf_3=Int_3s/Tp;
Int_4s=0.0;
for i=1:(length(touch_4)-1)
    Int_4= touch_4(i+1)-touch_4(i);
    Int_4s=Int_4s+Int_4;
end
Vf_4=Int_4s/Tp;
```

```
    Int_5s=0.0;
    for i=1:(length(touch_5)-1)
        Int_5= touch_5(i+1)-touch_5(i);
        Int_5s=Int_5s+Int_5;
    end
    Vf_5=Int_5s/Tp;
    Int_6s=0.0;
    for i=1:(length(touch_6)-1)
        Int_6= touch_6(i+1)-touch_6(i);
        Int_6s=Int_6s+Int_6;
    end
    Vf_6=Int_6s/Tp;
    Int_7s=0.0;
    for i=1:(length(touch_7)-1)
        Int_7 = touch_7(i+1)-touch_7(i);
        Int_7s=Int_7s+Int_7;
    end
    Vf_7=Int_7s/Tp;

    k=k+1;
    Vf_t= [Vf_2 Vf_3 Vf_4 Vf_5 Vf_6 Vf_7];
    Vf_M= mean(Vf_t);
    CC=CC+1;
    Er1(CC)=abs(Vf_1- Vf_M);
    if Er1(CC)<=Er;
        Er=Er1(CC);
    end

end
m =1;
min_touch = [length(touch_1),
length(touch_2),length(touch_3),length(touch_4),length(touch_5),length(touch_6),length(touch_7)];
times_touch = min(min_touch);
maybe_right_touch = 0;
judge_T = 0.01/T;
```

```
i = 1;
j = 1;
while j < times_touch
   if touch_1(i)< touch_2(i)
      if touch_1(i)<touch_3(i)
         if touch_1(i)<touch_4(i)
            if touch_1(i)<touch_5(i)
               if touch_1(i)<touch_6(i)
                  if touch_1(i)<touch_7(i)
                     max_judge =
[touch_1(i+1),touch_2(i+1),touch_3(i+1),touch_4(i+1),touch_5(i+1),touch_6(i+1),touch_7(i+1)];
                     interval_begin_end = max(max_judge)-touch_1(i);
                     if interval_begin_end<=judge_T
                        maybe_right_touch(m) = touch_1(i);
                        maybe_right_touch(m+2) = touch_2(i);
                        maybe_right_touch(m+4) = touch_3(i);
                        maybe_right_touch(m+6) = touch_4(i);
                        maybe_right_touch(m+8) = touch_5(i);
                        maybe_right_touch(m+10) = touch_6(i);
                        maybe_right_touch(m+12) = touch_7(i);
                        maybe_right_touch(m+1) = touch_1(i+1);
                        maybe_right_touch(m+3) = touch_2(i+1);
                        maybe_right_touch(m+5) = touch_3(i+1);
                        maybe_right_touch(m+7) = touch_4(i+1);
                        maybe_right_touch(m+9) = touch_5(i+1);
                        maybe_right_touch(m+11) = touch_6(i+1);
                        maybe_right_touch(m+13) = touch_7(i+1);
                        m= m+14;
                        touch_1 = touch_1(i+2:length(touch_1));
                        touch_2 = touch_2(i+2:length(touch_2));
                        touch_3 = touch_3(i+2:length(touch_3));
                        touch_4 = touch_4(i+2:length(touch_4));
                        touch_5 = touch_5(i+2:length(touch_5));
                        touch_6 = touch_6(i+2:length(touch_6));
                        touch_7 = touch_7(i+2:length(touch_7));
```

```
                    i = 1;
                    j = j+2;
                    min_touch_temp =
[length(touch_1),length(touch_2),length(touch_3),length(touch_4),length(touch_5),length(touch_6),
length(touch_7)];
                    if min(min_touch_temp)==0
                        j = times_touch+1;
                    end
                else
                    touch_1 = touch_1(i+2:length(touch_1));
                    i = 1;
                    if length(touch_1)==0
                        j = times_touch+1;
                    end
                end
            else
                touch_7 = touch_7(i+2:length(touch_7));
                i = 1;
                if length(touch_7)==0
                    j = times_touch+1;
                end
            end
        else
            touch_6 = touch_6(i+2:length(touch_6));
            i = 1;
            if length(touch_6)==0
                j = times_touch+1;
            end
        end
    else
        touch_5 = touch_5(i+2:length(touch_5));
        i = 1;
        if length(touch_5)==0
            j = times_touch+1;
        end
```

```
            end
        else
            touch_4 = touch_4(i+2:length(touch_4));
            i = 1;
            if length(touch_4)==0
                j = times_touch+1;
            end
        end
    else
        touch_3 = touch_3(i+2:length(touch_3));
        i = 1;
        if length(touch_3)==0
            j = times_touch+1;
        end
    end
else
    touch_2 = touch_2(i+2:length(touch_2));
    i = 1;
    if length(touch_2)==0
        j = times_touch+1;
    end
end
end
maybe_right_touch;
num_bubble = length(maybe_right_touch)/14;
right_touch = rand(num_bubble,14);
for i = 1:num_bubble
    for j = 1:14
        right_touch(i,j) = maybe_right_touch(j);
    end
    k = 15;
    maybe_right_touch = maybe_right_touch(k:length(maybe_right_touch));
end
right_touch;
%*-*-*-*-*-*-*-*-*-*-*-*-*-*-*-*-*-*-*-*-*-*-*-*-*-*-*-*-*-*-*-*-*-*-*-*-*%
```

```
unit = 0.000001;      % Micrometre %
%*-*-*-*-*-*-*-*-*-*-*-*-*-*-*-*-*-*-*-*-*-*-*-*-*-*-*-*-*-*-*-*-*-*-*-*-*-*-*-*-*-*%
%       The seven-sensor probe dimensions (measured 20_oct)   %
%*-*-*-*-*-*-*-*-*-*-*-*-*-*-*-*-*-*-*-*-*-*-*-*-*-*-*-*-*-*-*-*-*-*-*-*-*-*-*-*-*-*%
global X1;
global X2;
global X3;
global X4;
global X5;
global X6;
global Y1;
global Y2;
global Y3;
global Y4;
global Y5;
global Y6;
global Z1;
global Z2;
global Z3;
global Z4;
global Z5;
global Z6;
X1 = 0.21158/1000;
X2 =-0.905474/1000;
X3 = -1.200210/1000;
X4 = -0.2526315/1000;
X5 = 0.8421/1000;
X6 = 1.1578947/1000;
Y1 = -1.474316/1000;
Y2 = -0.905263/1000;
Y3 = 0.21158/1000;
Y4 = 0.947368/1000;
Y5 = 0.73705/1000;
Y6 = -0.442105/1000;
Z1 = 1.03/1000;
```

```
Z2 = 1.07/1000;
Z3 = 0.616;
Z4 = 0.868/1000;
Z5 = 1.24/1000;
Z6 = 0.868/1000;
%*-*-*-*-*-*-*-*-*-*-*-*-*-*-*-*-*-*-*-*-*-*-*-*-*-*-*-*-*-*-*-*-*-*-*-*-*-*%
%          The seven time intervals (dt) calculation          %
%*-*-*-*-*-*-*-*-*-*-*-*-*-*-*-*-*-*-*-*-*-*-*-*-*-*-*-*-*-*-*-*-*-*-*-*-*-*%
dt_numb = zeros(num_bubble,7);
for m = 1:num_bubble
   dt0 = (right_touch(m,2)-right_touch(m,1))*T;
   dt_1 = (right_touch(m,3)-right_touch(m,1))*T;
   dt_2 = (right_touch(m,5)-right_touch(m,1))*T;
   dt_3 = (right_touch(m,7)-right_touch(m,1))*T;
   dt_4 = (right_touch(m,9)-right_touch(m,1))*T;
   dt_5 = (right_touch(m,11)-right_touch(m,1))*T;
   dt_6 = (right_touch(m,13)-right_touch(m,1))*T;
   dt_numb (m,:) = [dt0,dt_1,dt_2,dt_3,dt_4,dt_5,dt_6];
end
dt_numb;
% ME=mean(dt_numb);
ME=dt_numb;
global dt1;
global dt2;
global dt3;
global dt4;
global dt5;
global dt6;
dt1= ME(1,2);
dt2= ME(1,3);
dt3= ME(1,4);
dt4= ME(1,5);
dt5= ME(1,6);
dt6= ME(1,7);
guess=[0.1,0.1,1.1,0.01,0.01,0.1];
```

```
options = optimset('Display','off');
[result, fval, exitflag, outout]=fsolve(@eqsensor,guess,options);
Vx=result(1,1);
Vy=result(1,2);
Vz=result(1,3);
RX=abs(result(1,4));
RY=abs(result(1,5));
RZ=abs(result(1,6));
disp( '.-.-.-.-.-.-.-.-.-.-.-.-.-.-.-.-.-.-.-.-.-.-.-.-.-.-.-.-.-.-.-.-.-.-.-.-.')
disp( '      Vx        Vy        Vz        Rx        Ry        Rz')
disp( '     ----      ----      ----      ----      ----      ----')
disp( result)
disp( '.-.-.-.-.-.-.-.-.-.-.-.-.-.-.-.-.-.-.-.-.-.-.-.-.-.-.-.-.-.-.-.-.-.-.-.-.')
Bubble_Velocity=(Vx^2+Vy^2+Vz^2)^1/2
disp ('The volume fraction='); disp(Vf_M);
figure(3)
[xs,ys,zs] = ellipsoid(0,0,0,RX,RY,RZ,200);
surf(xs, ys, zs);
hMesh = mesh(xs,ys,zs);
colormap (gray);
function fseven=eqsensor_cc(z)
global dt1;
global dt2;
global dt3;
global dt4;
global dt5;
global dt6;
global X1;
global X2;
global X3;
global X4;
global X5;
global X6;
global Y1;
global Y2;
```

```
global Y3;
global Y4;
global Y5;
global Y6;
global Z1;
global Z2;
global Z3;
global Z4;
global Z5;
global Z6;
Vx=z(1);
Vy=z(3);
Vz=z(2);
Rx=z(4);
Ry=z(5);
Rz=z(6);
fseven(1)=((dt1^2)*(Vx.^2))+(dt1^2*Vy.^2)+(dt1^2*Vz.^2)+-(2*dt1*Vx*Rx)-(2*dt1*Vy*Ry)-
(2*dt1*Vz*Rz)-(2*dt1*X1*Vx)-(2*dt1*Y1*Vy)-...
 (2*dt1*Z1*Vz)+(X1.^2)+(Y1.^2)+(Z1.^2)+(2*X1*Rx)+(2*Y1*Ry)+(2*Z1*Rz);
fseven(2)=(dt2^2*Vx.^2)+(dt2^2*Vy.^2)+(dt2^2*Vz.^2)-(2*dt2*Vx*Rx)-(2*dt2*Vy*Ry)-(2*dt2*Vz*Rz)-
(2*dt2*X2*Vx)-(2*dt2*Y2*Vy)-...
 (2*dt2*Z2*Vz)+(X2.^2)+(Y2.^2)+(Z2.^2)+(2*X2*Rx)+(2*Y2*Ry)+(2*Z2*Rz);
fseven(3)=(dt3^2*Vx.^2)+(dt3^2*Vy.^2)+(dt3^2*Vz.^2)-(2*dt3*Vx*Rx)-(2*dt3*Vy*Ry)-(2*dt3*Vz*Rz)-
(2*dt3*X3*Vx)-(2*dt3*Y3*Vy)-...
 (2*dt3*Z3*Vz)+(X3.^2)+(Y3.^2)+(Z3.^2)+(2*X3*Rx)+(2*Y3*Ry)+(2*Z3*Rz);
fseven(4)=(dt4^2*Vx.^2)+(dt4^2*Vy.^2)+(dt4^2*Vz.^2)-(2*dt4*Vx*Rx)-(2*dt4*Vy*Ry)-(2*dt4*Vz*Rz)-
(2*dt4*X4*Vx)-(2*dt4*Y4*Vy)-...
 (2*dt4*Z4*Vz)+(X4.^2)+(Y4.^2)+(Z4.^2)+(2*X4*Rx)+(2*Y4*Ry)+(2*Z4*Rz);
fseven(5)=(dt5^2*Vx.^2)+(dt5^2*Vy.^2)+(dt5^2*Vz.^2)-(2*dt5*Vx*Rx)-(2*dt5*Vy*Ry)-(2*dt5*Vz*Rz)-
(2*dt5*X5*Vx)-(2*dt5*Y5*Vy)-...
 (2*dt5*Z5*Vz)+(X5.^2)+(Y5.^2)+(Z5.^2)+(2*X5*Rx)+(2*Y5*Ry)+(2*Z5*Rz);
fseven(6)=(dt6^2*Vx.^2)+(dt6^2*Vy.^2)+(dt6^2*Vz.^2)-(2*dt6*Vx*Rx)-(2*dt6*Vy*Ry)-(2*dt6*Vz*Rz)-
(2*dt6*X6*Vx)-(2*dt6*Y6*Vy)-...
 (2*dt5*Z5*Vz)+(X5.^2)+(Y5.^2)+(Z5.^2)+(2*X5*Rx)+(2*Y6*Ry)+(2*Z6*Rz);
end
```

Appendix B. *Image processing code*

```
%*-*-*-*-*-*-*-*-*-*-*-*-*-*-*-*-*-*-*-*-*-*-*-*-*-*-*-*-*-*-*-*-*-*-*-*-*-*%
%              The Image processing Code                                      %
%*-*-*-*-*-*-*-*-*-*-*-*-*-*-*-*-*-*-*-*-*-*-*-*-*-*-*-*-*-*-*-*-*-*-*-*-*-*%
clc;
close all;
clear all;
movieObj = VideoReader('Y-Z1.AVI'); % open file
get(movieObj) % display all information about movie
nFrames = movieObj.NumberOfFrames;
width = movieObj.Width; % get image width
height = movieObj.Height; % get image height
% Read every other frame from this movie.
images = read(movieObj);
Frames=zeros(height,width,nFrames); % Height is Y axis, width is X axis therefore: (y,x).
for iFrame=1:10;
   I(:,:,:,iFrame) = images(:,:,:,iFrame); %?'Grayscale', without ?specifying'native'?uint8?
[H,W,1,iFrame]
end
frame01= I(:,:,1);
frame01=medfilt2(frame01,[5,5]);
imshow(frame01);
 foregroundDetector = vision.ForegroundDetector('NumGaussians', 3, ...
   'NumTrainingFrames', 50);
obj.blobAnalyser = vision.BlobAnalysis('BoundingBoxOutputPort', true, ...
   'AreaOutputPort', true, 'CentroidOutputPort', true, ...
   'MinimumBlobArea', 400);
videoReader = vision.VideoFileReader('Y-
Z1.AVI','ImageColorSpace','Intensity','VideoOutputDataType','uint8');
converter = vision.ImageDataTypeConverter;
opticalFlow = vision.OpticalFlow('ReferenceFrameDelay', 1);
opticalFlow.OutputValue = 'Horizontal and vertical components in complex form';
shapeInserter = vision.ShapeInserter('Shape','Lines','BorderColor','Custom', 'CustomBorderColor',
255);
videoPlayer = vision.VideoPlayer('Name','Motion Vector');
```

```
j=1;
AllArea=zeros();
AllPerimeter=zeros();
AllMajorAxis=zeros();
AllMinorAxis=zeros();
AllOrientation=zeros();
Allcentroidn=zeros();
Z=0; x1=0; y1=0;
ZZ=zeros(480,640,1000);
xxx1=[]; yyy1=[];
nextId = 1; % ID of the next track
% while ~isDone(videoReader)
for oo=1:150
   Z=Z+1;
   Frame = step(videoReader); % read the next video frame
   foreground = step(foregroundDetector, Frame);
   %     figure; imshow(Frame); title('Video Frame');
   %     figure; imshow(foreground); title('Foreground');
   se = strel('square', 1);
   filteredForeground = imopen(foreground, se);
   im =filteredForeground;
   im=bwareaopen(im, 50);
   im = imfill(im, 'holes');
   cc =bwconncomp(im,8);
   n =cc.NumObjects;   % The number of the bubbles in each frame
   Area = zeros(n,1);
   Perimeter = zeros(n,1);
   MajorAxis = zeros(n,1);
   MinorAxis = zeros(n,1);
   Orientation= zeros(n,1);
   centroid= zeros(n,1);
   k = regionprops(im,'Area','Perimeter','MajorAxisLength','MinorAxisLength', 'Centroid',
'Orientation');

   for i=1:n
```

```
Area(i) = k(i).Area;
Perimeter(i) = k(i).Perimeter;
MajorAxis(i)= k(i).MajorAxisLength;
MinorAxis(i) = k(i).MinorAxisLength;
Orientation(i) = k(i).Orientation;
centroid = cat(1,k.Centroid);  % Concatenate arrays along specified dimension
labeledImage = bwlabel(im);
allAreas =  Area(i);
figure(2); imshow(im); title('im fill');
hold on
phi = linspace(0,2*pi,50);  %Generate linearly spaced vector
cosphi = cos(phi);
sinphi = sin(phi);
for  po= 1:length(k)
    xbar = k(po).Centroid(1);
    ybar = k(po).Centroid(2);
    a = k(po).MajorAxisLength/2;
    b = k(po).MinorAxisLength/2;
    theta = pi*k(po).Orientation/180;
    R = [ cos(theta)   sin(theta)
       -sin(theta)   cos(theta)];
    xy = [a*cosphi; b*sinphi];
    xy = R*xy;
    x = xy(1,:) + xbar;
    y = xy(2,:) + ybar;
    plot(x,y,'r','LineWidth',2);
end
x1=centroid(:,1);
xx=round(x1);
y1=centroid(:,2);
yy=round(y1);
plot( xx,yy,'b*')
set(text,'Color','red')
text(xx+5,yy,num2str(centroid));
hold off
```

```
    end

    frame = step(videoReader);
    im = step(converter, frame);
    VSQ = step(opticalFlow, im);
    B_v_x_y(Z)= max(max(VSQ));
    B_v(Z)=abs(max(max(VSQ)));
    lines = videooptflowlines(VSQ, 50);
    if ~isempty(lines)
        out =  step(shapeInserter, im, lines);
        step(videoPlayer, out);
        opticFlow = opticalFlowFarneback;
    end
    AllArea(1:n,j)= Area;
    AllPerimeter(1:n,j)= Perimeter;
    AllMajorAxis(1:n,j)= MajorAxis;
    AllMinorAxis(1:n,j)= MinorAxis;
    AllOrientation(1:n,j)= Orientation;
    xxx1(1:n,Z)=x1;
    yyy1(1:n,Z)=y1;
    j=j+1;
end
Vx=((xxx1(1,16)-xxx1(1,20))*12.36/6.5)/1000
Vy=((yyy1(1,16)-yyy1(1,20))*12.36/6.5)/1000
release(videoReader);
AAREA=AllArea(find (AllArea>0));
Max_Area=max(max (AAREA));
Min_Area=min(min(AAREA));
Mean_Area=median(AAREA)*((12.36/65)^2);

PPerimeter=AllPerimeter(find (AllPerimeter>0));
Max_Perimeter=max(max (PPerimeter));
Min_Perimeter=min(min(PPerimeter));
Mean_Perimeter=(median(PPerimeter))*12.36/65;
```

```
MAllMajorAxis=AllMajorAxis(find (AllMajorAxis>0));
Max_MajorAxis=max(max (MAllMajorAxis));
Min_MajorAxis=min(min(MAllMajorAxis));
Mean_MajorAxis=median(MAllMajorAxis)*12.36/65

MAllMinorAxis=AllMinorAxis(find (AllMinorAxis>0));
Max_MinorAxis=max(max (MAllMinorAxis));
Min_MinorAxis=min(min(MAllMinorAxis));
Mean_MinorAxis=median(MAllMinorAxis)*12.36/65

hh=AllOrientation ((find (AllOrientation>5 & AllOrientation<50)));
Min_Orientation=min(min(hh));
Mean_Orientation=median(hh);

T = table( Mean_Area,Mean_Perimeter,Mean_MajorAxis,Mean_MinorAxis,Mean_Orientation, Vx,
Vy)
```

Appendix C. *LabVIEW code*

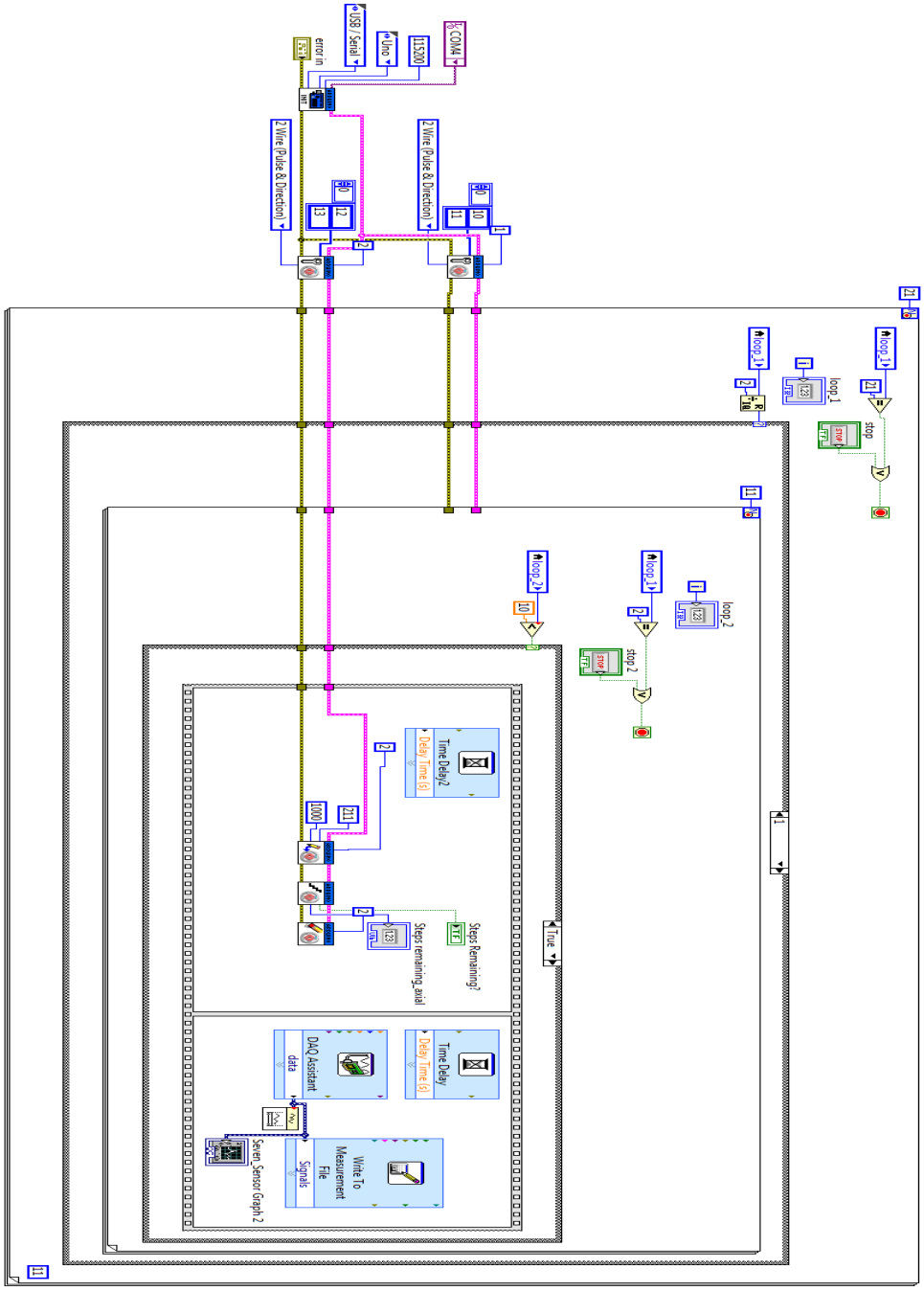

Figure C-1. Lab View code for traverse movement control.

Appendix D. *The coalescence and shearing off process in bubble*

CFD simulation of cap bubbles during the coalescence and shearing off process in bubble column.

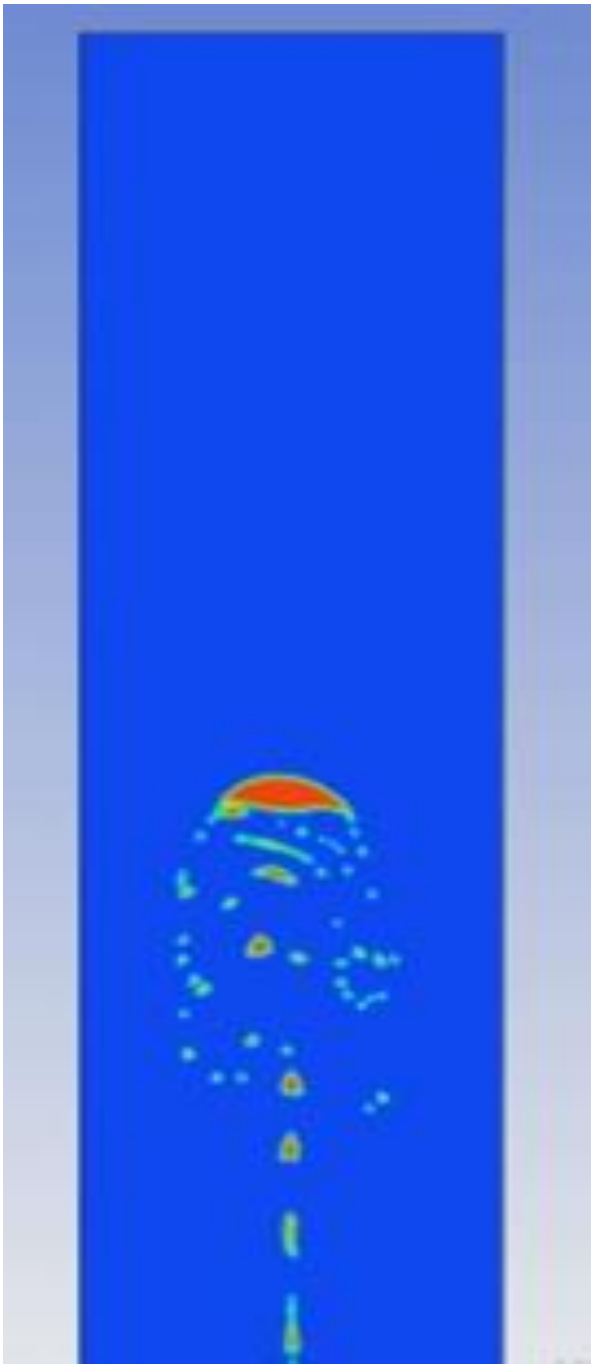

Figure D-1. Contour plot of bubble coalescence and shearing off process.

List of publications

- Albarzenji, D., Kartash, H., & Hamad, F. (2012). Simulation of kerosene-water two-phase flow in vertical and inclined pipes. WIT Transactions on Engineering Sciences, 81, 243-254.

- Albarzenji, D., Pradhan, S. R., Mishra, R., & Zala, K. (2014). Effect of a swirl on void fraction profiles in multiphase flows. Springer.

- Hamad, F. A., Albarzenji, D., & Ganesan, P. B. (2014). Study of kerosene–water two-phase flow characteristics in vertical and inclined pipes. *The Canadian Journal of Chemical Engineering*, *92*(5), 905-917.

- Freegah, B., Asim, T., Albarzenji, D., Pradhan, S. and Mishra, R. (2014) 'Effect of the shape of connecting pipes on the performance output of a closed-loop hot water solar Thermo-syphon'. In: 3rd International Workshop and Congress on eMaintenance, 17th - 18th June 2014, Lulea, Sweden

- Mishra, R., Albarzenji, D., Shrawasti, S., Sendanayake, I. and Pradhan, S. (2015) 'Flow diagnostics'. *In: FLUVISU 2015, 16th - 20th November 2015*, Pleumeur-Bodou/Lannion, France

- Albarzenji, D. and Mishra, R. (2017) 'A Novel Technique to Reduce Measurement Errors due to Flow–Sensor Interactions in Multi-Sensor Conductivity Probes'. In: COMADEM 2017, 10 -13 July 2017, University of Central Lancashire, Preston, UK.